Technische Universität München
TUM School of Engineering and Design

Improvement of geodetic reference frame and Earth orientation parameters by reduction of non-tidal loading effects in Very Long Baseline Interferometry

Matthias Glomsda

Vollständiger Abdruck der von der TUM School of Engineering and Design der Technischen Universität München zur Erlangung eines

Doktors der Ingenieurwissenschaften (Dr.-Ing.)

genehmigten Dissertation.

Vorsitz: Prof. Dr. rer. nat. Niklas Boers

Prüfer der Dissertation:

1. Prof. Dr.-Ing. Florian Seitz
2. Prof. Dr. Johannes Böhm,
   Technische Universität Wien
3. Prof. Dr. Benedikt Soja,
   Eidgenössische Technische Hochschule Zürich

Die Dissertation wurde am 22.11.2022 bei der Technischen Universität München eingereicht und durch die TUM School of Engineering and Design am 03.03.2023 angenommen.

Abstract

Accurate and stable terrestrial reference frames (TRF) are the basis for a wide range of applications of great scientific and socio-economic relevance. These include, e.g., navigation or the monitoring of physical processes related to geodynamics and global change. Reference frames are realizations of theoretical concepts, called reference systems. The International Terrestrial Reference System (ITRS), for example, is defined as a three-dimensional Cartesian coordinate system co-rotating with the Earth. Its realization, given by the positions of particular reference points within this system, is called International Terrestrial Reference Frame (ITRF). Four geodetic space techniques are used for its computation, i.e., Very Long Baseline Interferometry (VLBI), Satellite Laser Ranging (SLR), the Global Navigation Satellite Systems (GNSS), and Doppler Orbitography and Radio Positioning Integrated by Satellite (DORIS), and the positions of the corresponding observing stations define the reference points. These positions are not fixed but vary linearly with time within the ITRF and other secular TRFs, to approximate the long-term tectonic motion.

The solid Earth is continually deformed by, e.g., the gravitational forces of extra-terrestrial bodies like the sun and the moon, and by the centrifugal forces of the rotation of the Earth itself. The same forces further induce the permanent redistribution of air and water mass at the Earth's surface, and the gravitational potential of this mass creates additional deformations of the solid Earth. As a consequence, the instantaneous positions of the reference points on the Earth's surface are displaced from (but fairly fluctuating around) their secular TRF positions in a non-linear way. To approximate the pure linear motions of the reference points as good as possible, the non-linear effects/displacements must be reduced in the analysis of the observations of the geodetic space techniques.

One class of non-linear effects that is not conventionally reduced from the observations yet is non-tidal loading (NTL). It refers to the redistribution of air and water that cannot be attributed to the tidal forces, and the geophysical models for the description of surface displacements due to NTL are assumed to not be sufficiently accurate. Nevertheless, various studies indicate the benefits of the reduction of NTL in the analysis of the geodetic space techniques, and hence also a positive impact on the ITRS realization is expected.

In this thesis, which is based on four journal articles, we investigate the advantages of the reduction of NTL in the analysis of observations from VLBI. First, we take a look at NTL data sets provided by distinct institutions and computed from different

geophysical models. We aim to capture their properties and mutual agreement, and we examine their suitability for the application in both VLBI analysis and the computation of secular TRFs. Second, we revisit the mathematical model for the estimation of geodetic target parameters from the VLBI observations, such as station positions and the Earth orientation parameters (EOP). We explore the theoretical impact on the estimates when the surface displacements induced by NTL are applied at different levels of the model, which represent a rigorous and an approximate reduction.

After these preparatory steps, we actually reduce NTL in the analysis of about 40 years of VLBI observations. The last two articles are devoted to the different types of solutions, i.e., single-session and secular TRF solutions. The first type represents the separate estimation of target parameters from distinct VLBI sessions, which provides a (non-linear) time series of station positions, for example. The second type creates a VLBI-only TRF, which contains long-term linear station positions. It involves the combination of all the session-wise observations. The EOP can be estimated in both solutions, and the single-session solutions usually provide additional target (e.g., tropospheric) and auxiliary (e.g., clock) parameters.

We show that the reduction of NTL decreases the variability of the estimated positions and hence the residuals w.r.t. the long-term linear motions of the VLBI stations, especially in the single-session solutions. Since the secular TRFs take advantage of long observation time spans to filter out non-linear behaviour, mainly the positions and velocities of stations with only short observation histories (i.e., a few years) benefit from the reduction of NTL. In particular the hydrological component of the NTL contains a strong seasonal signal, and the reduction of the total NTL also lessens the amplitudes of the corresponding residual signals in the estimated station heights. The latter are highly correlated with tropospheric and clock parameters, and hence the aliasing between these parameters is mitigated as well. In most cases, the approximate application of the surface displacements provides results very close to those of the rigorous application. However, since the former includes a deterioration of the temporal resolution in the displacements, target parameters with enlarged time dependence such as the EOP rates are more sensitive to the application level. The impact on the EOP is generally smaller than for the station positions, but the former still profit from the diminished aliasing due to the latter being reduced by NTL.

In total, we support the reduction of NTL in VLBI analyses, albeit there is a model uncertainty for the hydrological component. Nevertheless, we observe improvements with all different data sets that we examine, and we assume that the impact of the reduction will be even more obvious when further error sources in the VLBI analysis are mitigated, or when the measurement precision is enhanced by the next generation VLBI Global Observing System (VGOS).

Zusammenfassung

Genaue und stabile erdgebundene Referenzrahmen (terrestrial reference frames, TRF) sind die Grundlage für eine breite Palette von Anwendungen von großer wissenschaftlicher und sozioökonomischer Bedeutung. Dazu gehören z.B. die Navigation oder die Beobachtung von physikalischen Prozessen der Geodynamik oder des globalen (Klima-) Wandels. Ein Referenzrahmen ist die Realisierung eines theoretischen Konstrukts, genannt Referenzsystem. Das Internationale Terrestrische Referenzsystem (ITRS) ist z.B. als ein dreidimensionales, kartesisches Koordinatensystem definiert, das mit der Erde rotiert. Seine Realisierung, die durch die Positionen bestimmter Referenzpunkte innerhalb dieses Systems gegeben ist, wird als Internationaler Terrestrischer Referenzrahmen (International Terrestrial Reference Frame, ITRF) bezeichnet. Für die Berechnung der Realisierung werden vier geodätische Raumverfahren verwendet, nämlich die Very Long Baseline Interferometry (VLBI), das Satellite Laser Ranging (SLR), die Global Navigation Satellite Systems (GNSS) und die Doppler Orbitography and Radio Positioning Integrated by Satellite (DORIS), und die Positionen der zugehörigen Beobachtungsstationen dienen gerade als die Referenzpunkte. Aufgrund von geodynamischen Prozessen sind diese Positionen jedoch nicht konstant. Im ITRF und in anderen säkularen TRFs werden langfristige, tektonische Plattenbewegungen als lineare Veränderungen der Stationspositionen beschrieben.

Die feste Erde unterliegt ständigen Verformungen, z.B. durch die Gravitationskräfte der Himmelskörper wie Sonne und Mond oder durch die Zentrifugalkräfte der Erdrotation. Die gleichen Kräfte (unter anderem) bewirken auch eine ständige Umverteilung der Luft- und Wassermassen auf der Erdoberfläche, und das Gravitationspotenzial dieser Massen bewirkt wiederum zusätzliche Verformungen der Erdkruste. Dies hat zur Folge, dass die tatsächlichen Positionen der Referenzpunkte auf der Erdoberfläche auf nichtlineare Weise von ihren säkularen TRF-Positionen abweichen, auch wenn sie im zeitlichen Verlauf in guter Näherung um die lineare Bewegung schwanken. Um die rein linearen Bewegungen der Referenzpunkte so gut wie möglich zu schätzen, müssen die nichtlinearen Effekte/Abweichungen bei der Analyse der Beobachtungen der geodätischen Raumverfahren reduziert werden.

Eine Klasse von nichtlinearen Effekten, die noch nicht per Konvention aus den Beobachtungen reduziert wird, sind die nicht-gezeitenbedingten Auflasteffekte (non-tidal loading, NTL). NTL bezieht sich auf den Anteil der Umverteilung von Luft- und Wassermassen auf der Erdoberfläche, der nicht auf die üblichen Gezeitenkräfte zurückgeführt werden kann. Die geophysikalischen Modelle zur Berechnung von Verformungen der Erdkruste aufgrund von NTL werden bislang zwar nicht als hinreichend genau

angesehen. Dennoch lassen die Ergebnisse diverser Studien darauf schließen, dass das Reduzieren von NTL bei der Analyse der geodätischen Raumverfahren zu einer Verbesserung der geschätzten Zielparameter führt. Daher kann auch eine positive Auswirkung auf die ITRS-Realisierungen erwartet werden.

In dieser Dissertation untersuchen wir die potenziellen Vorteile der Reduktion von NTL bei der Analyse von VLBI-Beobachtungen. Die Arbeit basiert im Wesentlichen auf vier Zeitschriftenartikeln, die unterschiedliche Aspekte behandeln. Als Erstes betrachten wir mehrere NTL-Datensätze, die von verschiedenen Institutionen zur Verfügung gestellt und mit unterschiedlichen geophysikalischen Modellen erzeugt wurden. Wir vergleichen ihre Eigenschaften und prüfen sie im Hinblick auf ihre Eignung für die Anwendung sowohl in der VLBI-Analyse als auch für die Berechnung eines säkularen TRF. Im zweiten Artikel rekapitulieren wir das mathematische Modell für die Schätzung geodätischer Zielparameter aus den VLBI-Beobachtungen, wie z.B. Stationspositionen und Erdorientierungsparameter (EOP). Wir untersuchen die theoretischen Auswirkungen auf die geschätzten Parameter, wenn die durch das NTL induzierten Ortsverschiebungen auf verschiedenen Ebenen des Modells angebracht werden. Dabei repräsentiert eine Ebene die saubere Reduktion, die andere eine approximative Reduktion.

Nach diesen vorbereitenden Schritten reduzieren wir das NTL schließlich bei der Analyse von VLBI-Beobachtungen über ca. 40 Jahre. Die letzten beiden Artikel befassen sich mit unterschiedlichen Arten von Lösungen, nämlich der Einzelsession- und der TRF-Lösung. Beim ersten Lösungstyp werden die geodätischen Zielparameter aus den einzelnen VLBI-Beobachtungskampagnen, den sogenannten Sessions, bestimmt, wobei diese nicht direkt untereinander in Beziehung stehen. Das Resultat sind nichtlineare Zeitreihen von Stationspositionen, d.h. eine Position pro Station und Session. Die zweite Lösungsart erstellt einen säkularen VLBI-Referenzrahmen, der lineare Stationspositionen erzeugt. Dabei werden die Beobachtungen aller Sessions kombiniert. Die EOP können in beiden Lösungen geschätzt werden, und die Einzelsession-Lösungen liefern in der Regel zusätzliche Ziel- (z.B. Troposphärenparameter) und Hilfsparameter (z.B. Uhrenparameter).

Wir zeigen, dass das Reduzieren des NTL die Streuung der geschätzten Positionen und damit auch die Residuen in Bezug auf die linearen Bewegungen der VLBI-Stationen verringert. Dies gilt vor allem für die Einzelsession-Lösungen. Durch die Betrachtung langer Beobachtungszeiträume glätten die säkularen TRFs die nichtlinearen Bewegungen, so dass vor allem die Positionen und Geschwindigkeiten von Stationen mit kurzen Beobachtungszeiträumen (d.h. wenige Jahre) von der Reduktion des NTL profitieren. Weil insbesondere die hydrologische Komponente des NTL ein starkes, saisonales Signal enthält, bewirkt die Reduktion aller NTL-Komponenten eine deutliche Verringerung der Amplituden der jährlichen Restsignale in den geschätzten Stationshöhen. Diese Höhen sind stark mit den Troposphären- und Uhrenparametern korreliert, und daher profitieren auch Letztere von den verbesserten Stationspositionen, weil sie weniger nichtberücksichtigte Effekte auffangen. In den meisten Fällen liefert die approxima-

tive Reduktion des NTL sehr ähnliche Ergebnisse zur sauberen Reduktion. Allerdings beinhaltet die approximative Reduktion eine Verschlechterung der zeitlichen Auflösung der durch das NTL induzierten Ortsverschiebungen, welche im mathematischen Modell angebracht werden. Daher reagieren die Zielparameter mit einer signifikanten Abhängigkeit von der zeitlichen Auflösung, wie z.B. die EOP-Raten, stärker auf die gewählte Modellebene für die Reduktion. Die Auswirkungen auf die EOP sind im Allgemeinen geringer als bei den Stationspositionen, aber auch Erstere profitieren wieder von den verbesserten Schätzungen für Letztere.

Insgesamt befürworten wir die Reduktion des NTL in der VLBI-Analyse. Zwar gibt es eine gewisse Modellunsicherheit für die hydrologische Komponente, aber wir haben mit allen untersuchten Datensätzen ähnliche Verbesserungen für die Zielparameter beobachtet. Wir erwarten, dass die Auswirkungen der Reduktion des NTL noch deutlicher werden, wenn weitere Fehlerquellen in der VLBI-Analyse beseitigt oder abgemildert worden sind, oder die Messgenauigkeit durch die nächste Generation von VLBI-Beobachtungen (das VLBI Global Observing System, VGOS) gestiegen ist.

Contents

1 Introduction

1.1 Background and motivation

The description/monitoring of geophysical processes in the Earth system and of the motion of the Earth in space relies on accurate and stable reference frames. The same holds for navigation both on Earth and in space. The corresponding International Terrestrial Reference System (ITRS; Petit and Luzum, 2010) and International Celestial Reference System (ICRS; Arias et al., 1995) are realized by four geodetic space techniques. These are Very Long Baseline Interferometry (VLBI), Satellite Laser Ranging (SLR), the Global Navigation Satellite Systems (GNSS), and Doppler Orbitography and Radio Positioning Integrated by Satellite (DORIS).

Earth-fixed reference systems, which represent theoretical concepts only, are realized by terrestrial reference frames (TRF). The particular realization of the ITRS is called International Terrestrial Reference Frame (ITRF). Conceptually, the latter consists of positions and linear motions of reference points, which belong to the observing stations of the four techniques and are fixed to the Earth's crust. For long time scales, this linear parameterization is reasonable and mainly reflects the motion of the tectonic plates. But, the instantaneous station positions reveal significant non-linear variations. These are caused by short-term deformations of the Earth, or are only apparent variations due to insufficient modelling of technique-specific biases. Many geophysical and technique-specific reasons for the instantaneous deviations from the long-term linear motions are known and can be reduced in the calculations. The corresponding recommended models can be found in the latest 2010 Conventions (Petit and Luzum, 2010) of the International Earth Rotation and Reference Systems Service (IERS).

The solid but approximately elastic Earth is deformed by external gravitational forces (e.g., exerted by the sun and the moon), by centrifugal forces due to its own rotation, or by the loading through fluid mass (i.e., water and air) on its surface. Loading, if driven by tidal forces, is further called tidal loading. There are conventional models for tidal loading, which are used to compute surface (or site) displacements that are added to the a priori positions of the observing stations in the theoretical functions for the geodetic measurements. In this way, the estimated positions are said to be reduced by tidal loading.

In contrast to the tidal loading, the models for the remaining non-tidal loading (NTL) are not sufficiently accurate according to the IERS Conventions 2010. As a consequence, it is recommended to not reduce station positions by NTL in the context of official

IERS analyses, but to let the residuals w.r.t. the estimated linear positions contain the NTL signals. On the other hand, the community is encouraged to investigate the effect of NTL, and there are various studies for the distinct geodetic space techniques which promote the reduction of NTL (e.g., Williams and Penna, 2011; Eriksson and MacMillan, 2014; Roggenbuck et al., 2015; Männel et al., 2019).

Depending on the underlying fluid, the NTL is separated into non-tidal atmospheric, non-tidal oceanic, and hydrological loading. The three parts have different proportions w.r.t. the total NTL in different regions of the world. For example, the displacements due to the atmospheric component are large at mid-latitudes and on the continents, while those induced by the hydrological part are generally larger in tropical regions (e.g., Schuh et al., 2003). The oceanic component is most relevant near the oceans, of course. While it appears reasonable to combine all parts, the corresponding models must be assembled with care to ensure the conservation of mass. The International VLBI Service for Geodesy and Astrometry (IVS; Nothnagel et al., 2017), however, asks its members to reduce the non-tidal atmospheric loading only, and the services for the other techniques do not request any NTL reductions at all.

Finally, the site displacements induced by NTL can be applied at distinct levels in the analysis of geodetic measurements. The most rigorous way is to reduce the NTL in the theoretical model for each observation (e.g., Eriksson and MacMillan, 2014). This is called the observation level, in which the temporal resolution of the available displacement series is preserved. An alternative is to reduce the subsequent (in the parameter estimation procedure) normal equation system by average displacements per station (Seitz et al., 2022). This approximation is called application at the normal equation level. At last, the solution level refers to the case in which the site displacements are directly subtracted from the estimated station positions (e.g., Collilieux et al., 2009).

With this thesis, we want to contribute to the research on NTL and take a step towards the conventional reduction of this geophysical effect. Though we focus on VLBI, some of our findings are also valid for the other geodetic space techniques. We cover a broad range of the research spectrum by examining i) two types of VLBI solutions (single-session and secular TRF solutions), ii) distinct NTL components (atmospheric, oceanic, and hydrological), iii) different application levels (mainly the observation and the normal equation level), and iv) almost the full range of geodetic parameters estimated by VLBI (antenna positions, Earth orientation parameters, tropospheric delays, and clock corrections). Next to actual results based on about 40 years of VLBI observations, we also investigate the Gauss-Markov model (e.g., Koch, 1999), which we use for the parameter estimation, and derive the theoretical impact of the application of site displacements.

1.2 Research goals

Given the aforementioned motivation, the following key questions are addressed in this thesis:

Q-1 What is the relation between the three NTL components, and how well do particular geophysical models agree per component?

Q-2 Which properties of NTL data (e.g. temporal resolution, trends, consistency) are most relevant for the distinct applications?

Q-3 What is the relevance of the application level for each of the solution types?

Q-4 Which geodetic parameters benefit from the reduction of NTL, i.e., by which NTL components should VLBI measurements conventionally be reduced?

These questions are answered in four journal articles, of which three have been published and one has been submitted for publication. The articles are included by summaries in dedicated subsections of the main body of this thesis, and listed in their entirety (except for the second article, due to copyright reasons) together with further information in the Appendix.

1.3 Thesis outline

As mentioned before, this thesis is based on the following journal articles:

P-1 Glomsda M., Bloßfeld M., Seitz M., Angermann D., and Seitz F. (2022): **Comparison of non-tidal loading data for application in a secular terrestrial reference frame**, *Earth, Planets and Space*, Vol. 74 (1), doi:10.1186/s40623-022-01634-1

P-2 Glomsda M., Bloßfeld M., Seitz M., and Seitz F. (2021): **Correcting for site displacements at different levels of the Gauss-Markov model - a case study for geodetic VLBI**, *Advances in Space Research*, Vol. 68 (4), pp. 1645-1662, doi:10.1016/j.asr.2021.04.006

P-3 Glomsda M., Bloßfeld M., Seitz M., and Seitz F. (2020): **Benefits of non-tidal loading applied at distinct levels in VLBI analysis**, *Journal of Geodesy*, Vol. 94 (90), doi:10.1007/s00190-020-01418-z

P-4 Glomsda M., Seitz M., Bloßfeld M., and Seitz F. (submitted): **Effects of non-tidal loading applied in VLBI-only terrestrial reference frames**, submitted to *Journal of Geodesy*.

In **P-1**, we examine the characteristics of NTL data in the most thorough way, and we are not yet focusing on VLBI. These data are then applied in the analysis of VLBI observations in all the other articles, even though the data providers are partly interchanged. Furthermore, **P-1** identifies those properties of the NTL data which are

relevant for the computation of a secular TRF, which is performed in **P-4**. The theoretical implications of the application of NTL data in VLBI analysis with the common Gauss-Markov model are studied in **P-2**. These lay the foundation for the geodetic investigations with various NTL data and the long history of VLBI measurements in **P-3** and **P-4**. Each one of the latter two is dedicated to a different type of solution for the positions of VLBI antennas: **P-3** covers single-session solutions, where a time-series of more or less uncorrelated positions is estimated per antenna, while **P-4** examines TRF solutions, in which linear positions are estimated across the full set of VLBI sessions. In both articles, we also take a look at the accompanying geodetic parameters for the respective solution type.

NTL data, i.e., the time series of site displacements, can be applied at various levels of the Gauss-Markov model, and this thesis contains a focus on the differences between these levels. In particular, **P-2** investigates the solution, the observation, and the normal equation level theoretically, and the displacements are considered in real geodetic analyses at the latter two levels in both **P-3** and **P-4**.

NTL data is supplied by various research groups on the basis of different geophysical models, and their properties and results may deviate, of course. For this reason, we compare two data sets in each **P-1** and **P-3**. In **P-1**, we consider i) the operational NTL data by the Earth System Modelling group of the Deutsches GeoForschungsZentrum (ESMGFZ, *http://esmdata.gfz-potsdam.de:8080*), and ii) the NTL data prepared for the ITRS 2020 realizations by the Global Geophysical Fluid Center (GGFC, *http://loading.u-strasbg.fr/ITRF2020*). The data by ESMGFZ is applied in both **P-2** and **P-3**, while the data by GGFC is applied in **P-4**. The second provider in **P-3** is the International Mass Loading Service (IMLS, *http://massloading.net/*).

The interrelations of the four articles and the key research questions are depicted in Figure 1.1. Basically, the first two articles are assigned to a foundation part, while the last two articles form the geodetic application part. Both application articles rely on both foundation articles to a certain extent. **P-3** and **P-4** have an overlap w.r.t. the underlying VLBI observations, but the analysis models (including the NTL data) are partly different.

The thesis is organized as follows. In Chapter 2, we introduce the different reference systems which are relevant for VLBI (i.e., the terrestrial reference system for the antenna positions, and the celestial reference system for the radio source positions), as well as the parameters that allow for transformations between them. The corresponding geodetic parameters are examined in **P-2**, **P-3**, and **P-4**. The computation of NTL data, i.e., the displacements of the reference points in the terrestrial frame, is explained in Chapter 3, in which **P-1** is a subsection. Chapter 4 contains a summary of the VLBI technique, including both practical and theoretical considerations, as well as **P-2** as a subsection. Finally, in Chapter 5, the geodetic results of the application of NTL data at the distinct levels in VLBI analyses are presented. It consists of three sections: **P-3**, **P-4**, and a discussion on the magnitude of the impact of the reduction of NTL in VLBI. The thesis ends with the conclusions and an outlook in Chapter 6.

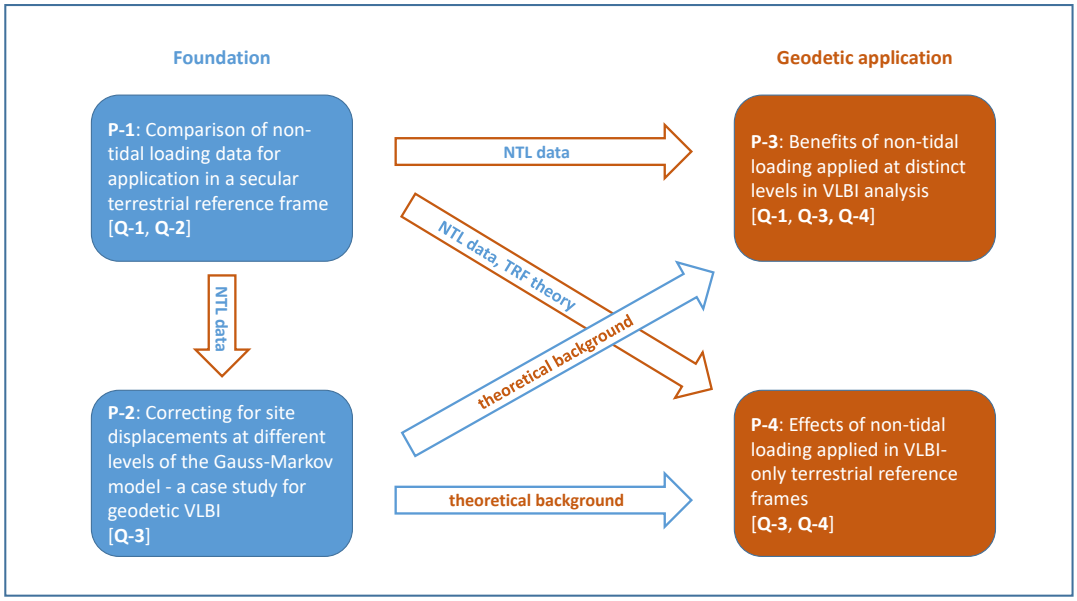

Figure 1.1: The connections between the four articles of this thesis. Blue boxes refer to the background articles, while the red boxes refer to the application articles. The arrows indicate the type of information exchanged between them. The key questions, which are addressed by each article, are also provided in square brackets.

2 Reference systems

Basically all geodetic applications depend on accurate and stable reference frames. In fact, the computation of these frames, which are realizations of the corresponding reference systems, is one of the most important tasks in geodesy. In this chapter, we will introduce the terrestrial reference system, the celestial reference system, and the parameters that allow for a transformation of positions from one system into the other. The VLBI technique contributes to all of these entities, and the investigations of this thesis are closely related to them. An extensive treatment of the reference systems can be found in the 2010 Conventions of the IERS. Our summary here is largely based on this document.

2.1 Terrestrial Reference System

A terrestrial reference system (TRS) is fixed to the Earth's crust, i.e., it is co-rotating with the Earth. In principle, it is a right-handed, three-dimensional Cartesian coordinate system, defined by an origin and three orthogonal axis vectors, which all have the same scale. Points within such a TRS are hence given by three-dimensional position vectors $\boldsymbol{p}(t) = [x(t), y(t), z(t)]$, and the dependence on the epoch t is due to contingent deformations of the Earth. For two different TRSs (subscripts 1 and 2), the transformation of a position from one system into the other is given by

$$\boldsymbol{p}_2(t) = \boldsymbol{o}_{12}(t) + \lambda_{12}(t)\, \boldsymbol{R}_{12}(t)\, \boldsymbol{p}_1(t), \tag{2.1}$$

where $\boldsymbol{o}_{12}$ is the translation vector between the origins, λ_{12} a scale factor, and $\boldsymbol{R}_{12}$ a rotation matrix. This conversion is called similarity transformation, and the corresponding translation, scale, and rotation parameters are also time-dependent (usually linearly, i.e., they are represented by an offset and a rate).

The ITRS has been defined and adopted by the International Association of Geodesy (IAG) Resolution of 1991, and the International Union of Geodesy and Geophysics (IUGG) Resolution 2 of 2007, respectively (IERS Conventions 2010). Its origin is close to the geocenter, which is the center of mass (CM) of the whole Earth including the oceans and the atmosphere. Its time coordinate, which is relevant for the scale determination, is the Temps Coordonnées Géocentric (TCG). Apart from that, the scale is close to the SI (Système International d'unités) meter. The z-axis of the Cartesian coordinate system is close to the axis of Earth rotation, so the x-y-plane is close to its equator. The x-axis is pointing towards the Greenwich meridian. See Figure 2.1 for an

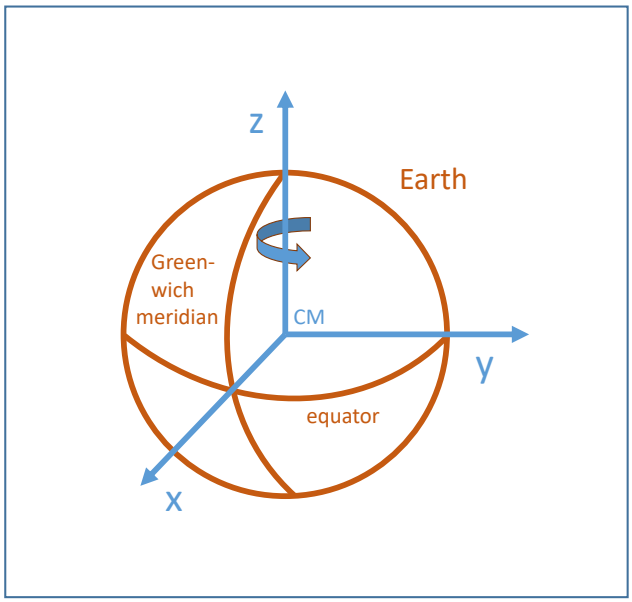

Figure 2.1: Sketch of the ITRS.

illustration of the ITRS. The time evolution of the orientation is such that there are no net rotations over the whole Earth w.r.t. the horizontal tectonic motions, and the orientation agrees with that defined by the Bureau International de l'Heure (BIH) for epoch 1984.0 [year.dec].

The IERS is in charge of publishing the ITRF. ITRF88, which was based on geodetic observations made until the end of 1988, was the first such realization. The current computation strategy was basically introduced with ITRF2005 (Altamimi et al., 2007): for each of the four geodetic space techniques VLBI, SLR, GNSS, and DORIS, a single time series of positions of the corresponding observing station is provided. These time series are published by the IERS Technique Centers (TC), i.e., the IVS, the International Laser Ranging Service (ILRS; Pavlis et al., 2021), the International GNSS Service (IGS; Johnston et al., 2017), and the International DORIS Service (IDS; Willis et al., 2010), and are themselves combinations of the time series created from the TCs' Analysis Centers (AC). From each of the four sets of time series, first an intra-technique TRF solution is computed, and then the time series are combined to create an inter-technique TRF solution.

The ITRF solutions consist of regularized, i.e., linear positions $\boldsymbol{p}_R$ for each observing station. Such solutions are also called secular TRFs. In particular, station offsets $\boldsymbol{p}_0$ at a suitable reference epoch t_0 and station velocities $\dot{\boldsymbol{p}}$ are estimated, so that

$$\boldsymbol{p}_R(t) = \boldsymbol{p}_0 + (t - t_0)\,\dot{\boldsymbol{p}} \tag{2.2}$$

for all other epochs t. While the regularized positions basically reflect long-term motions due to the Earth's plate tectonics, the instantaneous station positions are obtained

by adding corrections $\boldsymbol{\Delta p}_i$ referring to other, short-term geophysical effects (compare Chapter 3):

$$\boldsymbol{p}(t) = \boldsymbol{p}_R(t) + \sum_i \boldsymbol{\Delta p}_i(t). \tag{2.3}$$

Furthermore, the ITRF must realize the geodetic datum, which again comprises the origin, the orientation, and the scale, as well as their time derivatives. Nowadays, the origin is realized by SLR, since this satellite technique is most sensitive to the CM. The orientation is usually defined by requiring no net rotation of a stable station subset w.r.t. their positions at a particular epoch in the previous ITRF. Finally, the scale has lately been set equal to a combination of the SLR and VLBI scales (e.g., Altamimi et al., 2016).

At the time of writing, the most recent ITRF2020 had just been published by the Institut national de l'information géographique et forestière (IGN, *https://itrf.ign.fr/en/solutions/ITRF2020*) in France. IGN, as well as NASA's Jet Propulsion Laboratory (JPL) in the USA, and the Deutsches Geodätisches Forschungsinstitut der Technischen Universität München (DGFI-TUM) in Germany represent the three IERS ITRS Combination Centers (CC). The existence of multiple ITRS realizations ensures that the results can be validated against each other, and that contingent biases can be detected. IGN and DGFI-TUM, whose ITRS realization is called DTRF, basically follow the linearized approach in Eq. (2.2), but with different combination and reduction strategies (e.g., Altamimi et al., 2016; Seitz et al., 2022). The JPL, on the other hand, whose ITRS realization is called JTRF, creates an epoch reference frame consisting of times series of station positions (Abbondanza et al., 2017). In general, there are new ITRS realizations every 3-6 years, which take into account the latest geophysical and technique-specific models and the extended amount of observation data by the existing or newly established stations.

2.2 Celestial Reference System

A celestial reference system (CRS) is not attached to the Earth but designed to describe the rotation and motion of the latter in space. A historical, dynamical definition of a CRS, realized by the Fifth Fundamental Catalogue of stars (FK5; Fricke et al., 1988), for example, is depicted in Figure 2.2. Like the ITRS, it is a Cartesian coordinate system with three orthogonal axes, but this time the origin is supposed to be close to the solar system barycenter (SSB). The x-y-plane shall contain the mean Earth equator as of J2000.0 (2000-01-01, noon), and the x-axis shall point towards the dynamical equinox at the same epoch (e.g., Arias et al., 1995).

In 1991, the International Astronomical Union (IAU) recommended to replace this dynamical definition by a kinematic one in Resolution A4 (IERS Conventions 2010). While keeping the SSB as the origin, the axes should now be fixed by the positions of extra-galactic radio sources (mostly quasars, compare Figure 2.2 again). Due to their

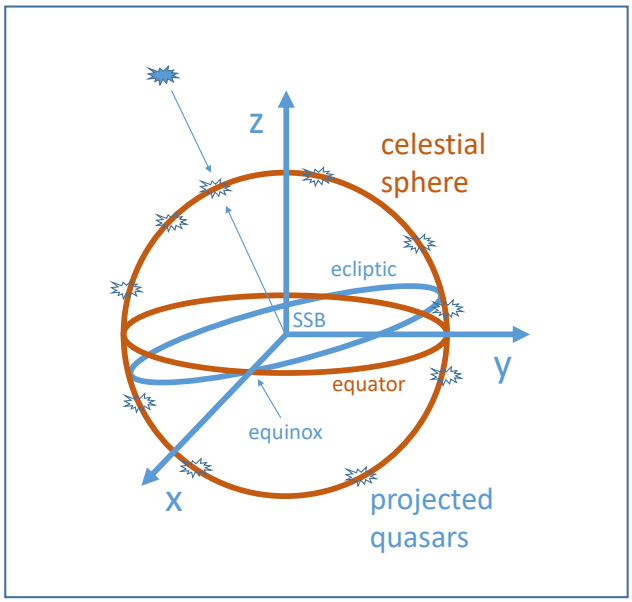

Figure 2.2: Sketch of celestial reference systems: the dynamical CRS is based on the mean equinox as of J2000.0, while the kinematic one is based on quasi-fix quasar positions.

huge distances from the Earth, the sources' positions are given in terms of unit vectors (directions), and they are supposed to have no detectable proper motions. Hence, the corresponding CRS is quasi-inertial and independent from any epoch. However, for continuity, the initial axes of this new International Celestial Reference System (ICRS; Arias et al., 1995) are aligned to the conventional axes at J2000.0 of the previous systems, which were based on optical rather than radio frequencies.

Quasars are quasi-stellar radio sources with a supermassive black hole at their center (e.g., Schmidt, 1963; McNally, 1964; Longair, 1967). The latter is attracting matter (a process called accretion), which leads to the formation of an accretion disk. Heating due to friction makes the disk emit electro-magnetic radiation, and if the disk has a strong magnetic field, two jets consisting of accelerated matter appear in the two perpendicular directions of the disk. The radiation is utilized by VLBI, and hence (only) this geodetic space technique is capable of the determination of the quasar positions in the ICRS.

As with the terrestrial system, the realization of a CRS is called celestial reference frame (CRF), and the realization of the ICRS is the International Celestial Reference Frame (ICRF). The ICRF is basically generated as follows: once the radio source positions have been estimated from VLBI, they are aligned with the ICRS by a rotation of a set of very stable sources (the so-called defining sources) onto their positions in the previous realization (Ma et al., 1998; Fey et al., 2015; Charlot et al., 2020). In Table 2.1, the three available versions of the ICRF are summarized. An overview about the past and current developments has recently been published by de Witt et al. (2022).

Table 2.1: History and properties of the ICRF.

	ICRF1	ICRF2	ICRF3 (X)
valid from	1998-01-01	2010-01-01	2019-01-01
number of sources	608	3,414	4,536
number of defining sources	212	295	303
median right ascension uncertainty [mas]	0.35	0.40	0.13
median declination uncertainty [mas]	0.40	0.74	0.22
noise floor [mas]	0.25	0.04	0.03
axes stability [mas]	0.02	0.01	0.01
epoch	n/a	n/a	2015.0

With each new ICRF, the number of included radio sources increased, and the formal errors have improved as a result of the larger amount of observations. The latest realization, ICRF3, is the first frame with positions for different observation frequencies. While Table 2.1 refers to measurements in X-band with radio frequencies at about 8 GHz (compare Section 4.2.2), ICRF3 also contains positions for the K- (about 24 GHz) and Ka-bands (about 32 GHz). The reason is, that the radio sources are not point-like but reveal time- and frequency-dependent structure, which influences the estimated VLBI positions (compare Section 4.3.4). Furthermore, ICRF3 has a reference epoch again. With the current VLBI precision and observation history, it is possible to detect Galactic aberration (Kovalevsky, 2003), which creates apparent proper motions of the radio sources (compare Section 4.3.4 again) and has been accounted for in ICRF3.

The ICRS is a Barycentric Celestial Reference System (BCRS), but there are also Geocentric Celestial Reference Systems (GCRS). As the name suggests, the origin of the corresponding Cartesian coordinate system is the geocenter, and the orientation of the axes is such that there is no rotation w.r.t. the BCRS (e.g., IERS Conventions 2010). Usually, coordinates in the GCRS are not provided as vectors $[\bar{x}, \bar{y}, \bar{z}]$, but as pairs of right ascension α and declination δ, which correspond to the longitude (or azimuth angle) and 90° minus the polar distance of the ITRS, respectively. A radial distance, on the other hand, does not exist for the GCRS, because the celestial objects are just assumed to be projections on the celestial sphere. Figure 2.3 shows the X-band radio source positions of the ICRF3 in the GCRS. As the reader might have noticed, the formal errors in Table 2.1 are also given for the geocentric coordinates. Right ascension is conventionally provided in hour angles, while declination is given in degrees. From the figure, we recognize that the distribution of estimated radio source positions in the Southern hemisphere is less dense than in the North. The reason is the smaller number of VLBI antennas in the South (compare Figure 4.4 in Section 4.4), and this situation also creates generally larger formal position errors for this part of the sky.

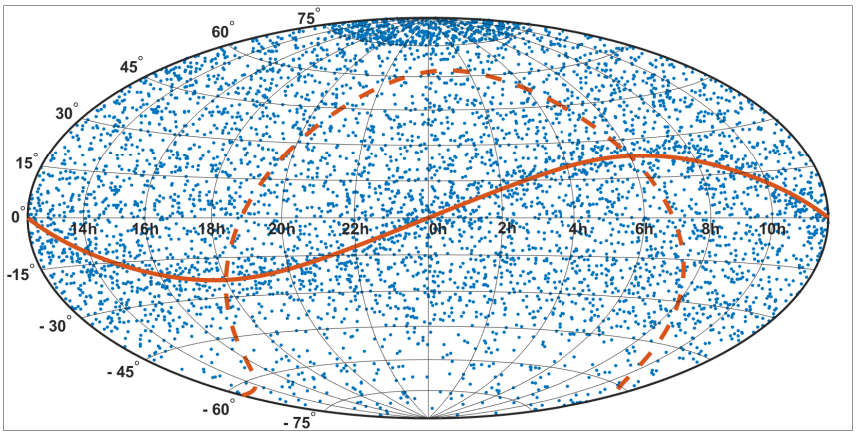

Figure 2.3: The right ascensions (x-axis) and declinations (y-axis) of the ICRF3 X-band source positions in the GCRS. The solid red line marks the ecliptic plane, while the dashed red line represents the Galactic plane.

2.3 Earth orientation parameters

Positions in the ITRS can be transformed into positions in the GCRS (and vice versa) by a series of rotations. The latter depend on the instantaneous orientation of the ITRS in the quasi-inertial celestial system, and the variables of the rotation matrices are called Earth orientation parameters (EOP). While there are different models and sets of EOP, we restrict ourselves to the parameters that have been applied in this thesis. They refer to the IAU 2000/2006 resolutions as summarized in the IERS Conventions 2010.

To relate the rotation axes of the ITRS and the GCRS at some epoch t, an intermediate rotation axis corresponding to the Celestial Intermediate Pole (CIP) is introduced. The CIP is close to the instantaneous rotation axis of the Earth, which varies w.r.t. both the ITRS and the GCRS. The position of the CIP in the ITRS is represented by the so-called polar motion, while the position of the CIP in the GCRS is described by effects called precession and nutation. The transformation between ITRS and GCRS is hence separated into a terrestrial and a celestial part, and the classification is provided in the IERS Conventions 2010: all motions of the CIP with absolute frequencies less than 0.5 cycles per sidereal day (cpsd) in the GCRS are assigned to the celestial part, and the others are assigned to the terrestrial part. (Since the ITRS rotates once per sidereal day in the GCRS, the interval $[-0.5, 0.5]$ cpsd in the GCRS corresponds to $[-1.5, -0.5]$ cpsd in the ITRS. The latter is called retrograde diurnal band.)

2.3.1 Polar motion

The position of the instantaneous rotation axis of the Earth w.r.t. its crust varies with time. One reason is the asymmetric distribution of mass in the Earth system, which makes the rotation axis differ from the polar principal axis of inertia. As a result, the instantaneous rotation axis revolves on a cone around the Earth's axis of angular momentum with a period of about 435 days (Chandler wobble; e.g., Moritz and Mueller, 1987). Another effect is the seasonal redistribution of (air and water) mass, which adds an annual signal to the circular motion of the rotation axis. The center of this motion, called mean pole, is not fixed, either, because there are long-term mass redistributions, mainly caused by the glacial isostatic adjustment (GIA; e.g., Steffen and Wu, 2011). The current distance between the mean pole and the conventional pole of the ITRS is about 12 m, and the diameter of the (quasi) circular motion is about 18 m.

The location of the CIP w.r.t. the conventional pole of the ITRS is given by the parameters $x_p(t)$ and $y_p(t)$. They represent the deviations on a plane tangential to the Earth at the conventional pole in the x-axis direction (the Greenwich meridian) and in the negative y-axis direction (90° West), respectively. The position of the instantaneous pole in the ITRS would hence be $[x_p(t), -y_p(t), z(t)]$, but we are interested in counterclockwise rotations $\boldsymbol{R}$ around the x- and y-axis of the ITRS (compare Figure 2.4), i.e.,

$$\boldsymbol{R}_x(y_p(t)), \quad \boldsymbol{R}_y(x_p(t)). \tag{2.4}$$

The Earth-fixed Cartesian coordinate system defined by the CIP is called Terrestrial Intermediate Reference System (TIRS), but we still need to specify the corresponding orientation of the x-axis. The IAU 2000 Resolution B1.8 recommends to use the kinematically non-rotating origin, which is then called Terrestrial Intermediate Origin (TIO). The rotation around the z-axis to establish the TIO in the TIRS is performed with the so-called TIO locator

$$s'(t) = \frac{1}{2} \int_{t_0}^{t} [x_p(u)\dot{y}_p(u) - \dot{x}_p(u)y_p(u)]\, du \tag{2.5}$$

and t_0 = J2000.0, so that the final transformation of coordinates in the ITRS to coordinates in the TIRS is given by the matrix

$$\boldsymbol{W}(t) = \boldsymbol{R}_z(-s'(t))\, \boldsymbol{R}_y(x_p(t))\, \boldsymbol{R}_x(y_p(t)). \tag{2.6}$$

2.3.2 Precession and nutation

The instantaneous rotation axis of the Earth also varies w.r.t. the z-axis of the GCRS. Due to the rotation itself, the Earth is flattened at the poles. Furthermore, the equator is tilted w.r.t. the plane of the Earth's orbit around the sun, i.e., the ecliptic. The tilt amounts to about 23.4°, and the same angle exists between the Earth rotation axis and the normal vector of the ecliptic plane. A gravitational torque created by the

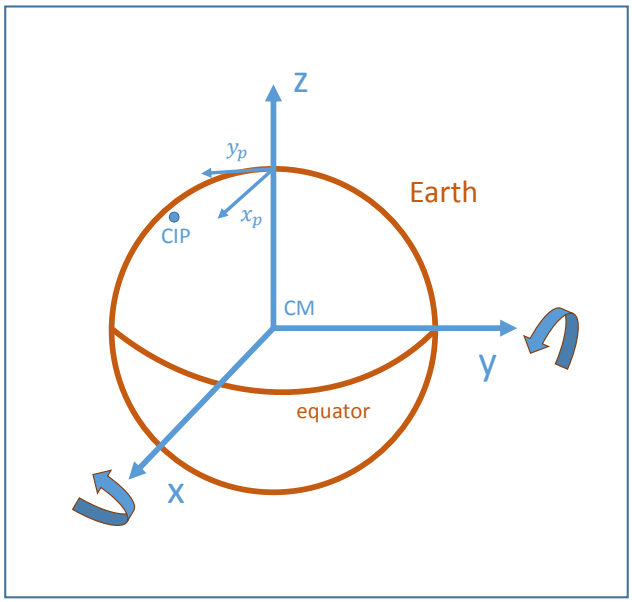

Figure 2.4: Rotation from the conventional ITRS pole to the CIP due to polar motion.

sun pulls the equatorial towards the ecliptic plane, while the centrifugal force of Earth rotation counteracts. As a consequence, the instantaneous rotation axis revolves on a cone around the normal vector of the ecliptic plane (see Figure 2.5), and this motion is called precession (e.g., Capitaine et al., 2003). The angle of this cone remains at about 23.4°, and the period of the circular motion is about 25,800 years. After half of this time, the stellar constellations visible from the Earth will have switched between summer and winter, since the rotation axis points into the opposite direction. The leap year rule ensures that, e.g., August will remain a summer month in the Northern hemisphere.

The instantaneous rotation axis is further influenced by the periodic constellation of the celestial bodies w.r.t. the Earth, i.e., by their recurrent gravitational forces. The corresponding variations of the rotation axis are called nutation and superimpose the precession (e.g., Mathews et al., 2002). However, the amplitude of the nutation is much smaller (see Figure 2.5 again), and so are its periods, which range from a few days to 18.6 years (e.g., Moritz and Mueller, 1987).

Similarly to polar motion, there are parameters $X(t)$ and $Y(t)$ representing the projections of the distance vector between the conventional pole and the CIP onto the x- and y-axis of the GCRS, respectively (e.g., Capitaine, 1990). The two parameters can be computed quite accurately from models for precession and nutation (IAU 2006/2000, IERS Conventions 2010), except for an effect called free core nutation (FCN). The latter is the result of a disparate alignment of the axes of rotation of the Earth's outer core and mantle (e.g., Amoruso and Crescentini, 2020). The differences between the

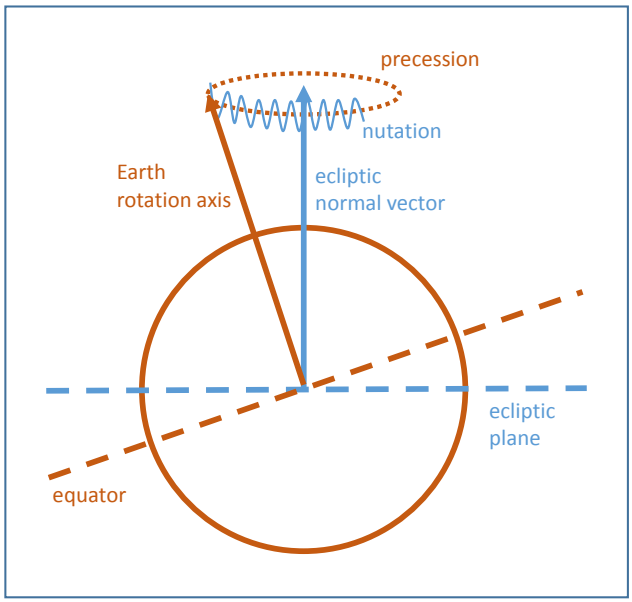

Figure 2.5: Motion of the Earth rotation axis in the GCRS due to precession and nutation.

true values and the model values,

$$\begin{aligned} \Delta X &= X(t) - X_{IAU}(t), \\ \Delta Y &= Y(t) - Y_{IAU}(t), \end{aligned} \tag{2.7}$$

mainly contain the FCN and are called celestial pole offsets. The latter are usually estimated (from VLBI observations) and then added to the model values to obtain the rotation matrix

$$\bar{\boldsymbol{Q}}(X(t), Y(t)) = \bar{\boldsymbol{Q}}(X_{IAU}(t) + \Delta X, Y_{IAU}(t) + \Delta Y) \tag{2.8}$$

between the pole of the GCRS and the CIP. The new celestial coordinate system defined by the CIP is called Celestial Intermediate Reference System (CIRS), and again the orientation of the new x-y-plane is provided by the kinematically non-rotating origin, now called Celestial Intermediate Origin (CIO). The corresponding CIO locator $s(t)$ in the GCRS can be approximated by

$$s(t) = -\frac{X(t)Y(t)}{2} + 94 + 3808.65\,t - 122.68\,t^2 - \ldots \quad [\mu\text{as}], \tag{2.9}$$

with t in days per century since J2000.0 (IERS Conventions 2010). The transformation from the CIRS to the GCRS is then given by

$$\boldsymbol{Q}(t) = \bar{\boldsymbol{Q}}^T(X(t), Y(t))\, \boldsymbol{R}_z(s(t)). \tag{2.10}$$

2.3.3 Earth rotation angle

The final step to relate the ITRS and the GCRS is to connect the intermediate terrestrial and celestial systems, i.e., the TIRS and the CIRS. Both systems have the same pole (the CIP) and hence the same equator, but the origins of the latter are different. The angle between the CIO and the TIO is the Earth Rotation Angle (ERA) and, given its value at epoch t, the transformation from the TIRS to the CIRS is simply performed with the matrix

$$\boldsymbol{R}(t) = \boldsymbol{R}_z(-\mathrm{ERA}(t)). \tag{2.11}$$

The ERA is conventionally related to Universal Time No. 1 (UT1, the actual duration of Earth rotation), or the difference between UT1 and Coordinated Universal Time (UTC, atomic time),

$$\Delta\mathrm{UT1} = \mathrm{UT1} - \mathrm{UTC}. \tag{2.12}$$

The difference exists, e.g., because tidal friction caused by the gravitational forces of the moon exerted on the oceans decelerates the Earth rotation (MacDonald, 1964; Brosche, 1990). With

$$\begin{aligned} t &= \text{Julian UT1 date - J2000.0} = \text{Julian UT1 date} - 2451545.0, \\ \mathrm{UT1} &= \mathrm{UTC} + \Delta\mathrm{UT1}, \end{aligned} \tag{2.13}$$

the ERA is given by

$$\mathrm{ERA}(t) = 2\pi\,(0.7790572732640 + 1.00273781191135448\,t). \tag{2.14}$$

All these formulas can again be found in the 2010 Conventions of the IERS.

2.3.4 Transformation from ITRS to GCRS

Following Equations (2.6), (2.10), and (2.11), a point $\boldsymbol{p}(t)$ in the ITRS is transformed into a point $\bar{\boldsymbol{p}}(t)$ in the GCRS by

$$\bar{\boldsymbol{p}}(t) = \boldsymbol{Q}(t)\,\boldsymbol{R}(t)\,\boldsymbol{W}(t)\,\boldsymbol{p}(t), \tag{2.15}$$

in which care has to be taken w.r.t. to the different time units for the epoch t. The actual EOP in this context are:

- x_p and y_p, the terrestrial pole offsets;
- ΔX and ΔY, the celestial pole offsets (to be added to X_{IAU} and Y_{IAU});
- ΔUT1, the difference between UT1 and UTC.

These five parameters are either estimated during the analysis of geodetic space observations, or taken from external providers, e.g., the IERS. The corresponding values as published in the IERS 14 C04 series (Bizouard et al., 2019) are shown in Figures 2.6 (terrestrial pole offsets) and 2.7 (ΔUT1 and celestial pole offsets). In

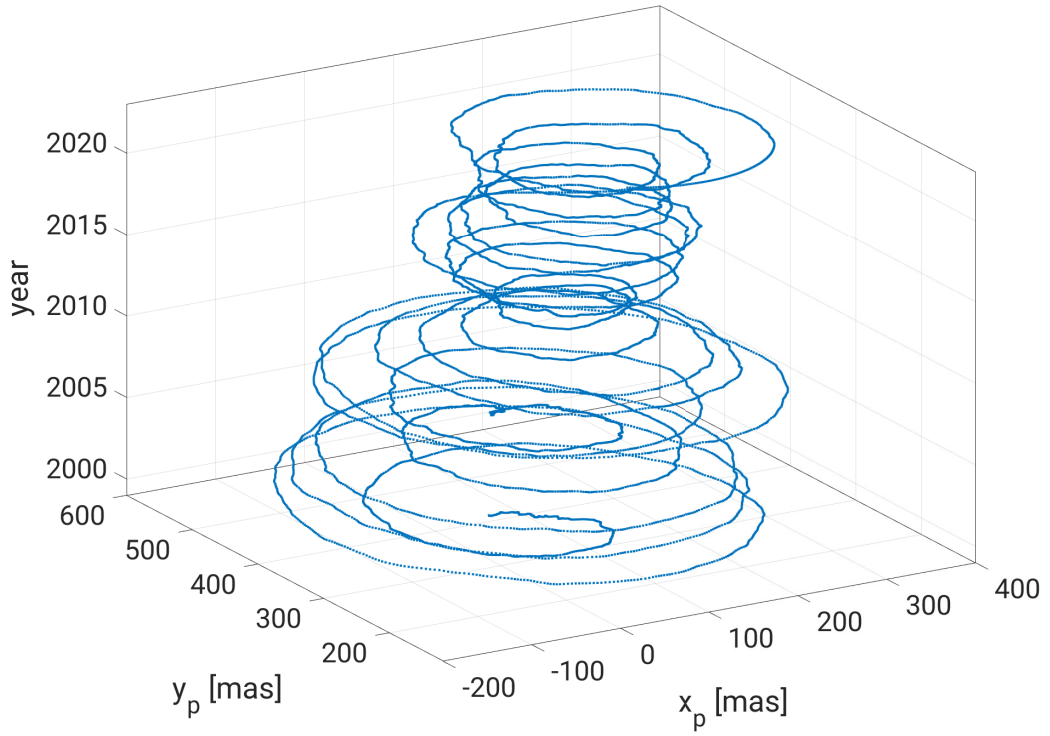

Figure 2.6: Polar motion: the position of the CIP w.r.t. the conventional pole of the ITRS.

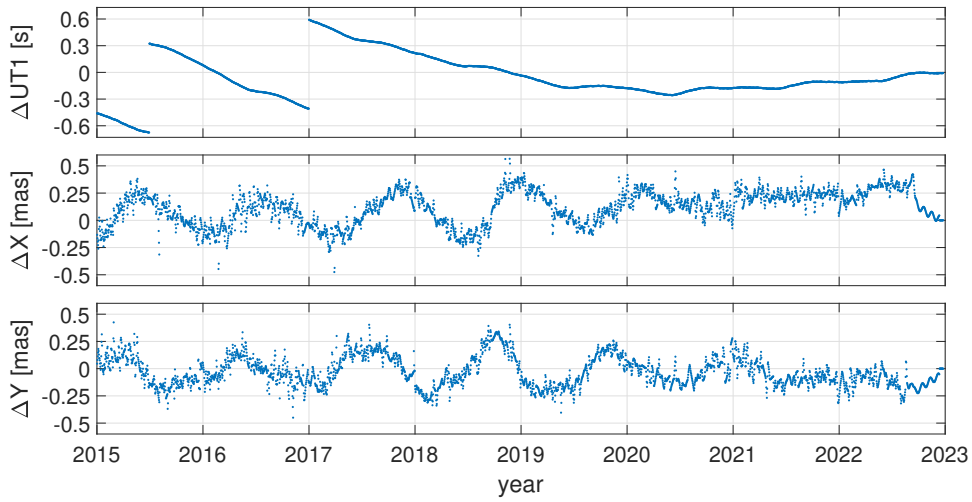

Figure 2.7: Top: ΔUT1. The jumps represent the two latest leap seconds at June 30, 2015, and December 31, 2016. Since about 2020, Earth rotation is uncommonly accelerating. Middle and bottom: the celestial pole offsets ΔX and ΔY, respectively. The period of FCN is about 430 sidereal days (Amoruso and Crescentini, 2020).

June 2022, a preliminary version of the new IERS 20 C04 series became available (*https://hpiers.obspm.fr/iers/eop/eopc04_20/*), which is related to the ITRF2020.

As we will see in Chapter 4, all five EOP can be obtained from VLBI.

3 Loading effects

3.1 Displacements of reference points

In Section 2.1 we described a secular TRF, which contains linear positions $\boldsymbol{p}_R$ of reference points. In Eq. (2.3), the instantaneous positions $\boldsymbol{p}(t)$ at epoch t are derived as the sum of $\boldsymbol{p}_R(t)$ and some corrections $\boldsymbol{\Delta p}_i(t)$. The latter comprise displacements of the Earth's crust caused by geophysical effects, and are separated into recommended and non-recommended corrections by the IERS Conventions 2010. The displacements that should conventionally be reduced in the geodetic analyses for the IERS are essentially related to tidal effects. We will shortly summarize them here before we turn to the non-tidal effects, which are the subject of our thesis.

The first conventional tidal reduction listed by the IERS refers to the solid Earth tides. These are deformations of the solid Earth due to changes in the gravitational potential induced by the sun and most importantly the moon. As a result, the positions of reference points in the TRF can be displaced by several decimeters. The same gravitational forces are also responsible for the displacements generated by the ocean tides. When the ocean water is redistributed by the gravitational attraction, the Earth's crust is lifted up or pushed down by the corresponding load. In contrast to the solid Earth tides, this tidal ocean loading depends on local conditions like coast lines, for example. It can be computed from models for the tide height (e.g., Egbert and Erofeeva, 2002), and the respective displacements of reference points in the TRF can be as large as 10 cm.

Just like the ocean water, atmospheric pressure can induce a local loading on the Earth's surface. The atmospheric tides with diurnal and semi-diurnal frequency components are driven by pressure variations due to daily solar heating (e.g., van den Dool et al., 1997). The corresponding displacements of the crust are similar to those for the ocean tides, and one way of computation involves numerical weather models (NWM) providing surface pressure on regional or global grids (e.g., Ray and Ponte, 2003).

Next to changes in the gravitational potential, there are also changes in the centrifugal potential of Earth rotation that lead to deformations of the solid Earth. The pole tide is generated by the temporal variation of the rotation axis (e.g., Munk and MacDonald, 1960), i.e., the polar motion as described in Section 2.3.1. It produces displacements of a few centimeters for the reference points in the TRF. The same alterations in the centrifugal potential further have an impact on the ocean water distribution, so there are additional deformations due to the so-called ocean pole tides. The corresponding

model by Desai (2002) provides radial (horizontal) displacements of usually less than 2 (0.5) cm. The horizontal displacements are generally smaller than the vertical ones for each deformation listed here.

3.2 Non-tidal loading

In the previous section, we introduced the tidal reductions for obtaining regularized TRF positions as recommended by the IERS Conventions 2010. If the corresponding displacements were related to the redistribution of air or water mass, we spoke of loading effects. Hence, ocean tides, atmospheric tides, and ocean pole tides belong to the category of tidal loading. The opposite, NTL, refers to deformations of the solid Earth which are also induced by the redistribution of mass, but the frequency spectrum of these deformations is much wider than that of the tidal forces. Depending on the type of mass that represents the loading, we distinguish non-tidal atmospheric, non-tidal oceanic, and hydrological (i.e., related to land water storage) loading. In this thesis, we examine the impact of the reduction of NTL in the analysis of VLBI observations, in particular on the estimated TRF positions and the EOP. But first, we will explain how the surface/site displacements for (antenna) positions induced by NTL are computed.

3.2.1 Gravitational potential

Displacements of the Earth's surface due to NTL are the result of the redistribution of air and water mass in the Earth system. Hence, we need to examine the involved gravitational forces. The following introduction is based on the book by Hofmann-Wellenhof and Moritz (2006).

According to Newton, the gravitational force between two point masses M_1 and M_2 with distance l is given by

$$F = G\frac{M_1 M_2}{l^2}, \tag{3.1}$$

where $G = 6.67428 \cdot 10^{-11}$ $\mathrm{m^3 kg^{-1} s^{-2}}$ is the gravitational constant. This actually symmetric system is often transformed by setting $M_2 = 1$ for the mass that is assumed to be attracted, and $M_1 = M$ for the mass that is assumed to be attracting. Then, we get the following equation for the gravitational force acting on a point with unit mass and distance l from M:

$$F = G\frac{M}{l^2}. \tag{3.2}$$

If we multiply this equation with the distance l, we get the so-called gravitational potential

$$V = G\frac{M}{l} \tag{3.3}$$

for a unit mass at a distance l from the point mass M. Thus, the potential is a property of the unit mass, i.e., it is a function of the position of the latter. The potential has several convenient properties. First, the gradient of this scalar function provides the components of the force vector $\boldsymbol{F}$ with length F, which is directed from the point mass M to the unit mass located at Cartesian coordinates $[x, y, z]$:

$$\nabla V = \left[\frac{\partial V}{\partial x}, \frac{\partial V}{\partial y}, \frac{\partial V}{\partial z}\right] = \boldsymbol{F}. \tag{3.4}$$

Second, the potential is linear: if there are N point masses M_j, then the total gravitational potential for the unit mass at distances l_j is

$$V = G \sum_{j=1}^{N} \frac{M_j}{l_j}. \tag{3.5}$$

Now, the Earth could be described as a continuous system of point masses. In this case, the finite sum in Eq. (3.5) would become a three-dimensional integral. Furthermore, with the density $\rho = dm/dv$ given by the quotient of the total mass dm in a volume dv of the Earth, one can show that Poisson's equation (with the Laplacian operator Δ) holds for the attracted unit mass:

$$\Delta V = \left(\frac{\partial^2}{\partial x^2} + \frac{\partial^2}{\partial y^2} + \frac{\partial^2}{\partial z^2}\right) V = \frac{\partial V^2}{\partial x^2} + \frac{\partial V^2}{\partial y^2} + \frac{\partial V^2}{\partial z^2} = -4\pi G \rho. \tag{3.6}$$

If the unit mass is located outside the Earth, we have

$$\Delta V = 0, \tag{3.7}$$

which is Laplace's equation, and its solutions are called harmonic functions. Hence, the gravitational potential is a harmonic function for a unit mass located outside the system of the attracting masses (e.g., the Earth).

3.2.2 Spherical Harmonics

Spherical harmonics are very useful basis functions for describing effects at the Earth's surface. Again following the lines of Hofmann-Wellenhof and Moritz (2006), they are derived from Laplace's equation (3.7) in spherical coordinates.

Figure 3.1 shows the connection between the spherical coordinates

$$\begin{aligned} r &= \sqrt{x^2 + y^2 + z^2} \quad \text{(radius)} \\ \vartheta &= \tan^{-1} \frac{\sqrt{x^2 + y^2}}{z} \quad \text{(polar distance)} \\ \lambda &= \tan^{-1} \frac{x}{y} \quad \text{(geocentric longitude)} \end{aligned} \tag{3.8}$$

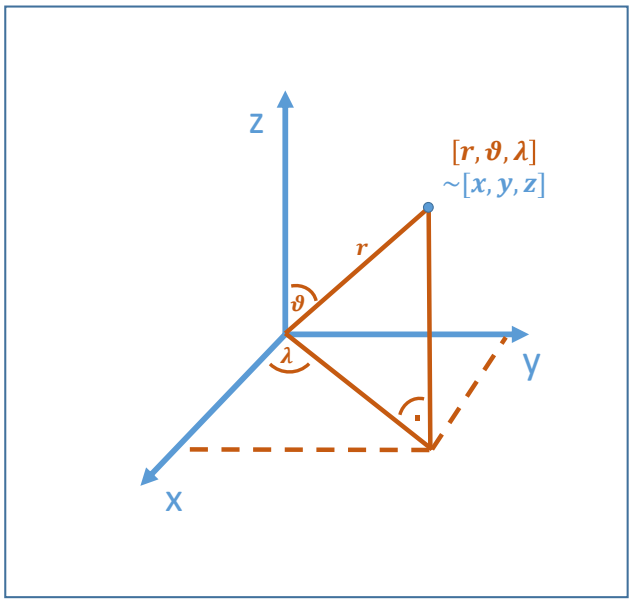

Figure 3.1: Spherical coordinates in the Cartesian system, inspired by Hofmann-Wellenhof and Moritz (2006).

and the Cartesian ones. With the former, Laplace's (partial differential) equation reads

$$r^2\frac{\partial V^2}{\partial r^2} + 2r\,\frac{\partial V}{\partial r} + \frac{\partial V^2}{\partial \vartheta^2} + \cot\vartheta\,\frac{\partial V}{\partial \vartheta} + \frac{1}{\sin^2\vartheta}\,\frac{\partial V^2}{\partial \lambda^2} = 0, \tag{3.9}$$

and it can be solved by using the method of separation of variables. Separating the radius r first by letting

$$V(r,\vartheta,\lambda) = f_1(r)\,Y(\vartheta,\lambda), \tag{3.10}$$

we obtain the following solutions with integers $n = 0, 1, 2, \ldots$:

$$V_n = r^n\,Y_n(\vartheta,\lambda), \quad V_n = r^{-(n+1)}\,Y_n(\vartheta,\lambda). \tag{3.11}$$

These functions V_n are called solid spherical harmonics, while the yet unknown functions Y_n are called (Laplace's) surface spherical harmonics. The latter are obtained by separating polar distance and longitude, i.e., by letting

$$Y_n(\vartheta,\lambda) = f_2(\vartheta)\,f_3(\lambda). \tag{3.12}$$

Possible solutions for $f_3(\lambda)$ are $\cos(m\lambda)$ and $\sin(m\lambda)$ with arbitrary constants m, which are independent from n. The corresponding solutions for $f_2(\vartheta)$, however, only have a physical relevance for $m \le n$ both being integers $0, 1, 2, \ldots$, and are equal to the Legendre functions $P_{nm}(\cos\vartheta)$. Hence, possible solutions for the surface spherical harmonics are

$$Y_{nm}(\vartheta,\lambda) = P_{nm}(\cos\vartheta)\,\cos(m\lambda), \quad Y_{nm}(\vartheta,\lambda) = P_{nm}(\cos\vartheta)\,\sin(m\lambda), \tag{3.13}$$

with the aforementioned conditions for m (called order) and n (called degree).

Laplace's equation (3.9) is a linear differential equation, so the sum of particular solutions is also a solution. Putting everything together, we arrive at the following general solutions for $\Delta V(r,\vartheta,\lambda) = 0$ with arbitrary constants c_{nm} and s_{nm}:

$$\begin{aligned} V_i(r,\vartheta,\lambda) &= \sum_{n=0}^{\infty} r^n \sum_{m=0}^{n} [c_{nm} P_{nm}(\cos\vartheta)\cos(m\lambda) \\ &\quad + s_{nm} P_{nm}(\cos\vartheta)\sin(m\lambda)], \\ V_o(r,\vartheta,\lambda) &= \sum_{n=0}^{\infty} r^{-(n+1)} \sum_{m=0}^{n} [c_{nm} P_{nm}(\cos\vartheta)\cos(m\lambda) \\ &\quad + s_{nm} P_{nm}(\cos\vartheta)\sin(m\lambda)]. \end{aligned} \tag{3.14}$$

Every harmonic function inside (outside) a sphere can be represented by some series V_i (V_o).

The surface spherical harmonics from Eq. (3.13) have advantageous geometrical properties on a sphere. With the substitution $u := \cos\vartheta$, we obtain

$$P_{nm}(u) = \frac{1}{2^n\, n!}(1-u^2)^{m/2}\frac{d^{n+m}}{du^{n+m}}(u^2-1)^n \tag{3.15}$$

for the Legendre functions, which leads to Legendre's polynomials for the order $m = 0$,

$$P_n(u) = \frac{1}{2^n\, n!}\frac{d^n}{du^n}(u^2-1)^n, \tag{3.16}$$

and the so-called associated Legendre functions for orders $m = 1,\ldots,n$:

$$P_{nm}(u) = (1-u^2)^{m/2}\frac{d^m}{du^m}P_n(u). \tag{3.17}$$

Then, for $m = 0$, the surface spherical harmonics are $P_0(cos\,\vartheta)$, $P_1(cos\,\vartheta)$, $P_2(cos\,\vartheta)$ and so on. They do not depend on the longitude λ. Furthermore, Legendre's polynomial $P_n(u)$ has n zeros in $[-1,1]$, which corresponds to n zeros in $[0,\pi]$ for $P_n(cos\,\vartheta)$ as a function of ϑ. As a consequence, each such polynomial changes sign n times for increasing polar distance from 0 to π and separates a sphere into zones (see Figure 3.2, left).

Likewise, there are $n-m$ zeros in $[0,\pi]$ for the associated Legendre functions w.r.t. ϑ, and $\cos(m\lambda)$ and $\sin(m\lambda)$ both have $2m$ zeros for λ in the interval $[0,2\pi]$. For, e.g., the surface spherical harmonic $P_{nm}(cos\,\vartheta)\cos(m\lambda)$ with $n = m$, a sphere is hence separated into sectors with alternating signs as λ moves from 0 to 2π (Figure 3.2, middle), and for $n > m$ the sphere is finally separated into tesseracts (Figure 3.2, right). With these basis functions, it becomes clear how the value of a harmonic function V of any point (r,ϑ,λ) at the Earth's surface can be generated with appropriate coefficients c_{nm}, s_{nm} in Eq. (3.14). Actually, any function on the sphere can be expanded into surface spherical harmonics (Hofmann-Wellenhof and Moritz, 2006).

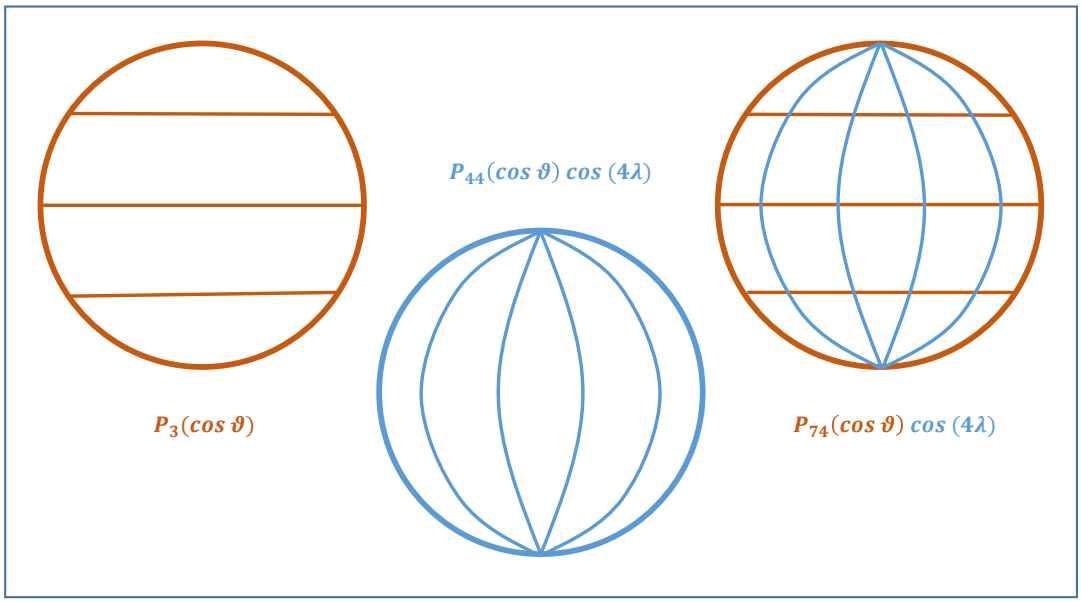

Figure 3.2: Left: zonal harmonic ($m = 0$). Middle: sectorial harmonic ($n = m$). Right: tesseral harmonic (else). Inspired by Hofmann-Wellenhof and Moritz (2006).

3.2.3 Displacements in SNREI Earth models

In the following, we assume that the Earth is spherical (S), non-rotating (NR), elastic (E), and isotropic (I). The latter means that the mechanical properties of the Earth (or sphere) only depend on the distance from its center and not on its orientation. Such theoretical constructs are called SNREI Earth models, and the corresponding assumptions have been appropriate w.r.t. the accuracy of deformation observations so far (Bos and Scherneck, 2013).

If a unit mass is put onto the surface of an SNREI Earth, the effects of this point load are axially symmetric (e.g., Farrell, 1972). In particular, they consist of a change in the gravitational potential V and a displacement $\boldsymbol{\delta}$. Among others, the former is comprised of the potential of the deformation due to the load, V_1, and the potential of the unit mass itself, V_2. As outlined in Section 3.2.2, functions on the sphere like V and $\boldsymbol{\delta}$ can be expanded into series of surface spherical harmonics. Due to the missing azimuth dependence, zonal harmonics are sufficient, and hence the expansion is limited to the order $m = 0$. Following Farrell (1972), the vertical and horizontal components of $\boldsymbol{\delta}$ at a point with distance r from the center of the Earth and angular distance ϑ from the load are given by

$$\delta_u(r, \vartheta) = \sum_{n=0}^{\infty} U_n(r)\, P_n(\cos\vartheta), \tag{3.18}$$

and

$$\delta_h(r, \vartheta) = \sum_{n=0}^{\infty} H_n(r)\, \frac{\partial P_n(\cos\vartheta)}{\partial \vartheta}, \tag{3.19}$$

respectively. Likewise, the expansion of the change in gravitational potential reads

$$V(r,\vartheta) = \sum_{n=0}^{\infty} V_n(r)\, P_n(\cos\vartheta). \tag{3.20}$$

The coefficients U_n, H_n, and V_n are obtained by solving the equations of motion for the corresponding Earth model. These equations describe the propagation of seismic waves inside the Earth, which is mainly characterized by its density profile and the velocities for P- and S-waves (e.g., Wang et al., 2012). Different parameterizations for the corresponding differential equations exist, but they are eventually solved by a numerical integration starting at some initial sphere inside the Earth and ending at the Earth's surface (e.g., Na and Baek, 2011; Bos and Scherneck, 2013). Thereby, appropriate boundary conditions have to be chosen at the core-mantle transition and the surface.

Usually, the so-called load Love numbers (LLN) $h_n^{'}$, $l_n^{'}$, and $k_n^{'}$ (Munk and MacDonald, 1960) are used instead of the coefficients U_n, H_n, and V_n. They are dimensionless and defined by (e.g., Farrell, 1972)

$$\begin{bmatrix} U_n(r) \\ H_n(r) \\ V_{1,n}(r) \end{bmatrix} = V_{2,n}(r) \begin{bmatrix} \frac{h_n^{'}(r)}{g} \\ \frac{l_n^{'}(r)}{g} \\ k_n^{'}(r) \end{bmatrix}, \tag{3.21}$$

with $g \approx 9.78\ \mathrm{ms}^{-2}$ being the Earth's mean gravity at its surface (i.e., for r equal to the Earth's radius $a \approx 6,378$ km) and $V_{1,n}$, $V_{2,n}$ being components of V_n. The original Love numbers (without superscript) have been introduced by Love (1909) and Shida (1912) and are related to the deformations caused by the tidal forces of the sun and the moon rather than surface loading. Nevertheless, both types are functions of the spherical harmonic degree n and the radius r. At the Earth's surface, it holds (Farrell, 1972)

$$V_{2,n}(a) = \frac{a\,g}{M_E}, \tag{3.22}$$

with $M_E \approx 5.97 \cdot 10^{24}$ kg being the Earth's mass, so that

$$\begin{bmatrix} U_n(a) \\ H_n(a) \\ V_{1,n}(a) \end{bmatrix} = \begin{bmatrix} \frac{a\,h_n^{'}(a)}{M_E} \\ \frac{a\,l_n^{'}(a)}{M_E} \\ \frac{a\,g\,k_n^{'}(a)}{M_E} \end{bmatrix}. \tag{3.23}$$

Hence, the equations of motion are actually solved to obtain the LLNs for a particular Earth model.

Table 3.1: Load Love numbers for $r = a$ and three different Earth models: Gutenberg-Bullen (Gutenberg, 1945; Bullen, 1950), PREM (Dziewonski and Anderson, 1981), and IASP91 (Kennett and Engdahl, 1991). $l_n^{'}$ and $k_n^{'}$ are scaled by n to provide a homogeneous magnitude.

degree	Gutenberg-Bullen (from Farrell, 1972)			PREM (from Jentzsch, 1997)			IASP91 (from Na and Baek, 2011)		
n	$h_n^{'}$	$nl_n^{'}$	$nk_n^{'}$	$h_n^{'}$	$nl_n^{'}$	$nk_n^{'}$	$h_n^{'}$	$nl_n^{'}$	$nk_n^{'}$
0	-	-	-	-	-	-	-0.132	0.0	0.0
1	-0.290	0.113	0.0	-0.290	0.113	0.0	-0.283	0.105	0.0
2	-1.001	0.059	-0.615	-1.006	0.457	-0.648	-1.003	0.049	-0.616
3	-1.052	0.223	-0.585	-1.049	0.212	-0.602	-1.063	0.216	-0.592
4	-1.053	0.247	-0.528	-1.047	0.235	-0.540	-1.066	0.243	-0.537
10	-1.433	0.303	-0.682	-1.412	0.283	-0.689	-1.443	0.300	-0.687
100	-3.058	0.973	-1.461	-2.937	0.899	-1.454	-3.176	0.975	-1.486
1000	-4.906	1.623	-2.431	-5.850	1.657	-2.833	-5.578	1.853	-2.725
10000	-4.956	1.637	-2.469	-6.177	1.875	-3.056	-5.636	1.892	-2.770
∞	-5.005	1.673	-2.482	-6.239	1.893	-3.072	-5.637	1.892	-2.771

In Table 3.1, subsets of the LLNs for three different SNREI Earth models are listed. The degrees 0 and 1 are special: for $n = 0$ and a compressible model, there is no horizontal surface deformation or perturbation in the potential, since the corresponding load is applied uniformly across the Earth. The load for $n = 1$, on the other hand, induces a translation of the center of mass of the solid, i.e., undeformed Earth (CE), which is the natural origin for describing the deformations according to Farrell (1972). Changing the origin to the center of mass of the total Earth including the loads (CM), or the center of figure of the Earth (CF), is equal to a change in the LLNs for $n = 1$ (e.g., Blewitt, 2003). For example, the degree-1 LLNs in the CM-frame are obtained by subtracting 1 from the respective numbers in the CE frame, which are provided in Table 3.1. The (CE frame) values for $h_n^{'}$ with piecewise cubic interpolation are also shown in the left panel of Figure 3.3.

Replacing the original coefficients in Eq. (3.18) and (3.19) with the LLNs, we arrive at a vertical displacement of

$$\delta_u(\vartheta) = \frac{a}{M_E} \sum_{n=0}^{\infty} h_n^{'}(a)\, P_n(\cos\vartheta), \tag{3.24}$$

and a horizontal displacement of

$$\delta_h(\vartheta) = \frac{a}{M_E} \sum_{n=1}^{\infty} l_n^{'}(a)\, \frac{\partial P_n(\cos\vartheta)}{\partial\vartheta} \tag{3.25}$$

at the Earth's surface, respectively, both caused by a unit point load at angular distance ϑ. Similar expressions are derived for the perturbation of the gravitational potential,

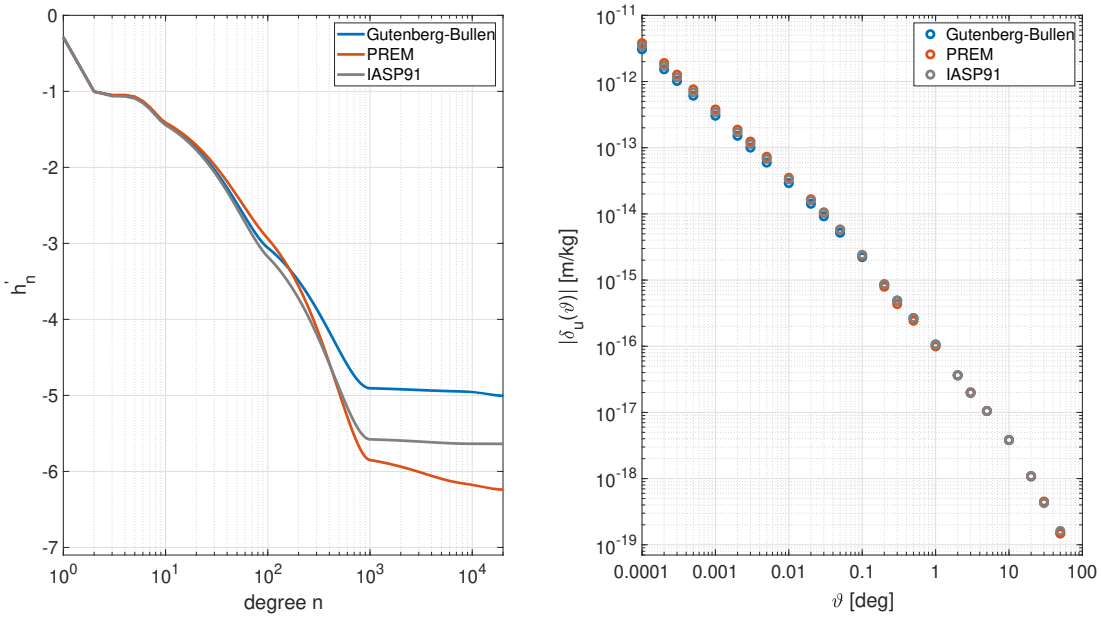

Figure 3.3: Left: Load Love numbers h_n' from Table 3.1 with piecewise cubic interpolation. Right: the corresponding vertical displacements for the unit point load (1 kg), i.e., the weighting Green's functions $|\delta_u|$ in absolute values for distinct angles ϑ.

but these are not relevant for our thesis. Since VLBI is not directly sensitive to gravitation, it suffices to compute the displacements of the antenna reference points.

Farrell (1972) further stated that LLNs up to a degree $n = 10,000$ are necessary for accurate results. In recent NTL products with large spatial resolutions, a maximum degree of $n > 40,000$ is even used (e.g., Wang et al., 2012; Dill and Dobslaw, 2013). However, it is not necessary to solve the equations of motion for all of them, but the remaining LLNs can be interpolated from a suitable set of computed ones. For some large degree N, the LLNs are sufficiently close to their limits h_∞' and l_∞' (and k_∞', compare Wang et al., 2012). As a consequence, the infinite sums in Eqs. (3.24) and (3.25) can be solved with Kummer's transformation (Kummer, 1837; Farrell, 1972), e.g.,

$$\begin{aligned} \delta_u(\vartheta) &= \frac{a}{M_E} \sum_{n=0}^{\infty} \left[h_n'(a) - h_\infty'(a) \right] P_n(\cos\vartheta) + \frac{a}{M_E} \sum_{n=0}^{\infty} h_\infty'(a)\, P_n(\cos\vartheta) \\ &= \frac{a}{M_E} \sum_{n=0}^{N} \left[h_n'(a) - h_\infty'(a) \right] P_n(\cos\vartheta) + \frac{a\, h_\infty'(a)}{2\, M_E \sin(\vartheta/2)} \end{aligned} \tag{3.26}$$

for the vertical displacement with $h_\infty'(a) = h_n'(a)$ for $n > N$.

The functions δ_u and δ_h refer to unit point loads. To obtain the site displacements $\tilde{\delta}$ due to a load with an arbitrary mass M at the angular distance ϑ, this mass is multiplied

with the original displacement functions, e.g.,

$$\tilde{\delta}_u(\vartheta, M) = M\,\delta_u(\vartheta). \tag{3.27}$$

If there are point loads with masses dM distributed all over the Earth's surface at geocentric locations $(\lambda_{dM}, \phi_{dM})$, and if these masses are small enough such that superposition holds (compare Bos and Scherneck, 2013), then the vertical displacement $\tilde{\delta}_u$ at a particular location $(\bar{\lambda}, \bar{\phi})$ is given by

$$\tilde{\delta}_u(\bar{\lambda}, \bar{\phi}) = \int \delta_u(\vartheta(\bar{\lambda}, \bar{\phi}, \lambda_{dM}, \phi_{dM}))\, dM. \tag{3.28}$$

Likewise, the corresponding horizontal displacement reads

$$\tilde{\delta}_h(\bar{\lambda}, \bar{\phi}) = \int \delta_h(\vartheta(\bar{\lambda}, \bar{\phi}, \lambda_{dM}, \phi_{dM}))\, dM. \tag{3.29}$$

The displacement functions for the unit load in Eqs. (3.24) and (3.25) are called weighting Green's functions, and the reason for this phrase will be explained in the next section. Prior to that, we let

$$\begin{aligned} \tilde{\mathcal{G}}_u(\bar{\lambda}, \bar{\phi}, \lambda, \phi) &:= \delta_u(\vartheta(\bar{\lambda}, \bar{\phi}, \lambda, \phi)), \\ \tilde{\mathcal{G}}_h(\bar{\lambda}, \bar{\phi}, \lambda, \phi) &:= \delta_h(\vartheta(\bar{\lambda}, \bar{\phi}, \lambda, \phi)), \end{aligned} \tag{3.30}$$

and the variables δ_u^{NTL} and δ_h^{NTL} will represent the vertical and horizontal site displacements that are induced by NTL, respectively. The weighting Green's functions $\tilde{\mathcal{G}}_u$ for the vertical displacements are shown in the right panel of Figure 3.3 for distinct Earth models and angular distances ϑ. The weights for large angular distances are dominated by LLNs with low degrees (e.g., Farrell, 1972).

3.2.4 Computation of displacements due to NTL

In the previous section, we derived the formulas for the vertical and horizontal site displacements induced by masses M. Regarding NTL, these masses correspond to air or water at the Earth's surface. These two physical entities are permanently loading the Earth, so that the surface is always displaced in principle. However, the size of the displacements is changing with the global redistribution of air and water, which is usually represented by the change in atmospheric or water related pressures P. By computing reference pressure values for each site on the surface, an equilibrium state with zero deformation can be defined for this location. Then, the surface displacements due to NTL are expressed as the relative deformations w.r.t. the equilibrium state, which are generated from the deviations ΔP from the reference pressures. These time and space dependent deviations are called pressure anomalies. Thus, we need global pressures $P(\lambda, \phi)$ for the distinct components of NTL: atmospheric pressures, ocean bottom pressure, hydrological pressure. These are usually derived from NWMs, ocean tide models, and hydrological models. The reference pressures can be computed from

the average model pressures over appropriate time periods, i.e., for each site the reference pressure is interpolated from the average pressures of the surrounding model grid points. In particular for the atmospheric pressure, there also exist analytical formulas for a reference pressure (compare, e.g., Böhm et al., 2008).

In Figure 3.4, the atmospheric pressure anomalies for epoch 1988-02-03 11:00 UTC as generated from the ERA5 reanalysis (Hersbach et al., 2020) of the European Center for Medium-range Weather Forecasts (ECMWF) are shown. At this epoch, for example, the atmospheric pressure above Siberia and Mongolia was about 20 hPa lower than the reference pressure, while is was up to 40 hPa larger than the reference pressure above Canada and the Arctic ocean. In Figure 3.5, we present the vertical site displacements that are computed from the pressure anomalies in Figure 3.4 by ESMGFZ (compare Dill and Dobslaw, 2013). Most naturally, they reveal a negative correlation: if the atmospheric pressure is larger (smaller) than the reference pressure around some location $(\bar{\lambda}, \bar{\phi})$, the surface is pushed down (lifted up). As a consequence, there are negative displacements in Canada and positive ones in Siberia, which attain absolute values greater than 10 mm. The site displacements by ESMGFZ have been used in **P-1**, **P-2**, and **P-3**.

To compute the displacements, we need to transform the pressure anomalies ΔP at all available locations (λ, ϕ) into point mass anomalies ΔM and perform a global convolution with the corresponding weighting Green's functions as in Eqs. (3.28) and (3.29). The pressure P is equal to a force divided by some area A, and the mass M times gravity g is the corresponding force:

$$P = \frac{M\,g}{A} \quad \Leftrightarrow \quad M = \frac{P\,A}{g}. \tag{3.31}$$

The surface of the spherical Earth amounts to $4\pi a^2$, and when dividing it into chunks of $\cos(\phi)\,d\lambda\,d\phi$ with $\lambda \in [0, 2\pi]$ and $\phi \in [-\pi/2, \pi/2]$, the respective areas are

$$A = \cos(\phi)\,d\lambda\,d\phi\,a^2 \tag{3.32}$$

(compare Eq. (5-49) in Moritz and Mueller, 1987). Hence, the formulas for the vertical and horizontal displacements are given by

$$\begin{aligned} \delta_u^{NTL}(\bar{\lambda}, \bar{\phi}) &= \iint \Delta P(\lambda, \phi)\,\frac{a^2}{g}\,\tilde{\mathcal{G}}_u(\bar{\lambda}, \bar{\phi}, \lambda, \phi)\,\cos(\phi)\,d\lambda\,d\phi \\ &= \iint \Delta P(\lambda, \phi)\,\mathcal{G}_u(\bar{\lambda}, \bar{\phi}, \lambda, \phi)\,\cos(\phi)\,d\lambda\,d\phi, \end{aligned} \tag{3.33}$$

$$\begin{aligned} \delta_h^{NTL}(\bar{\lambda}, \bar{\phi}) &= \iint \Delta P(\lambda, \phi)\,\frac{a^2}{g}\,\tilde{\mathcal{G}}_h(\bar{\lambda}, \bar{\phi}, \lambda, \phi)\,\cos(\phi)\,d\lambda\,d\phi \\ &= \iint \Delta P(\lambda, \phi)\,\mathcal{G}_h(\bar{\lambda}, \bar{\phi}, \lambda, \phi)\,\cos(\phi)\,d\lambda\,d\phi, \end{aligned} \tag{3.34}$$

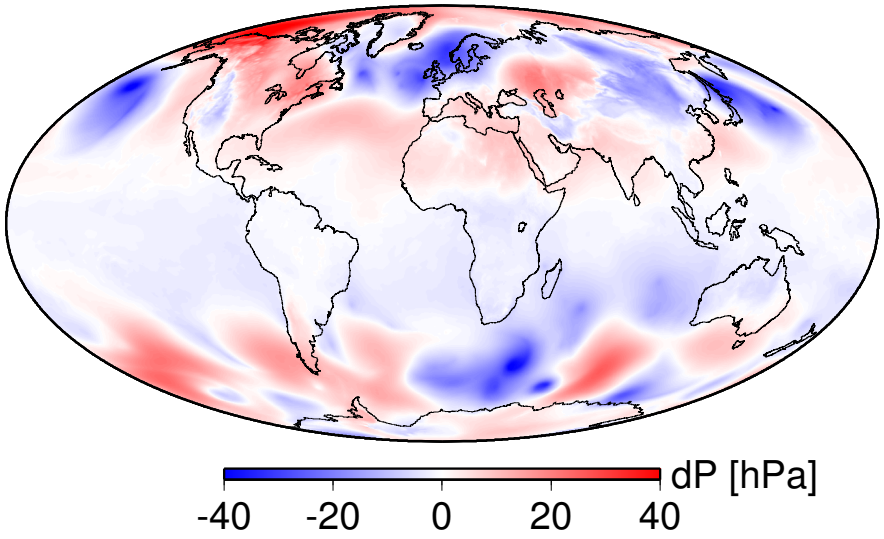

Figure 3.4: Atmospheric pressure anomalies derived from the ERA5 reanalysis data by the ECMWF. The corresponding epoch is 1988-02-03 11:00 UTC. Courtesy of Kyriakos Balidakis, GFZ Potsdam.

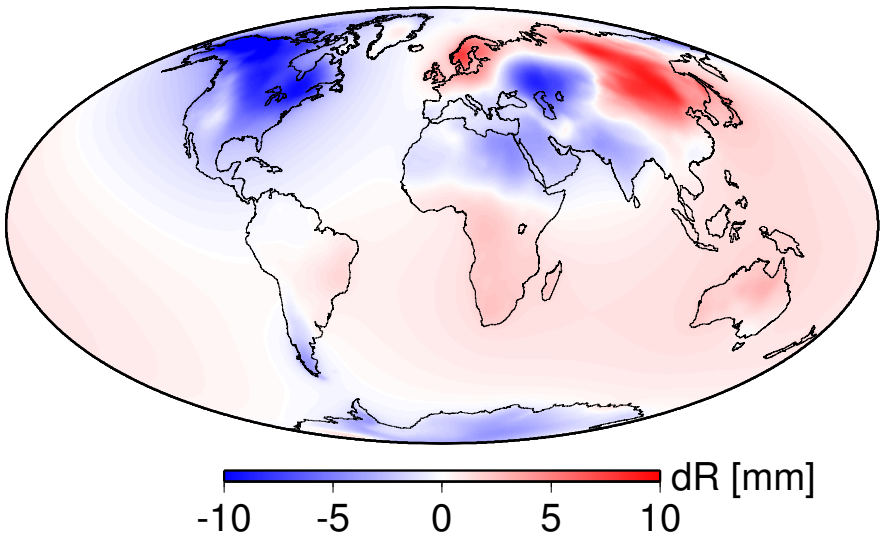

Figure 3.5: Vertical site displacements induced from the ERA5 reanalysis pressure anomalies as of 1988-02-03 11:00 UTC. The displacements have been generated in the CM-frame by ESMGFZ. Courtesy of Kyriakos Balidakis, GFZ Potsdam.

respectively, where we omitted the aforementioned limits for λ and ϕ, and

$$\mathcal{G}_u(\bar{\lambda},\bar{\phi},\lambda,\phi) \;:=\; \frac{G\,a}{g^2}\sum_{n=0}^{\infty} h'_n(a)\,P_n(\cos\vartheta(\bar{\lambda},\bar{\phi},\lambda,\phi)), \tag{3.35}$$

$$\mathcal{G}_h(\bar{\lambda},\bar{\phi},\lambda,\phi) \;:=\; \frac{G\,a}{g^2}\sum_{n=1}^{\infty} l'_n(a)\,\frac{\partial P_n(\cos\vartheta(\bar{\lambda},\bar{\phi},\lambda,\phi))}{\partial\vartheta} \tag{3.36}$$

are the weighting Green's functions for pressures rather than masses (e.g., Petrov and Boy, 2004), using $g = G\,M/a^2$. The horizontal displacement can be separated into displacements in East and North directions by introducing sine and cosine terms w.r.t. the azimuth angles $\alpha(\bar{\lambda},\bar{\phi},\lambda,\phi)$ towards the loads, respectively (e.g., Wijaya et al., 2013):

$$\delta_e^{NTL}(\bar{\lambda},\bar{\phi}) \;=\; \iint \Delta P(\lambda,\phi)\,\mathcal{G}_h(\bar{\lambda},\bar{\phi},\lambda,\phi)\,\sin(\alpha(\bar{\lambda},\bar{\phi},\lambda,\phi))\,\cos(\phi)\,d\lambda\,d\phi, \tag{3.37}$$

$$\delta_n^{NTL}(\bar{\lambda},\bar{\phi}) \;=\; \iint \Delta P(\lambda,\phi)\,\mathcal{G}_h(\bar{\lambda},\bar{\phi},\lambda,\phi)\,\cos(\alpha(\bar{\lambda},\bar{\phi},\lambda,\phi))\,\cos(\phi)\,d\lambda\,d\phi. \tag{3.38}$$

According to Hofmann-Wellenhof and Moritz (2006), the sine and cosine terms can be computed by

$$\sin(\alpha(\bar{\lambda},\bar{\phi},\lambda,\phi)) \;=\; \frac{\cos\phi\,\sin(\lambda-\bar{\lambda})}{\sin\vartheta(\bar{\lambda},\bar{\phi},\lambda,\phi)}, \tag{3.39}$$

$$\cos(\alpha(\bar{\lambda},\bar{\phi},\lambda,\phi)) \;=\; \frac{\cos\bar{\phi}\,\sin\phi \;-\; \sin\bar{\phi}\,\cos\phi\,\cos(\lambda-\bar{\lambda})}{\sin\vartheta(\bar{\lambda},\bar{\phi},\lambda,\phi)}. \tag{3.40}$$

The expressions for the site displacements are convolutions, which resemble the solutions

$$w(x) \;=\; \int f(y)\,\mathcal{G}(x,y)\,dy \tag{3.41}$$

of a linear differential equation $L\,w(x) = f(x)$, where $\mathcal{G}$ satisfies

$$L\,\mathcal{G}(x,y) \;=\; \delta(x-y) \tag{3.42}$$

with the Dirac delta function $\delta(\cdot)$. The latter is different from 0 only for the single argument 0, so a point load basically equals such a delta function, too. The corresponding functions $\mathcal{G}$ are called Green's functions, and hence the same phrase is used for the weighting functions $\mathcal{G}_u$ and $\mathcal{G}_h$ above, "though they are not true Green's functions in the strict mathematical sense" (Farrell (1972), p.778).

Practical information about the implementation of the above formulas is given by, e.g., Petrov and Boy (2004). For example, since the effect of the atmospheric pressure above land is different from that above the oceans, land-sea-masks are applied to distinguish the corresponding numerical algorithms. We also provide a short summary of this issue in **P-3**. Since the weighting Green's functions decay exponentially (compare, e.g., Dill et al., 2015; or Figure 3.3), the convolution can actually be restricted to the area within a distance of a few thousand kilometers of the respective location $(\bar{\lambda},\bar{\phi})$. Given the

corresponding pressure anomalies, the Green's functions approach can be applied to all three components of NTL, of course. There are also alternative approaches, like the empirical model by Rabbel and Zschau (1985), who perform a linear regression between pressure anomalies and vertical site displacements. Since we are referring to NTL, the signals from the tidal frequency bands are removed from the final site displacements for the atmospheric and oceanic components (e.g., Petrov, 2015).

As a final remark, the site displacements due to NTL can be computed in different frames, that is, w.r.t. different origins. The frame simply depends on the choice of the degree-1 LLNs (compare Section 3.2.3). If one subtracts the displacements of the CM-frame from the corresponding displacements of the CF-frame, for example, one obtains the contribution of NTL to geocenter motion (GM; e.g., Dong et al., 2003), which is also examined in **P-1**.

3.2.5 Assessment of different NTL data

As mentioned before, multiple institutions provide NTL data that is generated from different underlying geophysical models. Several sources for such data are linked at the website of the GGFC (*http://loading.u-strasbg.fr/GGFC/*). Another source is the IMLS, whose data we have used in **P-3**.

Beforehand, in **P-1**, we analyse two recent NTL data sets and their applicability in the realization of the ITRS:

P-1 Glomsda M., Bloßfeld M., Seitz M., Angermann D., and Seitz F. (2022): **Comparison of non-tidal loading data for application in a secular terrestrial reference frame**, *Earth, Planets and Space*, Vol. 74 (1), doi:10.1186/s40623-022-01634-1

Summary We take a look at the NTL data of two out of various providers. The ultimate goal is to find the most suitable data set for the ITRS 2020 realization at DGFI-TUM, the DTRF2020. As with the previous DTRF2014 (Seitz et al., 2022), the site displacements induced by NTL shall be applied at the normal equation level.

The first data set is GGFC's dedicated contribution to the ITRS 2020 realizations. It contains site displacements for the CM- and the CF-frames, separated into three parts: i) non-tidal atmospheric loading (NTAL) with inverted barometer hypothesis (IB; e.g., Wunsch and Stammer, 1997) for the ocean response, ii) NTAL with a dynamic model for the ocean response, and iii) hydrological loading (HYDL). The underlying numerical (weather) models and other properties are given in Table 3.2. The second set is the operational NTL data by ESMGFZ. In contrast to the aforementioned GGFC data, it is available on a daily basis and would hence enable a continuous extrapolation of the DTRF2020. It consists of four types of site displacements in the CM- and CF-frames: 1) NTAL with IB for the ocean response, 2) non-tidal oceanic loading (NTOL), 3) HYDL, and 4) sea-level loading (SLEL). While ESMGFZ uses SLEL to ensure the conservation of mass together with the sum of 1), 2), and 3), the GGFC data is mass

Table 3.2: Summary of the non-tidal loading data sets compared in **P-1** (Table 1 therein).

	GGFC	ESMGFZ
atmospheric model	ECMWF ERA5	ECMWF ERA-40, ERA-interim, operational ECMWF
oceanic model	TUGO-m	MPIOM
hydrological model	ECMWF ERA5	LSDM
mass conservation	included in single components	separated as sea level loading
spatial resolution	selected sites	global $0.5^\circ \times 0.5^\circ$ grid
temporal resolution	1 hour	3 hours (atmosphere, ocean), 24 hours (hydrology, sea level)
data start epoch	1979/01/01 (ERA5 IB & hydro) 1980/01/01 (ERA5 TUGO-m)	1976/01/01
update frequency	every few months	daily
frames	CM, CF	CM, CF
displacements	North, East, up	North, East, up

conserving when adding the parts ii) and iii). The details of the ESMGFZ data are also provided in Table 3.2.

We begin by comparing the different NTL parts of the two providers. Due to the separation of SLEL by ESMGFZ, it becomes obvious that we can only reasonably compare the NTAL parts (with IB), as well as the total NTL. We find that NTAL agrees very well, which can be quite expected since both GGFC and ESMGFZ rely on the NWMs of the ECMWF, albeit in different versions. The total NTL, however, shows significant discrepancies, and this is mainly due to HYDL. On the one hand, the underlying hydrological models are simply different, but on the other hand the ESMGFZ data has not been continuously reprocessed over the whole time interval for the displacement series. Some of the driving factors of HYDL, i.e., precipitation and evaporation, are taken from the ECMWF models for NTAL, and these have been subject to model updates and transitions during the processing interval (compare Table 3.2). As a consequence, the displacement series for HYDL and the total NTL by ESMGFZ contain various intervals with different trends.

The same holds for the GM contributions of the NTL parts. The contributions are given by the differences between the corresponding site displacements in the CM- and CF-frame for the same epoch (compare Section 3.2.4). The time series of GM contributions for ESMGFZ reveal the same changes in trends as the site displacements, while the contributions for our GGFC data basically show a single trend in all cases.

Next, we compare the displacements series (in the CF-frame) by both providers with the position residuals of GNSS stations, which have not been reduced by NTL. Although the

level of agreement can be quite different for GGFC and ESMGFZ at single stations, we could not draw the general conclusion that either data center provides a more accurate geophysical representation of NTL - under the assumption that the GNSS residuals adequately reflect the NTL signal in the first place.

Returning to our original objective, we eventually decided to use the GGFC data for the DTRF2020. The main reason, given that the geophysical quality of both NTL data sets is indistinguishable to us, are the variable trends in the ESMGFZ site displacements and GM contributions. These are not geophysically justified but the result of model updates, and would hence distort the linear position estimates and geocenter time series in the realization of a secular TRS. The single trend in the GGFC displacement series, on the other hand, can easily be removed before their application in the DTRF2020. The impact of these trends is investigated in **P-4**.

As was observed in other studies, e.g., Roggenbuck et al. (2015) or **P-3**, we still see a significant model uncertainty w.r.t. the hydrological loading and the handling of the ocean response to NTAL.

4 Very Long Baseline Interferometry

Since the investigations of this thesis focus on VLBI, we will introduce its functionalities here. Generally, we are following the explanations of Nothnagel (2022), which is an extension of Nothnagel (2019). Other exhaustive or compact summaries are provided by Sovers et al. (1998) and Schuh and Behrend (2012), respectively. Among the geodetic space techniques, only VLBI is able to determine all EOP and realize the ICRS.

4.1 Measurement technique

VLBI originates from radio astronomy. The objects of interest are extra-galactic radio sources, mostly quasars, i.e., the same objects as used for the realization of the ICRS (compare Section 2.2). At the time of VLBI's invention in the mid 1960s, two single radio antennas have jointly been operated to increase the virtual diameter of their dishes to the distance between them, which could be as large as the Earth's diameter. By pointing at the same radio source at the same time, the angular resolution of the image of this source was improved significantly (e.g., Matveenko et al., 1965; Broten et al., 1967; Moran et al., 1967). A few years later, geodetic and astrometric applications have been developed (Cohen and Shaffer, 1971; Hinteregger et al., 1972; Ong et al., 1976), which basically rely on the same setup, but involve a global network of radio antennas.

In Figure 4.1, we show a schematic description of the VLBI measurements. Again, two antennas are receiving electro-magnetic radiation from the same extra-galactic source in the same time interval T. As this source is extremely far away, the fronts of the radio waves are assumed to be straight lines, and due to the curvature of the Earth the same part of the radio signal hits the first antenna A_1 at an earlier epoch $t_1 < t_2$ than the second antenna A_2. In an idealized situation, the wave front, the so-called baseline $\boldsymbol{B}$ between the two antenna reference points, and the distance vector with length d travelled by the wave front between t_1 and t_2 form a right-angled triangle. With the assumption that the radio signal moves at the speed of light c in vacuum, we obtain the time delay

$$\tau = t_2 - t_1 = \frac{d}{c} \tag{4.1}$$

between the arrival times at the two antennas. With $\boldsymbol{S}$ representing the unit vector in the direction of the radio source, we further get the geometric relation

$$-\boldsymbol{B} \cdot \boldsymbol{S} = c\tau \quad \Rightarrow \quad \tau = -\frac{\boldsymbol{B} \cdot \boldsymbol{S}}{c}, \tag{4.2}$$

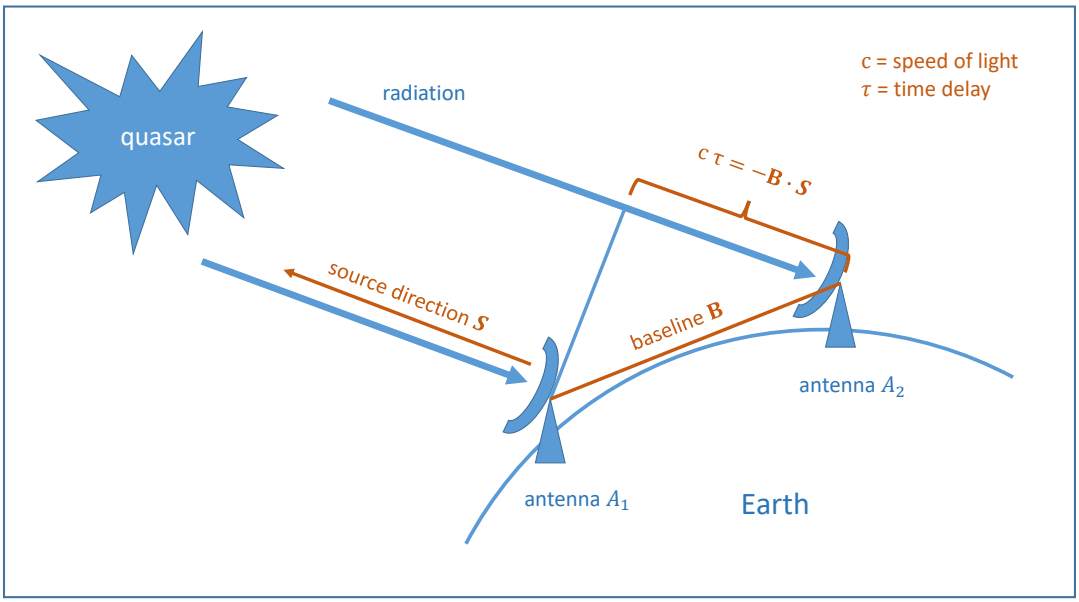

Figure 4.1: The basic functionality of the VLBI technique.

i.e., the travel distance vector is the projection of the baseline onto the unit source vector (whose direction is responsible for the minus sign). From this simplified equation, we recognize how VLBI connects the ITRS, ICRS, and EOP. The terrestrial positions $\boldsymbol{p}_i$ of the antennas A_i $(i = 1, 2)$ are defined in the ITRS, but they have to be transformed into positions $\boldsymbol{P}_i$ in the BCRS to compute the inner product of the baseline vector

$$\boldsymbol{B} = \boldsymbol{P}_2 - \boldsymbol{P}_1 \tag{4.3}$$

with the source vector $\boldsymbol{S}$. Namely, the position of the radio source is defined in the ICRS. An intermediate step is the rotation of the ITRS positions into the GCRS positions,

$$\bar{\boldsymbol{p}}_i = \boldsymbol{Q}\,\boldsymbol{R}\,\boldsymbol{W}\,\boldsymbol{p}_i \quad (i = 1, 2), \tag{4.4}$$

with the rotation matrices for the EOP from Section 2.3. Hence, all relevant ITRS, ICRS, and Earth orientation parameters are involved.

As will be shown in the following, the theoretical model for the VLBI time delay is much more complicated, and we did not yet explain how the delay can actually be measured. However, the basic functionality of VLBI is wrapped up by saying that there usually is not just one pair of antennas within a VLBI experiment, but a whole network of globally distributed antennas (compare Figure 4.4 in Section 4.4), which observe a large set of sources all across the sky for mostly a full day (24 h). Only with such a bulk of heterogeneous observations, the antenna positions, the source positions, and the EOP can be estimated sufficiently well by comparing the observed with the computed time delays. These VLBI experiments are called sessions, and the corresponding scans,

which connect observing antennas and observed source at the same reference epoch, are put together weeks ahead in a special scheduling process. The global VLBI efforts by various private, scientific, and federal institutions are organized by the IVS, and the history and statistics of these efforts have recently been summarized by Malkin (2020).

As with most geodetic applications, the analysis of VLBI observations is based on the fit of a theoretical model to the actually observed time delay. In Section 4.4, the corresponding least-squares minimization technique (see, e.g., Koch, 1999) will be explained in more detail. Before discussing the delay model in Section 4.3, we will now focus on the measurement of the time delay.

4.2 Observed time delay

4.2.1 Distinct observables

The radio antennas are basically free to observe in any frequency (band) that is not blocked by the Earth's atmosphere. We postpone the exact definition of the radio signal, and instead we state that a single radio wave with any frequency f [Hz $= \mathrm{s}^{-1}$] arrives at the second antenna with a phase shift ϕ_f [rad] compared to its arrival at the first one. If we interpret this wave as a sinusoid, and the phase (shift) is 0 at the first antenna, we have

$$\sin(\phi_f) = \sin(2\pi f \tau_{ph}) = \sin(\omega_f \tau_{ph}) \tag{4.5}$$

at the second antenna, where

$$\omega_f = 2\pi f \quad [\mathrm{rad/s}] \tag{4.6}$$

is the angular frequency, and

$$\tau_{ph} = \frac{\phi_f}{\omega_f} = \frac{\phi_f}{2\pi f} \quad [\mathrm{s}] \tag{4.7}$$

is the phase delay. In contrast to the phase shift and the angular frequency, the latter does not depend on the frequency f, since there is only one time delay for the signal. However, there is an ambiguity of integer multiples of 2π in the result of Eq. (4.5) w.r.t. the phase shift, which needs to be resolved to find the actual time delay. With suitable conditions for two frequencies f_1 and f_2, this can be achieved by letting (e.g., Moritz and Mueller, 1987)

$$\tau = \frac{\phi_{f_2} - \phi_{f_1}}{2\pi\,(f_2 - f_1)} \quad [\mathrm{s}]. \tag{4.8}$$

Using even more frequencies, this procedure provides the so-called group delay

$$\tau_{gr} = \frac{1}{2\pi}\frac{\partial \phi_f}{\partial f} \quad [\mathrm{s}], \tag{4.9}$$

which hence equals the partial derivative of the phase (shift) w.r.t. angular frequency. Finally, the phase delay rate is its derivative w.r.t. time:

$$\dot{\tau}_{ph} = \frac{\partial \tau_{ph}}{\partial t} = \frac{1}{\omega_f} \frac{\partial \phi_f}{\partial t} = \frac{1}{2\pi f} \frac{\partial \phi_f}{\partial t} \quad [\mathrm{s/s}]. \tag{4.10}$$

4.2.2 Correlation and fringe fitting

Due to the VLBI observation geometry (compare Figure 4.1), the maximum absolute time delay is

$$\tau = \frac{a}{c} \approx 21\,\mathrm{ms}, \tag{4.11}$$

which would be obtained for, e.g., one antenna located at the North pole and the other one at the equator of the Earth with radius a. To compute it, the arrival times at the two antennas must be determined. The first step is the digitization of the radio signal. In its simplest form, the 1-bit sampling, the voltage $V(t)$ measured by an antenna at epoch t is compared to a threshold value V^*, and an 1 is recorded with time tag t if $V(t) > V^*$, and a 0 otherwise. This procedure can be extended with more thresholds and corresponding bits, which comes at the expense of a larger amount of data. Anyways, the recorded and time tagged bit streams represent the digitized radio signal and are shipped from the VLBI stations to the so-called correlators. These collect the data from the different antennas involved in a session and extract the corresponding time delays.

The time tags in the bit streams depend on the clocks at the antennas. Although these are highly stable atomic clocks (mostly microwave amplification by stimulated emission of radiation (MASER) frequency standards; e.g., Oh et al., 2004), the synchronization with UTC is not equally good among all antennas, and the clocks can also deviate from their nominal frequency standards. The latter will generate delay rate-like effects, which is one reason why the delay rate will be important in the computation of the time delay. Another reason is the rotation of the Earth: in the non-rotating CRS, the position of the second antenna changes w.r.t. the position of the first antenna between t_1 and t_2. This creates a Doppler effect in the signal digitization which must be accounted for by the delay rate (e.g., Moritz and Mueller, 1987).

The group delay is computed from various observation frequencies. Hence, VLBI does not only consider a single frequency f_0, but the antennas observe in multiple frequency channels belonging to distinct frequency bands. The classical, or legacy frequency bands are the S- and X-bands, with frequencies at about 2 GHz and 8 GHz, respectively (compare Figure 4.5 in Section 4.5). The actual observations are taken from the X-band, while the S-band is basically used for determining the influence of the Earth's ionosphere on the time delay (compare Section 4.3.5). The number of channels in S- and X-band is usually 6 and 8, respectively, and the width of the channels is 8 MHz. The distribution of channels is important for the precision of the VLBI measurements, which is based on the signal-to-noise ratio (SNR, compare Section 4.2.3). The advantage of

using separate, smaller channels inside a band is the reduced amount of recorded data, while the total recorded bandwidth still resembles that of the distance between the two outer channels. This procedure is called bandwidth synthesis (Rogers, 1970).

Before we return to the frequency channels, we will explain the mathematical background of finding the time delay. It is obtained by maximizing the cross-correlation function

$$C(\tau) = \frac{1}{T}\int_0^T V_1(t-\tau)V_2(t)\,dt. \tag{4.12}$$

Its discrete version is

$$\tilde{C}(\tau) = \frac{1}{N}\sum_{j=1}^{N} V_1(t_j-\tau)V_2(t_j), \tag{4.13}$$

with the recorded bit streams $V_i(t_j)$ $(i = 1,2)$ of the antennas, which consist of N distinct measurements during the integration time interval T. In other words, the argument τ is varied until the shifted bit streams agree most. The cross correlation function (4.12) is very similar to the convolution of V_1 and V_2,

$$V_1 * V_2 = \int_{-\infty}^{\infty} V_1(\tau-t)V_2(t)dt = F^{-1}[F[V_1]\,F[V_2]], \tag{4.14}$$

where F and F^{-1} are the Fourier transform and its inverse, respectively (e.g., Christensen and Christensen, 2006). Hence, to equalize the two functions, only the sign of the argument of V_1 needs to be reversed. Since

$$F[-V] = \bar{F}[V], \tag{4.15}$$

with $\bar{F}$ representing the complex conjugate of F, we finally get

$$\tilde{C}(\tau) = \frac{1}{N}FFT^{-1}\left[F\bar{F}T[V_1]\,FFT[V_2]\right] \tag{4.16}$$

for the cross-correlation, in which FFT is the discrete version of the Fourier transform (Fast Fourier transform; e.g., Christensen and Christensen, 2006). Instead of $\tilde{C}(\tau)$, the cross-spectrum with frequency arguments f is usually considered for the correlation of the time delay. It is defined as

$$\tilde{C}[f] = F\bar{F}T[V_1]\,FFT[V_2] = FFT\left[N\,\tilde{C}(\tau)\right], \tag{4.17}$$

and can thus be computed in two ways. Either, the FFT is performed first for both antenna bit streams and then the results are multiplied (FX correlation), or the cross-correlation is computed first and the FFT is performed afterwards (XF correlation). Nowadays, the FX-correlation is more efficient and widely used (e.g., Deller et al., 2011).

The cross-spectrum provides amplitudes and phases for different frequencies and can hence directly be related to the observables phase delay (4.7) and group delay (4.9).

However, this correlation process is conducted not only once, but for various sub-intervals of the integration period T. The corresponding time series of cross-spectra enables us to determine a pair of group delay and (phase) delay rate that maximizes the two-dimensional cross-correlation function which now depends on both frequency and time. This subsequent process is called fringe fitting and delivers the final values for the observables (e.g., Cappallo, 2017).

The actual correlation and fringe fitting procedures are much more complicated, but for our purpose of an introduction to VLBI we will only continue by quoting some information (e.g., Petrov et al., 2011) on the combination of the aforementioned frequency channels (bandwidth synthesis). Instead of generating a single-band group delay and delay rate from a single channel, one can also use the full information from all observed channels (multi-band) in a frequency band. The first way is to compute cross-spectra for the reference frequencies of all distinct channels and then apply the inverse FFT to these spectra in a multi-band fringe fitting afterwards. The alternative is to determine the single- and multi-band group delays and delay rates jointly in a common process. Generally speaking, using as much bandwidth as possible increases the precision of the VLBI observables (compare Section 4.2.3), but the gaps between the frequency channels also pose some procedural challenges.

Finally, we make a remark on the third observable, the phase delay. While it is more precise than the group delay, its computation is also more complicated, and many analysis softwares - including the current version of the DGFI Orbit and Geodetic parameter estimation Software (DOGS) used for this thesis - still stick to the group delay observable. Hence, we will not explain the determination of the phase delay, but the reader is referred to, e.g., Nothnagel (2022). Nevertheless, the following equation shows how phase delay, phase delay rate, and group delay are connected by the Taylor-expansion of the two-dimensional phase function $\phi(f,t)$ from the cross-spectrum (compare Sovers et al., 1998):

$$\begin{aligned} \phi(f,t) &= \phi(f_0,t_0) + \frac{\partial\phi}{\partial t}(f_0,t_0)[t-t_0] + \frac{\partial\phi}{\partial f}(f_0,t_0)[f-f_0] \\ &= \phi(f_0,t_0) + 2\pi f_0 \dot{\tau}_{ph}[t-t_0] + 2\pi\tau_{gr}[f-f_0] \qquad (4.18) \\ \Rightarrow \quad \frac{\phi(f,t)}{2\pi f_0} &= \tau_{ph} + \dot{\tau}_{ph}[t-t_0] + \frac{1}{f_0}\tau_{gr}[f-f_0]. \end{aligned}$$

4.2.3 Measurement precision

We still need to identify the signal of the extra-galactic radio sources. Although the electro-magnetic radiation is basically white noise, we define this pure radiation to be the actual signal, while any other components added along the way through the Earth's atmosphere and the electronic devices of the antennas are defined to be the noise. According to Whitney (1974), the SNR is given by

$$\mathrm{SNR} = \eta \frac{FD}{2\,k} \sqrt{\frac{D_1 D_2}{N_1 N_2}} \sqrt{2\,\Delta f\, T}, \qquad (4.19)$$

where $\eta \in [0.5, 0.7]$ is a digitizing loss factor, FD the correlated flux density (i.e., strength) of the radio source, k Boltzmann's constant, D_i and N_i the effective antenna area and system noise temperature of antenna i ($i = 1, 2$), respectively, Δf the total observed frequency bandwidth, and T the integration time.

The formal errors of the VLBI observables, which are expressed by standard deviations, can now be related to this SNR (Whitney, 1974). For the phase delay, we have

$$\sigma_{\tau_{ph}} \approx \frac{1}{2\pi f_0 \,\mathrm{SNR}}. \tag{4.20}$$

For the phase delay rate, it holds

$$\sigma_{\dot{\tau}_{ph}} \approx \frac{1}{2\pi f_0 \,\Delta T_{rms} \,\mathrm{SNR}}, \tag{4.21}$$

with

$$\Delta T_{rms} = \sqrt{\frac{1}{T}\sum_k (t_k - \bar{t})^2} \tag{4.22}$$

being the rms integration time based on the sample epochs t_k and the mean epoch $\bar{t}$. Lastly, the standard deviation of the group delay is given by

$$\sigma_{\tau_{gr}} \approx \frac{1}{2\pi \,\Delta f_{rms} \,\mathrm{SNR}}, \tag{4.23}$$

where

$$\Delta f_{rms} = \sqrt{\frac{1}{L}\sum_{l=1}^{L} (f_l - \bar{f})^2} \tag{4.24}$$

is the effective bandwidth based on the L distinct channel frequencies f_l providing the mean frequency $\bar{f}$.

Most of the components of the SNR are antenna or source dependent, i.e., D_i, N_i, and FD. To improve the SNR, and consequently the precision of the observables, one can thus basically increase the (effective) bandwidth or the integration time. The latter contradicts the intention to have as many observation as possible during a VLBI session, so the best choice is to optimize the distribution of the frequency channels f_l. Practically, the SNR is determined during fringe fitting (e.g., Petrov et al., 2011).

4.3 Theoretical time delay

The relativistic consensus model for the time delay τ is provided by Eubanks (1991) and summarized in Chapter 11 of the IERS Conventions 2010. Our following introduction is also based on Nothnagel (2022).

4.3.1 Vacuum delay

We start with the geometric relation (compare Section 4.1) in the BCRS, so the time delay is given in the barycentric coordinate time TCB (Temps Coordonné Barycentrique):

$$T_2 - T_1 = -\frac{[\boldsymbol{P}_2(T_2) - \boldsymbol{P}_1(T_1)] \cdot \boldsymbol{S}}{c}. \tag{4.25}$$

The BCRS positions of the antennas are computed from

$$\boldsymbol{P}_i(T_i) = \boldsymbol{P}_{GC}(T_i) + \bar{\boldsymbol{p}}_i(T_i) \quad (i = 1, 2), \tag{4.26}$$

where $\boldsymbol{P}_{GC}$ is the BCRS position of the geocenter, and the $\bar{\boldsymbol{p}}_i$ equal the GCRS positions of the antennas from Eq. (4.4). They are used to compute the total gravitational delay component

$$\Delta T_{grav} = \sum_k \Delta T_{grav,k} \tag{4.27}$$

of the time delay, which is the sum of the single delay components $\Delta T_{grav,k}$ (IERS Conventions 2010, Equations 11.1 - 11.7). The latter are induced by all relevant gravitating bodies k in the solar system, i.e., the sun, the moon, the Earth, and all planets. The radio signal is deflected when passing them on its way to the antennas due to General Relativity, so the new time delay reads

$$T_2 - T_1 = -\frac{[\boldsymbol{P}_2(T_2) - \boldsymbol{P}_1(T_1)] \cdot \boldsymbol{S}}{c} + \Delta T_{grav}, \tag{4.28}$$

and is also called vacuum delay.

Eq. (4.28) now needs to be transformed into the GCRS, since the clocks at the antennas can only measure proper (atomic) terrestrial time. This affects two components: the barycentric positions $\boldsymbol{P}_i$ of the antennas, and the epochs T_i which are still given in TCB. The time scale of the GCRS is TCG (compare Section 2.1), and it is connected to the atomic time TT (Terrestrial Time, valid at the geoid) by a constant $L_G = 6.969290134 \cdot 10^{-10}$, which implies

$$\tau_{TCG} = \frac{\tau_{TT}}{1 - L_G} \tag{4.29}$$

for the corresponding time delays. The epoch t_1, the geocentric point of time of the signal's arrival at the first antenna, is defined to be the reference epoch for the time delay. Regarding the antenna positions, we note that the barycentric position $\boldsymbol{P}_2$ of the second antenna has changed between t_1 and t_2, the geocentric point of time of the signal's arrival at the second antenna, due to the Earth's rotation around the sun. Likewise, its geocentric position $\bar{\boldsymbol{p}}_2(t_2)$ has changed from $\bar{\boldsymbol{p}}_2(t_1)$ due to the Earth's rotation around itself. The first effect is called annual aberration, the second one is called daily aberration. To correct for them, we need to know the barycentric velocity $\boldsymbol{W}_{GC}$ of the geocenter, and the geocentric velocity $\boldsymbol{\omega}_2$ of the second antenna, respectively.

The corresponding relativistic modification of Eq. (4.28) is a Lorentz transformation, and the final formula for the vacuum delay τ_{vac} is

$$t_2 - t_1 = \frac{\Delta T_{grav} - \frac{\boldsymbol{S}\cdot\bar{\boldsymbol{b}}}{c}\left[1 - \frac{(1+\gamma)U}{c^2} - \frac{|\boldsymbol{W}_{GC}|^2}{2c^2} - \frac{\boldsymbol{W}_{GC}\cdot\boldsymbol{\omega}_2}{c^2}\right] - \frac{\boldsymbol{W}_{GC}\cdot\bar{\boldsymbol{b}}}{c^2}\left(1 + \frac{\boldsymbol{S}\cdot\boldsymbol{W}_{GC}}{2c}\right)}{1 + \frac{\boldsymbol{S}\cdot(\boldsymbol{W}_{GC}+\boldsymbol{\omega}_2)}{c}}, \quad (4.30)$$

where γ is the parameterized post-Newtonian parameter (equal to 1 in General Relativity), U is the gravitational potential at the geocenter without the Earth's mass, and $\bar{\boldsymbol{b}}$ is the baseline vector in the GCRS.

4.3.2 Terrestrial time scales

A remark regarding the terrestrial time delays is necessary. Using τ_{TCG} complies with Resolution 2 (1991) of the IUGG and Resolution B6 (1997) of the IAU. However, the correlators provide τ_{TT}, which is also used by the ACs of the IVS. As a consequence, the corresponding coordinates $\bar{\boldsymbol{p}}_i$ of the antennas do not exactly refer to the GCRS until they have been scaled by $1/(1 - L_G)$. But, according to the resolutions of the ITRF Workshop in 2000, this scaling is not applied, so that the VLBI antenna coordinates (like those of the other geodetic space techniques) actually refer to TT in the ITRS realizations starting with ITRF2000 (IERS Conventions 2010).

4.3.3 Technical delay components

The vacuum delay in Eq. (4.30) needs further corrections due to various physical and technical effects. We start with the latter.

The radio antennas consist of a main reflector (the dish) and one or two sub-reflectors to direct the radio signals into the feed horn at the focal point (compare Figure 4.2). From the feed horn, the radiation is lead by cables to the receiver and other technical devices for amplifying and digitizing the signal. To aim at basically every position of the celestial sphere, the antenna dishes move around two perpendicular axes, and their invariant intersection is the reference point for the antenna positions in the ITRS realizations. Mostly for constructional reasons, many antennas have an axis offset (AO) between the invariant reference point at the primary axis and the secondary one (compare Figure 4.2 again). The length of the signal path from the main reflector to the reference point and the receiver will be relevant for the measured time delay, so this length must be modelled carefully.

One of the most important factors of signal path variation is the elevation of the antenna, i.e., the angle between the horizon and the observed radio source. First, the path length changes with elevation due to the AO (Nothnagel, 2009), so we obtain a delay component $\Delta\tau_{AO}$ taking into account the corresponding variations at the two antennas. Second, the elevation is crucial for gravitational deformations of the whole antenna dish structure, i.e., for path length variations between the main and the sub-reflector(s), as well as between the sub-reflector(s) and the feed horn (e.g., Sarti et

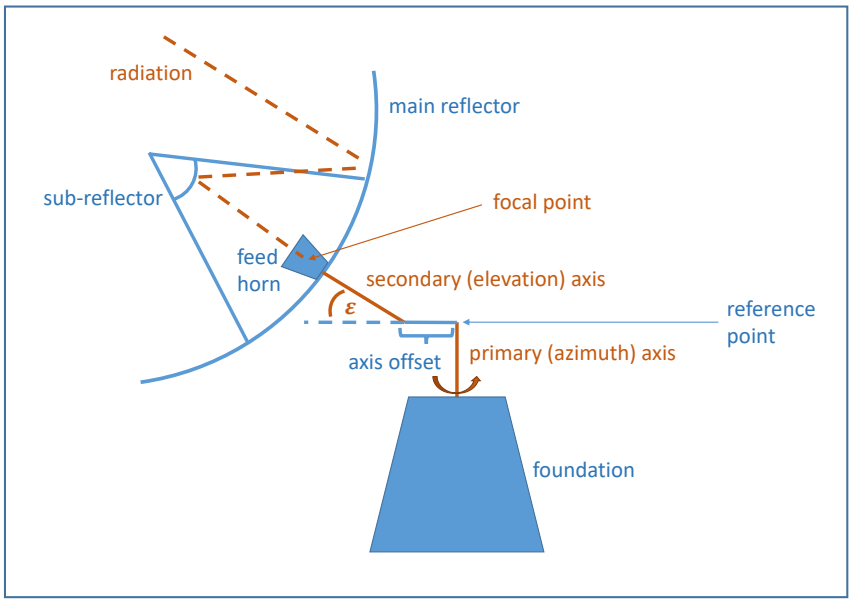

Figure 4.2: Sketch of a radio antenna with azimuth-elevation mount and one hyperbolic sub-reflector (Cassegrain style; a parabolic sub-reflector is called Gregorian), inspired by Nothnagel (2022).

al., 2011; Nothnagel et al., 2014). Hence, we must apply a respective delay correction $\Delta\tau_{GD}$ (Gipson and Sikstrom, 2018). Third, the elevation plays a role in the thermal deformations of the antennas, which are mainly driven by the surrounding temperature and the thermal expansion coefficients of the antenna material, i.e., mostly concrete and steel (Nothnagel, 2009). We denote the corresponding time delay component by $\Delta\tau_{TD}$.

Next to these elevation-dependent effects, there are also delays which are simply created by the electric system itself, because the signal has to run through cables and other technical devices. These delays are approximated by so-called cable- and phase calibrations (e.g., Moran and Dhawan, 1995) during the VLBI observations and lead to delay corrections $\Delta\tau_{cal}$. Finally, the clocks at the distinct antennas are not perfectly synchronized with atomic time (UTC, or Temps Atomique International, TAI, which only differ by the leap seconds), so a part of the time delay originates from an offset $\Delta\tau_{clo}$ between the antenna clocks.

To summarize, we arrive at an intermediate time delay of

$$t_2 - t_1 = \tau_{vac} + \Delta\tau_{AO} + \Delta\tau_{GD} + \Delta\tau_{TD} + \Delta\tau_{cal} + \Delta\tau_{clo}. \tag{4.31}$$

Except for $\Delta\tau_{clo}$, all correction terms are obtained from (empirical) models taking into account known antenna properties or measurable parameters such as elevation and temperature. At the time of writing, models for the gravitational deformation have only been available for six antennas, however. Hence, $\Delta\tau_{GD}$ cannot be computed in

many cases. The clock offsets, on the other hand, are completely unknown. The corresponding antenna-dependent parameters, which usually consist of the coefficients of i) quadratic and ii) additional continuous piecewise linear functions, are estimated during the analysis of the VLBI observations (compare Section 4.4).

4.3.4 Radio source related components

Now, we turn to the physical effects which influence the time delay, and we start with the radio sources. The latter are assumed to have fixed positions, so that they can realize the ICRS as an inertial frame. However, with the current precision and long-term history of VLBI measurements, we are actually able to observe proper motions of the radio sources (e.g., Titov et al., 2011). These are related to the acceleration of the SSB towards the Galactic center, which creates an aberration effect (Kovalevsky, 2003). Hence, the motions of the radio sources are only apparent, and we have to correct for this Galactic aberration effect. The corresponding recommendation of the IVS Working Group (WG) 8 is to apply an additional delay component

$$\Delta\tau_{GA} = -\frac{\bar{\boldsymbol{b}} \cdot \Delta\boldsymbol{S}}{c}, \tag{4.32}$$

where $\Delta\boldsymbol{S}$ is the apparent change in the radio source position based on a secular aberration drift of 5.8 μas/a (MacMillan et al., 2019).

Another issue is source structure. Many sources are not point-like, i.e., there is no clearly defined center to which its position can be referred (e.g., Xu et al., 2017; Plavin et al., 2019). The shape and size of a source can even change with time and observation frequency. This creates measurement noise and needs to be corrected for (Anderson and Xu, 2018). However, while some proposals already exist (e.g., Xu et al., 2021), there is no conventional correction model yet.

4.3.5 Atmospheric delay components

On its way from the radio source to the antennas, the signal has to pass the Earth's atmosphere, which is separated into a charged (ionosphere) and a neutral part (troposphere). As already mentioned in Section 4.2.2, the influence of the dispersive ionosphere can be determined by measuring the signal delay in two different frequency bands. For legacy VLBI, these are the S- and the X-band. The impact on the radio signal depends on the total electron content (TEC) in the ionosphere, which is basically driven by the radiation of the sun. Hence, the TEC is lower during night- than during day-time of an antenna. The formulas for the frequency-dependent ionospheric delays can be found in, e.g., Nothnagel (2022), and the signs are opposite for phase (acceleration) and group (retardation) delay. The author also provides the final ionospheric delay correction in X-band,

$$\Delta\tau_{io,X} = (\tau_S - \tau_X)\,\frac{f_S^2}{f_S^2 - f_X^2}, \tag{4.33}$$

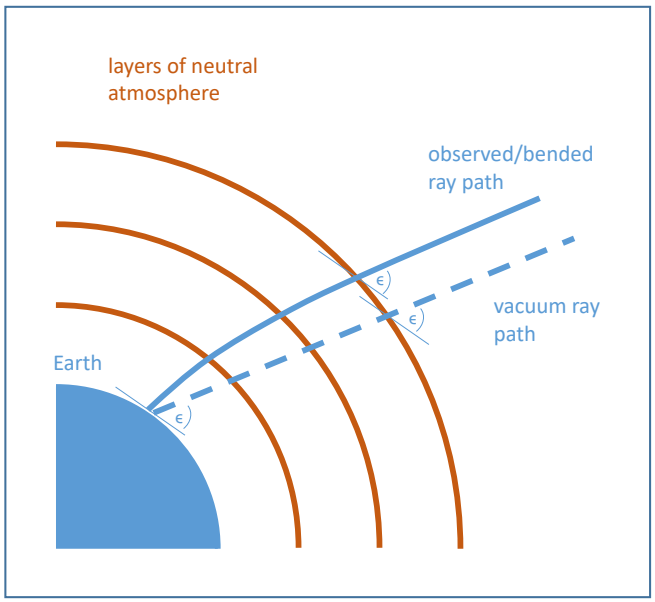

Figure 4.3: Simplified bending and delay of radio signals due to a stratified neutral atmosphere, inspired by Hofmeister (2016). The outgoing (after the last layer) and vacuum elevation angles ϵ are identical.

where τ_S and τ_X are the measured time delays in S- and X-band with average (across all channels) frequencies f_S and f_X, respectively. These values are computed during correlation and fringe fitting, and are hence available to the ACs.

For the non-dispersive troposphere, the situation is more complicated. By interaction with dry gases and water vapor, the electro-magnetic radiation is bended and delayed when passing through the neutral atmosphere, compare Figure 4.3. Measuring the size of the delay is basically impossible, so it needs to be modelled (e.g., Hofmeister, 2016). Most accurately, this is done by ray-tracing methods (e.g., Hobiger et al., 2008), where the stepwise refraction of a radio signal by different horizontal and vertical layers of the atmosphere is approximated by means of NWMs. Since the effort of ray-tracing would be too large for each and every geodetic observation, a simpler procedure has been devised to map the obtained zenith delays to the delays for different observation elevations.

If the time delay component induced by the troposphere for an observation with elevation ϵ is denoted by $\Delta\tau_{tr}(\epsilon)$, it is initially modelled by

$$\Delta\tau_{tr}(\epsilon) = \Delta Z_w \; MF_w(\epsilon) + \Delta Z_h \; MF_h(\epsilon). \tag{4.34}$$

Here, ΔZ_w and ΔZ_h are the delays in zenith direction generated by the wet and hydrostatic components of the neutral atmosphere, respectively. Likewise, MF_w and MF_h are the mapping functions for the wet and hydrostatic components, which transform the zenith delays to their corresponding values depending on ϵ. Mostly, the mapping

functions are continued fractions depending on $\sin(\epsilon)$ and three coefficients a, b, and c (e.g., Marini, 1972; Herring, 1992; Niell, 2000). Thereby, a often depends on the ray-tracing, i.e., the NWM, while b and c are empirically determined, but also other combinations are possible (compare Landskron and Böhm, 2017). There are service centers providing the corresponding coefficients on a daily basis for particular geodetic sites, e.g., the VMF data server of TU Vienna (*https://vmf.geo.tuwien.ac.at/*).

The hydrostatic zenith delay, which is mainly induced by the dry gases in the troposphere, can sufficiently accurately be computed a priori if the atmospheric surface pressure at a site is available (Saastamoinen, 1972; Davis et al., 1985). The wet zenith delay, however, is unknown and must be estimated during the analysis of the (VLBI) observations. For each antenna, ΔZ_w is usually parameterized as a piecewise linear function depending on time, and it is driven by the amount of water particles in the troposphere.

The time delay in Eq. (4.34) is further refined by including a horizontal dependence next to the vertical one. For example, the rotation of the Earth creates a thicker troposphere at the equator than at the poles, and spatially variable parameters like temperature and pressure also affect the size of the delay of the radio signal in the neutral atmosphere (e.g., Landskron and Böhm, 2017). The extended formula for the tropospheric delay with observation azimuth angle α reads

$$\begin{aligned} \Delta\tau_{tr}(\epsilon,\alpha) &= \Delta Z_w\ MF_w(\epsilon) + \Delta Z_h\ MF_h(\epsilon) \\ &+ GMF_w(\epsilon)\ [GN_w\ \cos(\alpha) + GE_w\ \sin(\alpha)] \\ &+ GMF_h(\epsilon)\ [GN_h\ \cos(\alpha) + GE_h\ \sin(\alpha)]\,, \end{aligned} \tag{4.35}$$

in which the wet and hydrostatic mapping functions

$$GMF_{w/h}(\epsilon) = \frac{1}{\sin(\epsilon)\tan(\epsilon) + C_{w/h}} \tag{4.36}$$

by Chen and Herring (1997) have been empirically determined with $C_w = 0.0007$ and $C_h = 0.0031$, respectively. The so-called gradients GN and GE in North and East direction, respectively, are often estimated like the wet zenith delays. Usually, they are parameterized as piecewise linear functions of time per antenna, too, but with a lower temporal resolution. Alternatively, single North and East gradients (i.e., without the separation into wet and hydrostatic parts) can be modelled and estimated. A priori values for the latter are available from the Data Assimilation Office of NASA's Goddard Space Flight Center, for example.

According to the model described by the IERS Conventions 2010, the impact of the troposphere on the theoretical time delay is twofold. If $\Delta\tau_{tr,i}$ represents the tropospheric delay at antenna i, then the actual propagation delay induced by the neutral atmosphere is

$$\Delta\tau_{tr} = \Delta\tau_{tr,2} - \Delta\tau_{tr,1}. \tag{4.37}$$

However, there is another term to be added to Eq. (4.31), namely

$$\Delta\tau_{tr,1}\,\frac{\boldsymbol{S}\cdot(\boldsymbol{\omega}_2-\boldsymbol{\omega}_1)}{c}, \tag{4.38}$$

which accounts for the additional aberration (i.e., time for rotation) of antenna A_2 w.r.t. A_1 during the propagation delay. The sum of this term and the vacuum delay is called the geometric time delay τ_{geo}.

Altogether, we obtain the theoretical time delay

$$t_2 - t_1 \;=\; \tau_{geo} + \Delta\tau_{AO} + \Delta\tau_{GD} + \Delta\tau_{TD} + \Delta\tau_{cal} + \Delta\tau_{clo} + \Delta\tau_{GA} + \Delta\tau_{io} + \Delta\tau_{tr}. \tag{4.39}$$

4.4 Parameter estimation

The analysis of geodetic (space) observations is usually based on the Gauss-Markov model. It defines a set of parameters to be inserted into the theoretical observation equations and solves for those parameter values which agree best (in a particular mathematical sense) with the actual measurements. In the case of VLBI, these parameters mostly are

- antenna coordinates,
- radio source coordinates,
- EOP,
- wet zenith delays,
- tropospheric gradients,
- clock offsets.

Since this technique relies on the baselines between the antennas, i.e., on their relative positions only, the resulting system of equations is singular w.r.t. to the absolute location and orientation of the antenna network. Likewise, the system is singular w.r.t. the orientation of the radio sources. The corresponding geodetic datum (compare Section 2.1) hence needs to be added in the form of extra model constraints. The scale of the antenna network, on the other hand, can intrinsically be determined by VLBI.

In Figure 4.4, we show the VLBI network of legacy antennas that we examine in **P-4**. As already mentioned in Section 2.2, the global distribution of antennas is unbalanced, since there are many more of them in the Northern than in the Southern hemisphere. To obtain the most accurate estimates for the target parameters, a more homogeneous antenna network is needed, so that the volume of the polyhedron formed by the baselines gets close to the volume of the Earth. To make things worse, only about 8–12 antennas usually participate in a VLBI session, i.e., far fewer antennas than those presented in Figure 4.4.

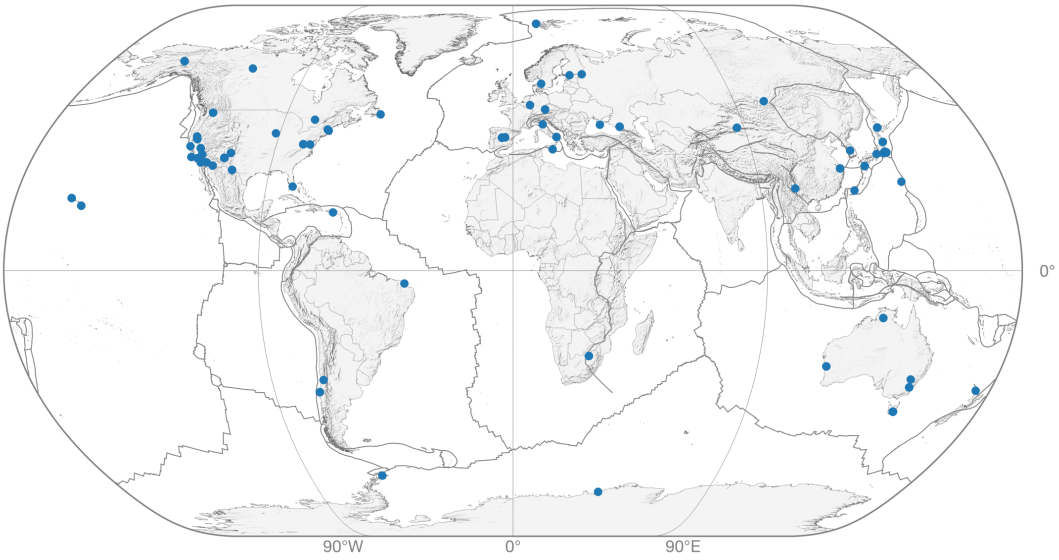

Figure 4.4: The legacy VLBI network examined in **P-4**, including both former and current antennas. Courtesy of Daniel Scherer, DGFI-TUM.

At DGFI-TUM, we use the software package DOGS for the analysis of VLBI observations with the Gauss-Markov model. The component DOGS-RI (Radio Interferometry; Kwak et al., 2017) implements the theoretical delay model and can either directly solve for the parameters or delegate this task to the component DOGS-CS (Combination & Solution; Gerstl et al., 2000).

The Gauss-Markov model is described in detail in **P-2**. The latter focuses on the impact of the application of site displacements (e.g., due to NTL) at the different levels of the model:

P-2 Glomsda M., Bloßfeld M., Seitz M., and Seitz F. (2021): **Correcting for site displacements at different levels of the Gauss-Markov model - a case study for geodetic VLBI**, *Advances in Space Research*, Vol. 68 (4), pp. 1645-1662, doi:10.1016/j.asr.2021.04.006

Summary This article is the most theoretical one in our thesis. It recaps the well-known Gauss-Markov model and explains the changes to the formulas when displacements are added to the station coordinate parameters. We consider three different application levels for the displacements: at the observation level, the displacements are added in the original observation equations; at the normal equation level, the subsequent (unconstrained) normal equation system is modified with average displacements; at the solution level, the average displacements are directly subtracted from the final (constrained) coordinate estimates. While we focus on VLBI single-session solutions, many results are also valid for other geodetic measurements.

The theoretical results are supported by numerical examples. On this occasion, the workflow of our analysis software DOGS is explained for VLBI. The site displacements can basically refer to any geophysical effect, but since we are investigating NTL in this thesis, we used displacements generated for non-tidal atmospheric loading by ESMGFZ for the computations in this article.

At the observation level, the functional model changes after the application of site displacements, and so do the partial derivatives in the Jacobi matrix. As a consequence, both the matrix and the right-hand-side of the normal equation system are affected. Since different displacement values can be used for each observation, the temporal resolution of the original displacement series is preserved. At the normal equation level, on the other hand, the change in the functional model is only approximated by multiplying the original partial derivatives with average site displacements for the whole time interval of observations. Hence, the normal equation matrix remains unchanged, while only the right-hand-side is affected, and the original temporal resolution is lost. The latter also holds for the solution level, and the main difference to the previous two levels is the fact that the (average) displacements are only applied after the addition of the datum constraints (which remove the singularity of the normal equation system).

The derived formulas and the numerical examples show that the impact on the Jacobi and normal equation matrices at the observation level is negligible for NTL. Furthermore, the approximation of the change in the functional model at the normal equation level is very good for VLBI, while the loss of temporal resolution in the displacement series is much more significant. Hence, if the variation in the displacements is small during a VLBI session, the numerical results for observation and normal equation level strongly agree. Anyways, it is shown that the differences between the estimated parameters for these two levels are generally much smaller than the differences to the case where no (NTL) site displacements are applied at all. On the one hand, this is because the station coordinates, which are affected most by the site displacements, are only represented by a constant position throughout a VLBI session. On the other hand, the parameters which are set up with a larger temporal resolution themselves, e.g., tropospheric zenith delays, and which actually show differences between the two application levels, are only affected on scales significantly smaller than their formal errors.

Subtracting the site displacements directly from the estimated station coordinates, however, generally provides deviating coordinates w.r.t. those for the observation and normal equation levels. We show that this is related to the datum constraints for the stations. The number and distribution of stations which are considered for the no-net-translation (NNT) and no-net-rotation (NNR) conditions in a VLBI session determine how the changes in coordinate estimates differ from the corresponding (average) site displacements. Furthermore, while the frame of the displacements, i.e., CM or CF, is irrelevant at the observation and normal equation levels for VLBI (since GM is a translation that is cancelled on baselines), only the frame that the estimates have been aligned to (by the datum constraints) may be used at the solution level.

To conclude, the article shows that - and why - the estimates of VLBI station positions agree very well after site displacements have been applied at the observation or the normal equation level. While this is explicitly shown for single-session solutions only, these results provide a basis for similar considerations on secular TRF solutions.

4.5 Next generation: VGOS

The legacy VLBI system is operational since 1979 and has generated millions of observations with more than a hundred different antennas (Malkin, 2020). To push the capabilities of VLBI to the next level, IVS WG 3 - called IVS Working Group on VLBI2010 - was founded in 2003. Its objective was to make recommendations on how to improve the whole process chain, i.e., on how to obtain highest-precision geodetic and astrometric results with low latencies and low costs of construction and operation. The final report of WG 3 (Niell et al., 2006) was approved by the IVS Directing Board in 2005, and further findings and simulations were published by Petrachenko et al. (2009). In 2012, the project was renamed from VLBI2010 to VLBI Global Observing System (VGOS), not least to commit to the accuracy goals of 1 mm and 0.1 mm/a for station positions and velocities in TRFs, respectively, which were defined by the Global Geodetic Observing System (GGOS; Miyahara et al., 2020) of the IAG. Next to the construction of new radio antennas, new correlation and fringe fitting procedures and capacities had to be established, and prototype VGOS measurements could finally be performed on a 600 km baseline in North America in 2017 (Niell et al., 2018).

The main finding of WG 3 was, that the modelling of the propagation delay due to refraction in the neutral atmosphere (compare Section 4.3.5) is deteriorating the VLBI results most (Niell et al., 2006). To improve the estimation of the wet zenith delays and the gradients, more observations per unit time at different elevation and azimuth angles are needed. Hence, it was proposed to build smaller antennas that allow for faster slewing times from one radio source to another. (Besides, these antennas are supposed to be less prone to gravitational deformations.) However, according to Eq. (4.19) for the SNR, the precision of the VLBI observations will decrease with smaller antennas. To mitigate this effect, one could either increase the integration time of the observations, or increase the (effective) bandwidth. Since the first alternative would again reduce the number of observations, the VGOS broadband measurements were introduced.

In the legacy S/X system, there are usually six channels at frequencies of about 2 GHz and eight channels at about 8 GHz, which are connected by bandwidth synthesis (compare Section 4.2.2 and Figure 4.5). The ionospheric delay is computed from the results of these two bands (compare Section 4.3.5). With the new VGOS broadband measurements, there are various channels in four bands from a potential frequency range of 2-14 GHz (see Figure 4.5 again), and the ionospheric delay is fitted together with the broadband time delay in a joint process (e.g., Cappallo, 2014). The formal errors of the VGOS observations are significantly smaller than the legacy ones (Niell

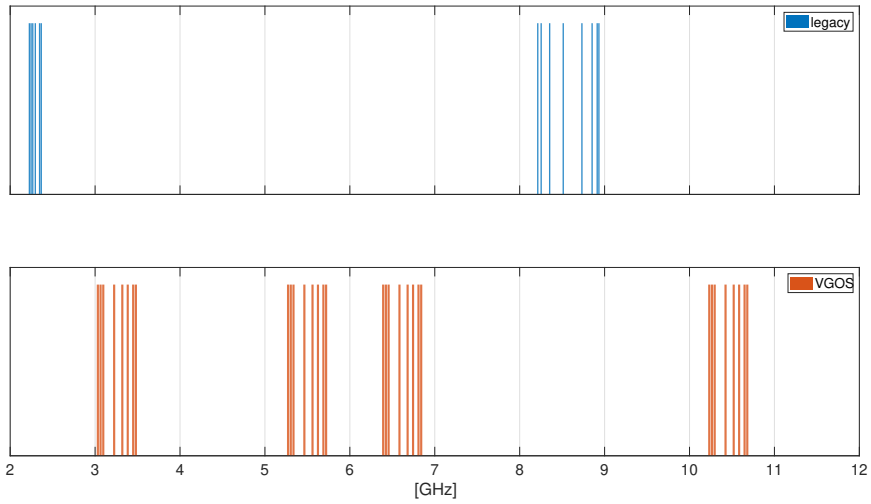

Figure 4.5: Top: the S- and X-band channels of the legacy VLBI session 22JAN07XA. Bottom: the new VGOS broadband channels in session 22MAY19VG.

et al., 2018), and first results also indicate that the tropospheric modelling is improved (Mikschi et al., 2021).

As of the beginning of 2022, there were 9 operational VGOS antennas, all located in the Northern hemisphere (Behrend et al., 2022). Hence, the VGOS network is rather small and poorly distributed at the time of writing. Since 2019, about two 24h-sessions with 5-9 VGOS antennas have been scheduled and conducted per month, in addition to five 24h-sessions during the continuous VLBI campaign in 2017 (CONT17). Given this rather sparse data, we did not include VGOS observations in the investigations of this thesis.

5 Application of non-tidal loading in VLBI analysis

In this chapter, we finally discuss the impact of the reduction of NTL on most of the geodetic parameters that can be derived from VLBI measurements (compare Section 4.4). In particular, we focus on the antenna coordinates, the EOP, and some of the auxiliary tropospheric and clock parameters. First, we examine single-session solutions in **P-3**, then we investigate secular VLBI-only TRFs in **P-4**. Finally, we provide a discussion of the magnitude of the impact.

5.1 Single-session solutions

P-3 Glomsda M., Bloßfeld M., Seitz M., and Seitz F. (2020): **Benefits of non-tidal loading applied at distinct levels in VLBI analysis**, *Journal of Geodesy*, Vol. 94 (90), doi:10.1007/s00190-020-01418-z

Summary We perform a systematic investigation of the reduction of NTL in VLBI single-session solutions. We use about 33 years of VLBI observations that were analysed at the IVS AC DGFI-TUM with our DOGS software and include all (41) antennas that participated in at least 100 of the corresponding sessions. NTL is applied at both the observation and the normal equation level, and the respective site displacements are taken from two different providers: ESMGFZ and IMLS. The three components of NTL are considered both individually and in total: NTAL, NTOL, and HYDL. All in all, we have $2 \cdot 2 \cdot 4 = 16$ different NTL scenarios, which are compared to the scenario without reducing any NTL.

But first, the NTL data of ESMGFZ and IMLS are examined. In contrast to **P-1**, we compare the corresponding site displacements (in the CM-frame) per baseline. Namely, in VLBI, the baselines rather than the individual antenna sites are relevant for the observables. Just as in **P-1**, however, the displacements agree very well between the providers for NTAL (and NTOL), but deviate significantly for HYDL. This again emphasizes the model uncertainty w.r.t. the land water storage. Another finding is the baseline-dependent dominance of the NTL parts: for each baseline, either NTAL, NTOL, or HYDL can represent the strongest effect. Hence, all components should be included when reducing NTL.

NTL is mainly affecting the antenna coordinates (compare **P-2**). We take a look at the WRMS values of the single-session coordinate residuals w.r.t. a long-term linear motion

for each antenna, and observe a decrease for about 90% of the antenna heights when the sum of all NTL parts is reduced jointly. On average, the WRMS values are lessened by 4%. For the horizontal (North, East) coordinates, the mean decrease is only about 1-2%, and the pattern is less systematic across the distinct antennas. However, all this holds for both application levels and both NTL data sets.

In contrast to NTAL and NTOL, the site displacements for HYDL contain hardly any intra-session (i.e., sub-diurnal) temporal variation. Since the session average is applied at the normal equation level, there is basically no difference to the application at the observation level for HYDL, either. The deviations for the same application level but with different providers are generally larger, however. For NTAL and NTOL, we observe the opposite behaviour, as there is more intra-session variability in the site displacements, which also agree better between ESMGFZ and IMLS. This is in line with the result of **P-2**, that the temporal variation in the displacement series is the main driver of differences between the application levels. Even though the site displacements for HYDL deviate more between the providers, both series contain the dominant seasonal signal, which significantly mitigates the annual signal in the antenna height residuals for many stations when we reduce this NTL part. As a consequence, also the scale parameter in a Helmert-transformation between the antenna coordinates and the DTRF2014 reveals a decrease in the annual signal when HYDL is applied at any level. NTAL and NTOL do not have this property.

According to **P-2**, the EOP are not as strongly affected by the reduction of NTL in absolute terms. Nevertheless, we obtain larger differences between the application levels for the estimated EOP rates (in contrast to the EOP offsets in a linear representation), as these are sensitive to intra-session variations, which only exist at the observation level.

Finally, we analyse the parameters which are not represented by constant or linear functions throughout a VLBI session. Zenith wet delays (ZWD) and clock corrections (CC), for example, are parameterized by piecewise linear functions at hourly grid points, and are strongly correlated with the antenna heights. While the latter capture most of the NTL effects, we can sometimes observe striking - albeit small in absolute magnitude - differences in the estimated ZWDs and CCs between the application levels. The two parameter types absorb a part of the temporal variation in the site displacements (i.e., for NTAL and NTOL at the observation level only) which a constant antenna height cannot reflect. Hence, if one fixes the antenna coordinates and is mainly interested in the tropospheric parameters, the application level of NTL would be a more crucial choice.

To conclude, the reduction of NTL systematically decreases the scatter of antenna height residuals. HYDL is as important as NTAL in general, and even NTOL is the dominant component for single baselines. Hence, the sum of all NTL parts should be reduced, and especially HYDL is relevant for the mitigation of the seasonal signal in the height residuals and the scale parameter. The application level is only of minor rel-

evance, while an uncertainty w.r.t. the geophysical models chosen by the data providers remains, in particular for HYDL.

5.2 Secular VLBI-only TRF

P-4 Glomsda M., Seitz M., Bloßfeld M., and Seitz F. (submitted): **Effects of non-tidal loading applied in VLBI-only terrestrial reference frames**, submitted to *Journal of Geodesy*.

Summary We compute various secular VLBI-only TRFs with and without the reduction of NTL at both the observation and the normal equation level. The used NTL data are the GGFC contribution to the ITRS 2020 realizations, which we discuss in **P-1** and apply in the DTRF2020. Since the corresponding time series of site displacements contain trends that affect the estimated antenna velocities in a secular TRF, we remove these trends before application in most of the TRF scenarios. However, we also investigate the impact of these trends. To be precise, we consider a reference scenario without any reduction of NTL, and four NTL scenarios: only NTAL (excluding trends) applied at the observation level (OBS), the total NTL (excluding trends) applied at OBS, the total NTL (excluding trends) applied at the normal equation level, and the total NTL (including trends) applied at OBS.

The article also contains a section recapping the mathematical background of the computation of a secular TRF by a combination of single-session normal equations. We further explain the impact on the combination when site displacements are added at the observation or the normal equation level, and we refer to the corresponding results for the single-session solutions in **P-2**. The actual analysis of VLBI measurements is no longer based on the same geophysical and technique-specific models as used in **P-2** and **P-3**, however, since the reprocessing for the ITRS 2020 realizations was performed in the meantime. Hence, we used the latest models available, and in particular the ITRF2020 positions as a priori values for the computation of the single-session normal equations.

We find that the impact of NTL on the estimated antenna positions and velocities is small, at least for those antennas with a long observation history. The linear nature of the TRF diminishes the instantaneous displacements of the reference points to a great extent. Only for antennas with short observation intervals, i.e., a few years, the reduction of non-linear displacements contingently affects the estimated velocities more strongly. By comparing the estimated velocities of sample antennas for different, artificially shortened observation periods to the respective velocities of long observation periods, we suggest that the reduction of NTL might improve these short-term velocities.

The choice of the application level for NTL is basically negligible for the estimated positions and velocities. The influence of the trends in the displacement series, however, is clearly visible. The estimated linear antenna positions change by about the values

of the corresponding trends when in- or excluding the latter in the reduction of NTL. A small part of these trends is also absorbed by the jointly estimated Earth rotation parameters (ERP).

Speaking of ERP, the impact of NTL in the VLBI-only TRF solutions is also investigated for all EOP. These are available per session epoch and hence provide a larger temporal resolution than the linear antenna positions. Since the temporal variation of the site displacements is most important for the differences between the results for the distinct application levels (compare **P-2**), we can thus expect stronger systematic effects for the EOP. We can confirm the findings of **P-3**, i.e., the application level is more relevant for the EOP rates, as these are more sensitive to temporal variations than the EOP offsets (in a linear representation). Comparing the estimated EOP of single-session and secular TRF solutions, we observe that the polar motion offsets x_p and y_p agree significantly better with external EOP series for the TRF solutions, while the impact of the reduction of NTL is also lower for the latter. We explain this with the correlation of the linear antenna positions and the ERP offsets in the TRF solutions: considering long observation time spans has a stabilizing effect on both positions and ERP, which is hardly influenced by (trend-less) instantaneous site displacements. Finally, there is an annual signal in the differences between the ERPs estimated with and without the reduction of NTL. The signal is larger with the total NTL than with NTAL only, and given the corresponding reduction of the annual signals for antenna heights as observed in **P-3**, for example, we assume that the ERP series is also improved by the reduction of the total NTL in the TRF solution.

5.3 Discussion

The impact of the reduction of NTL in VLBI analysis is rather small. In **P-2**, we derived formulas for the changes in the estimated coordinate corrections Δp_{ij} ($j \in \{x, y, z\}$ or $j \in \{e, n, u\}$) to the a priori values of antenna i in the single sessions when site displacements are applied at the observation and the normal equation level. In principle, the changes after the reduction at, e.g., the normal equation level should be close to the respective negative average site displacements during this session,

$$\Delta_{ij} \coloneqq \Delta p_{ij}^{NTL} - \Delta p_{ij} \approx -\bar{\delta}_{ij}^{NTL}. \tag{5.1}$$

Likewise, the changes after the reduction at the observation level should also be close to the negative values of the displacements during the session. In the top panel of Figure 5.1, we see that this approximation holds for both application levels and many VLBI antennas such as WETTZELL, Germany, at least under certain conditions.

As shown in **P-2**, the datum constraints (NNT, NNR) play an important role for the actual changes Δ_{ij}. For the m datum stations in a VLBI session it holds, e.g., for all x-coordinates due to NNT:

$$\sum_{i=1}^{m} \Delta p_{ix} \approx 0, \quad \sum_{i=1}^{m} \Delta p_{ix}^{NTL} \approx 0. \tag{5.2}$$

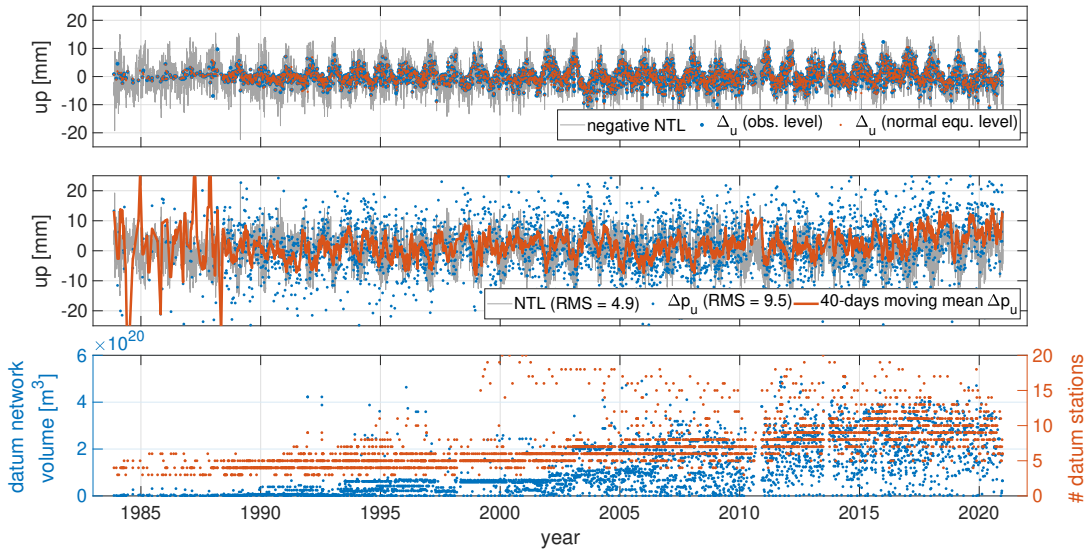

Figure 5.1: Top panel: changes in the estimated up-coordinates of VLBI antenna WETTZELL after the application of NTL at the observation (blue) and the normal equation level (red) for each session, plotted on top of the negative CF site displacements (grey). Middle panel: estimated corrections to the a priori up-coordinates of WETTZELL without the reduction of NTL, per session (blue) and as a 40-days moving average (red), plotted on top of the site displacements with original sign (grey). Bottom panel: the datum station network volume (blue) and the number of datum stations (red) per session. All data is identical to the ones used in **P-4**.

Consequently, the same condition is fulfilled for the changes Δ_{ix} in Eq. (5.1),

$$\sum_{i=1}^{m} \Delta_{ix} = \sum_{i=1}^{m} \Delta p_{ix}^{NTL} - \sum_{i=1}^{m} \Delta p_{ix} \approx 0, \tag{5.3}$$

which is a direct mathematical imperative. On the other hand, the sum of the corresponding (average) site displacements depends on the locations of the datum stations and does not necessarily equal 0, in particular for rather regional networks where the site displacements might adopt similar magnitudes for all antennas. Hence,

$$-\sum_{i=1}^{m} \bar{\delta}_{ix}^{NTL} \neq 0 \quad \Rightarrow \quad \Delta_{ix} \neq -\bar{\delta}_{ix}^{NTL} \tag{5.4}$$

for at least one i (and analogous for y, z, e, n, u).

Returning to station WETTZELL in Figure 5.1, we observe the inequality from Eq. (5.4) roughly for the sessions of the previous century, especially in the 1980s (top panel). The number of datum stations and the respective network volumes per session are depicted in the bottom panel, and we find a strong connection between the size

of the networks and the equality of Δ_{iu} and $-\bar{\delta}_{iu}^{NTL}$. As Petrov and Boy (2004) state on p.7, "the influence of position variations of other observing stations of the network on position variations of a station of interest is not diluted to a negligible level" for small networks. Likewise, Böhm et al. (2009) mention that unmodelled loading effects are distributed between the few VLBI antennas by the NNT and NNR conditions. As a consequence, the Δ_{ij} are smaller than the respective site displacements in the early years, since a part of the latter is already contained in the corrections Δp_{ij} of the scenario without NTL. Only if the number of datum stations is large enough (maybe 8-10 antennas) and the corresponding network volume is close to the volume of the Earth, the global deformation pattern is represented reasonably, and the aliasing of site displacements to other antennas is restricted due to sufficiently heterogeneous observations. (Besides, in the early years, Southern hemisphere antennas with contingently opposite seasonal deformations were completely absent from the VLBI networks.) In the computation of a secular TRF, this network effect should be rather irrelevant, since a large number of stable and global datum stations is defined for the whole observation time span, and no aliasing due to NNT/NNR conditions happens in the single-session normal equations any more.

In the middle panel of Figure 5.1, we directly compare the (CF) site displacements with the corrections Δp_{iu} in the scenario without reducing NTL. The variability of the corrections - expressed by an RMS error of 9.5 mm - is much larger than that of the displacements, which only have an RMS error of 4.9 mm (we apply the unweighted RMS here because there are no formal errors for the distinct displacements). Thus, the site displacements induced by NTL are not large enough to completely remove the variability of the antenna positions in the first place. There are other technique-specific or geophysical effects which still restrict the precision of VLBI analysis, like radio source structure or gravitational deformation (compare Section 4.3). The heterogeneous antenna networks and sub-networks of datum stations in the distinct sessions introduce further noise to the estimated positions. As a consequence, the correlation between the site displacements and the position residuals is probably not very large. Van Dam and Herring (1994) as well as Petrov and Boy (2004) already mention that the smaller (atmospheric) loading signal is hard to detect in the larger scatter of the VLBI residuals. Nevertheless, the figure also shows a 40-days moving mean of the corrections, which follows the time series of site displacements quite well. We observe a similar behaviour for the up-coordinate of other VLBI antennas with a sufficiently long and dense time series, e.g., ZELENCHK, Russia; GILCREEK, Alaska; WESTFORD, USA. This might confirm that NTL is a systematic effect which should be reduced, anyway, and that its impact might become more significant once the other sources of variability are diminished, or once the VGOS observations take full effect.

6 Conclusions

The articles **P-1** to **P-4** have addressed the reduction of NTL in VLBI analysis as well as in the realization of secular TRFs. We investigated whether NTL could and should be conventionally reduced. In the following, we return to our four key research questions and provide the corresponding answers.

6.1 Research goals

Q-1 What is the relation between the three NTL components, and how well do particular geophysical models agree per component?

There are three classic NTL components: non-tidal atmospheric (NTAL), non-tidal oceanic (NTOL), and hydrological loading (HYDL). Mostly, these components have been examined separately for the geodetic space techniques. The IVS ACs already apply NTAL in routine VLBI analysis, but the other techniques' services do not reduce NTL at all. The reason for the privilege of NTAL might be its dominance in the existing research. The underlying NWMs probably are the best established, and the impact of the atmospheric pressure anomalies might be considered to be the most significant among the three NTL components. Our results partly agree with these assumptions.

In **P-1** and **P-3**, we compare the distinct NTL components between different providers. In both articles, we find a very good agreement between the time series of site displacements for NTAL, which has also been shown by other studies (e.g., Roggenbuck et al., 2015). At least, this holds if the loading effect above the oceans is represented by the IB hypothesis, which basically compensates an increase in atmospheric pressure by an equivalent displacement of water. We conclude that the NWMs for the atmosphere have a quite low model uncertainty, i.e., the corresponding parameters and processes are quite well understood and little prone to ambiguities.

For NTOL, the situation starts to be less definite. The IB hypothesis is not very accurate for periods less than 20 days (e.g., Petrov and Boy, 2004), and the available dynamic ocean models show more diversity. For instance, they differ in considering effects like heat, wind, or freshwater fluxes. In **P-1**, we were not able to separate a clear NTOL component for the GGFC contribution to the ITRS 2020 realizations at all. This emphasizes that the distinction of NTAL and NTOL is not trivial. The degree of model uncertainty is larger than for NTAL with the IB hypothesis. However, the impact of NTOL, expressed as the peak-to-peak variations in the corresponding

displacement series, is the smallest among the three NTL components (e.g., Schuh et al., 2003), except for (baselines including) stations near the coast.

Finally, HYDL is the component with the largest discrepancies between the underlying geophysical models and (consequently) the displacement series. This was observed in both **P-1** and **P-3**. All models induce a strong seasonal signal for the site displacements, but the corresponding amplitudes and even the phases can differ significantly for particular regions of the world (see **P-1**). The modelling of land water storage is quite complicated, since many different effects must be considered: soil moisture, glacier run-off, river water flow, evaporation, precipitation, etc. **P-3** reveals that the size of the displacements and the number of stations for which HYDL is the dominant component are comparable with NTAL.

To summarize, NTAL and HYDL generate the largest site displacements for most of the VLBI antennas, while the effect of NTOL usually is relatively small. However, at antennas located close to the coast, NTOL can also be more significant than the other two components. And, since the displacements at both ends of a baseline are relevant in VLBI, the importance of NTOL should not be underrated. The uncertainty of the underlying numerical (weather) models is smallest for NTAL and largest for HYDL.

The remaining disagreement complicates the determination of a conventional set of models. Another issue is the conservation of mass. At the IMLS, for example, whose data is used in **P-3**, various underlying models for each NTL component are available. While this offers a great flexibility, a full consistency between the models, e.g., in terms of water exchange between the models for HYDL and NTOL, may not be guaranteed. On the other hand, the data set by ESMGFZ and the GGFC contribution to the ITRS 2020 realizations ensure mass conservation. This is an important condition when assembling a joint model for NTL (compare **Q-2**).

Q-2 Which properties of NTL data (e.g. temporal resolution, trends, consistency) are most relevant for the distinct applications?

Next to their peak-to-peak variations, the site displacements of the NTL components are also characterized by their frequency spectrum. While the displacement series for NTAL and NTOL contain significant sub-diurnal variations, the series for HYDL basically consists of a seasonal signal and can very well be represented by daily or session-wise averages. The corresponding HYDL data by ESMGFZ, for example, has a temporal resolution of 24 h, anyways (compared to 3 h for their NTAL and NTOL series). According to **P-2**, the application level is hence irrelevant for HYDL, as the differences in results between the levels are dominated by the (loss of) temporal resolution in the displacement series during a VLBI session. For NTAL and NTOL, however, the application level is relevant in principle, and so it is for the total NTL.

Besides the periodic signals, we observe long-term trends in the displacement series in **P-1**. For the GGFC contribution to the ITRS 2020 realizations, these trends are basically constant for the whole time interval. The ESMGFZ displacements for HYDL

and SLEL, on the other hand, reveal various changes in the trend. As it turns out, these different regimes do not reflect real geophysical phenomena, but are generated by intermediate updates in the atmospheric forcing model. In particular, the modelled Earth system has to adapt itself to the precipitation and evaporation between two adjacent model versions, which leads to transition phases with different offsets and drifts for the displacements. In contrast to the continuously (i.e., daily) prolongated ESMGFZ data, the GGFC data have been generated from single models throughout the whole time interval for which they are available, and hence do not contain such transitions. After all, it was produced for a particular purpose and is not available on a daily basis.

For VLBI single-session solutions, the trends in the displacement series are not immediately dangerous, although they will affect the long-term properties of the time series. Secular TRFs, on the other hand, explicitly estimate linear station positions, i.e., trends, over long observation histories. If the input normal equations are reduced by NTL, and the corresponding displacement series contain systematic deviations from zero, then the estimated linear motions will reflect such trends (compare **P-4**). In other words, the offsets and velocities do not represent the full linearized positions $\boldsymbol{p}_R$ of the stations any more, but a part of the linear motion will be shifted to the instantaneous corrections $\boldsymbol{\Delta p}_i$. This is not the original objective of a secular TRF, and one would prefer to remove the trends from the displacement series, so that all linear motions are again contained in the TRF. This is a trivial task for series with a constant trend, like the GGFC data. For series with variable trends, however, like the ESMGFZ data, one first has to determine the epochs of the discontinuities and then to compute and subtract all distinct trends in between.

If these changes in trend are not geophysically justified, we would not want to perform this task in the first place. If, on the contrary, the various trends were real effects of NTL, we would actually need to divide the linear station motions into the same time intervals as the displacement series. Though geophysically required, these additional discontinuities in the linear station motions would degrade the long-term stability of the secular TRF. For the DTRF2020 and the VLBI-only TRFs in **P-4**, however, we do not face these issues, as the changes in trends in the ESMGFZ series can be explained with (artificial) model updates, and the GGFC series represents a valid and convenient alternative.

The NTL data by ESMGFZ and GGFC as used in **P-1** and **P-4** satisfy mass conservation between the distinct NTL components. Obviously, this is a desirable property to avoid double counting or the omission of particular contributions. However, in **P-3**, we also applied data by the IMLS, which offers several geophysical background models, and the composition of the latter is generally not mass conserving. Since we were interested in and examined the individual contributions of the distinct components as well, this was not a major issue. Besides, we could investigate the impact of mass conservation by using the example of ESMGFZ: we added their distinct NTL components with and without the SLEL part in that article, and the differences between the results were

rather small. Nevertheless, the conservation of mass should definitely not be neglected to achieve the best possible accuracy when reducing NTL.

Last but not least, when combining the different components of NTL, it is important that the underlying geophysical models agree sufficiently well in terms of spatial and temporal resolution to properly handle their interactions. Furthermore, the atmospheric forcing data for the ocean and hydrology models should match with the model for NTAL. Otherwise, the response of one model does not comply with the stimulus of the other model, and erroneous systematic effects are created. The data by ESMGFZ and GGFC fulfill these requirements to our best knowledge (compare **P-1**). After all, they have been created to be used as a combined NTL product. In the case of the IMLS data, we cannot guarantee that our choice of the underlying model for NTOL is the best possible combination with the corresponding non-tidal atmospheric and hydrological loading. However, the underlying models for NTAL and HYDL are the same (compare **P-3**).

Q-3 What is the relevance of the application level for each of the solution types?

In **P-2**, we examine the Gauss-Markov model w.r.t. the impact of station position (site) displacements. This model represents a least-squares optimization: it determines a set of parameter values that produce theoretical measurements as close as possible to the actual measurements, i.e., the sum of squared residuals between computed and observed measurements is minimized. This procedure involves the generation of a normal equation system,

$$(\boldsymbol{N} + \boldsymbol{N}_D)^{-1}\, \boldsymbol{\Delta x} = \boldsymbol{y}, \tag{6.1}$$

where $\boldsymbol{N}$ is the normal matrix, $\boldsymbol{y}$ the right-hand-side, $\boldsymbol{N}_D$ a matrix of datum constraints, and $\boldsymbol{\Delta x}$ the vector of corrections to some a priori parameter values. The derivation of these entities is shown in column REF in Table 6.1. The application of site displacements, which are, e.g., induced from NTL, leads to different modifications of this normal equation system. At the observation level (column OBS), both the normal matrix and the right-hand-side are affected, because each single observation equation is augmented with the corresponding displacement. At the normal equation level (column NEQ), only the right-hand-side is modified by the product of the original normal matrix and the vector of average (or other representative single values of the) site displacements per parameter. At the solution level (column SOL), the original normal equation system is solved for $\boldsymbol{\Delta x}$, and the average site displacements are simply subtracted from the latter.

The solution level deviates from the other two application levels in one important aspect: the reduction of NTL only happens after the addition of the datum constraints $\boldsymbol{N}_D$. In our VLBI solutions, this matrix contains NNT and NNR conditions w.r.t. the a priori antenna positions, which have been taken from ITRF2014 (**P-2** and **P-3**) or DTRF2014 (**P-4**). As a consequence, the estimated positions have been aligned

Table 6.1: Table 1 of **P-2**, showing the components of the Gauss-Markov model for different application levels of site displacements. Variables given in gray font are usually not available at the corresponding level.

component	REF (reference)	OBS (modified functional model)	NEQ (modified normal equation system)	SOL (modified estimates)
real observations	$\boldsymbol{b}$	$\boldsymbol{b}$	b	b
functional model	$\boldsymbol{f}$	$\tilde{\boldsymbol{f}}$	$f + A\delta\bar{x}$	f
OMC	$\boldsymbol{l} = \boldsymbol{b} - \boldsymbol{f}$	$\tilde{\boldsymbol{l}} = \boldsymbol{b} - \tilde{\boldsymbol{f}}$	$\bar{l} = b - (f + A\delta\bar{x})$	$l = b - f$
Jacobi matrix	A	$\tilde{A}$	A	A
normal matrix	$N = A^T P A$	$\tilde{N} = \tilde{A}^T P \tilde{A}$	$N = A^T P A$	$N = A^T P A$
right-hand side	$\boldsymbol{y} = A^T P \boldsymbol{l}$	$\tilde{\boldsymbol{y}} = \tilde{A}^T P \tilde{\boldsymbol{l}}$	$\bar{\boldsymbol{y}} = \boldsymbol{y} - N\,\boldsymbol{\delta}\bar{\boldsymbol{x}}$	$y = A^T P l$
correction	$\boldsymbol{\Delta x} = (N + N_D)^{-1}\boldsymbol{y}$	$\boldsymbol{\Delta}\tilde{\boldsymbol{x}} = (\tilde{N} + N_D)^{-1}\tilde{\boldsymbol{y}}$	$\boldsymbol{\Delta}\bar{\boldsymbol{x}} = (N + N_D)^{-1}\bar{\boldsymbol{y}}$	$\boldsymbol{\Delta}\hat{\boldsymbol{x}} = \boldsymbol{\Delta x} - \boldsymbol{\delta}\hat{\boldsymbol{x}}$

to TRFs representing CF-frames (e.g., Dong et al., 2003), and only (average) site displacements from the CF-frame may be subtracted from them. At the observation and normal equation levels, on the other hand, site displacements from both frames may be used, since no alignment has taken place yet, and the translation between the two frames is cancelled on (VLBI) baselines.

The theoretical relations between the application levels are also investigated in **P-2**. It is shown that the most significant difference is the loss of temporal resolution in the (average) site displacements at the normal equation level, while the linear approximation of the changes in the right-hand-side is very close to the actual changes at the observation level. Furthermore, the differences between the normal matrices for both levels are negligible for site displacements induced by NTL.

These results are confirmed by **P-3**, where we apply NTL at these two levels in VLBI single-session solutions. There are hardly any differences between the results, e.g., in terms of estimated antenna positions and EOP, if we only reduce HYDL, since this NTL component generally has no intra-session variation. If we reduce NTAL, NTOL, or the sum of all components, the estimated parameters differ noticeable between the two levels, but these differences are significantly smaller than the differences w.r.t. the case where no NTL is applied at all. Hence, the choice of the application level is much less relevant than the question whether NTL should be reduced in the first place. This also holds for the scale parameters in the Helmert-transformations between the single-session solutions and DTRF2014 in **P-3**. Reducing NTAL and NTOL does not decrease the annual signal of the scale, while the reduction of HYDL does, and this behaviour is observed for both the observation and the normal equation level.

So far, we referred to parameters with no (antenna coordinates, celestial pole offsets) or only linear (ERP) time-dependence during a VLBI session. The tropospheric and clock parameters, on the other hand, are estimated as piecewise linear functions and have a resolution of up to 1 h. Furthermore, they are correlated with the antenna

heights, which represent the direction which is most affected by the reduction of NTL. Thus, they are able to reflect the temporal resolution of the site displacements at the observation level, and they indeed show noticeable deviations w.r.t. the estimated values at the normal equation level. As long as the antenna heights are estimated as well (like in our solutions), these deviations do not exceed a small fraction of the formal errors of the corresponding parameters, anyways. But if the antenna coordinates are fixed, because one wants to mainly estimate tropospheric parameters, the application level gets more relevant and the observation level should be preferred.

For secular TRFs, as computed in **P-4**, the single-session normal equations are accumulated, i.e., summed up. Hence, even though the discrepancies between the application of NTL at the observation and the normal equation level are quite negligible in single-sessions, they might accumulate as well and produce more significant deviations in the TRF. For the estimated antenna offsets and velocities in our secular VLBI-only TRFs, this concern is not confirmed: we can hardly distinguish the linear antenna motions after the reduction of the total NTL at both levels. For antennas with long observation histories, the impact of any (trend-less) displacement series on the regularized antenna positions is very low, anyways.

Next to the linear antenna positions, we also estimate EOPs in our TRF solutions. Since the EOP are still determined per session epoch, they might be more sensitive to (the temporal resolutions of) the instantaneous site displacements. Indeed, we find that the application level does not significantly influence the estimated ERP offsets, i.e., their constant parts, but it has a noticeable impact on the ERP rates. This is reasonable, since the temporal variation in the site displacements during a session mainly affects the time-dependent parameters. A similar result has been obtained for the single-session solutions in **P-3** already, but the deviations between the rates estimated from the reduction of NTL at the observation and the normal equation level are even larger in this case. The EOP in the secular TRF are stabilized by their correlation with the antenna positions and their counterparts from other sessions, so that their variation is generally lower, and that the effect of the application level on the ERP rates is qualitatively different.

To summarize: the application of site displacements induced by NTL at the normal equation level is a suitable approximation for the application at the observation level. The deviations between the estimated parameters are slightly larger for VLBI single-session solutions, and become the more important the more emphasis is put on parameters with a high temporal resolution. In terms of practical results, we did not focus on the application at solution level in the form we defined it. A different and more sophisticated approach is used by Collilieux et al. (2009), who compute a secular TRF reduced by NTL and based on the combination at solution level.

Q-4 Which geodetic parameters benefit from the reduction of NTL, i.e., by which NTL components should VLBI measurements conventionally be reduced?

Reducing NTL means adding corresponding displacements to the regularized positions of observing stations in the theoretical computation of geodetic observations. In **P-2** we find that, in VLBI analysis, the estimated antenna coordinates are by far the most affected parameters. The same article shows that the relation between the size of the displacements and the amount of change in the coordinate corrections depends on the datum constraints, i.e., on the number and distribution of antennas which are considered for the NNT and NNR conditions. Ideally, the change in corrections equals the (session-wise average) negative site displacements, but this is only achieved for large and well-distributed antenna networks (compare Section 5.3). Since these are more characteristic for the second half of VLBI's observation history, the benefit of NTL is rather poor for the sessions in the early years. The vertical (as opposed to the horizontal) site displacements are the largest, so the largest impact of NTL is also obtained for the vertical coordinates of the antennas, i.e., their estimated heights.

In **P-3**, we consider NTAL, NTOL, and HYDL, and apply all three components separately in VLBI single-session solutions. Furthermore, we compare the displacements of the distinct components to their sum, which represents the displacements for the total NTL. These displacements are not summed per site but per baseline, because each VLBI observation involves the two sites forming that baseline, and hence the displacements of both sites are relevant. We find that each baseline has a different dominant NTL component, because each component is more or less pronounced in different regions of the world. Likewise, the changes in estimated heights are largest for different NTL components at different antennas. Thus, to capture the dominant effect at each and every antenna, one should not only reduce a single NTL component (like the IVS ACs do with NTAL) but all of them.

In fact, we obtain the largest decrease in antenna height and baseline length repeatabilities for the reduction of the total NTL in **P-3**. The repeatability is given by WRMS values w.r.t. long-term linear heights and baseline lengths, respectively. The mitigation is systematic, as it encompasses about 80 to 90% of all antennas depending on the NTL data provider, and the mean decrease is about -3 to -4% (about -0.4 mm). For the horizontal antenna coordinates, the impact is less clear, but the repeatabilities are still improved for more than two thirds of the antennas.

Station or antenna heights are also relevant for the scale parameter in Helmert-transformations between the single-session solutions and secular TRFs. We find that the reduction of NTL, in particular HYDL, lessens the annual signal in the heights of the majority of antennas that are used for the NNT and NNR conditions in the DTRF2014. Consequently, the annual amplitude of the scale parameter in the transformations w.r.t. DTRF2014 decreases from about 1.7 mm to about 0.95 mm. This way, the most significant signal in the scale is strongly mitigated.

As mentioned before, the impact on the other parameters is very small, so that it is hard to deduce a clear benefit. However, we can state that the parameters with intra-session time-dependence, i.e., ERP rates, tropospheric and clock parameters, are influenced by the temporal variation of the site displacements. Besides, the tropospheric and clock parameters are strongly correlated with the antenna heights. Hence, every correction that improves the heights will also reduce the aliasing between these parameters.

In **P-4**, we finally investigate the impact of the reduction of NTL on secular VLBI-only TRFs. That is, we estimate long-term linear antenna positions by combining the datum-free normal equations of the single VLBI sessions. As a consequence, the instantaneous, non-linear positions are smoothed for antennas with sufficiently long observation periods. Furthermore, correlations among the jointly estimated EOP of distinct session epochs, and between the EOP and the linear antenna positions are induced. This implies different properties for the EOPs estimated in the TRF w.r.t. those estimated in the single-session solutions.

First, the EOP series of the secular TRF show less variation, as the stability of the long-term linear antenna positions also stabilizes the former. Second, while the ERP rates are hardly affected by NTL applied at the normal equation level in the single-session solutions, they become sensitive to this reduction in the TRF solution. The rates are mainly influenced by the intra-session variation in the site displacements, which does not exist for the application of NTL at the normal equation level. Only in the TRF solutions the rates are correlated with the other estimated parameters of distinct session epochs, and so the effect of NTL gets transferred to them. As a result, the corresponding ERP offsets react differently to the NTL as well, and the effect of the reduction is split more equally between the offsets and rates in the TRF solutions. This does not only hold for the application at the normal equation level, but also for the application at the observation level.

The differences between the EOP estimated within the secular TRF and the single-session solutions get slightly smaller when NTL is reduced in both solutions. Furthermore, there is an annual signal in the difference between the ERP offsets estimated with and without reducing NTL in the TRF solutions. This signal is larger when the total NTL is reduced than when only NTAL is reduced. Since the application of the total NTL decreases the annual signal in the estimated antenna heights, for example, we have good reason to assume that it also mitigates (rather than strengthens) a residual annual signal in the estimated ERP.

Returning to the linear antenna positions, the reduction of NTL basically affects the offsets and velocities of antennas with only short (i.e., a few years) observation periods. For these, the reliable estimation of velocities is difficult, since non-linear signals like NTL can distort them. Given an appropriate model with matching amplitudes and phases for these signals, and provided that the density of observations (i.e., sessions in the case of VLBI) is sufficient, the reduction of these non-linear signals should improve the estimated velocities for such short periods. With VLBI-only TRFs as in **P-4**, it is hard to demonstrate the improvement of the velocities by the reduction of NTL.

We offer some hints by comparing the estimated velocities of artificially created short observation periods to those of corresponding long periods for some antennas, but the definite proof is outstanding and must probably include the data of co-located stations of the other geodetic space techniques. However, the systematic improvements for the station positions of the single-session solutions are encouraging indications for a positive effect of the reduction of NTL on the secular TRFs, too.

To conclude, we recommend to apply all components of NTL in VLBI analyses. Even though the hydrological background models still show significant differences, we obtained similar results for every data provider in our studies. The antenna positions are systematically improved and seasonal signals are decreased for several geodetic parameters including the scale in similarity transformations.

6.2 Outlook

The size of the surface displacements due to NTL is smaller than the current variation in the estimated antenna coordinates in VLBI single-sessions (compare Section 5.3). Hence, VLBI still suffers from other unmodelled effects next to NTL. According to Anderson and Xu (2018), for example, source structure may account for about 40% of the total error budget in geodetic VLBI. Furthermore, the estimated height for the six antennas that have a model for gravitational deformation changes between a few millimeters for the 20-30 m diameter antennas and 12 cm for the 100 m diameter antenna EFLSBERG (e.g., Gipson and Sikstrom, 2018) when this model is actually applied. These two effects thus have a potential to significantly improve the antenna position precision and accuracy, respectively. A higher precision for the observables is also expected to be achieved by the next generation VLBI system, VGOS (compare Section 4.5). Yet, the latter is limited by the lack of operational VGOS antennas in the Southern hemisphere and the short history of broadband observations. But, once the VGOS network has attained a better global distribution, and/or there are new or more correction models for source structure and gravitational deformation, respectively, the impact of NTL might become more significant than in our studies and is worth to be revisited.

The influence of the reduction of NTL on the estimated source positions is expected to be negligible. Since the tropospheric parameters have a high temporal resolution and are correlated with the antenna heights, they offer more potential for a stronger sensitivity w.r.t. the vertical site displacements induced by NTL (see **P-3**). For tropospheric studies, in which the antenna positions are fixed, the application of NTL could hence be considered (compare also Böhm et al., 2009).

Although we recommend to reduce all components of NTL, we did not identify definite choices for conventional models for NTOL and HYDL. While the impact for NTOL might be low, anyways, the discrepancies between the hydrological models are still

significant. As a consequence, more time and research efforts are needed to make the underlying models for HYDL converge to a generally accepted one.

Bibliography

Abbondanza C., Chin T.M., Gross R.S., Heflin M.B., Parker J.W., Soja B.S., van Dam T., and Wu X. (2017), JTRF2014, the JPL Kalman filter and smoother realization of the International Terrestrial Reference System, J. Geophys. Res. Solid Earth, Vol. 122 (10). pp. 8474–8510. doi:10.1002/2017JB014360

Altamimi Z., Collilieux X., Legrand J., Garayt B., and Boucher C., ITRF2005: A new release of the International Terrestrial Reference Frame based on time series of station positions and Earth Orientation Parameters, J. Geophys. Res., Vol. 112, B09401 (2007). doi:10.1029/2007JB004949.

Altamimi Z., Rebischung P., Metivier L., and Collilieux X., ITRF2014: A new release of the International Terrestrial Reference Frame modeling nonlinear station motions, J. Geophys. Res. Solid Earth, Vol. 121 (2016). doi:10.1002/2016JB013098

Amoruso A., and Crescentini L., Parameters of the Earth's Free Core Nutation from Diurnal Strain Tides, Sci Rep 10, 9756 (2020). doi:10.1038/s41598-020-66426-7

Anderson J.M., and Xu, M.H., Source structure and measurement noise are as important as all other residual sources in geodetic VLBI combined, Journal of Geophysical Research: Solid Earth, Vol. 123, pp. 10,162–10,190 (2018). doi:10.1029/2018JB015550

Arias E.F., Charlot P., Feissel M., and Lestrade J.-F., The extragalactic reference system of the International Earth Rotation Service, ICRS, Astronomy & Astrophysics, Vol. 303, pp. 604-608 (1995).

Behrend D., et al., Status of the VGOS Infrastructure Rollout, IVS general meeting proceedings (2022).

Bizouard C., Lambert S., Gattano C., Becker O., and Richard J.Y., The IERS EOP 14C04 solution for Earth orientation parameters consistent with ITRF 2014, J. Geod., Vol. 93, pp. 621-633 (2019).

Blewitt, G., Self-consistency in reference frames, geocenter definition, and surface loading of the solid Earth, J. Geophys. Res., 108(B2), 2103 (2003). doi:10.1029/2002JB002082

Böhm J., Schuh H., and Heinkelmann R., Reference pressure for the global geodetic observing system GGOS, Technical report, IVS Memorandum 2008-002v0-1 (2008). *https://ivscc.gsfc.nasa.gov/publications/memos/ivs-2008-002v01.pdf*, accessed 2022-10-27.

Böhm J., Heinkelmann R., Mendes Cerveira P.J., et al., Atmospheric loading corrections at the observation level in VLBI analysis, J. Geod., Vol. 83, pp. 1107-1113 (2009).

Bos M.S., and Scherneck H.-G., Computation of Green's Functions for Ocean Tide Loading, in G. Xu (ed.), Sciences of Geodesy - II, Springer Berlin Heidelberg (2013). doi:10.1007/978-3-642-28000-9_1

Brosche P., Tidal Deceleration of the Earth, in: Variations in Earth Rotation, D.D. McCarthy and W.E. Carter (eds), Vol. 59 (1990). doi:10.1029/GM059p0047

Broten N.W., Legg T. H., Locke J. L., McLeish C.W., Richards R. S., Chisholm R. M., et al., Long base line interferometry: A new technique, Science, Vol. 156 (3782), pp. 1592–1593 (1967). doi:10.1126/science.156.3782.1592

Bullen K.E., An Earth model based on a compressibility-pressure hypothesis, Geophysical Journal International, Vol. 6 (s1), pp. 50-59 (1950). doi:10.1111/j.1365-246X.1950.tb02973.x

Capitaine N., The celestial pole coordinates, Celestial Mech Dyn Astr, Vol. 48, pp. 127–143 (1990). doi:10.1007/BF00049510

Capitaine N., Wallace P.T., and Chapront J., Expressions for IAU 2000 precession quantities, Astron. Astrophys., Vol. 412 (2), pp. 567–586 (2003). doi:10.1051/0004-6361:20031539

Cappallo R., Correlating and Fringe-fitting Broadband VGOS Data, IVS general meeting proceedings, pp. 91-96 (2014).

Cappallo R., fourfit user's manual, Version 1.0 (2017). *https://www.haystack.mit.edu/wp-content/uploads/2020/07/docs_hops_009_fourfit_users_manual.pdf*, accessed on 2022-11-11

Charlot, P., Gordon, D., et al., The third realization of the International Celestial Reference Frame by very long baseline interferometry, Astronomy and Astrophysics, Vol. 644 (2020).

Chen G., Herring T.A., Effects of atmospheric azimuthal asymmetry on the analysis of space geodetic data, J Geophys Res, Vol. 102 (B9), pp. 20489–20502 (1997). doi:10.1029/97JB01739

Christensen O., and Christensen K.L., Approximation Theory: From Taylor Polynomials to Wavelets (Applied and Numerical Harmonic Analysis), Birkhäuser Boston, Corr. 3rd printing (2006).

Cohen M. H., and Shaffer D. B., Positions of radio sources from long-baseline interferometry, Astronomical Journal, Vol. 76, pp. 76–91 (1971).

Collilieux X., Altamimi Z., Coulot D., van Dam T., and Ray J., Impact of loading effects on determination of the International Terrestrial Reference Frame, Adv. Sp. Res., Vol. 45, pp. 144-154 (2009).

Davis J.L., Herring T.A., Shapiro I.I., Rogers A.E.E., and Elgered G., Geodesy by radio interferometry: effects of atmospheric modeling errors on estimates of baseline length, Radio Sci, Vol. 20 (6), pp. 1593–1607 (1985).

Deller A.T., Brisken W.F., Phillips C.J., et al., DiFX-2: A More Flexible, Efficient, Robust, and Powerful Software Correlator, Publications of The Astronomical Society of The Pacific, Vol. 123, pp. 275-287 (2011). doi:10.1086/658907.

Desai S.D., Observing the pole tide with satellite altimetry, J. Geophys. Res., Vol. 107 (C11), 3186 2002. doi:10.1029/2001JC001224

de Witt A., Charlot P., Gordon D., and Jacobs C.S., Overview and Status of the International Celestial Reference Frame as Realized by VLBI, Universe, Vol. 8 (7), 374 (2022). doi:10.3390/universe8070374

Dill R., and Dobslaw H., Numerical simulations of global-scale high-resolution hydrological crustal deformations, J. Geophys. Res. Solid earth, Vol. 118 (2013). doi:10.1002/jgrb.50353

Dill R., Klemann V., Martinec Z., and Tesauro M., Applying local Green's functions to study the influence of the crustal structure on hydrological loading displacements, Journal of Geodynamics, Vol. 88, pp. 14-22 (2015). doi.10.1016/j.jog.2015.04.005.

Dong D., Yunck T., and Heflin M., Origin of the International Terrestrial Reference Frame, J. Geophys. Res., Vol. 108 (B4), 2200 (2003). doi:10.1029/2002JB002035

Dziewonski A.M., and Anderson D.L., Preliminary reference Earth model, Physics of the Earth and Planetary Interiors, Vol. 25, pp. 297— 356 (1981).

Egbert G.D., and Erofeeva S.Y., Efficient inverse modelling of barotropic ocean tides, J. Atmos. Oceanic Technol., Vol. 12, Nr. 2, pp. 183–204 (2002).

Eriksson D., and MacMillan D.S., Continental hydrology loading observed by VLBI measurements, J. Geod., Vol. 88, pp. 675-690 (2014).

Eubanks T. M. (ed.), Proceedings of the U. S. Naval Observatory Workshop on Relativistic Models for Use in Space Geodesy, U. S. Naval Observatory, Washington, D. C. (1991).

Farrell W. E., Deformation of the Earth by Surface Loads, Reviews of Geophysics and Space Physics, Vol. 10, No. 3, pp. 761-797 (1972).

Fey A.L., Gordon D., Jacobs C.S., Ma C., et al., The second realization of the International Celestial Reference Frame by Very Long Baseline Interferometry, The Astronomical Journal, Vol. 150, No. 2 (2015).

Fricke W., Schwan H.P., Lederle T., et al., Fifth Fundamental Catalogue (FK5), Veröffen. Astron. Rechen-Institut Heidelberg 32, Verlag G. Braun, Karlsruhe (1988).

Gerstl M., Kelm R., Müller H., and Ehrnsperger W., DOGS-CS - Kombination und Lösung großer Gleichungssysteme, Internal Report, DGFI-TUM, München (2000).

Gipson J.M., and Sikstrom T., Impact of Gravitational Deformation in VLBI analysis on the Reference Frame, AGU Fall Meeting (2018).

Gutenberg B., Amplitudes of P, PP, and S and magnitude of shallow earthquakes, Bulletin of the Seismological Society of America, Vol. 35, pp. 57-69 (1945).

Herring T.A., Modeling atmospheric delays in the analysis of space geodetic data, in: DeMunck J.C., Spoelstra T.A.T. (eds), Publications on geodesy, Vol. 36, Proceedings of refraction of transatmospheric signals in geodesy, pp. 157–164 (1992).

Hersbach H., Bell B., et al., The ERA5 global reanalysis, Q. J. R. Meteorol Soc., Vol. 146, pp. 1999-2049 (2020). doi:10.1002/qj.3803

Hinteregger H. F., Shapiro I. I., Robertson D. S., et al., Precision geodesy via radio interferometry, Science, Vol. 178, pp. 396–398 (1972). doi:10.1126/science.178.4059.396

Hobiger T., Ichikawa R., Koyama Y., and Kondo T., Fast and accurate ray-tracing algorithms for real-time space geodetic applications using numerical weather models, J. Geoph. Res., Vol. 113, D20302 (2008). doi:10.1029/2008JD010503

Hofmann-Wellenhof B., and Moritz H., Physical geodesy, 2nd edition, Springer Wien New York (2006). ISBN 3-211-33544-7

Hofmeister A., Determination of path delays in the atmosphere for geodetic VLBI by means of ray-tracing, Dissertation, Technische Universität Wien, reposiTUm (2016). doi:10.34726/hss.2016.21899

Jentzsch G., Earth tides and ocean tidal loading, in: Wilhelm, H., Zürn, W., Wenzel, HG. (eds), Tidal Phenomena. Lecture Notes in Earth Sciences, Vol 66, Springer, Berlin, Heidelberg (1997). doi:10.1007/BFb0011461

Johnston G., Riddell A., and Hausler G. (2017), The International GNSS Service, in Teunissen, Peter J.G. and Montenbruck O. (Eds.), Springer Handbook of Global Navigation Satellite Systems, 1st ed., pp. 967-982. doi:10.1007/978-3-319-42928-1

Kennett B.L.N., and Engdahl E.R., Traveltimes for global earthquake location and phase identification, Geophysical Journal International, Vol. 105 (2), pp. 429–465 (1991). doi:10.1111/j.1365-246X.1991.tb06724.x

Koch K.-R., Parameter Estimation and Hypothesis Testing in Linear Models, 2. edition, Springer-Verlag Berlin Heidelberg, original German edition published by Dümmlers, Bonn (1999).

Kovalevsky J., Aberration in proper motions. A&A, 404, 743 (2003).

Kummer E., Eine neue Methode, die numerischen Summen langsam convergirender Reihen zu berechnen, J. Reine Angew. Math., Vol. 16, pp. 206–214 (1837).

Kwak Y., Gerstl M., Bloßfeld M., Angermann D., Schmid R., and Seitz M., DOGS-RI: new VLBI analysis software at DGFI-TUM, Proceedings of the 23rd EVGA Meeting (2017).

Landskron D., and Böhm J., VMF3/GPT3: refined discrete and empirical troposphere mapping functions, J Geod, Vol. 92, pp. 349–360 (2017). doi:10.1007/s00190-017-1066-2

Longair M.S., Quasi-stellar radio sources, Contemporary Physics, Vol. 8 (4), pp. 357-372 (1967). doi:10.1080/00107516708202159

Love A.E.H., The yielding of the earth to disturbing forces, Proc. R. Soc. Lond., Vol. 82, pp. 73–88 (1909). doi:10.1098/rspa.1909.0008

Ma, C., Arias E.F., et al., The International Celestial Reference Frame as realized by Very Long Baseline Interferometry, The Astronomical Journal, Vol. 116, pp. 516-546 (1998).

MacDonald G.J.F., Tidal friction, Rev. Geophys., Vol. 2 (3), pp. 467– 541 (1964). doi:10.1029/RG002i003p00467

MacMillan D.S., Fey A., Gipson J., et al., Galactocentric acceleration in VLBI analysis: Findings of IVS WG8, Astronomy and Astrophysics, 630, 2019. doi:10.1051/0004-6361/201935379

Männel B., Dobslaw H., Dill R., Glaser S., Balidakis K., Thomas M., and Schuh H., Correcting surface loading at the observation level: impact on global GNSS and VLBI station networks, J. Geod., Vol. 93 (10), pp. 2003-2017 (2019). doi:10.1007/s00190-019-01298-y

Malkin Z., Statistical analysis of the results of 20 years of activity of the International VLBI Service for Geodesy and Astrometry, Astronomy Reports, Vol. 64, No. 2, pp. 168–188 (2020). doi:10.1134/S1063772920020043

Marini J.W., Correction of satellite tracking data for an arbitrary tropospheric profile, Radio Sci, Vol. 7 (2), pp. 223–231 (1972).

Mathews P.M., Herring T.A., and Buffett B.A., Modeling of nutation and precession: New nutation series for nonrigid Earth, and insights into the Earth's Interior, J. Geophys. Res., Vol. 107 (B4) (2002). doi:10.1029/2001JB000390

Matveenko L. I., Kardashev N. S., and Sholomitskii G. B., Large baseline radio interferometers, Soviet Radiophysics, Vol. 8 (4), pp. 461–463 (1965). doi:10.1007/bf01038318

McNally D., Quasi-stellar radio sources, Science Progress (1933-), Vol. 52 (207), pp. 426–433 (1964).

Mikschi M., Böhm J., and Schartner M., Unconstrained Estimation of VLBI Global Observing System Station Coordinates, Adv. Geosci., Vol. 55, pp. 23–31 (2021). doi:10.5194/adgeo-55-23-2021

Miyahara B., Sánchez L., Sehnal M., Global Geodetic Observing System (GGOS), in: Poutanen M., Rozsa S. (eds), The geodesist's handbook, J Geod, Vol. 94 (11), pp. 197–220 (2020). doi:10.1007/s00190-020-01434-z

Moran J.M., Crowther P.P., Burke B.F., Barrett A.H., et al., Spectral Line Interferometry with Independent Time Standards at Stations Separated by 845 Kilometers, Science, Vol. 157 (3789), pp. 676-677 (1967).

Moran J.M., and Dhawan V., Calibration techniques for VLBI, in: Zensus J.A., Diamond P.J., and Napier P.J. (eds), Very Long Baseline Interferometry and the VLBA, ASP Conference Series, Vol. 82 (1995).

Moritz H., and Mueller I.I., Earth Rotation: Theory and Observation, Ungar Publishing Company, New York (1987).

Munk W.H., and MacDonald G.J.F., The rotation of the Earth, Cambridge University Press (1960).

Na S.-H., and Baek J., Computation of the Load Love Number and the Load Green's Function for an Elastic and Spherically Symmetric Earth, Journal of the Korean Physical Society, Vol. 58 (5), pp. 1195-1205 (2011).

Niell A.E., Improved atmospheric mapping functions for VLBI and GPS, Earth Planets Space, Vol. 52 (10), pp. 699–702 (2000).

Niell A.E., Whitney A., Petrachenko B., et al., VLBI2010: Current and future requirements for geodetic VLBI systems, NASA/TP-2006-214136 (2006).

Niell A., Barrett J., Burns A., et al., Demonstration of a Broadband Very Long Baseline Interferometer System: A New Instrument for High-Precision Space Geodesy, Radio Science, Vol. 53, pp. 1269-1291 (2018).

Nothnagel A., Conventions on thermal expansion modelling of radio telescopes for geodetic and astrometric VLBI, J Geod, Vol. 83 (8), pp. 782–792 (2009). doi:10.1007/s00190-008-0284-z

Nothnagel A., Springer A., Heinz E., Artz T., and de Vicente P., Graviational Deformation Effects. The YEBES40M Case, IVS 2014 General Meeting Proceedings (2014).

Nothnagel A., Artz T., Behrend D., and Malkin Z., International VLBI Service for Geodesy and Astrometry – Delivering high-quality products and embarking on observations of the next generation, J. Geod., Vol. 91 (7), pp. 711–721 (2017). doi:10.1007/s00190-016-0950-5

Nothnagel A., Very Long Baseline Interferometry, in: Freeden W., Rummel R. (eds) Handbuch der Geodäsie, 1-58, Springer Reference Naturwissenschaften Book Series, Springer Spektrum, Berlin, Heidelberg (2019). doi:10.1007/978-3-662-46900-2_110-1

Nothnagel A., Elements of Geodetic and Astrometric Very Long Baseline Interferometry, version as of 2022-02-21 (2022). *https://www.vlbi.at/data/publications/2022_Nothnagel_Elements_of_VLBI_20220221.pdf*, accessed on 2022-09-01

Oh S.-J., Chung H.-S., Roh D.G., and Kim K.-D., Frequency Standard and Clock System in VLBI, Publications of The Korean Astronomical Society, Vol. 19, pp. 93-99 (2004). doi:10.5303/PKAS.2004.19.1.093.

Ong K.M., MacDoran P.F., Thomas J.B., Fliegel H.F., et al., A demonstration of a transportable radio interferometric surveying system with 3-cm accuracy on a 307-m base line, J. Geophys. Res., Vol. 81 (20), pp. 3587–3593 (1976). doi:10.1029/JB081i020p03587.

Pavlis E., Luceri V., Basoni A., Sarrocco D., Kuzmicz-Cieslak M., Evans K., and Bianco G. (2021), ITRF2020: The International Laser Ranging Service (ILRS) Contribution, presented at AGU Fall Meeting, December 13-17, 2021. doi:10.1002/essoar.10509208.1

Petit G., and Luzum B. (eds.), IERS Conventions (V. 1.3.0), IERS Technical Note 36, Verlag des Bundesamts für Kartographie und Geodäsie, Frankfurt am Main (2010).

Petrachenko B., Niell A., Behrend D., Corey B., Boehm J., Charlot P., et al., Design Aspects of the VLBI2010 System, Progress Report of the IVS VLBI2010 Committee (Tech. Rep.) (2009).

Petrov L., and Boy J.-P., Study of the atmospheric pressure loading signal in very long baseline interferometry observations, J. Geophys. Res., 109, B03405 (2004). doi:10.1029/2003JB002500

Petrov L., Kovalev Y.Y., Fomalont E.B., and Gordon D., The VLBA Galactic Plane Survey — VGaPS, Astron. J., Vol. 142 (35) (2011).

Petrov L., The International Mass Loading Service, arXiv:1503.00191 (2015). *https://arxiv.org/abs/1503.00191*, accessed on 2022-10-28

Plavin A.V., Kovalev Y.Y., Pushkarev A.B., and Lobanov A.P., Significant core shift variability in parsec-scale jets of active galactic nuclei, Monthly Notices of the Royal Astronomical Society, Vol. 485 (2), pp. 1822-1842 (2019). doi:10.1093/mnras/stz504

Rabbel W. and Zschau J., Static deformations and gravity changes at Earth's surface due to atmospheric loading, J. Geophys., Vol. 56, pp. 81-89 (1985).

Ray, R.D. and Ponte R.M., Barometric tides from ECMWF operational analyses, Ann. Geophys., Vol. 21 (8), pp. 1897–1910 (2003).

Rogers A.E.E., Very long baseline interferometry with large effective bandwidth for phase-delay measurements, Radio Science, Vol. 5 (10), pp. 1239–1247 (1970). doi:10.1029/RS005i010p01239

Roggenbuck, O., Thaller D., Engelhardt G., Franke S., Dach R. and Steigenberger P., Loading-Induced Deformation Due to Atmosphere, Ocean and Hydrology: Model Comparisons and the Impact on Global SLR, VLBI and GNSS Solutions, T. van Dam (eds), REFAG 2014, International Association of Geodesy Symposia, Vol. 146, Springer International Publishing Switzerland (2015).

Saastamoinen J., Atmospheric correction for the troposphere and stratosphere in radio ranging of satellites, in: Henriksen SW et al (eds), The use of artificial satellites for geodesy, Vol 15, AGU, Washington, pp. 247–251 (1972).

Sarti P., Abbondanza C., Petrov L., and Negusini M., Height bias and scale effect induced by antenna gravitational deformations in geodetic VLBI data analysis, J. Geod., Vol. 85, pp. 1-8 (2011).

Schmidt M., 3C 273: A Star-Like Object with Large Red-Shift, Nature, Vol. 197 (1040) (1963). doi:10.1038/1971040a0

Schuh H., Estermann G., Crétaux J.F., Bergé-Nguyen M., van Dam T., Investigation of Hydrological and Atmospheric Loading by Space Geodetic Techniques, Hwang C., Shum C.K., Li J. (eds), Satellite Altimetry for Geodesy, Geophysics and Oceanography, International Association of Geodesy Symposia, Vol. 126, Springer, Berlin, Heidelberg (2003).

Schuh H., and Behrend D., VLBI: A fascinating technique for geodesy and astrometry, Journal of Geodynamics, Vol. 61 , pp. 68-80 (2012). doi:10.1016/j.jog.2012.07.007

Seitz M., Bloßfeld M., Angermann D., and Seitz F., DTRF2014: DGFI-TUM's ITRS realization 2014, Advances in Space Research, Vol. 69 (6), pp. 2391-2420 (2022). doi:10.1016/j.asr.2021.12.037

Shida T., On the Body Tides of the Earth, A Proposal for the International Geodetic Association, Proceedings of the Tokyo Mathematico-Physical Society, 2nd Series, Vol. 6 (16), pp. 242-258 (1912). doi:10.11429/ptmps1907.6.16_242

Sovers O.J., Fanselow J.L., and Jacobs C.S., Astrometry and Geodesy with Radio Interferometry: Experiments, Models, Results, Reviews of Modern Physics, Vol. 70 (4), pp. 1393–1454 (1998).

Steffen H., and Wu P., Glacial isostatic adjustment in Fennoscandia — A review of data and modeling, Journal of Geodynamics, Vol. 52 (3–4), pp. 169-204 (2011). doi:10.1016/j.jog.2011.03.002

Titov O., Lambert S.B., and Gontier A.-M., VLBI measurement of the secular aberration drift, A&A, A91, 529 (2011).

van Dam T.M., and Herring T.A., Detection of atmospheric pressure loading using very long baseline interferometry measurements, J. Geophys. Res., Vol. 99, pp. 4505–4518 (1994).

van den Dool H.M., Saha S., Schemm J., and Huang J., A temporal interpolation method to obtain hourly atmospheric surface pressure tides in Reanalysis 1979–1995, J. Geophys. Res., Vol. 102 (D18), pp. 22013-22024 (1997). doi:10.1029/97JD01571

Wang H., Xiang L., Jia L., Jiang L., Wang Z., Hu B., and Gao P., Load Love numbers and Green's functions for elastic Earth models PREM, iasp91, ak135, and modified models with refined crustal structure from Crust 2.0, Computers & Geosciences, Vol. 49, pp. 190-199 (2012). doi:10.1016/j.cageo.2012.06.022

Wijaya D.D., Böhm J., Karbon M., Kràsnà H., and Schuh H., Atmospheric Pressure Loading, in: Böhm J., and Schuh H. (eds), Atmospheric Effects in Space Geodesy, Springer Atmospheric Sciences, Springer Berlin Heidelberg (2013). doi:10.1007/978-3-642-36932-2_4

Williams S.D.P. and Penna N.T., Non-tidal ocean loading effects on geodetic GPS heights, Geophys. Res. Lett., Vol. 38, L09314 (2011). doi:10.1029/2011GL046940

Willis P., Fagard H., Ferrage P., Lemoine F. G., Noll C. E., Noomen R., Otten M., Ries J. C., Rothacher M., Soudarin L., Tavernier G., and Valette J.-J. (2010), The International DORIS Service (IDS): toward maturity, Adv. Space Res., Vol. 45 (12), pp. 1408-1420. doi:10.1016/j.asr.2009.11.018

Whitney A. R., Precision geodesy and astrometry via very-long-baseline interferometry, Dissertation at Massachusetts Institute of Technology (MIT), 77 Massachusetts Av., Cambridge MA 02139, USA (1974).

Wunsch C., and Stammer D., Atmospheric loading and the oceanic "inverted barometer" effect, Reviews in Geophysics, Vol. 35 (1), pp. 79-107 (1997).

Xu M.H., Heinkelmann R., Anderson J.M., Mora-Diaz J., Karbon M., Schuh H., and Wang G. L., The impacts of source structure on geodetic parameters demonstrated by the radio source 3C371, Journal of Geodesy, Vol. 91 (7), pp. 767-781. doi:10.1007/s00190-016-0990-x

Xu M.H., Savolainen T., Zubko N., Poutanen M., Lunz S., Schuh H., and Wang G.L., Imaging VGOS observations and investigating source structure effects, Journal of Geophysical Research: Solid Earth, Vol. 126 (2021). doi:10.1029/2020JB021238

Acronyms

AC	Analysis Centre.
AO	axis offset.
BCRS	barycentric celestial reference system.
BIH	Bureau International de l'Heure.
CC	clock correction.
CF	centre-of-figure.
CIO	celestial intermediate origin.
CIRS	celestial intermediate reference system.
CM	centre-of-mass.
CRF	celestial reference frame.
CRS	celestial reference system.
DGFI-TUM	Deutsches Geodätisches Forschungsinstitut at the Technical University of Munich.
DOGS	DGFI Orbit and Geodetic Parameter estimation Software.
DOGS-CS	— Combination and Solution library.
DOGS-RI	— Radio Interferometry software.
DORIS	Doppler Orbitography and Radiopositioning Integrated by Satellite.
EOP	Earth orientation parameter.
ERP	Earth rotation parameter.
ESMGFZ	Earth System Modelling group at the Deutsches GeoForschungsZentrum Potsdam.
GC	geocenter.
GCRS	geocentric celestial reference system.
GGFC	Global Geophysical Fluid Center.
GGOS	Global Geodetic Observing System.
GM	geocenter motion.
GNSS	Global Navigation Satellite Systems.

HYDL	hydrological loading.
IAG	International Association of Geodesy.
IAU	International Astronomical Union.
IB	inverted barometer.
ICRF	International Celestial Reference Frame.
ICRS	International Celestial Reference System.
IDS	International DORIS Service.
IERS	International Earth Rotation and Reference Systems Service.
IGN	Institut national de l'information géographique et forestrière.
IGS	International GNSS Service.
ILRS	International Laser Ranging Service.
IMLS	International Mass Loading Service.
ITRF	International Terrestrial Reference Frame.
ITRS	International Terrestrial Reference System.
IUGG	International Union of Geodesy and Geophysics.
IVS	International VLBI Service for Geodesy and Astrometry.
JPL	Jet Propulsion Laboratory.
LOD	length-of-day.
NASA	National Aeronautics and Space Administration.
NNR	no-net rotation.
NNT	no-net translation.
NTAL	non-tidal atmospheric loading.
NTL	non-tidal loading.
NTOL	non-tidal oceanic loading.
NWM	numerical weather model.
PM	polar motion.
RMS	root mean square.
SLR	Satellite Laser Ranging.
TAI	Temps Atomique International.
TCB	Temps Coordonné Barycentrique.
TCG	Temps Coordonné Géocentrique.
TIO	terrestrial intermediate origin.
TIRS	terrestrial intermediate reference system.

TRF	terrestrial reference frame.
TRS	terrestrial reference system.
TT	Terrestrial Time.
TUM	Technische Universität München/Technical University of Munich.
UT1	Universal Time (No. 1).
UTC	Coordinated Universal Time.
VLBI	Very Long Baseline Interferometry.
WG	working group.
WRMS	weighted root mean square.
ZWD	zenith wet delay.

Appendix

Table 1: Overview of the author's contribution to the embedded articles.

Component \ article	**P-1**	**P-2**	**P-3**	**P-4**
Idea / concept	50%	90%	50%	80%
Realization / implementation	70%	95%	85%	85%
Analysis and discussion	75%	80%	70%	66%
Figure compilation	100%	100%	100%	95%
Manuscript writing	90%	95%	95%	95%
Total contribution	77%	92%	80%	84%

P-1 Glomsda M., Bloßfeld M., Seitz M., Angermann D., and Seitz F. (2022): **Comparison of non-tidal loading data for application in a secular terrestrial reference frame**, *Earth, Planets and Space*, Vol. 74 (1), doi:10.1186/s40623-022-01634-1

Abstract The Deutsches Geodätisches Forschungsinstitut der Technischen Universität München (DGFI-TUM) is one of the three Combination Centres of the International Earth Rotation and Reference Systems Service for the International Terrestrial Reference System (ITRS). In its upcoming realization of the ITRS, the DTRF2020, DGFI-TUM will again correct for non-tidal loading (NTL) effects at the normal equation level. Next to the dedicated NTL data set for the ITRS 2020 realizations provided by the Global Geophysical Fluid Center (GGFC), we also considered the data provided by the Earth System Modelling group of the Deutsches GeoForschungsZentrum (ESMGFZ). Besides also comprising all NTL components (atmospheric, oceanic, hydrological) and

being mass conserving, the ESMGFZ data has the advantage of daily availability and is already in use at DGFI-TUM. The decision for one or the other data set depends on their suitability for a secular terrestrial reference frame like the DTRF2020, which will be assessed in this work. Although we also compare the site displacements induced by NTL to the residuals of station positions of the Global Navigation Satellite Systems, we will not evaluate the quality of the underlying geophysical models per se. The two data sets differ w.r.t. the underlying hydrological models and the treatment of non-tidal oceanic loading, but the most relevant difference is given in terms of trends in the displacement time-series. After a close investigation of the latter, we finally decided to apply the GGFC contribution to the ITRS 2020 realization in the DTRF2020.

Author contributions The idea to separate this analysis from the main DTRF2020-article was born during the preparation of the DTRF2020. Matthias Glomsda prepared the original GGFC data and performed most of the investigations. He compiled all figures and wrote the majority of the manuscript. Mathis Bloßfeld prepared the original ESMGFZ data and transformed both data sets into their final format. He also computed the geocenter motion contribution by SLR. Manuela Seitz is the leader of the ITRS Combination Center at DGFI-TUM and computed the GNSS position residuals. Furthermore, she wrote a subsection of the manuscript. Detlef Angermann, like all aforementioned authors, was involved in the discussions and decisions w.r.t. the DTRF realization including the correction for non-tidal loading as examined in this study. Florian Seitz supervised the study and provides the basic resources. All authors read and improved the manuscript. The overall contribution of Matthias Glomsda is estimated to be 77%.

Glomsda *et al. Earth, Planets and Space* (2022) 74:87
https://doi.org/10.1186/s40623-022-01634-1

Earth, Planets and Space

FULL PAPER

Comparison of non-tidal loading data for application in a secular terrestrial reference frame

Matthias Glomsda*, Mathis Bloßfeld, Manuela Seitz, Detlef Angermann and Florian Seitz

Abstract

The Deutsches Geodätisches Forschungsinstitut der Technischen Universität München (DGFI-TUM) is one of the three Combination Centres of the International Earth Rotation and Reference Systems Service for the International Terrestrial Reference System (ITRS). In its upcoming realization of the ITRS, the DTRF2020, DGFI-TUM will again correct for non-tidal loading (NTL) effects at the normal equation level. Next to the dedicated NTL data set for the ITRS 2020 realization provided by the Global Geophysical Fluid Center (GGFC), we also considered the data provided by the Earth System Modelling group of the Deutsches GeoForschungsZentrum (ESMGFZ). Besides also comprising all NTL components (atmospheric, oceanic, hydrological) and being mass conserving, the ESMGFZ data has the advantage of daily availability and is already in use at DGFI-TUM. The decision for one or the other data set depends on their suitability for a secular terrestrial reference frame like the DTRF2020, which will be assessed in this work. Although we also compare the site displacements induced by NTL to the residuals of station positions of the Global Navigation Satellite Systems, we will not evaluate the quality of the underlying geophysical models per se. The two data sets differ w.r.t. the underlying hydrological models and the treatment of non-tidal oceanic loading, but the most relevant difference is given in terms of trends in the displacement time-series. After a close investigation of the latter, we finally decided to apply the GGFC contribution to the ITRS 2020 realization in the DTRF2020.

Keywords: Terrestrial reference frame, DTRF, Non-tidal loading, Site displacements, GGFC, ESMGFZ

*Correspondence: matthias.glomsda@tum.de

Deutsches Geodätisches Forschungsinstitut der Technischen Universität München (DGFI-TUM), Arcisstraße 21, 80333 München, Germany

Graphical Abstract

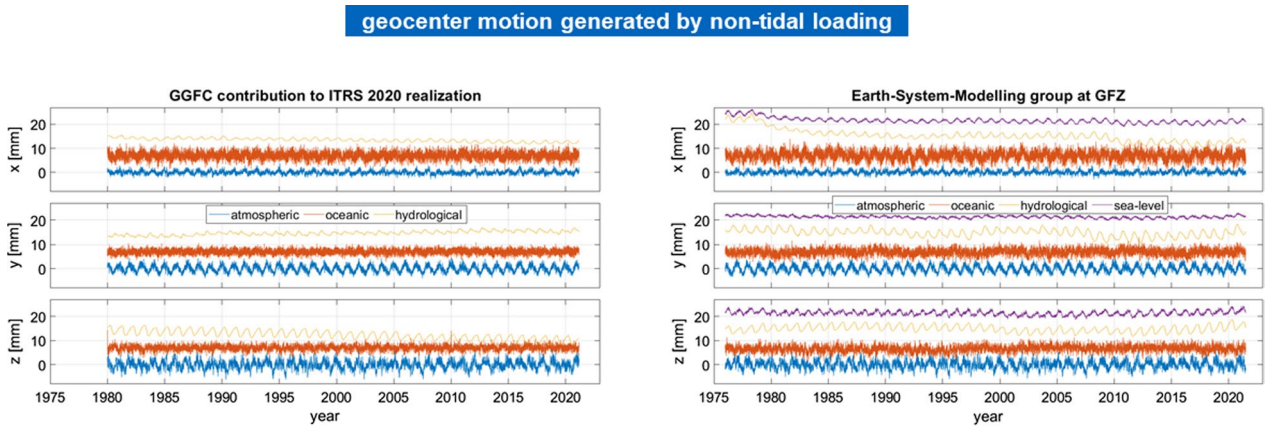

Introduction

Every 5–6 years, new realizations of the International Terrestrial Reference System (ITRS) are computed by the ITRS Combination Centres (CC) of the International Earth Rotation and Reference Systems Service (IERS). These realizations are called terrestrial reference frames (TRF), and the CC are the Institut national de l'information géographique et forestière (IGN) in France, NASA's Jet Propulsion Laboratory (JPL) in the USA, and the Deutsches Geodätisches Forschungsinstitut der Technischen Universität München (DGFI-TUM) in Germany. The ITRS is a conventional 3-dimensional Cartesian reference system co-rotating with the Earth, in which the x- and y-coordinate axes lie in the conventional equatorial plane, with the x-axis pointing towards the Greenwich meridian, and the z-axis is oriented to the IERS reference pole. The origin is identical to the centre of mass of the total Earth system including the oceans and the atmosphere. The scale of the ITRS is defined to be the SI meter (e.g., Petit and Luzum 2010).

The ITRS is realized by the positions of reference points w.r.t. this system. These reference points belong to the observing stations of the four geodetic space techniques: Very Long Baseline Interferometry (VLBI), Satellite Laser Ranging (SLR), the Global Navigation Satellite Systems (GNSS), and Doppler Orbitography and Radiopositioning Integrated by Satellite (DORIS). By applying conventional correction models (Petit and Luzum 2010) for geophysical effects like Earth tides, ocean tides, and tidal loading, the corresponding station motions can be reduced (or regularized) to a long-term linear motion with non-linear residuals. The realizations by IGN (e.g., ITRF2014; Altamimi et al. 2016) and DGFI-TUM (e.g., DTRF2014; Seitz et al. 2021) provide respective 3-dimensional position (at a specific reference epoch) and velocity vectors for each participating station, and hence represent secular reference frames. The realization by JPL (e.g., JTRF2014; Abbondanza et al. 2017), however, does not apply this parameterization but provides station position time-series instead.

In this study, we focus on the secular reference frames. The analysis of station position time-series reveals remaining (unmodelled) non-linear effects, that are still a major limiting factor for the accuracy of long-term reference frames. Such non-linear motions are induced by technique-specific effects like, e.g., the gravitational deformation of VLBI antennas (Nothnagel et al. 2019), or by geophysical effects that are not conventionally corrected for yet. One of the latter are non-tidal loading (NTL) effects: these are non-linear, elastic deformations of the Earth's crust, which are generated by the non-tidal redistribution of masses in the fluid components of the Earth system (e.g., Darwin 1882; van Dam and Wahr 1987; Schuh et al. 2003), i.e., the atmosphere, the oceans, and the continental water storage (hydrology). The corresponding deformations result in instantaneous displacements of the reference points by up to a few cm. This clearly indicates that the accuracy and stability requirements for TRFs—formulated by the Global Geodetic Observing System (GGOS) of the International Association of Geodesy (IAG)—at a level of 1 mm and 0.1 mm/year, respectively, will not be achieved without studying an

improved handling of these non-linear station motions in their realizations.

The correction for NTL effects is hence expected to be beneficial, not least for the determination of the geodetic datum (origin, orientation, scale) of the reference frames. For the JTRF2014, the signals induced by NTL are naturally included in the station position time-series. In the ITRF2014, NTL is not applied directly, but a part of the sum of all non-linear motions is taken into account by estimating and reducing annual and semi-annual signals from the station position time-series (Altamimi et al. 2016). In contrast to that, the DTRF2014 is the first ITRS realization that explicitly uses the displacements generated from geophysical NTL models (for the atmospheric and hydrological components, provided by the chair of the Global Geophysical Fluid Center, GGFC) to correct for the corresponding effects at the normal equation (NEQ) level (Seitz et al. 2021). The phrase "NEQ level" refers to the solution of the normal equation system in the Gauss–Markov model (Koch 1999; Angermann et al. 2004). Accounting for NTL by modifying the NEQs resembles a reduction of the original observations through daily, weekly, or session-wise mean displacements. This procedure offers the possibility to subsequently take into account NTL corrections that were not made at the observation level of the input data (Glomsda et al. 2021).

As shown by Seitz et al. (2021), the application of NTL reduces the root-mean-square (RMS) values of the estimated station positions, and it improves the linear motions for stations with short observation intervals (i.e., less than 2.5 years). Since NTL effects generally have a strong seasonal signal, the correction for the corresponding displacements also reduces the amplitudes of the annual and semi-annual signals in the station positions and consequently in the time-series of the geodetic datum parameters used to realize the ITRF datum, namely the translation and scale time-series.

Therefore, NTL will again be corrected for in the upcoming ITRS realization by DGFI-TUM, the DTRF2020. The amount of available geophysical NTL models has increased in the meantime. Thus, even though there is a data set explicitly designed for the ITRS 2020 realization by the GGFC, we are in principle free to pick the model that copes best with our task, i.e., the correction of input data at NEQ level in a secular reference frame. In this study, we hence compare the GGFC contribution to the ITRS 2020 realization with the NTL data of the Earth System Modelling group at the Deutsches GeoForschungsZentrum (ESMGFZ). We consider the latter, because we already use this data for VLBI analyses (Glomsda et al. 2020), and because it is available on a daily basis, which will enable a timely extrapolation of the DTRF2020. This means an improvement w.r.t. DTRF2014, as the respective site displacements have only been available for epochs up to the year 2015 back then, and extrapolation has to be realized by fitting trigonometric functions to the truncated displacement series. Furthermore, since both data sets include all three NTL components, the DTRF2020 will now contain non-tidal oceanic loading next to the atmospheric and hydrological ones.

In the following, we introduce the two providers and the scope and format of their data. Afterwards, the site displacements induced by the corresponding NTL effects are compared. Since the influence of NTL on geocentre motion is of particular interest for the determination of the TRF origin, the subsequent section is devoted to this topic. Then, we compare the displacement series with the position residuals of GNSS stations. Finally, we assess the properties of the NTL data w.r.t. their applicability in secular reference frames.

Non-tidal loading data

In this section, we describe the origin and format of the NTL data that we considered for application in the DTRF2020.

Global Geophysical Fluid Center

First, there is the GGFC contribution to the ITRS 2020 realization (Boy 2021), which we will abbreviate with GCTI20 in the following. GGFC is a service of the IERS, which collects models describing the effects on Earth's rotation, deformation, and gravity caused by the redistribution of geophysical fluids. These are the fluids of the Earth's interior, as well as air and water on the Earth's surface and in the near-Earth environment. While different (non-tidal) loading data sets are available at GGFC, we only considered GCTI20 (Petrov and Boy 2004; Mémin et al. 2020) for this study. It includes displacements in local directions (North, East, up) of the different components of NTL for all VLBI, SLR, GNSS, and DORIS stations that will be included in the ITRS 2020 realizations. The displacements have a temporal resolution of 1 hour and cover the period from January 1979 or 1980 to June 2021 at the time of writing, but the series is prolongated every few months. Furthermore, they are available for both the centre of mass of the total Earth system (CM) frame and the centre of figure of the solid Earth (CF) frame (for details on these frames, see Blewitt 2003). For each frame, there are five consistently processed displacement file sets:

- ERA5 IB (including or excluding air tides, starting in 1979);

- ERA5 TUGO-m (including or excluding air tides, starting in 1980);
- ERA5 hydro (starting in 1979).

ERA5 is the latest ECMWF (European Center for Medium-range Weather Forecasts; https://www.ecmwf.int/) reanalysis model considering atmospheric pressure, soil-moisture, and snow (Hersbach et al. 2020). The air and water pressure anomalies (i.e., differences from long-term mean pressures) implied by ERA5 are convolved with weighting Green's functions to compute the corresponding elastic displacements at any site of the Earth according to the classic approach described by Farrell (1972) and Petrov and Boy (2004).

ERA5 hydro represents the hydrological component of the NTL, while the other four represent the atmospheric and oceanic components. However, one should only use either ERA5 IB or ERA5 TUGO-m, and each either with or without the air tides. IB is the abbreviation for the Inverted Barometer hypothesis, which assumes that atmospheric pressure changes ΔP_a above the oceans are offset by a change in sea level and hence ocean bottom pressure ΔP_w (van Dam and Wahr 1987; Wunsch and Stammer 1997). The conservation of ocean mass for the IB is achieved by fulfilling Eq. (5) in Petrov and Boy (2004),

$$\Delta P_a \; + \; \Delta P_w \quad = \quad \Delta \bar{P}_0, \tag{1}$$

with $\Delta \bar{P}_0$ representing the mean atmospheric pressure over all oceans. With the ERA5 TUGO-m data, on the other hand, the oceans' response to atmospheric pressure is extended by the Toulouse Unstructured Grid Ocean model, which is an update of the model of Carrère and Lyard (2003), according to Boy (2021). The latter is not a static but a hydrodynamic (barotropic) sea level model (Mémin et al. 2020), and mass conservation is achieved with the help of the Boussinesq approximation, i.e., the density of the resting ocean is assumed to be constant in "the appropriate governing equations of motion representing conservation of [oceanic] mass, momentum, and density" (Wunsch and Stammer 1997, p. 84). TUGO-m and IB will provide different results especially at high latitudes and in shallow seas (Carrère and Lyard 2003; Mémin et al. 2020). Finally, there is also an exchange of water between land and the oceans due to evaporation, precipitation, and river flow, for example, and hence ERA5 hydro is enhanced with a mass conservation component as well: uniform ocean layers are added or removed depending on the changes in the land water reservoir (Boy 2021).

Since we are interested in models for the non-tidal effects, we picked the data sets excluding the air tides. A summary of the GCTI20 data is given in Table 1.

Earth System Modelling group in Potsdam

Another provider for NTL data—also listed at GGFC—is ESMGFZ (Deutsches GeoForschungsZentrum 2021). In general, ESMGFZ also generates site displacements following an (optimized) Green's functions approach (Dill and Dobslaw 2013; Dill et al. 2018), but there are several differences w.r.t. GCTI20.

First of all, ESMGFZ applies different underlying numerical (weather) models for non-tidal atmospheric, oceanic, and hydrological loading, respectively:

- ECMWF reanalysis ERA-40 (Kållberg et al. 2004), ERA-Interim (Berrisford et al. 2011), and operational ECMWF data (Hersbach et al. 2018);
- Max-Planck-Institute for Meteorology Ocean Model (MPIOM; Jungclaus et al. 2013);

Table 1 Summary of the non-tidal loading data sets compared in this study

	GCTI20	ESMGFZ
Atmospheric model	ECMWF ERA5	ECMWF ERA-40, ERA-interim, Operational ECMWF
Oceanic model	TUGO-m	MPIOM
Hydrological model	ECMWF ERA5	LSDM
Mass conservation	Included in single components	Separated as sea level loading
Spatial resolution	Selected sites	Global 0.5° × 0.5° grid
Temporal resolution	1 h	3 h (atmosphere, ocean), 24 hours (hydrology, sea level)
Data start epoch	1979/01/01 (ERA5 IB & hydro), 1980/01/01 (ERA5 TUGO-m)	1976/01/01
Update frequency	Every few months	Daily
Frames	CM, CF	CM, CF
Displacements	North, East, up	North, East, up

- Hydrological Land Surface Discharge Model (LSDM; Dill 2008).

The local site displacements (North, East, up) of the three components are stored separately, but not for a predetermined bunch of stations, but on a $0.5° \times 0.5°$ spatial grid, with temporal resolutions of 3 (atmosphere, ocean) or 24 hours (hydrology). However, ESMGFZ also provides a software for interpolating the displacements at any site on the Earth. For the global conservation of mass, ESMGFZ computes a fourth component, the sea level loading. It is generated from solving the sea level equation for the atmospheric mass of the ECMWF models and the terrestrial water storage of the LSDM. Summing up all four components hence leads to a consistent, mass-conserving NTL data set. Like the hydrological component, the sea level loading has a 24 h resolution.

small latency and high spatial resolution, instead of data designed for a particular (and maybe non-permanent) purpose. The big advantage of the ESMGFZ data is the availability of site displacements on a daily basis, which is not given for GCTI20.

Apart from these differences, the site displacements of ESMGFZ are also generated in both the CM- and the CF-frame. Table 1 contains a summary of the data.

Data preparation

CM-frame

We downloaded the time-series of site displacements for GCTI20 (in the CM-frame, excluding air tides) for all VLBI, SLR, GNSS, and DORIS stations relevant for the ITRS 2020 realization. After reducing the resolution from 1 to 3 hours for each time-series, we chose the following categorization according to the common separation of NTL components:

ERA5 IB → non-tidal atmospheric loading (NTAL)
(ERA5 TUGO-m) - (ERA5 IB) → non-tidal oceanic loading (NTOL)
ERA5 hydro → hydrological loading (HYDL).

A last important difference to GCTI20 is the fact that the ESMGFZ displacements have not been generated from a single reanalysis set of atmospheric forcing data over their complete history (Dobslaw and Dill 2018). Site displacements are available from January 1, 1976, but the ECMWF reanalysis ERA-Interim data only starts at January 1, 1979. Hence, before that epoch, the reanalysis ERA-40 data were used. ERA-Interim itself is only available until August 31, 2019, so the ECMWF operational data have to be applied after this epoch at the latest. Effectively, ESMGFZ uses the operational data for epochs after 2007.0 already. While the atmospheric surface pressure is adjusted between the distinct products (Dobslaw 2016), other forcing variables like precipitation and evaporation differ significantly between ERA-40, ERA-Interim, and the operational data. The latter itself is subject to model updates, so the operational data contain contingent breaks in these variables as well. As a result, there are transition periods after each change in the ECMWF model, in which the dependent NTL products (all four components, compare Dobslaw and Dill 2018) adapt themselves to the new forcing situation. This is particularly relevant for the hydrological loading (and hence ultimately for the sea level loading), as the LSDM heavily depends on the precipitation in the distinct ECMWF models (Robert Dill and Henryk Dobslaw, personal communication). The reason for not using unique reanalysis data in the first place is a different motivation: ESMGFZ wants to provide operational NTL data with a

As explained above, the IB describes the static effect of atmospheric pressure above the oceans, without taking other oceanic (or wind) dynamics into account. TUGO-m, on the other hand, is a hydrodynamic model and adds sea level variations that are not solely related to atmospheric pressure fluctuations. Hence, it seems reasonable to let the ERA5 IB data represent the non-tidal atmospheric loading, while the non-tidal oceanic loading effect is approximated by the differences between the site displacements for ERA5 TUGO-m and ERA5 IB. Mémin et al. (2020) point out that TUGO-m only represents a part of the NTOL, as it does not consider heat and freshwater fluxes like other, baroclinic, ocean models. However, they show that there is no significant improvement by using the baroclinic models rather than the barotropic TUGO-m for NTOL.

ESMGFZ directly provides the distinct NTL components, so the separation into NTAL, NTOL, HYDL, and sea level loading (SLEL) is trivial. We downloaded the global grids of site displacements in the CM-frame for each component and interpolated the displacements at the same station sites as with GCTI20. Afterwards, the data referring to HYDL and SLEL were interpolated to the same 3 h epoch grid as the NTAL, NTOL, and GCTI20 data.

CF-frame (and geocentre motion)

We did not download and prepare the complete CF-frame data for neither GCTI20 nor ESMGFZ. Instead, we computed the geocentre motion referring to each NTL

component and provider, and used this information to recover the CF-frame displacements from the CM-frame displacements when needed.

Geocentre motion is the time-series of the vector from the centre of figure of the solid Earth, CF, to the centre of mass of the total Earth system including air and water, CM. Put differently, it is the time-series of the position of CM in the CF-frame, where CF = (0, 0, 0). It is generated by the redistribution of mass in the total Earth system, and hence the redistribution of mass in connection with NTL effects contributes to geocentre motion (e.g., Dong et al. 2003). For example, the component $\boldsymbol{g}_{NTAL}(t)$ of geocentre motion referring to non-tidal atmospheric loading at an epoch t is given by the difference between the corresponding site displacements $\boldsymbol{\delta}^{CF}_{NTAL}(t)$ and $\boldsymbol{\delta}^{CM}_{NTAL}(t)$ in the CF- and CM-frames, respectively:

$$\boldsymbol{g}_{NTAL}(t) \quad = \quad \boldsymbol{\delta}^{CF}_{NTAL}(t) \; - \; \boldsymbol{\delta}^{CM}_{NTAL}(t). \tag{2}$$

In contrast to the original data, these site displacements (and geocentre motion) are now given in the xyz-coordinate system of the ITRS, which means that they must be transferred from the local horizontal frame to the ITRS with rotation matrices $\boldsymbol{R}_s$, which depend on the location of a particular site s.

Any site's displacements can be chosen to compute the geocentre motion contribution, since CM and CF are the same for all sites at the same epoch t. We generated the distinct contributions for both GCTI20 and ESMGFZ by using the CM- and CF-displacements of a subset of 12 globally distributed SLR stations. As expected, the contributions were identical for each of the 12 stations, and the corresponding time-series will be shown in the next but one section. The CF-frame displacements for any site can now be computed from the respective CM-frame displacements with Eq. (2).

Comparison of site displacements

Several studies (e.g., Roggenbuck et al. 2015; Glomsda et al. 2020) have compared NTL data by different providers. In general, the vertical displacements are larger than the horizontal ones for each NTL component by a factor of 2–5 and can reach peak-to-peak variations of 10–30 mm. NTOL usually is the least relevant contributor, except for coastal areas. The models for NTAL mostly agree very well, while those for HYDL tend to show the largest discrepancies. Atmospheric pressure anomalies are rather strong at mid-latitudes and continental sites, while terrestrial water storage (i.e., hydrology) is most relevant near lakes, rivers, and the equator (e.g., Dill and Dobslaw 2013). Thus, there is a latitudinal dependence in particular (compare, e.g., Gobron et al. 2021). All NTL components contain oscillations, and the amplitude is generally largest for the annual signal, especially for HYDL. These general properties pretty much hold for the GCTI20 and ESMGFZ data, too. In the following, we will hence focus on their peculiarities and the difference between CM- and CF-frame.

Atmospheric loading

We defined the ERA5 IB data of GCTI20 to represent NTAL, and hence we compare the corresponding site displacements with those for NTAL by ESMGFZ. In

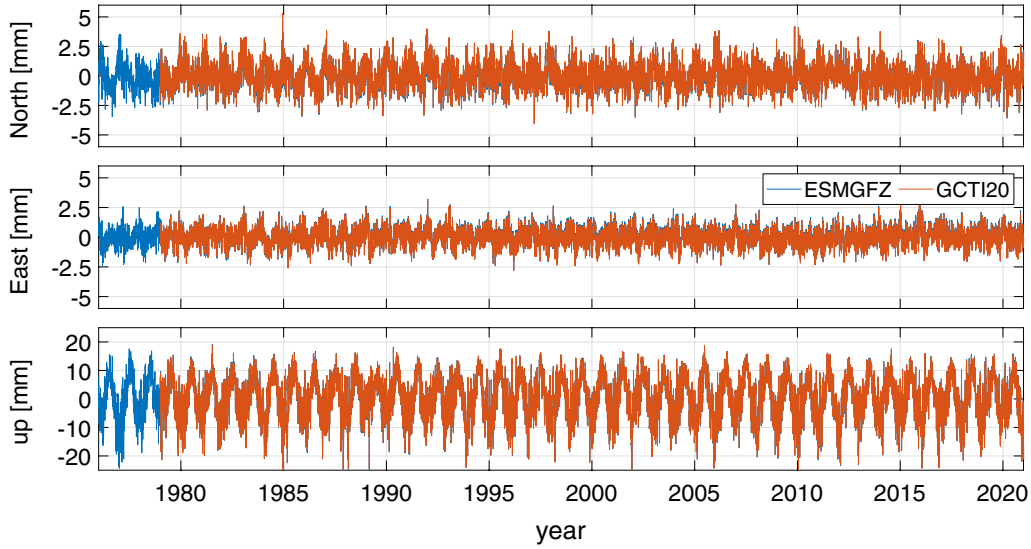

Fig. 1 Site displacements for non-tidal atmospheric loading (NTAL) in the CM-frame at the SLR station 1879 in Altay, Russia. Blue: ESMGFZ, red: GCTI20. Please note the different scale for the up direction

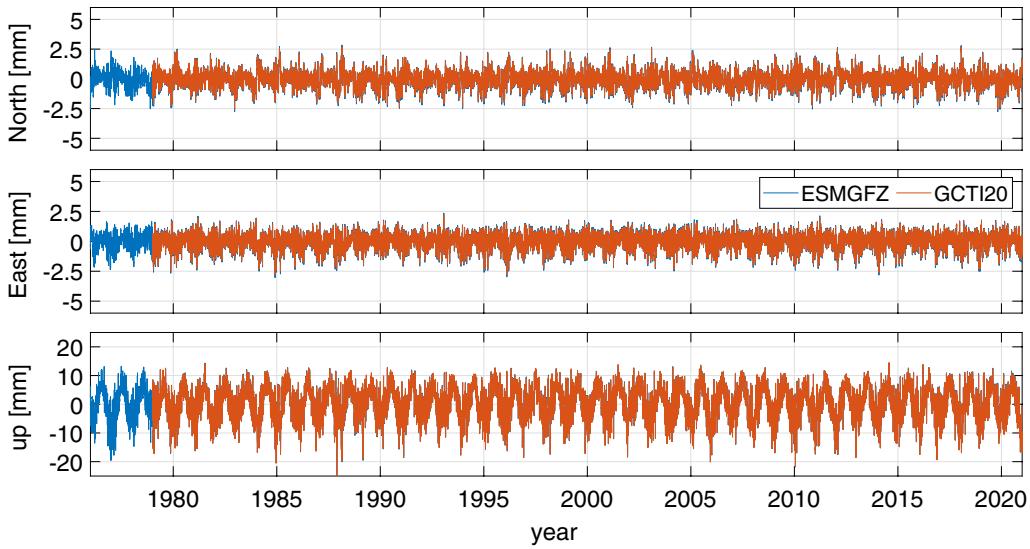

Fig. 2 Same as Fig. 1, but this time the site displacements refer to the CF-frame

Figs. 1 and 2, as for basically all sites, we observe that the respective displacements agree very well between the two providers, for both the CM- and the CF-frame. This is not really surprising, since both GCTI20 and ESMGFZ use ECMWF data, and at least the atmospheric surface pressure in the distinct underlying ECMWF models with ESMGFZ has been adjusted to avoid jumps (compare above). The agreement further confirms that also ESMGFZ makes use of the IB hypothesis for NTAL (Dobslaw and Dill 2018). Displacements in the CF-frame are usually smaller than those in the CM-frame.

Oceanic and hydrological loading

The comparison of the non-tidal oceanic and hydrological components is less straightforward. Previously, we stated that ESMGFZ separates (at least a part of) the mass conservation, i.e., the sea level variation due to atmospheric and hydrological fluctuations, into the SLEL component. GCTI20, on the other hand, considers parts of the mass conservation in both the ERA5 TUGO-m and the ERA5 hydro data. Since we define the NTOL of GCTI20 to be given by the differences in the site displacements for ERA5 TUGO-m and ERA5 IB, and since ERA5 IB is approximately equal to the NTAL of ESMGFZ, we must assume that the oceanic loading of GCTI20 contains a mass conservation part, while that of ESMGFZ does not. Furthermore, Mémin et al. (2020) wrote that TUGO-m only partly includes NTOL. Hence, the NTOL components of the two providers will presumably not match. The same holds for the two HYDL components, as the site displacements for ERA5 hydro in GCTI20 include their mass conservation part, while the conservation part from the hydrological mass loads has been transferred to the SLEL component in case of ESMGFZ.

In Fig. 3, we plotted the RMS values of the differences between the site displacements of GCTI20 and ESMGFZ for the distinct loading components in the CM-frame. Next to the single components NTAL, NTOL, HYDL, and SLEL, we also added the sum of all components per provider. The site displacements refer to the more than 1400 GNSS stations which will be considered in the DTRF2020, and the RMS values are ordered by the latitudinal position of their respective GNSS station. The values are actually smallest for NTAL (compare the previous subsection), with mean values of about 0.1 and 0.2 mm for the horizontal and vertical directions, respectively. As expected, the differences between the ESMGFZ and GCTI20 data increase for NTOL, with RMS values of about 0.7 and 1.1 mm on average. The RMS values for SLEL do not belong to a difference but directly to the time-series of corresponding site displacements by ESMGFZ, since there is no such component provided by GCTI20. Their mean values of about 0.6 and 1.0 mm are similar to those of the differences for NTOL. Finally, the RMS values of differences for a single component are largest for HYDL, a result which was also obtained in previous studies (compare the preliminary remarks of this section): the mean values are 2.3, 1.4, and 4.3 mm for the North, East, and up directions, respectively. The corresponding discrepancy between GCTI20 and ESMGFZ is composed of two parts: (1) the model differences between ERA5 hydro and LSDM, and (2) an ocean mass conservation component which only prevails for GCTI20. Reflecting the proportions between the distinct

components, the RMS values for the combined loading are closest to those for HYDL.

The order by latitude in Fig. 3 reveals some spatial correlation. For the North direction, the overall pattern of the differences between GCTI20 and ESMGFZ resembles a kind of continuous curve, with its maximum values between 30°S and 30°N. While the effect is most pronounced for HYDL, this basically holds for all NTL components. For the East direction, there is hardly any latitude dependence, but for the up direction we can again observe a cluster of large RMS values, this time at about 45°N for HYDL, and about 60°S and 60°N for NTOL. The latter is in line with the study of Gobron et al. (2021), who take other measures but also recognize the strongest impact of non-tidal oceanic (and atmospheric) loading at high latitudes. That is to say, we might expect the differences between GCTI20 and ESMGFZ to be largest in those regions where a particular NTL component is most relevant. For HYDL, these are the low latitudes, which matches the pattern for the North direction at least.

Combined loading

Given the distinct treatment of mass conservation between GCTI20 and ESMGFZ, which is facilitated by the contrast of separated displacements in Fig. 3, it is (apart from NTAL with the IB hypothesis) only consistent to compare the sum of all loading components per provider. Since we are not going to separate the single components in the context of the DTRF2020, this is not a concern at all. In Fig. 4, we plotted the RMS values of the differences in the combined site displacements between GCTI20 (NTAL + NTOL + HYDL) and ESMGFZ (NTAL + NTOL + HYDL + SLEL) for both the CM- and the CF-frame on world maps, which unveil the latitude dependence of Fig. 3 in more detail. We can confirm immediately that the RMS values are generally larger in the CM-frame (left column) and the up direction (bottom row). The largest RMS values for the up direction in both frames are observed in the USA, in Antarctica, and near the equator, especially in South America. This is in line with our statements in the previous subsections, claiming that the largest discrepancies between GCTI20 and ESMGFZ stem from the hydrological models. The rain forest area is particularly sensitive to HYDL, and ERA5 hydro (compare Fig. 3 in Boy 2021) assigns comparatively more hydrological loading to the USA than the LSDM (compare Fig. 2 in Dill and Dobslaw 2013).

In Figs. 5 and 6, we show the time-series of combined site displacements for the GNSS station BRAZ in Brasilia, Brazil. First of all, we observe the usual pattern of the CM-frame displacements (Fig. 5) showing larger peak-to-peak variation than the CF-frame displacements (Fig. 6). The new insight, however, is the presence of distinct drifts and base level offsets for the otherwise seasonal variations. These differ between the providers, between the directions, and between the frames that the displacements have been computed in. Such shifts in trends are critical when NTL is applied in the context of a secular reference frame, as they will be transferred to

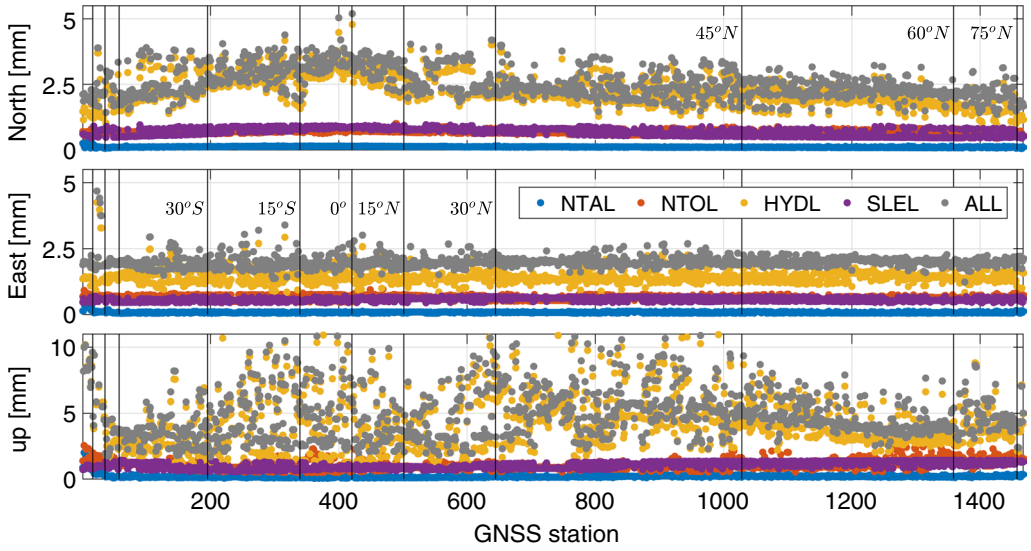

Fig. 3 RMS values of the differences between the site displacements of GCTI20 and ESMGFZ in the CM-frame at GNSS stations, ordered by latitude. Distinct loading components as well as their combination (ALL = NTAL + NTOL + HYDL [+ SLEL]) are considered in the local coordinate system. Please note the different scale for the up direction. The vertical lines indicate the borders between 15° latitude groups

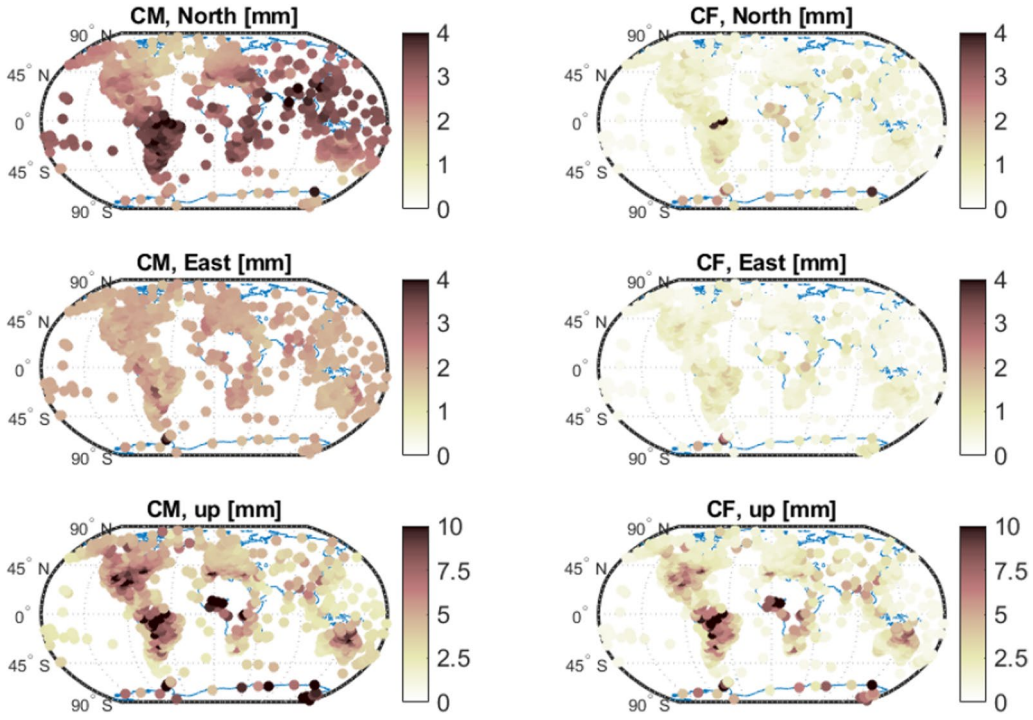

Fig. 4 RMS values of the differences between the site displacements of GCTI20 and ESMGFZ for the combined loading (NTAL + NTOL + HYDL [+ SLEL]) at GNSS stations. Left column: CM-frame, right column: CF-frame. Top: North, middle: East, bottom: up (different scale compared to the horizontal components)

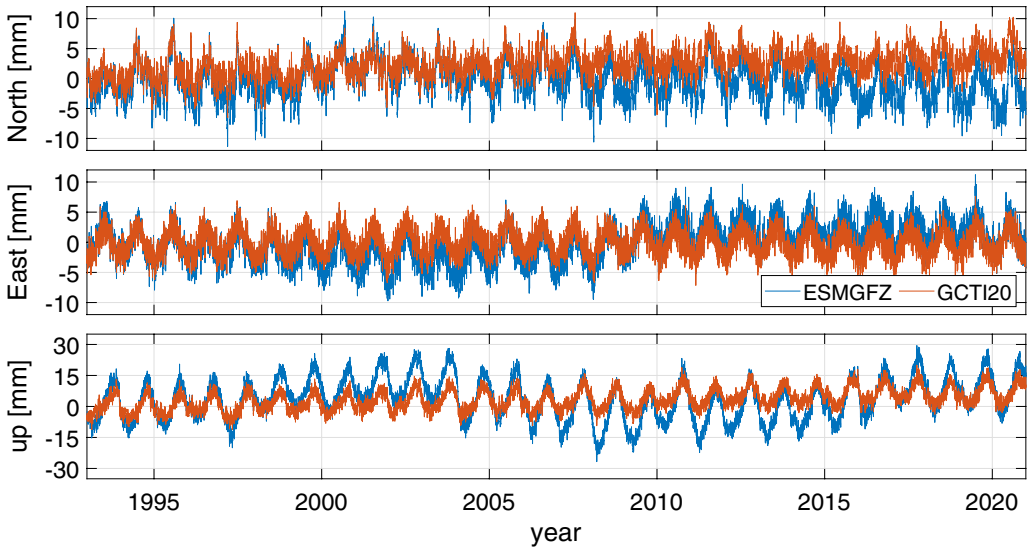

Fig. 5 Site displacements for the combined loading (NTAL + NTOL + HYDL [+ SLEL]) in the CM-frame at the GNSS station BRAZ in Brasilia, Brazil. Blue: ESMGFZ, red: GCTI20. Please note the different scale for the up direction

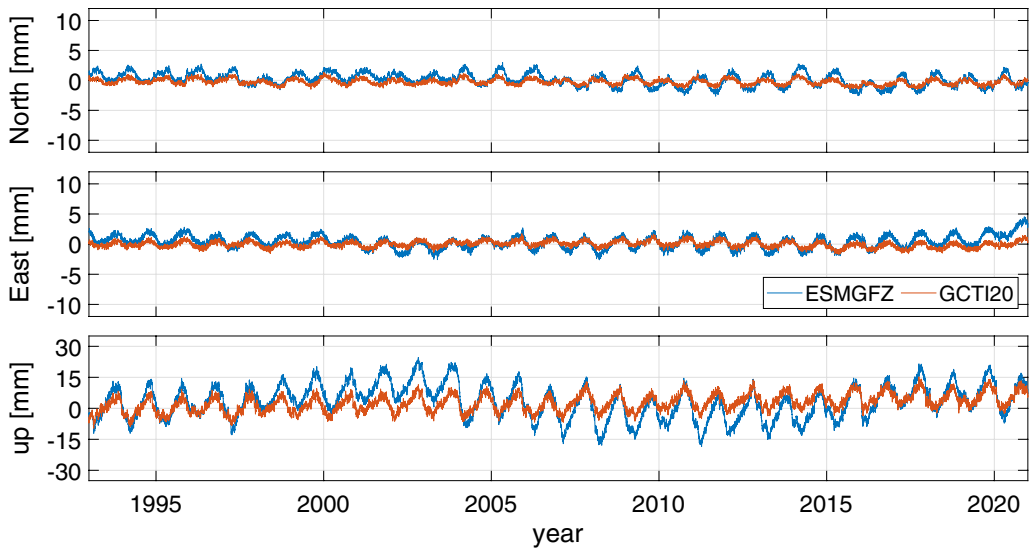

Fig. 6 Same as Fig. 5, but this time the site displacements refer to the CF-frame

the estimated positions and velocities and thus affect the linear motions of the reference points. Hence, we need to investigate the long-term behaviour of the displacement time-series in more detail in the following.

Geocentre motion contribution

Geocentre motion is important for the realization of the origin of the ITRS. The latter is performed with SLR, since CM is the dynamical origin of satellite orbits. When applying NTL in the DTRF2020, the corresponding contribution to geocentre motion hence influences the realized origin. As a consequence, we must analyse the contributions in connection with the site displacements of GCTI20 and ESMGFZ.

Separate loading components

The geocentre motion contributions separated by NTL component are shown in Figs. 7 and 8. For the GCTI20 data (Fig. 7), the motions connected with NTAL and NTOL basically vary around zero without any apparent drift. The seasonal signal is more pronounced for NTAL, especially for the y- and z-coordinates. NTOL, on the other hand, induces a larger contribution than NTAL for the x-coordinate. This might well be related to the diverse land distribution in the x- and y-directions of the TRF. The contribution by HYDL is the smallest for the x- and y-coordinates, and at the same level as NTOL for the z-coordinate. For all coordinates, however, the annual signal of HYDL's contribution is clearly visible, as well as a drift which is quite constant over the whole period from 1980 to 2021. Even though the regional redistribution of land water storage (LWS) is more diverse (e.g., Rodell et al. 2018), these drifts indicate that the global integration of LWS generates a quite stable systematic contribution of HYDL to geocentre motion in the GCTI20 model.

For ESMGFZ (Fig. 8), we observe an analogous behaviour for NTAL and NTOL. The contribution by HYDL, on the other hand, is significantly different. In particular for the x-coordinate, we can identify five major regimes. From 1976 until 1978, the time-series of the respective geocentre motion contribution attains strictly positive values without any significant drift. From 1979 to about 1982, the time-series shows a strong negative drift. From 1983 to about 2009, the negative drift is much smaller, but the time-series values are still mostly positive. Then, at the end of 2009, the values sharply decrease for about one year, before the contribution continues with a small drift and mostly negative values. A similar, but less pronounced pattern is observed for the contribution by SLEL, which is separated for ESMGFZ only. The y- and z-coordinates also reveal changes in offset and drift, but these are less striking than for the x-coordinate. These regimes are most probably related to the transition periods between the distinct underlying ECMWF models, i.e., to the jumps in the corresponding forcing data (mainly precipitation and evaporation), which are driving HYDL and SLEL (compare above).

Combined loading

In Fig. 9, the combined geocentre motion contribution is presented for both GCTI20 and ESMGFZ. It is the sum

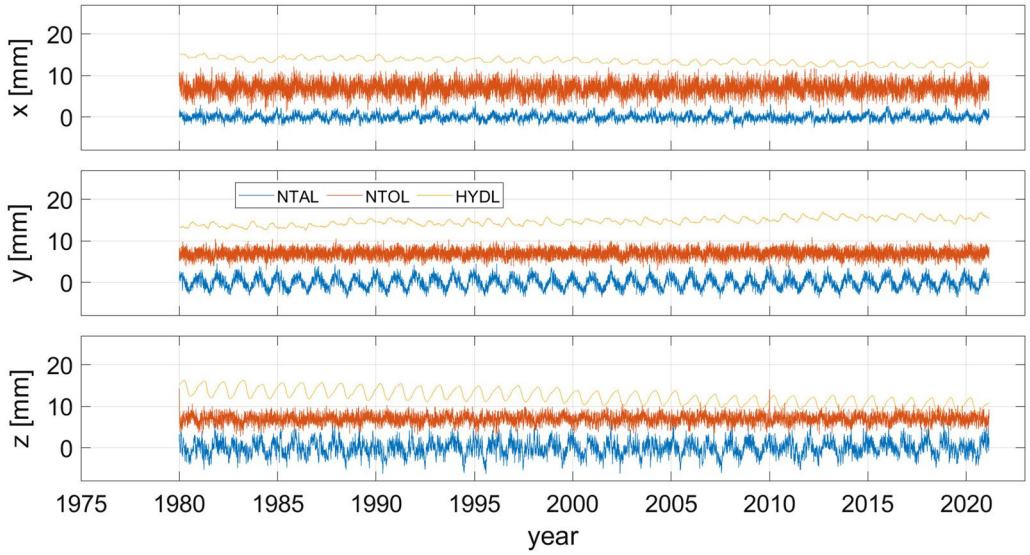

Fig. 7 Geocentre motion connected with the distinct non-tidal loading components of GCTI20. It is computed as the difference between the site displacements in the CF- and the CM-frame according to Eq. (2). The time-series for NTOL and HYDL have been shifted by 7 and 14 mm, respectively

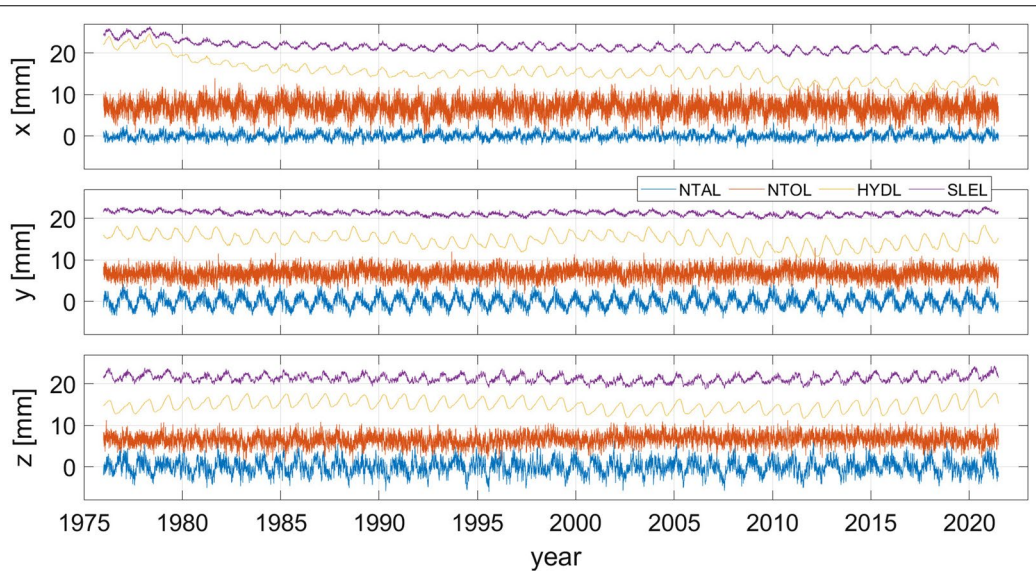

Fig. 8 Same as Fig. 7, but this time the geocentre motion contributions refer to ESMGFZ. Hence, there is an additional component generated by the sea level loading (SLEL), which has been shifted by 21 mm

of the distinct NTL components' contributions, and we can clearly see how the different regimes (trends) for the hydrological and sea level components of ESMGFZ are transferred into the combined contribution. The third geocentre motion contribution in Fig. 9 has been generated from the official SLR solution by the International Laser Ranging Service (ILRS; Pearlman et al. 2019) for the ITRS 2020 realization (Pavlis et al. 2021). It covers the time period between 1983 and 2021 and includes up to four satellites (LAGEOS-1/2, Etalon-1/2), but LAGEOS-1 is the only satellite that was observed before 1993. The contribution is obtained by the network shift approach (e.g., Dong et al. 2003), i.e., by the time-series of translation parameters between the weekly (before 1993: 15-daily) ILRS solutions (CM-frame) and the long-term reference frame that we computed from these solutions (mean CM-frame, i.e., approximately CF-frame). NTL has not been reduced in these solutions, so the resulting

geocentre motion includes NTL effects. However, it also includes other unmodelled geophysical or technique-specific effects, like changes in the SLR observation networks (e.g., Collilieux et al. 2009; Riddell et al. 2017). As a consequence, the ILRS geocentre motion has a less regular pattern and reveals a larger variability, especially for the z-coordinate due to the inhomogeneous station distribution between the northern and southern hemispheres. Before 1993, the variance is even larger for all coordinates, since only one satellite has been observed.

To get some numerical evidence for the long-term behaviour of the distinct geocentre motion contributions, we fitted linear trends to each time-series and listed the corresponding offsets (at 2000.0) and drifts in Table 2. Different start epochs were considered for the fitting intervals:

- 1976.0, the start epoch for the ESMGFZ data;
- 1980.0, the start epoch for the GCTI20 data;

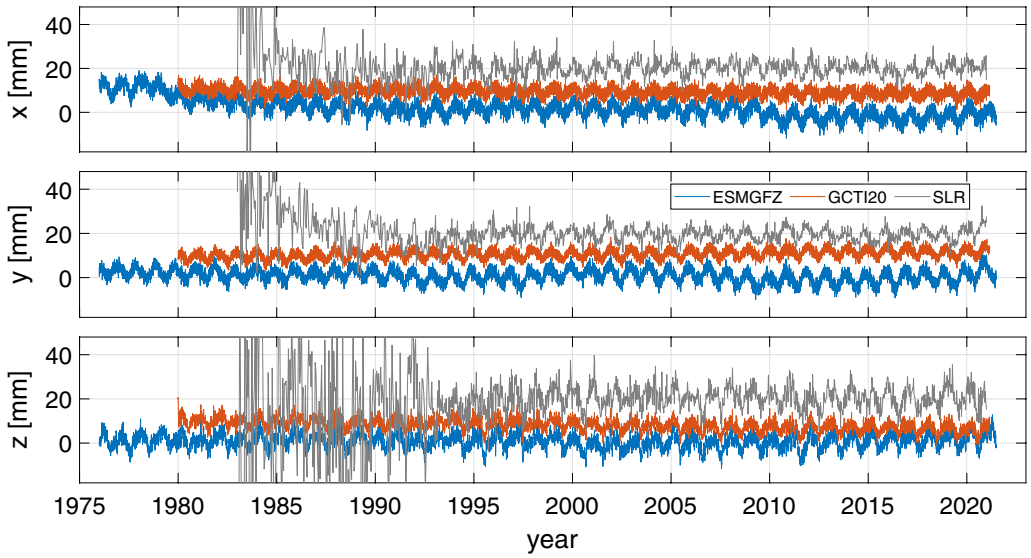

Fig. 9 Geocentre motion contributions as computed for the combined loading of both GCTI20 (NTAL + NTOL + HYDL, red) and ESMGFZ (NTAL + NTOL + HYDL + SLEL, blue). For comparison, also the geocentre motion estimated by SLR is shown (grey). The time-series for GCTI20 and SLR have been shifted by 10 and 20 mm, respectively

Table 2 Fitted trends (offsets at 2000.0 in [mm], and drifts in [mm/year]) for the geocenter motion as computed from ESMGFZ, GCTI20, and ILRS data (see text). In each case, the trends have been fitted from the corresponding time-series period listed in column "period". Formal errors are given in parentheses

Provider	Period	*x*		*y*		*z*	
		Offset	Drift	Offset	Drift	Offset	Drift
ESMGFZ	1976.0–2021.5	1.74 (0.01)	− 0.23 (0.00)	0.83 (0.01)	− 0.06 (0.00)	0.93 (0.01)	− 0.01 (0.00)
	1980.0–2021.5	1.27 (0.01)	− 0.16 (0.00)	0.75 (0.01)	− 0.04 (0.00)	0.91 (0.01)	− 0.01 (0.00)
	1993.0–2021.5	1.48 (0.01)	− 0.17 (0.00)	0.63 (0.01)	− 0.03 (0.00)	0.37 (0.02)	0.04 (0.00)
	2000.0–2021.5	2.07 (0.02)	− 0.22 (0.00)	1.31 (0.03)	− 0.08 (0.00)	− 1.37 (0.03)	0.17 (0.00)
	2010.0–2021.5	− 3.20 (0.07)	0.09 (0.00)	− 4.67 (0.08)	0.28 (0.01)	− 3.94 (0.09)	0.33 (0.01)
GCTI20	1980.0–2021.2	− 0.49 (0.01)	− 0.06 (0.00)	0.69 (0.01)	0.06 (0.00)	− 1.65 (0.01)	− 0.11 (0.00)
	1993.0–2021.2	− 0.48 (0.01)	− 0.06 (0.00)	0.62 (0.01)	0.06 (0.00)	− 1.52 (0.01)	− 0.12 (0.00)
	2000.0–2021.2	− 0.57 (0.02)	− 0.05 (0.00)	0.57 (0.02)	0.07 (0.00)	− 1.97 (0.02)	− 0.09 (0.00)
	2010.0–2021.2	− 0.74 (0.05)	− 0.04 (0.00)	1.70 (0.05)	− 0.00 (0.00)	− 1.88 (0.07)	− 0.09 (0.00)
SLR	1993.0–2021.0	0.21 (0.12)	− 0.00 (0.01)	− 0.58 (0.11)	0.02 (0.01)	− 0.38 (0.18)	0.06 (0.02)
	2000.0–2021.0	0.38 (0.20)	− 0.01 (0.02)	− 0.65 (0.18)	0.02 (0.01)	0.83 (0.30)	− 0.04 (0.02)
	2010.0–2021.0	− 0.12 (0.63)	0.01 (0.04)	− 1.21 (0.63)	0.06 (0.04)	− 0.65 (1.05)	0.05 (0.07)

- 1993.0, the start epoch for the multi-satellite ILRS data;
- 2000.0, an intermediate epoch;
- 2010.0, an apparent discontinuity in the ESMGFZ data.

We observe that the estimated offsets and drifts strongly deviate for ESMGFZ depending on the chosen time period, especially after the years 2000 and 2010. In contrast to that, the trends for the geocentre motion contribution by the GCTI20 data are quite stable, only for the y-coordinate the drift flattens slightly starting in 2010. The geocentre motion estimated from the ILRS solution after 1993 is also rather stable and reveals no significant drifts. Only for the z-coordinate, which is the most variable one as mentioned above, the offsets and drifts show a larger dependence on the time period.

Annual signals

When applying NTL in a secular reference frame, whose origin is realized with SLR, we long for a reduction of the signals in the corresponding geocentre motion. Hence, there shall be a good agreement of the amplitudes and phases of the contributions estimated from the NTL data by GCTI20 and ESMGFZ with those of the ILRS solution. To investigate this, we performed a spectrum analysis of the combined geocentre motion contributions by Fast-Fourier transforms. For consistency, and for leaving out the highly variable period of SLR translations, we only used the time-series starting at 1993.0 for GCTI20, ESMGFZ, and the ILRS solution. However, the spectrum did not change significantly when we considered the full time-series for GCTI20 and ESMGFZ.

The results indicate that the most important signal is the annual one (365.25 days) for all data sets and all directions, and the respective amplitudes and phases are listed in Table 3. For comparison, we also provide the parameters from the study by Wu et al. (2017), who determine geocentre motion by a combination of geodetic and GRACE (Gravity Recovery and Climate Experiment) observations. Looking at the values at large, we observe that neither the GCTI20 nor the ESMGFZ data provide amplitudes and phases that match perfectly with those for the ILRS solution or the solution by Wu et al. (2017). However, considering that the latter two also contain effects other than NTL, the agreement is quite good for individual values (e.g., amplitude and phase of ESMGFZ and ILRS for the x-coordinate, or phase of GCTI20 and ILRS for the z-coordinate). The amplitudes for GCTI20 are always smaller than those for ESMGFZ, but we cannot conclude that one NTL data set will outperform the other w.r.t. this spectrum analysis. Given the dominance of the annual signal for all four geocentre motion contributions, as well as the similarity of the corresponding phases for all three directions, we can nevertheless expect both the GCTI20 and the ESMGFZ data to significantly reduce this signal in geocentre motion.

Comparison with GNSS position residuals

Up to here, we have simply analysed the provided site displacements without any confirmation that they actually agree with the motion of geodetic reference points caused by NTL effects. In this section, we will hence compare the displacements with the (residual) positions of GNSS stations. The impact of NTL on the height of GNSS stations has been studied by various authors, see Tregoning and van Dam (2005) or Williams and Penna (2011), for example. Männel et al. (2019) have even compared these heights with the site displacements of ESMGFZ for the hydrological and a combined (NTAL + NTOL + HYDL) loading.

Time-series statistics

We consider the residuals of a 7 parameter Helmert transformation of daily GNSS station positions (in North, East, and up directions) w.r.t. their linear positions in a combined multi-year GNSS solution. The daily positions have been taken from the 3rd IGS (International GNSS Service; Johnston et al. 2017) reprocessing campaign (repro3; http://acc.igs.org/repro3/repro3.html) and the multi-year solution already incorporates the same

Table 3 Annual amplitudes (in [mm]) and phases (in [d] since January 1st) from a spectrum analysis of the coordinate-wise geocentre motions generated by the combined NTL of ESMGFZ and GCTI20, the ILRS solution, and the unified approach by Wu et al. (2017) (see their Table 1). The corresponding time-series periods are listed in the column "period". Formal errors are given in parentheses

Provider	Period	*x*		*y*		*z*	
		Amplitude	Phase	Amplitude	Phase	Amplitude	Phase
ESMGFZ	1993.0–2021.5	2.70 (0.01)	48.6 (0.01)	3.21 (0.00)	321.1 (0.20)	3.11 (0.02)	44.5 (0.01)
GCTI20	1993.0–2021.2	1.60 (0.01)	23.4 (0.15)	2.12 (0.00)	349.9 (0.20)	2.15 (0.01)	22.1 (0.13)
ILRS	1993.0–2021.0	2.66 (0.15)	46.8 (0.07)	2.53 (0.02)	309.2 (2.73)	3.81 (0.23)	24.8 (1.19)
Wu et al. (2017)	2002.2–2009.0	1.3 (0.1)	46 (4)	3.0 (0.1)	330 (2)	3.3 (0.2)	26 (3)

time-series discontinuities as those that will be applied for the DTRF2020 (we use our own list based on a manual inspection of the time-series). The positions have not been corrected for any NTL, so the corresponding non-linear signals should still be contained in the residual time-series. Furthermore, the residuals refer to the CF-frame, since no information regarding the geocentre motion (by SLR) has been provided to the GNSS solutions yet. Hence, we can only use the site displacements of the CF-frame for comparison.

In Fig. 10, we plotted the position residuals together with the site displacements of GCTI20 and ESMGFZ for the GNSS station SALU in Sao Luis, Brazil. The displacements refer to the sum of all NTL components (NTAL + NTOL + HYDL [+ SLEL]) in the CF-frame. In this example, the match between the residuals and the site displacements is quite good, a fact which cannot be generalized, unfortunately. In particular, the agreement is often rather bad for the horizontal directions. However, the vertical site displacements conform well with the position residuals for many GNSS stations, and the overall impression is that the seasonal amplitudes of the ESMGFZ data match better.

To get the general picture, we computed the correlations between the GNSS position residuals and the site displacements (again for the combined NTL), as well as the RMS values of the differences between them, i.e., of the residuals corrected for the site displacements. For reliability, we only used those DTRF2020 stations whose residual time-series fulfils two conditions: (1) it has a length of at least 2.5 years, and (2) there are at least 250 epochs on average per year. Altogether, 1273 stations pass this filter. Furthermore, we computed the averages of the site displacements within ±0.5 days of the epochs of the residuals (like Mémin et al. 2020), instead of comparing with the snapshot displacement of each epoch only.

In the top row of Fig. 11, we plotted the histograms of the correlations for both providers. For all directions, most of the correlations are positive, indicating a generally common movement of position residuals and site displacements. Negative correlations mainly exist for the horizontal directions (especially for East), and there seems to be a regional cluster in Europe. The correlation values for the horizontal directions are rather small in general, with medians of about 0.24 and 0.26 for ESMGFZ and GCTI20, respectively. For the vertical direction, the correlations are significantly larger, with medians of about 0.46 for ESMGFZ and 0.50 for GCTI20. Hence, the histograms and the median values indicate slightly larger correlations for the GCTI20 data. Männel et al. (2019) have computed similar correlations between their combined ESMGFZ site displacements and the 7 day moving average of their GNSS time-series. While a moving average reduces some noise, we keep the original time-series, as we will apply daily site displacements to daily GNSS normal equations in the DTRF2020. A test calculation showed that the impact on the correlations is not significant, anyway.

In the bottom row of Fig. 11, we show the histograms of the differences

$$\Delta RMS = RMS^{ESMGFZ} - RMS^{GCTI20} \quad (3)$$

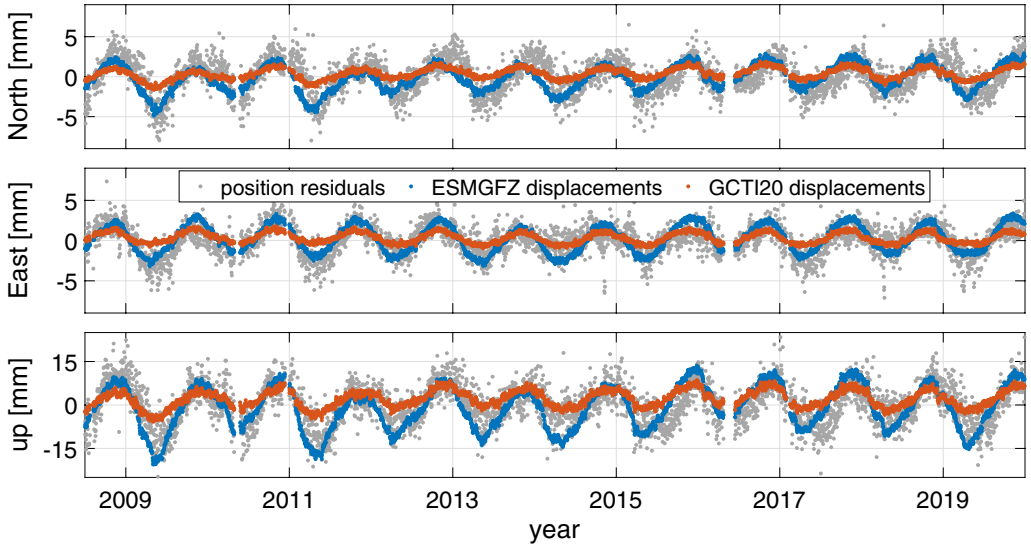

Fig. 10 Position residuals (grey) and combined (NTAL + NTOL + HYDL [+ SLEL]) non-tidal loading site displacements from the CF-frame provided by GCTI20 (red) and ESMGFZ (blue) for the GNSS station SALU in Sao Luis, Brazil. Please note the different scale for the up direction

per GNSS station and local direction, where RMS^p refers to the RMS value of the differences between a station's position residuals and the combined (average) site displacements of provider p. For the horizontal directions, the absolute values of ΔRMS are rather small, and the median is about 0.011 mm. Hence, it does not make a significant difference whether the horizontal position residuals are corrected with the site displacements of GCTI20 or those of ESMGFZ. For the vertical direction, however, the median is about 0.113 mm, indicating a slightly better fit of the GCTI20 data again.

Seasonal signals

The previous subsection left us with the apparent contradiction that the (CF-frame) site displacements of ESMGFZ better match the corresponding GNSS position residuals visually, while the correlations and RMS values suggest a marginally better statistical match for GCTI20. To investigate this in more detail, we fitted the following trigonometric function to the displacement time-series for the combined loading of each GNSS station and provider:

$$\begin{aligned} h(t) \quad = \quad & o \; + \; d \cdot t \; + \; A_1 \cdot \cos\left([t - \phi_1]/T \cdot 2\pi\right) \\ & + \; A_2 \cdot \cos\left([t - \phi_2]/T \cdot 4\pi\right), \end{aligned} \tag{4}$$

with o being an offset, d a drift, A_1 and ϕ_1 the annual amplitude and phase, and A_2 and ϕ_2 the semi-annual amplitude and phase, respectively. t is the epoch in days since 2000.0, and $T = 365.25$ is the number of days per cycle, i.e., in one year.

As can be expected, the estimated offsets and drifts already differ between GCTI20 and ESMGFZ (not shown here). However, the interpretation of these differences is beyond the scope of this paper. At this point, we are more interested in the agreement of the seasonal signals between the displacements and the GNSS position residuals. Hence, we also fitted $h(t)$ to the time-series of these residuals. Although it is widely accepted that GNSS time-series contain temporally variable, i.e., coloured noise (e.g., Zhang et al. 1997; Gobron et al. 2021), we do not apply a sophisticated noise model in the functional fits, amongst others because corresponding information is missing for the displacement time-series, and because it will most likely not change the final results of our comparisons. To obtain the most reliable fits, however, we again restricted ourselves to the 1273 time-series of the previous subsection. In the end, we also dropped those GNSS stations with a formal error greater than 5 days for the estimated annual phase in vertical direction.

In Fig. 12, we plotted the differences between the estimated annual signals for the vertical directions of the remaining 1041 GNSS stations on world maps. In the left column, we compare the annual amplitudes. The mean amplitudes for the vertical displacements of GCTI20 and

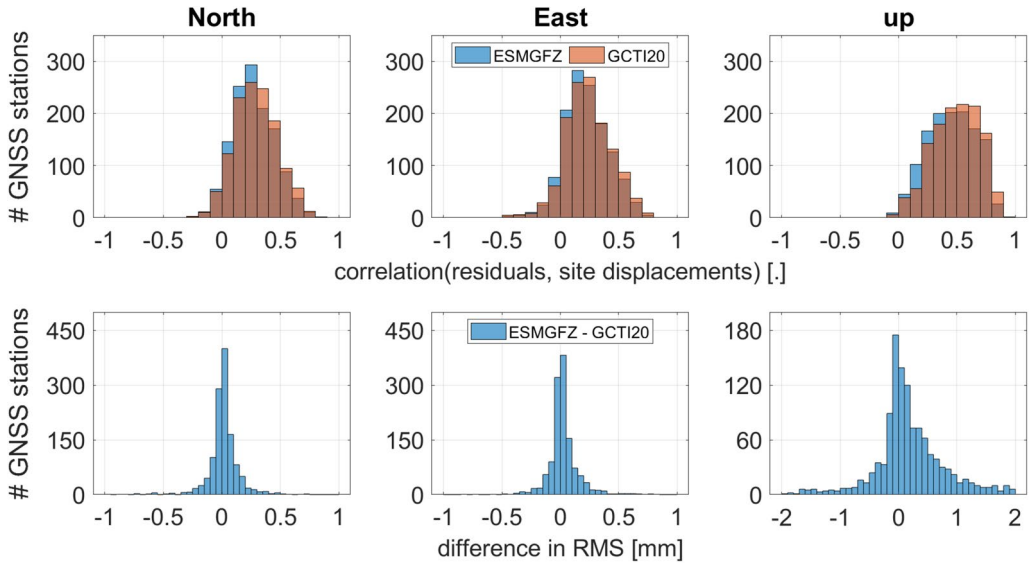

Fig. 11 Top row: histograms of the correlations between GNSS position residuals and the corresponding (24 h average) site displacements for the combined (NTAL + NTOL + HYDL [+ SLEL]) non-tidal loading by either GCTI20 or ESMGFZ. Bottom row: histograms of the differences ΔRMS in Eq. (3). Left column: North, middle column: East, right column: up (different scale for ΔRMS)

ESMGFZ are 2.4 and 3.2 mm for this GNSS station subset, respectively, and most of them differ from the fitted amplitudes for the height residuals (mean value: 3.5 mm) by less than 5 mm. For the largest part of the Earth, in particular Europe, Latin America, East Asia, and Australia, the amplitudes for GCTI20 and ESMGFZ agree very well. The most striking area of disagreement, however, is the Northern part of South America (including the Amazon basin), where HYDL is very strong. Here, the amplitudes partly differ by more than 10 mm, and while the fitted values for ESMGFZ are generally larger than those for the GNSS height residuals, the fitted values for GCTI20 are generally smaller.

In the right column of Fig. 12, the differences between the fitted annual phases are shown. In contrast to the annual amplitudes, they agree particularly well between GCTI20 and ESMGFZ in South America, and differ most in East Asia and at Hawaii. The disagreement with the fitted phases for the GNSS height residuals is largest in Europe and the USA, with a lead of about 50 to 150 days. For about 6% of these stations, the absolute phase lag is actually greater than 100 days. For about 76% of the GNSS stations, the absolute phase lag is smaller than 50 days for both GCTI20 and ESMGFZ, while the fraction of stations with an absolute phase lag of less than 30 days is about 11% larger for the GCTI20 data. Männel et al. (2019) have analysed the connection between GNSS station heights and the ESMGFZ site displacements for HYDL in the Amazon basin, and they also report small phase lags in this region. This might serve as a confirmation, since we can assume that the hydrological loading is the main component of the total one here.

In this context, we observed an interesting pattern when plotting the fitted annual phases for the GCTI20 and ESMGFZ displacements against each other. For each GNSS station, the fitted phase for the ESMGFZ displacements is shown on the x-axes of Fig. 13, while the corresponding fitted phase for the GCTI20 displacements is shown on the y-axes. The majority of the respective plotted dots curls around the line of identity for both frames, CM (blue) and CF (red), confirming the similarity of fitted phases for GCTI20 and ESMGFZ. Beyond that, there is a systematic behaviour, e.g., for the East direction: if the phase of the ESMGFZ displacements for a particular GNSS station is between about 30 and 120 days (or between about 210 and 300 days), then the phase of the corresponding GCTI20 displacements is generally smaller. On the other hand, if this phase is between about 120 and 210 days (or

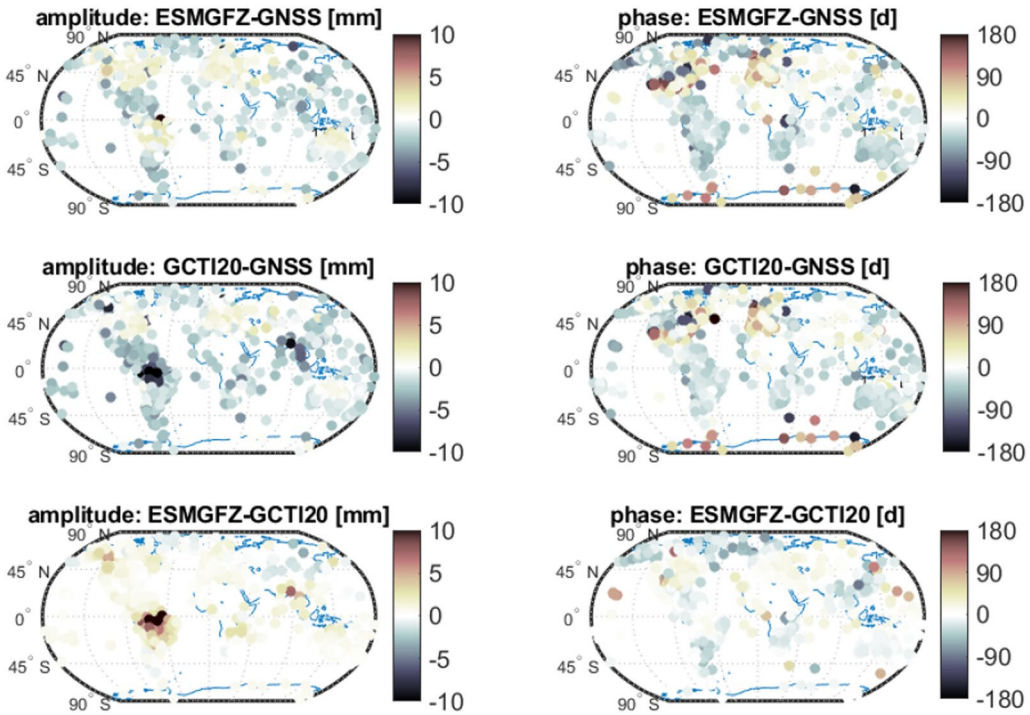

Fig. 12 Differences between the fitted annual amplitudes A_1 (left column) and annual phases ϕ_1 (right column) of Eq. (4) for the vertical displacements of the combined loading (NTAL + NTOL + HYDL [+ SLEL]) of ESMGFZ and GCTI20 in the CF-frame, and for the corresponding GNSS stations' height residuals. Top row: ESMGFZ minus GNSS, middle row: GCTI20 minus GNSS, bottom row: ESMGFZ minus GCTI20

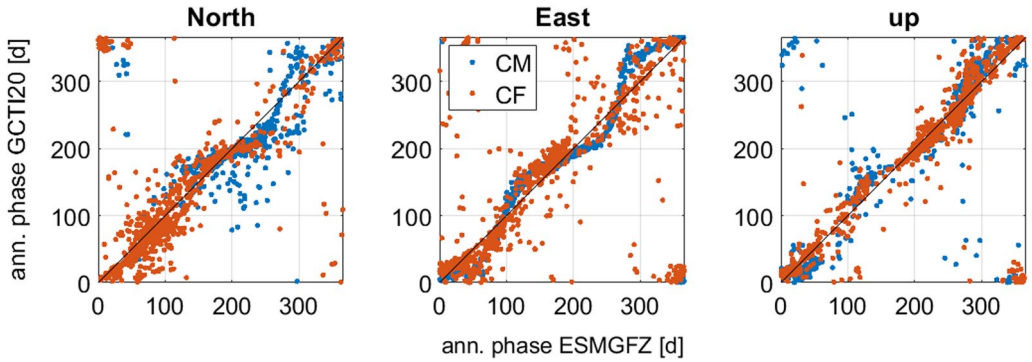

Fig. 13 Fitted annual (ann.) phases in days for the combined (NTAL + NTOL + HYDL + [SLEL]) site displacements of ESMGFZ (x-axes) versus those of GCTI20 (y-axes). Blue dots refer to the CM-frame displacements, and red dots represent the CF-frame displacements

between about 300 and 30 days), then the respective phase for GCTI20 is generally larger. The curve of dots looks sinusoidal, even though the pattern is less pronounced for the North and up directions. The reason for this property probably lies in the peculiarities of the distinct models used by the two providers and is beyond the scope of this paper.

To summarize, discrepancies between the GNSS height residuals and the NTL site displacements arise from both annual phase lags and differences in the annual amplitude. For both GCTI20 and ESMGFZ, one or the other effect is relevant in different regions of the Earth, in particular South America (amplitudes), Europe, and the USA (both: phase lags). In general, the fitted amplitudes for the site displacements of GCTI20 are slightly smaller, so the negative effect—in terms of RMS^{ESMGFZ} and RMS^{GCTI20} from Eq. (3)—of a phase lag w.r.t. the GNSS height residuals is less significant, too. The better statistical match for GCTI20 might be a result of this. However, based on these findings, we cannot conclude that one data set is significantly more accurate for the correction of NTL (in GNSS position time-series).

Assessment w.r.t. the DTRF computation

The main intention of this study is to evaluate the two chosen NTL data sets in terms of their applicability in DGFI-TUM's realization of the ITRS 2020. Besides, it should provide guidance for the decision process of picking any NTL data set for the realization of a secular reference frame. Having described and analysed the data of GCTI20 and ESMGFZ, we will now explain our final choice for the DTRF2020.

Application at the normal equation level

The application of NTAL and HYDL in our previous ITRS realization, DTRF2014, is explained by Seitz et al. (2021). For the DTRF2020, it will basically be the same. The original input data from the International VLBI Service for Geodesy and Astrometry (IVS; Nothnagel et al. 2017), the ILRS, the IGS, and the International DORIS Service (IDS; Willis et al. 2010) for the geodetic space techniques have not been corrected for NTL at the observation level. Hence, we can only correct the input data afterwards at the NEQ level of the weighted least-squares estimation process that we use for the DTRF. (For a detailed description and comparison of the application levels for any site displacements see Glomsda et al. 2021.) This is not an issue, as we are combining the geodetic observations at the NEQ level, anyway. Furthermore, we ensure consistency by applying the same model for all techniques.

To ease the explanation, we provide a few formulas. The DTRF2020 will be a secular reference frame, which means that we are estimating linear motions. For each station (reference point) i, these are represented by an offset vector $\boldsymbol{p}_i$ at some reference epoch t_0 and a constant velocity vector $\boldsymbol{v}_i$, which provide a station position $\boldsymbol{s}_i$ at epoch t by:

$$\boldsymbol{s}_i(t) \quad = \quad \boldsymbol{s}_i(t_0) \, + \, (t - t_0)\, \dot{\boldsymbol{s}}_i \quad =: \quad \boldsymbol{p}_i \, + \, (t - t_0)\, \boldsymbol{v}_i. \tag{5}$$

The correction vectors $\boldsymbol{\Delta p}_i$, $\boldsymbol{\Delta v}_i$ to some a priori vectors $\boldsymbol{p}_i^0$, $\boldsymbol{v}_i^0$ for all stations i are gathered in the vector $\boldsymbol{\Delta x}$ (containing also corrections to other geodetic and auxiliary parameters) and obtained by solving the normal equation system (Koch 1999)

$$(\boldsymbol{N} + \boldsymbol{N}_D)\; \boldsymbol{\Delta x} \quad = \quad \boldsymbol{y} + \boldsymbol{y}_D \quad = \quad \boldsymbol{y}, \tag{6}$$

with normal matrix $\boldsymbol{N}$, normal matrix of datum-conditions $\boldsymbol{N}_D$, and right-hand-side $\boldsymbol{y}$. The right-hand-side of datum-conditions $\boldsymbol{y}_D$ is equal to $\boldsymbol{0}$, since we are using minimum conditions. For the DTRF2020, the final normal matrix (right-hand-side) will contain the sum of many single normal matrices $\boldsymbol{N}_j$ (right-hand-sides $\boldsymbol{y}_j$)

which refer to individual VLBI, SLR, GNSS, and DORIS observation intervals j.

Correcting for NTL at the NEQ level means applying the corresponding (xyz-coordinate) site displacements

$$\boldsymbol{\delta}_j = (\delta_{j1_x}, \delta_{j1_y}, \delta_{j1_z}, \ldots, \delta_{jn_x}, \delta_{jn_y}, \delta_{jn_z}, 0, \ldots, 0) \tag{7}$$

for all stations $i = 1, \ldots, n$ in the following way:

$$\boldsymbol{y}_j^{NTL} = \boldsymbol{y}_j - \boldsymbol{N}_j \boldsymbol{\delta}_j. \tag{8}$$

Hence, the right-hand-side for each observation interval j is reduced by the product of the interval's normal matrix and the vector of site displacements for this interval. $\boldsymbol{\delta}_j$ contains three non-zero values for each station, i.e., one site displacement for each coordinate of their instantaneous positions, which must be a single representative value of the displacements given for the respective observation interval. For VLBI, SLR, GNSS, and DORIS, the relevant observation intervals are (mostly) 24 hours, 1 week or 15 days, 1 day, and 1 week, respectively, and for the DTRF2020 we will apply average values of the corresponding site displacements. The original resolution of the NTL data by GCTI20 is 1 hour, of those by ESMGFZ it is 3 hours (NTAL, NTOL) or 1 day (HYDL, SLEL). As a consequence, both sets can provide at least one value for each technique's observation intervals, and no bridging of gaps is necessary in either case.

Centre of mass vs. centre of figure

The choice of (NTL) site displacements in the CM- or the CF-frame depends on the scope of application. If station positions are given in a CF-frame, and NTL is corrected at the solution level, the site displacements must be taken from the CF-frame as well. If NTL is corrected at the observation level or the NEQ level in VLBI analysis, the frame is irrelevant. This is because the site displacements at the two stations forming a baseline are subtracted from each other, and the geocentre motion is cancelled from the CM-frame displacements, leaving the same difference as for the CF-frame displacements (e.g., Eriksson and MacMillan 2014; Glomsda et al. 2021). Regarding GNSS, Männel et al. (2019) use CF-frame displacements for precise point positioning (PPP) solutions with fixed orbits, and CM-frame displacements for network solutions where the orbits are estimated.

CM is the dynamical origin of satellite orbits, hence the satellite techniques SLR, GNSS, and DORIS are basically able to realize this geocentre. The dedicated SLR satellites are spherical and best suited for determining CM: their cross-section is not attitude dependent, and so they are less affected by non-gravitational forces. The non-spherical GNSS and DORIS satellites, on the other hand, are more sensitive to their actual cross-sections and the non-gravitational forces. Due to aliasing effects, the latter distort the geocentre estimates of GNSS and DORIS solutions (e.g., Bloßfeld et al. 2016). For this reason, Helmert parameters are introduced to restore the degrees of freedom w.r.t. the origin for GNSS and DORIS. When applying NTL in a secular reference frame, the choice of CM- or CF-frame displacements is thus irrelevant for GNSS, DORIS, and VLBI (compare above). For SLR, however, the CM-frame displacements are the only option. Furthermore, CM is the origin of the ITRS, and it is just realized by assuming zero translation w.r.t. the origin of an SLR solution in the ITRS realizations of both IGN (Altamimi et al. 2016) and DGFI-TUM (Angermann et al. 2004; Seitz et al. 2021). As a consequence, and for consistency, we will use CM-frame displacements for all four techniques in the computation of the DTRF2020. Both GCTI20 and ESMGFZ provide these displacements, so either choice of data set is still possible.

Model uncertainties

From the comparison of the NTL data sets, we learned that the agreement of (in particular) the atmospheric and (to a certain extent) the oceanic components is quite good. However, there are significant discrepancies for the hydrological component, and the total NTL displacements do not perfectly match the GNSS position residuals for neither of the two sets. Hence, we must accept for the time being that there is a model uncertainty with respect to the application of NTL effects, especially since there are many other geophysical models and providers of NTL data. A measure of this uncertainty could be the RMS values of the differences between the corresponding site displacements as given in Figs. 3 and 4. Keeping this in mind for the computation of the DTRF2020, we are convinced that the correction for NTL with either of our two data sets will still be beneficial.

Trends in the displacement series

While the NTL data of GCTI20 and ESMGFZ have been deemed to be equivalent for the application in a secular reference frame up to here, we will now explain the reason to favour one over the other.

The modification of the right-hand-sides when applying NTL at the NEQ level, Eq. (8), is derived from the following approximation of the vector $\boldsymbol{f}_j^{NTL}$ of theoretical geodetic observations including the effect of NTL (Glomsda et al. 2021):

$$\boldsymbol{f}_j^{NTL} \approx \boldsymbol{f}_j + \boldsymbol{A}_j \boldsymbol{\delta}_j. \quad (9)$$

$\boldsymbol{f}_j$ is the vector of theoretical observations in interval j without considering NTL, and $\boldsymbol{A}_j$ is the matrix of partial derivatives of the functional model f w.r.t. the estimated parameters in $\boldsymbol{\Delta x}$. The site displacements in $\boldsymbol{\delta}_j$ are hence implicitly added to the a priori station positions in interval j, and the corresponding impact of NTL on the theoretical observations in $\boldsymbol{f}_j$ is approximated by the product $\boldsymbol{A}_j \boldsymbol{\delta}_j$. In a secular reference frame, the instantaneous station positions from the observation intervals j are turned into long-term linear motions as given in Eq. (5). The application of $\boldsymbol{\delta}_j$ to the a priori values according to Eqs. (8) and (9) changes the instantaneous position estimates. In particular, offsets and drifts in the time-series of site displacements are transferred to the instantaneous positions and will ultimately affect the estimated station offsets $\boldsymbol{p}_i$ and velocities $\boldsymbol{v}_i$.

Trends in the displacement series are either geophysically driven or artefacts which can be attributed to (updates in) the background models. As long as these trends are stable over the entire observation period of each station, both cases can be handled well when computing secular reference frames: the individual offsets and drifts are removed from each displacement time-series, and the correction for NTL is performed with the detrended series. If the trends are real geophysical phenomena confirmed by the geodetic observations, the reduced offsets and drifts will be reflected in the estimated station positions and velocities of the secular frame. Thus, all linear motions are finally contained in the latter and not hidden in the NTL corrections. If the trends are artefacts only, which are not supported by the observations of the geodetic techniques, their reduction from the NTL time-series probably results in unaffected estimated positions and velocities, however.

In contrast, if the trend in a displacement series is not constant over time but changes repeatedly during the observation period of the respective station, the single estimated position and velocity of that station will be significantly distorted. To cope with this situation, there are, in our view, two possibilities. First, one could introduce new station position and velocity parameters whenever the trend in the displacement series changes significantly. This option would contradict the nature of a secular reference frame but facilitates both cases, geophysical and artefact trends, if the corresponding offsets and drifts are again removed from the displacement series between each two discontinuities. The alternative, assuming that trend changes are geophysically caused, is to apply the original displacement series (including all trend changes over the entire observation period of a station) as a correction. However, the estimated station positions and velocities would then only reflect one part of the linear movement, namely the joint long-term one, while all trend variations are included in the NTL corrections. This means that a user would have to re-add the site displacements to the station coordinates to get the actual station motion.

Revisiting the available NTL data in this respect, the current ESMGFZ data are not suitable for the application in DTRF2020. As we have seen in our analyses, their displacement time-series contain various changes in offset and drift over the period from 1976 to 2021 (in particular) in the CM-framework. If these were driven by actual geophysical effects, we would have to decide between introducing station position discontinuities or leaving the trends in the NTL corrections. However, these changes simply are the result of transitions between the various underlying atmospheric forcing models. Hence, applying the original ESMGFZ displacements as a whole is not an option, since this would distort the estimated station positions and velocities. On the other hand, the introduction of additional position and velocity parameters per station for such non-geophysical effects seems to be unjustified and possibly harmful in the context of a secular reference frame.

GCTI20, on the contrary, was processed from consistent underlying models between 1980 and 2021. The corresponding time-series of site displacements do not show any significant intermediate changes in their trends, suggesting that there are not even geophysically induced ones. It follows that single offsets and drifts can be removed from the displacement series which are—after the application of the detrended NTL corrections—properly reflected in the estimated long-term linear motion of each station in the DTRF2020. The purpose of a secular TRF thus has been satisfactorily realized.

Geocentre motion

The behaviour of the geocentre motion contributions shown in Fig. 9 is intrinsically tied to that of the individual displacement time-series. For basically the same reason as given in the previous subsection, the GCTI20 data also has to be preferred over the ESMGFZ data when considering the realization of the DTRF2020 origin with NTL: there are changes in the trend of the geocentre motion contribution for ESMGFZ that are neither geophysically justified nor compatible with the contribution as inferred from the ILRS solution. Instead, they are introduced by the transitions in the underlying atmospheric forcing models and would likely distort the geocentre motion estimated in the DTRF2020. In contrast to that, the trends in geocentre motion as implied by the GCTI20 data are quite stable over the complete time interval (compare Table 2).

Processing of NTL corrections

Following the above assessment, we will apply the CM-frame site displacements of GCTI20 in the DTRF2020. The displacements will be handled in the following way: for each station, the time-series for each NTL component is cut down to the corresponding observation interval. Each such truncated series is detrended, and the respective offsets and drifts are stored for the final DTRF2020 release. The residual time-series are used to compute 15-daily, weekly, or daily averages for each NTL component, which will be part of the release as well. Finally, the sum of all components' averages is computed for each relevant observation interval, and each corresponding input normal equation is corrected for NTL by this sum. As a consequence, the trends in the original displacement series will be reflected by the estimated station positions and velocities of the DTRF2020. After all, this is the ultimate purpose of a secular reference frame: the total linear station motions have to be represented by the (estimated) station velocities.

Since the GCTI20 data will be prolongated every few months, the station positions of DTRF2020 can be extrapolated to future epochs with the aforementioned approach on a regular basis. Together with the separation of trends and the inclusion of NTOL, this is the main difference compared to the preceding DTRF2014 (w.r.t. NTL).

Conclusions

We have compared two non-tidal loading (NTL) data sets: that of the Global Geophysical Fluid Center (GGFC) directly devoted to the ITRS realization 2020 (GCTI20), and the operational one of the Earth System Modelling group of the Deutsches GeoForschungsZentrum (ESMGFZ). With both sets, it is possible to obtain site displacements due to non-tidal atmospheric, oceanic, and hydrological loading for all relevant VLBI, SLR, GNSS, and DORIS stations. Although the data are split into different components, both sets are mass conserving if the sum of all components is considered. The main discrepancy between the data stems from the underlying hydrological models, but it was not our intention to identify the best data in terms of geophysical modelling in this study.

Instead, we analysed which data set is the better choice for usage in DGFI-TUM's upcoming ITRS realization, the DTRF2020. Like the DTRF2014, the new realization will be a secular reference frame, which consists of linear station motions represented by offsets at a specific reference epoch and a constant velocity. Again, we will correct for NTL at the normal equation level (this time including the non-tidal oceanic loading), which is the same level that we use for the combination of the different geodetic space observations.

While we could not distinguish the applicability of the GCTI20 and ESMGFZ data in terms of resolution or the replicability of instantaneous station positions, we finally decided to use the GCTI20 data because of its lack of non-geophysical structure in the corresponding displacement time-series and geocentre motion. For GCTI20, the series generally contain a single trend only, whereas many displacement series and the geocentre motion for ESMGFZ reveal time-dependent offsets and drifts. The latter would distort the estimated station positions and velocities, as well as the realization of the origin of the DTRF2020, as these changes in trends do not reflect real geophysical phenomena, but are induced by updates in the underlying atmospheric forcing models. The resulting time-series of site displacements contain transition periods which cannot be brought into agreement with a secular reference frame. However, this does not impair the appropriateness of the operational ESMGFZ data for other applications.

If, in future ITRS realizations, geophysically caused trend changes are present in the (then) available NTL displacement time-series, the fundamental question of whether discontinuities should be introduced or whether the trend changes should remain in the NTL corrections must be discussed.

Acknowledgements

The authors would like to thank Robert Dill and Henryk Dobslaw at the Deutsches GeoForschungsZentrum for very fruitful discussions on their non-tidal loading data. We also thank Jean-Paul Boy and all other involved colleagues at the Global Geophysical Fluid Center and the Deutsches GeoForschungsZentrum for providing their data and hence enabling this research in the first place. Furthermore, we thank the editor and the two anonymous reviewers for their valuable feedback, which helped to significantly improve our manuscript.

Author contributions

MG, MB, MS, and DA conceptualized the study during the preparation of the DTRF2020. All authors are involved in the corresponding discussions on DTRF procedures and results under the lead of MS. MG prepared the GCTI20 data for analysis, while MB prepared the data by ESMGFZ and the final processing of both data sets for the DTRF2020. MB also computed the geocentre motion contribution of the SLR solution. MS provided the GNSS position residuals. MG performed most of the analyses, with modified scripts originally created by the other authors. FS coordinated the research at DGFI-TUM and provided the basic resources, making the study possible. MG compiled the figures and wrote the manuscript with input by MS, MB, DA, and FS. All authors read and approved the final manuscript.

Funding

Open Access funding enabled and organized by Projekt DEAL.

Availability of data and materials

The GGFC contribution to the ITRS 2020 realization is available at http://loading.u-strasbg.fr/ITRF2020/. The operational non-tidal loading data of ESMGFZ can be obtained from http://esmdata.gfz-potsdam.de:8080/. As soon as the DTRF2020 is generated, the corresponding non-tidal loading data, i.e., offsets, drifts, and residual average site displacements, will be published by DGFI-TUM together with the other components of their ITRS 2020 realization. Any remaining data sets used and/or analysed during the current study are only available from the corresponding author on reasonable request.

Declarations

Competing interests

The authors declare that they have no competing interests.

Received: 21 December 2021 Accepted: 20 April 2022
Published online: 06 June 2022

References

Abbondanza C, Chin TM, Gross RS, Heflin MB, Parker JW, Soja BS, van Dam T, Wu X (2017) JTRF2014, the JPL Kalman filter and smoother realization of the International Terrestrial Reference System. J Geophys Res Solid Earth 122(10):8474–8510. https://doi.org/10.1002/2017JB014360

Altamimi Z, Rebischung P, Metivier L, Collilieux X (2016) ITRF2014: a new release of the International Terrestrial Reference Frame modeling nonlinear station motions. J Geophys Res Solid Earth 121(8):6109–6131. https://doi.org/10.1002/2016JB013098

Angermann D, Drewes H, Krügel M, Meisel B, Gerstl M, Kelm R, Müller H, Seemüller W, Tesmer V (2004) ITRS combination center at DGFI: a Terrestrial Reference Frame Realization 2003, Deutsche Geodätische Kommission, Reihe B, Nr. 313, pp. 1-141. ISBN 3-7696-8593-8

Berrisford P, Dee D, Poli P, Brugge R et al (2011) The ERA-Interim archive Version 2.0. Reading 1:23

Blewitt G (2003) Self-consistency in reference frames, geocenter definition, and surface loading of the solid Earth. J Geophys Res 108(B2):2103. https://doi.org/10.1029/2002JB002082

Bloßfeld M, Seitz M, Angermann D, Moreaux G (2016) Quality assessment of IDS contribution to ITRF2014 performed by DGFI-TUM. Adv Space Res 58(12):2505–2519. https://doi.org/10.1016/j.asr.2015.12.016

Boy J-P (2021) GGFC contribution to the ITRS 2020 realization. http://loading.u-strasbg.fr/ITRF2020/ggfc.pdf. Accessed 16 December 2021.

Carrère L, Lyard F (2003) Modeling the barotropic response of the global ocean to atmospheric wind and pressure forcing - comparisons with observations. Geophys Res Lett 30:1275. https://doi.org/10.1029/2002GL016473

Collilieux X, Altamimi Z, Ray J, van Dam T, Wu X (2009) Effect of the satellite laser ranging network distribution on geocenter motion estimation. J Geophys Res 114:B04402. https://doi.org/10.1029/2008JB005727

Darwin GH (1882) On variations in the vertical due to elasticity of the Earth's surface. Science 14(90):409–427. https://doi.org/10.1080/14786448208628439

Deutsches GeoForschungsZentrum (2021) ESMGFZ Product Repository. http://esmdata.gfz-potsdam.de:8080/. Accessed 16 December 2021.

Dill R (2008) Hydrological model LSDM for operational Earth rotation and gravity field variations, Scientific Technical Report, p. 35, STR08/09, GFZ Potsdam, Germany. https://doi.org/10.2312/GFZ.b103-08095

Dill R, Dobslaw H (2013) Numerical simulations of global-scale high-resolution hydrological crustal deformations. J Geophys Res Solid Earth 118(9):5008–5017. https://doi.org/10.1002/jgrb.50353

Dill R, Klemann V, Dobslaw H (2018) Relocation of river storage from global hydrological models to georeferenced river channels for improved load-induced surface displacements. J Geophys Res 123(8):7151–7164. https://doi.org/10.1029/2018JB016141

Dobslaw H (2016) Homogenizing surface pressure time-series from operational numerical weather prediction models for geodetic applications. J Geod Sci 6:61–68. https://doi.org/10.1515/jogs-2016-0004

Dobslaw H, Dill R (2018) Predicting Earth orientation changes from global forecasts of atmosphere-hydrosphere dynamics. Adv Space Res 61(4):1047–1057. https://doi.org/10.1016/j.asr.2017.11.044

Dong D, Yunck T, Heflin M (2003) Origin of the International Terrestrial Reference Frame. J Geophys Res 108(B4):2200. https://doi.org/10.1029/2002JB002035

Eriksson D, MacMillan DS (2014) Continental hydrology loading observed by VLBI measurements. J Geod 88:675–690. https://doi.org/10.1007/s00190-014-0713-0

Farrell WE (1972) Deformation of the Earth by Surface Loads. Rev Geophys Space Phys 10(3):761–797. https://doi.org/10.1029/RG010i003p00761

Glomsda M, Bloßfeld M, Seitz M, Seitz F (2020) Benefits of non-tidal loading applied at distinct levels in VLBI analysis, J Geod. https://doi.org/10.1007/s00190-020-01418-z

Glomsda M, Bloßfeld M, Seitz M, Seitz F (2021) Correcting for site displacements at different levels of the Gauss-Markov model - a case study for geodetic VLBI. Adv Space Res 68(4):1645–1662. https://doi.org/10.1016/j.asr.2021.04.006

Gobron K, Rebischung P, Van Camp M, Demoulin A, de Viron O (2021) Influence of aperiodic non-tidal atmospheric and oceanic loading deformations on the stochastic properties of global GNSS vertical land motion time series. J Geo Res Solid Earth. https://doi.org/10.1029/2021JB022370

Hersbach H, de Rosnay P, Bell B, et al (2018) Operational global reanalysis: progress, future directions and synergies with NWP. ECMWF. https://doi.org/10.21957/tkic6g3wm

Hersbach H, Bell B et al (2020) The ERA5 global reanalysis. Q J R Meteorol Soc 146:1999–2049. https://doi.org/10.1002/qj.3803

Johnston G, Riddell A, Hausler G (2017) The International GNSS Service, In: Teunissen, Peter J.G. and Montenbruck O. (Eds.), Springer Handbook of Global Navigation Satellite Systems, 1st ed., pp. 967-982. https://doi.org/10.1007/978-3-319-42928-1

Jungclaus J, Fischer N, Haak H et al (2013) Characteristics of the ocean simulations in the Max Planck Institute Ocean Model (MPIOM) the ocean component of the MPI-Earth system model. J Adv Model Earth Syst 5:422–446. https://doi.org/10.1002/jame.20023

Kållberg P, Simmons A, Uppala S, Fuentes M (2004) The ERA-40 archive, Shinfield Park. Reading. https://www.ecmwf.int/node/10595. Accessed Oct 2007.

Koch K-R (1999) Parameter estimation and hypothesis testing in linear models, 2 edn, Springer-Verlag Berlin Heidelberg, original German edition published by Dümmlers, Bonn. ISBN: 978-3-642-08461-4

Männel B, Dobslaw H, Dill R, Glaser S, Balidakis K, Thomas M, Schuh H (2019) Correcting surface loading at the observation level: impact on global GNSS and VLBI station networks. J Geod 93(10):2003–2017. https://doi.org/10.1007/s00190-019-01298-y

Mémin A, Boy J-P, Santamaria-Gómez A (2020) Correcting GPS measurements for non-tidal loading. GPS Solut 24:45. https://doi.org/10.1007/s10291-020-0959-3

Nothnagel A, Artz T, Behrend D, Malkin Z (2017) International VLBI Service for Geodesy and Astrometry - Delivering high-quality products and embarking on observations of the next generation. J Geod 91(7):711–721. https://doi.org/10.1007/s00190-016-0950-5

Nothnagel A, Holst C, Haas R (2019) A VLBI delay model for gravitational deformations of the Onsala 20m radio telescope and the impact on its global coordinates. J Geod 93:2019–2036. https://doi.org/10.1007/s00190-019-01299-x

Pavlis E, Luceri V, Basoni A, Sarrocco D, Kuzmicz-Cieslak M, Evans K, Bianco G (2021) ITRF2020: The International Laser Ranging Service (ILRS) Contribution, presented at AGU Fall Meeting, December 13-17, 2021. https://doi.org/10.1002/essoar.10509208.1

Pearlman MR, Noll CE, Pavlis EC et al (2019) The ILRS: approaching 20 years and planning for the future. J Geod 93(11):2161–2180. https://doi.org/10.1007/s00190-019-01241-1

Petit G, Luzum B (eds.) (2010) IERS Conventions (V.1.3.0), IERS Technical Note 36, Verlag des Bundesamts für Kartographie und Geodäsie, Frankfurt am Main. ISBN 3-89888-989-6

Petrov L, Boy J-P (2004) Study of the atmospheric pressure loading signal in very long baseline interferometry observations. J Geophys Res 109(B3):B03405. https://doi.org/10.1029/2003JB002500

Riddell AR, King MA, Watson CS, Sun Y, Riva REM, Rietbroek R (2017) Uncertainty in geocenter estimates in the context of ITRF2014. J Geophys Res Solid Earth 122:4020–4032. https://doi.org/10.1002/2016JB013698

Rodell M, Famiglietti JS, Wiese DN et al (2018) Emerging trends in global freshwater availability. Nature 557:651–659. https://doi.org/10.1038/s41586-018-0123-1

Roggenbuck O, Thaller D, Engelhardt G, Franke S, Dach R, Steigenberger P (2015) Loading-induced deformation due to atmosphere, ocean and hydrology: model comparisons and the impact on global SLR, VLBI and GNSS Solutions, T. van Dam (eds), REFAG 2014, International Association of Geodesy Symposia, Vol. 146, pp. 71-77, Springer International Publishing Switzerland. ISBN: 978-3-319-45628-7

Schuh H, Estermann G, Crétaux JF, Bergé-Nguyen M, van Dam T (2003) Investigation of hydrological and atmospheric loading by space geodetic techniques. In: Hwang C., Shum C.K., Li J. (eds), Satellite altimetry for geodesy, geophysics and oceanography, International Association of Geodesy Symposia, Vol. 126, pp. 123-132, Berlin: Springer. https://doi.org/10.1007/978-3-642-18861-9_15

Seitz M, Bloßfeld M, Angermann D, Seitz F (2021) DTRF2014: DGFI-TUM's ITRS realization 2014. Adv Space Res. https://doi.org/10.1016/j.asr.2021.12.037

Tregoning P, van Dam T (2005) Atmospheric pressure loading corrections applied to GPS data at the observation level. Geophys Res Lett. https://doi.org/10.1029/2005GL024104

van Dam TM, Wahr J (1987) Displacements of the Earth's surface due to atmospheric loading: effects on gravity and baseline measurements. J Geophys Res 92:1281–1286. https://doi.org/10.1029/JB092iB02p01281

Williams SDP, Penna NT (2011) Non-tidal ocean loading effects on geodetic GPS heights. Geophys Res Lett 38:L09314. https://doi.org/10.1029/2011GL046940

Willis P, Fagard H, Ferrage P, Lemoine FG, Noll CE, Noomen R, Otten M, Ries JC, Rothacher M, Soudarin L, Tavernier G, Valette J-J (2010) The International DORIS Service (IDS): toward maturity. Adv Space Res 45(12):1408–1420. https://doi.org/10.1016/j.asr.2009.11.018

Wu X, Kusche J, Landerer FW (2017) A new unified approach to determine geocentre motion using space geodetic and GRACE gravity data. Geophys J Int 209:1398–1402. https://doi.org/10.1093/gji/ggx086

Wunsch C, Stammer D (1997) Atmospheric loading and the oceanic "inverted barometer" effect. Rev Geophys 35(1):79–107. https://doi.org/10.1029/96RG03037

Zhang J, Bock Y, Johnson H, Fang P, Genrich JF, Williams S, Wdowinski S, Behr J (1997) Southern California permanent GPS geodetic array: error analysis of daily position estimates and site velocities. J Geophys Res 102(B8):18035–18055. https://doi.org/10.1029/97JB01380

Publisher's Note

P-2 Glomsda M., Bloßfeld M., Seitz M., and Seitz F. (2021): **Correcting for site displacements at different levels of the Gauss-Markov model - a case study for geodetic VLBI**, *Advances in Space Research*, Vol. 68 (4), pp. 1645-1662, doi:10.1016/j.asr.2021.04.006

Abstract In a previous article, Glomsda et al. (2020) revisited the impact of distinct parts of non-tidal loading in the analysis of geodetic Very Long Baseline Interferometry (VLBI). The loading is represented by displacements of the reference positions of the observing VLBI antennas, which are variables of a corresponding Gauss-Markov model for estimating various geodetic target parameters. These displacements were applied at two different levels of the model, the observation and the normal equation level, and quite similar results were obtained for both cases. In this article, the authors provide a more detailed theoretical discussion of the application of site displacements at the distinct levels, which also comprises the a posteriori application at the solution level. For each case, the respective formulas and implications for the Gauss-Markov model are derived, and equations for assessing the differences between the estimated parameters are established. In this way, the authors aim to create a deeper understanding of the results of the previous article, which show the capability of the normal equation level to approximate the application of site displacements at the observation level with less effort and prerequisites, and to provide evidence for the claims made in that article (for VLBI only): (i) the chosen reference frame of the site displacements is basically irrelevant except for the solution level; (ii) the Jacobi matrix does not change substantially; (iii) the loss of temporal resolution of the site displacements is more important than the linear approximation of the functional model at the normal equation level; and (iv) the station coordinate estimates for all three levels strongly depend on the regularizing (datum-) conditions of the model. The theoretical results are substantiated with numerical examples, which consider site displacements generated from non-tidal atmospheric loading by the Earth-System-Modelling group of the Deutsches GeoForschungsZentrum (GFZ). However, the results are valid for site displacements of any source.

Author contributions Matthias Glomsda conceptualized the study as a follow-up of the initial non-tidal loading study. He prepared the data, performed most of the analyses, compiled all figures and wrote the majority of the manuscript. Mathis Bloßfeld and Manuela Seitz helped with the discussion and interpretation of the results. Florian Seitz supervised the study and provides the basic resources. All authors read and improved the manuscript. The overall contribution of Matthias Glomsda is estimated to be 92%.

P-3 Glomsda M., Bloßfeld M., Seitz M., and Seitz F. (2020): **Benefits of non-tidal loading applied at distinct levels in VLBI analysis**, *Journal of Geodesy*, Vol. 94 (90), doi:10.1007/s00190-020-01418-z

Abstract In the analysis of very long baseline interferometry (VLBI) observations, many geophysical models are used for correcting the theoretical signal delay. In addition to the conventional models described by Petit and Luzum [2010], we are applying different parts of non-tidal site loading, namely the atmospheric, oceanic, and hydrological ones. To investigate their individual contributions, these parts are considered both separately and combined to a total loading. The application of the corresponding site displacements is performed at two distinct levels of the geodetic parameter estimation process (observation and normal equation level), which turn out to give very similar results in many cases. To validate our findings internally, the site displacements are provided by two different data centres: the Earth-System-Modelling group at the Deutsches GeoForschungsZentrum in Potsdam (ESMGFZ, see Dill and Dobslaw, 2013) and the International Mass Loading Service (IMLS, see Petrov, 2015). We show that considering non-tidal loading is actually useful for mitigating systematic effects in the VLBI results, like annual signals in the station height time series. If the sum of all non-tidal loading parts is considered, the WRMS of the station heights and baseline lengths is reduced in 80–90% of all cases, and the relative improvement is about −3.5% on average. The main differences between our chosen providers originate from hydrological loading.

Author contributions Matthias Glomsda and Mathis Bloßfeld conceptualized the study. Matthias Glomsda prepared the non-tidal loading data and modified the VLBI analysis software (DOGS-RI) to incorporate the latter. He performed most of the investigations, compiled all figures and wrote the majority of the manuscript. Mathis Bloßfeld prepared the interfaces with the post-processing software (DOGS-CS) and discussed the results. Manuela Seitz helped to improve the theoretical derivations and discussed the results. Florian Seitz supervised the study and provides the basic resources. All authors read and improved the manuscript. The overall contribution of Matthias Glomsda is estimated to be 80%.

Journal of Geodesy (2020) 94:90
https://doi.org/10.1007/s00190-020-01418-z

ORIGINAL ARTICLE

Benefits of non-tidal loading applied at distinct levels in VLBI analysis

Matthias Glomsda[1] · Mathis Bloßfeld[1] · Manuela Seitz[1] · Florian Seitz[1]

Received: 19 February 2020 / Accepted: 6 August 2020 / Published online: 31 August 2020

Abstract
In the analysis of very long baseline interferometry (VLBI) observations, many geophysical models are used for correcting the theoretical signal delay. In addition to the conventional models described by Petit and Luzum (eds) (IERS Conventions, 2010), we are applying different parts of non-tidal site loading, namely the atmospheric, oceanic, and hydrological ones. To investigate their individual contributions, these parts are considered both separately and combined to a total loading. The application of the corresponding site displacements is performed at two distinct levels of the geodetic parameter estimation process (observation and normal equation level), which turn out to give very similar results in many cases. To validate our findings internally, the site displacements are provided by two different data centres: the Earth-System-Modelling group at the Deutsches GeoForschungsZentrum in Potsdam (ESMGFZ, see Dill and Dobslaw, J Geophys Res Solid Earth, 2013. https://doi.org/10.1002/jgrb.50353)] and the International Mass Loading Service [IMLS, see Petrov (The international mass loading service, 2015)]. We show that considering non-tidal loading is actually useful for mitigating systematic effects in the VLBI results, like annual signals in the station height time series. If the sum of all non-tidal loading parts is considered, the WRMS of the station heights and baseline lengths is reduced in 80–90% of all cases, and the relative improvement is about − 3.5% on average. The main differences between our chosen providers originate from hydrological loading.

Keywords VLBI · Non-tidal loading · Normal equation level · ESMGFZ · IMLS

1 Introduction

Due to various geophysical processes, the positions of reference points fixed to the Earth's crust change over time. When estimating the long-term linear motion of these points in the context of terrestrial reference frames (TRF), the instantaneous positions are regularized by subtracting a number of short-term periodic displacements. The conventional displacements are summarized in chapter 7.1 of the International Earth Rotation and Reference Systems Service (IERS) Conventions of 2010 (Petit and Luzum 2010) and include tidal effects at mainly diurnal and semi-diurnal periods.

Displacements by non-tidal loading, however, are usually not applied. The latter is induced by rather local and irregular changes in atmospheric pressure and the mass redistribution of ocean or land water (hydrology). According to Petit and Luzum (2010), the modelling of non-tidal loading is less accurate, and the impact on the geodetic parameters is less significant than for the conventional displacements. In recent years, however, the number of providers for site displacements computed from non-tidal loading has increased (compare, for example, the Global Geophysical Fluid Center (GGFC)), and the quality of the underlying (numerical) models has improved (see, for example, Dill and Dobslaw 2013; Gelaro et al. 2017). In recognition of this progress, the DTRF2014 was the first TRF to include non-tidal loading (compare Seitz et al. 2016, 2020), and the official contributions to the International VLBI Service for Geodesy and Astrometry (IVS[1]) must be computed with corrections for non-tidal atmospheric loading. Nevertheless, a general acceptance is not yet achieved.

Atmospheric loading effects have been investigated first by numerous authors (Rabbel and Zschau 1985; van Dam and Wahr 1987; van Dam and Herring 1994; Sun et al. 1995; MacMillan and Gipson 1994; Petrov and Boy 2004; Tregoning and van Dam 2005b; Böhm et al. 2009; Dach et al. 2010, for example), mostly by using VLBI or the Global Navigation Satellite System (GNSS). Afterwards, non-tidal loading

Matthias Glomsda
matthias.glomsda@tum.de

[1] Deutsches Geodätisches Forschungsinstitut der Technischen Universität München (DGFI-TUM), Arcisstr. 21, 80333 Munich, Germany

[1] https://ivscc.gsfc.nasa.gov/about/index.html.

generated from the redistribution of water has also been analysed. Eriksson and MacMillan (2014), for example, include hydrological loading next to the atmospheric one in VLBI analysis and find that the application of the corresponding site displacements leads to a significant improvement in the repeatability of vertical station coordinates. Similar results were found by van Dam et al. (2001) or Tregoning et al. (2009) for the Global Positioning System (GPS). Two of the few studies focusing on the application of non-tidal loading created from the redistribution of ocean water are those of Williams and Penna (2011) and van Dam et al. (2012), who observe a corresponding reduction in the scatter of many GPS station height time series. It should be noted that site displacements are also induced by processes not driven by surface loading, like the thermal expansion of antennas or bedrock, for example. While VLBI at least takes care of the former, we will not particularly focus on such effects in this study.

The joint application of the non-tidal loading parts (atmospheric, oceanic, hydrological) in VLBI analysis has been investigated by Schuh et al. (2003), for example. The authors use different combinations of numerical models for the associated site displacements, but although they find several improvements in station height and baseline repeatabilities, no best combination could be identified. MacMillan and Boy (2004), on the other hand, fix specific models for the site displacements and process VLBI experiments with different combinations of the non-tidal loading parts. Both studies, however, do not apply all parts separately. This is finally done by Roggenbuck et al. (2015), who use site displacements provided by the Goddard Space Flight Center (GSFC[2]) of the National Aeronautics and Space Administration (NASA) and examine the impact on global solutions for Satellite Laser Ranging (SLR), VLBI, and GNSS.

In this paper, we extend the existing research by exploring the application of non-tidal loading at different levels in the parameter estimation process. The straightforward approach of correcting for site displacements at the observation level (OBS) is basically followed by all aforementioned authors. This way, the original (sub-daily) temporal resolution of the site displacements can be exploited. An alternative is the application at normal equation level (NEQ), which is described by Seitz et al. (2020). Session-wise (e.g. average) displacements are computed, which lead to a loss of temporal resolution, but can be used to directly modify the normal equation without any need to recover the observation equation. By examining both levels, we want to determine whether the approximation of OBS by NEQ is a reasonable approach. By restricting ourselves to VLBI, we can cover the impact on a broad range of parameter types (including tropospheric and clock parameters, which are often neglected). By distinguishing all three parts of non-tidal loading (next to their combination), we identify their individual properties and contributions to the results at both levels. And finally, by using two different data sets for the site displacements, we can internally validate our findings and detect discrepancies. All these items also distinguish our work from the most recent study by Männel et al. (2019), who make use of one of the same data sets, but consider the joint application of all non-tidal loading parts at the observation level with respect to VLBI and GNSS.

We do not analyse the application at solution level, which was done by Böhm et al. (2009), for example, although we briefly compare this approach to OBS and NEQ.

As we are producing session-wise VLBI solutions and no long-term TRF, non-elastic loading effects will only be visible in the time series of the estimated station positions. However, we are particularly interested in the impact of elastic non-tidal loading, and other displacing effects are subject to future research.

The paper is organized as follows: in Sect. 2, we describe the used non-tidal loading parts, the data providers, and the properties of the corresponding displacement time series. Section 3 contains the derivation of the individual application levels. In Sect. 4, we provide the results of processing VLBI observations with various combinations of non-tidal loading parts, data providers, and application levels. Section 5 completes the paper with conclusions and an outlook on future research.

2 Non-tidal loading

2.1 Computation of site displacements

We are considering three parts of non-tidal loading:

1. non-tidal atmospheric loading (ATM),
2. non-tidal oceanic loading (OCE), and
3. hydrological loading (HYD).

In all three cases, variations in the distribution of particular masses, basically air and water, lead to deformations of the Earth's crust and hence to changes in the position of reference points which are fixed to the latter. In the case of ATM, atmospheric circulation moves air masses around the Earth, and the resulting variation of atmospheric pressure deforms the crust (Darwin 1882; Petrov and Boy 2004). With OCE, the deformations are caused by ocean bottom pressure, which is mainly influenced by three effects: ocean water redistribution by atmospheric circulation, in- and outflow of ocean water, and changes in the total atmospheric mass over the oceans (van Dam et al. 2012). Due to the connection with atmospheric pressure, it is important to note the common inverted

[2] https://www.nasa.gov/goddard.

barometer hypothesis (IBH, compare van Dam and Wahr 1987). The IBH assumes that an increase in atmospheric pressure over an ocean site is compensated by an equivalent decrease in sea level at this very position and hence a decrease in ocean bottom pressure of equal size. This hypothesis is supposed to be adequate only "for periods longer than 5–20 days" (Petrov and Boy 2004, p. 3), and its postulation is mostly relevant for sites located close to a coast, as the corresponding ATM displacements would be larger without the offsetting effect of the IBH (Sun et al. 1995). Finally, the relevant pressure for HYD is determined by the temporal variation of land water storage (LWS). It comprises soil moisture, snow coverage, or river water flows, for example (Dill and Dobslaw 2013; Eriksson and MacMillan 2014).

The transformation of surface pressure anomalies, i.e. deviations from a mean pressure, into local horizontal (ΔN, ΔE) and vertical (ΔU) displacements at a particular site is based on Farrell (1972). It involves a two-dimensional integration over the Earth's surface, where all pressure anomalies are weighted by a Green's function of the angular distance between the chosen site and the position of the anomaly. The details can be found in Petrov and Boy (2004), for example.

The transformation further depends on the applied TRF and its origin, which could be the centre of Earth's figure (CF), the centre of mass of the solid Earth (CE), or the centre of mass of the total Earth system (CM, including the fluid envelope of atmosphere and water) (compare Blewitt (2003)). As a consequence, there are different Green's functions and site displacements depending on the chosen frame (see Blewitt 2003; Tregoning and van Dam 2005a, for example), and one must pick the version that corresponds to the geodetic space technique under investigation. For VLBI, in particular, the frame is mostly irrelevant, as the observable is depending on the difference vector (the *baseline* $\boldsymbol{B}_{12}$) between each two observing stations at positions $\boldsymbol{S}_1$ and $\boldsymbol{S}_2$ (compare Sovers et al. 1998; Eriksson and MacMillan 2014). For example, if $\boldsymbol{T}_{CF}^{CM}(t)$ is the translation vector between CF and CM at epoch t, then the displaced baseline is given by

$$\begin{aligned}\boldsymbol{B}_{12}^{\Delta}(t) &= \left(\boldsymbol{S}_2(t) + \boldsymbol{\Delta}_2^{CM}(t)\right) - \left(\boldsymbol{S}_1(t) + \boldsymbol{\Delta_1}^{CM}(t)\right)\\ &= \left(\boldsymbol{S}_2(t) + \left[\boldsymbol{\Delta}_2^{CF}(t) + \boldsymbol{T}_{CF}^{CM}(t)\right]\right)\\ &\quad - \left(\boldsymbol{S}_1(t) + \left[\boldsymbol{\Delta}_1^{CF}(t) + \boldsymbol{T}_{CF}^{CM}(t)\right]\right)\\ &= \left(\boldsymbol{S}_2(t) + \boldsymbol{\Delta}_2^{CF}(t)\right) - \left(\boldsymbol{S}_1(t) + \boldsymbol{\Delta}_1^{CF}(t)\right), \qquad (1)\end{aligned}$$

where $\boldsymbol{\Delta}_i^{CF}$ and $\boldsymbol{\Delta}_i^{CM}$ are the site displacements at station i in the CF- and CM-frame, respectively. Hence, the translation is cancelled (except for minor effects related to the line of sight at each station), and this situation holds as long as the site displacements are applied at the observation or the normal equation level. If they are applied at the solution level, however, i.e. to the final estimated station positions, then the displacements must be taken from the same frame that the stations have been aligned to. We plan to return to this issue in a follow-up paper.

The actual and mean pressure values for the computation of site displacements are usually taken from numerical (weather) models for regular latitude and longitude grids. The two displacement providers in our study use different models with different spatial and temporal resolutions for the three parts of non-tidal loading. Their properties are summarized in Table 1. More providers can be found at the web page of the IERS Global Geophysical Fluid Center (GGFC[3]). Since ATM, OCE, and HYD are interrelated, it is desirable that the underlying models are consistent with each other and that the global mass is conserved.

2.2 Earth-System-Modelling group at GFZ

The first provider, the Earth-System-Modelling group at the Deutsches GeoForschungsZentrum (GFZ) in Potsdam (ESMGFZ[4]), basically follows the Green's functions approach to compute site displacements from non-tidal loading. However, a patched version is used to significantly reduce the computation time. The patch consists of applying a high spatial resolution for nearby pressure contributions and a lower spatial resolution for contributions far away, in connection with fast interpolation techniques (Dill and Dobslaw 2013; Dill et al. 2018). ESMGFZ supplies a software for interpolating the displacements in local horizontal coordinates for any site from regular $0.5° \times 0.5°$ spatial grids, with temporal resolutions depending on the loading part (compare Table 1). We used this software to obtain non-tidal atmospheric, non-tidal oceanic, and hydrological site displacements for the years 1984 to 2017 and all VLBI stations observing in the corresponding sessions. The data are available for both the CF- and the CM-frame, and we decided to use the CM-related displacements, as we plan to combine VLBI with SLR solutions in the future (and the latter definitely need displacements in the CM-frame).

ESMGFZ provides only one underlying model for each loading part (also listed in Table 1), such that consistency can be ensured among them. For the global conservation of mass, a fourth component, the sea-level loading (SLEL), is available. It is derived from barystatic sea-level variations and given with the same resolution as the hydrological displacements. We have applied it together with all the other non-tidal loading parts in one scenario, but since the results did not differ significantly from the scenario where it was left out, and since there is no equivalent part available from the second provider, we will mostly not consider SLEL in this

[3] http://loading.u-strasbg.fr/GGFC/index.php.

[4] http://rz-vm115.gfz-potsdam.de:8080/repository.

Table 1 Numerical models used to derive pressure anomalies for the computation of site displacements from non-tidal loading. The temporal and spatial resolutions refer to the original mass values of the models. If the resolution for the resampled pressure anomalies differs, it is given in brackets

Non-tidal loading part	ESMGFZ	IMLS
Atmospheric	ECMWF[a] operational data, 3h, 0.5° × 0.5° (0.125° × 0.125°)	MERRA-2[b], 6h, 0.5° × 0.625°
Oceanic	MPIOM[c], 3h, 1.0° × 1.0° (0.125° × 0.125°)	MPIOM06 (3h)
Hydrological	LSDM[d] Version 2, 24h, 0.5° × 0.5° (0.125° × 0.125°)	MERRA-2[e], 1h (3h), 0.5° × 0.625°

[a]European Centre for Medium-Range Weather Forecasts, www.ecmwf.int
[b]Modern-Era Retrospective Analysis for Research and Applications, version 2 (Gelaro et al. 2017)
[c]Max-Planck-Institute for Meteorology Ocean Model (Jungclaus et al. 2013)
[d]Hydrological Land Surface Discharge model (Dill 2008)
[e]Modern-Era Retrospective Analysis for Research and Applications, version 2 (Reichle et al. 2017)

study. Only some of the tables will contain the corresponding results for comparison.

2.3 International mass loading service

The other provider, the International Mass Loading Service (IMLS[5]), has also augmented the Green's function approach: as the two-dimensional integrations become computationally expensive with increasing spatial resolution of the geophysical models, a spherical harmonic transform approach is used (see Petrov 2015). The IMLS offers on-demand site displacements in local horizontal coordinates for any site in both the CF- and the CM-frame. Again, we requested non-tidal atmospheric, non-tidal oceanic, and hydrological loading displacements in the CM-frame for all VLBI stations taking part in our analysis. In contrast to ESMGFZ, there are several geophysical models per loading part to choose from, but we selected only the ones for which the full period from 1984 to 2017 was available. Their details are listed in Table 1, and at least for ATM and HYD we might assume consistency, since they are both based on the MERRA-2 model.

2.4 Comparison of site displacements

The properties of site displacements generated from non-tidal loading have been listed by various authors. For all three loading parts, the vertical displacements are generally significantly larger (peak-to-peak variation of 10 to 20 mm) than the horizontal ones (2 to 5 mm) and hence the estimated station heights will be affected most (compare, for example, Schuh et al. 2003; van Dam et al. 2012; Eriksson and MacMillan 2014). According to Böhm and Schuh (2013), Tregoning and

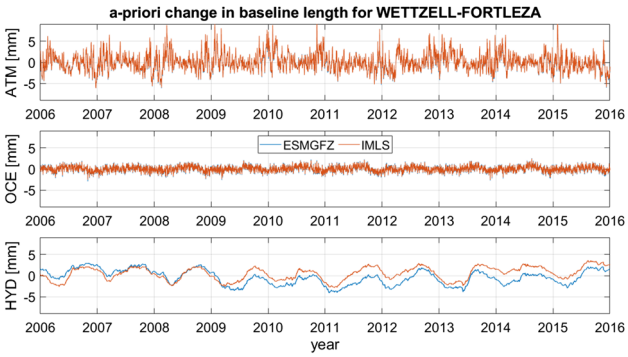

Fig. 1 The changes in the length of the corresponding baseline after the addition of site displacements generated from non-tidal atmospheric (top), oceanic (middle), or hydrological loading (bottom) to the VLBI stations WETTZELL (Germany) and FORTLEZA (Brazil). The displacements were taken from ESMGFZ (blue) and IMLS (red)

van Dam (2005b) and Dill and Dobslaw (2013), for example, atmospheric pressure varies strongly at mid-latitudes and continental sites, while the fluctuation is less pronounced close to the sea, also due to the IBH (Schuh et al. 2003). Most naturally, the displacements generated from ocean bottom pressure reveal their largest values at coastal or island sites, even though the effect of non-tidal oceanic loading is generally small (van Dam et al. 2012; Schuh et al. 2003). Eriksson and MacMillan (2014, p. 677) note that "the hydrologic variation is the largest within a 40° latitude band about the equator in South America, South Asia, and Africa". Additional sites with dominating hydrological loading are lake- and riversides, as well as the eastern part of the Rocky Mountains (see Dill and Dobslaw 2013).

Schuh et al. (2003) highlight important signals with periods of approximately two weeks and approximately one month for the time series of ATM and OCE, respectively.

[5] http://massloading.net/index.html.

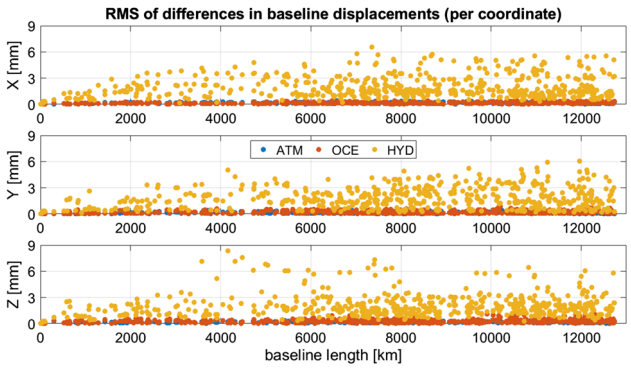

Fig. 2 Root mean square (RMS) errors of the differences between the combined site displacements of ESMGFZ and IMLS per baseline, separated by Cartesian station coordinates and non-tidal loading part

Furthermore, van Dam et al. (2012) state that the annual signal is the most powerful one for ocean bottom pressure, i.e. non-tidal oceanic loading. The site displacements for these two parts generally vary quite strongly, with a broad range of relevant frequencies. In contrast to that, there are basically only two dominant signals for hydrological loading: the semi-annual and the annual one (see Dill and Dobslaw 2013; Eriksson and MacMillan 2014).

As the differences between the displacements applied at two stations are most important for VLBI, we will present the comparison of ESMGFZ and IMLS data at the baseline level according to Eq. (1). In Fig. 1, we show the change in the length of the baseline WETTZELL–FORTLEZA after application of non-tidal atmospheric, oceanic, and hydrological loading at the observation level for both providers. In this example, and as we generally observed, for both ATM and OCE the displacements are very similar among the two data centres. This is in line with the results of Roggenbuck et al. (2015), who compare site displacements generated by the GSFC and l'Université de Luxembourg (ULux[6]) and also obtain rather small differences between the corresponding displacement time series for ATM and OCE.

The displacements computed from the two hydrological models, however, can deviate quite significantly (compare the bottom panel of Fig. 1). The amplitudes and also phases of the time series show considerable discrepancies between the two providers for many VLBI stations and hence for the displaced baselines, too. The continental water storage of the LSDM comprises soil moisture, the accumulation of snow, seasonal glacier run-off, and surface water in rivers and lakes, for example (see Dill and Dobslaw 2013). In contrast to this, the validation report of the MERRA-2 model (Reichle et al. 2017) highlights soil moisture, snow coverage, streamflow, and observation-based precipitation. There seem to be more serious modelling differences for HYD than for ATM, which

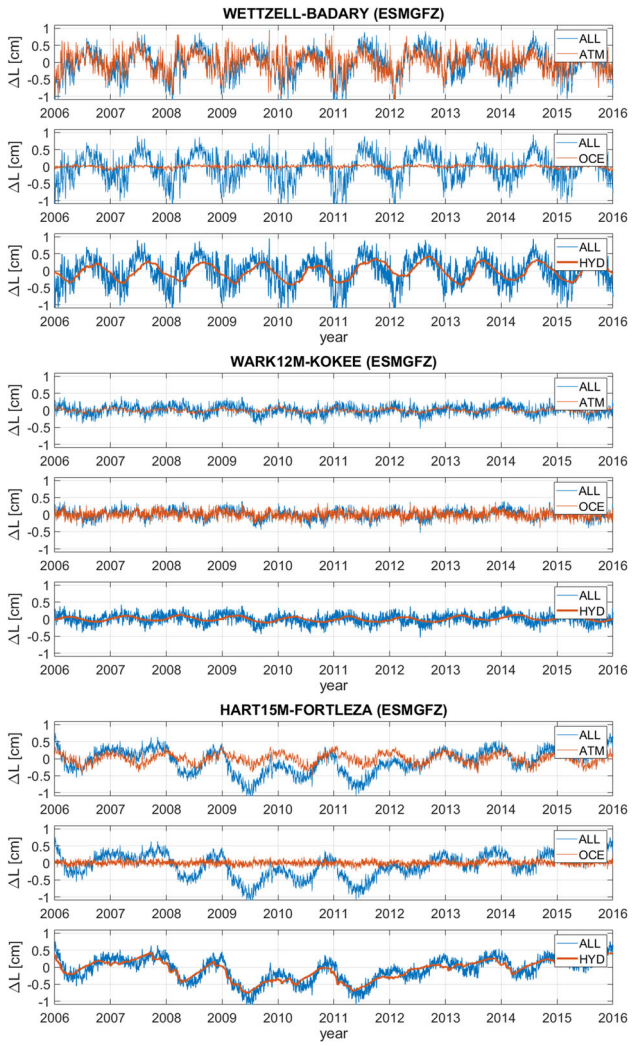

Fig. 3 Changes in the lengths of sample baselines after individual (red) and joint (blue) application of site displacements (to the a priori station coordinates) corresponding to the three non-tidal loading parts. For each baseline, a different part is dominant: ATM (top), OCE (middle), or HYD (bottom)

was also reported in the study by Roggenbuck et al. (2015). Figure 2 confirms this situation by showing the root mean square (RMS) errors of the differences between the combined site displacements of ESMGFZ and IMLS for a large subset of VLBI baselines. While the data of the two providers agree very well for ATM and OCE (sub-mm RMS), the most critical choice is that of the hydrological model (average RMS of about 2–3 mm).

The operational analysis centres (AC) of the IVS are asked to provide solutions containing corrections for non-tidal atmospheric loading only. However, ATM not necessarily is the most relevant non-tidal loading part, as Fig. 3 suggests. Each subplot shows the change ΔL in baseline length following the application of an individual loading part on top of the change following the joint application of all parts. We observe

[6] https://geophy.uni.lu/.

that the major contribution can originate from either ATM, OCE, or HYD, dependent on the respective stations which are involved. The dominant loading part at a station can even change per coordinate (East, North, or Up, not shown here), and it is sometimes different for ESMGFZ and IMLS (Fig. 3 only contains examples for the former). Consequently, one should take all three non-tidal loading effects into account when longing for an improvement of the VLBI solutions.

Finally, these figures confirm that the time series of site displacements derived from hydrological loading indeed is much smoother than those of ATM and OCE, as mostly semi-annual and annual signals exist for HYD. This will be a distinguishing feature when the application at normal equation level is considered.

3 Application levels

In the classic Gauss–Markov model (see Koch 1999), the *normal equation*

$$A^T P\, A\, \boldsymbol{\Delta x} \;=\; A^T P\, \boldsymbol{l} \tag{2}$$

is solved for $\boldsymbol{\Delta x} \in \mathbb{R}^n$, the vector of corrections to a priori values x_j^0 of particular parameters x_j, $j = 1, \ldots, n$. The latter are used within a functional model f to approximate $m >> n$ real observations $\boldsymbol{b} \in \mathbb{R}^m$. $\boldsymbol{l} \in \mathbb{R}^m$ is the vector of observed minus computed (OMC) values

$$l_i \;=\; b_i - f(i, \boldsymbol{x^0}) \quad (i = 1, \ldots, m), \tag{3}$$

and $A \in \mathbb{R}^{m \times n}$ is the Jacobi matrix of f with respect to the x_j.

$$P \;:=\; \sigma_0^2 \left[diag\left(\sigma_1^2, \ldots, \sigma_m^2\right) \right]^{-1} \;\in \mathbb{R}^{m \times m} \tag{4}$$

is a weight matrix, with σ_0^2 being a common a priori variance factor and the σ_i being the standard deviations (formal measurement errors) of the observations b_i for $i = 1, \ldots, m$. The constituents of (2) are labelled *normal equation matrix*

$$N \;:=\; A^T P\, A \;\in \mathbb{R}^{n \times n} \tag{5}$$

and *right-hand side*

$$\boldsymbol{y} \;:=\; A^T P\, \boldsymbol{l} \;\in \mathbb{R}^n. \tag{6}$$

Its outcome $\boldsymbol{\Delta x}$ solves the *observation equation*

$$A\, \boldsymbol{\Delta x} \;=\; \boldsymbol{l} + \boldsymbol{v}, \quad \boldsymbol{v} \in \mathbb{R}^m, \tag{7}$$

such that the weighted sum of squared observation residuals, $\boldsymbol{v}^T P\, \boldsymbol{v}$, is minimized.

In general geodetic applications, the matrix N is singular and cannot be inverted, unless certain conditions are applied. The most important ones are the datum conditions, which align the estimated station and source coordinates to their a priori networks (compare Angermann et al. 2004). The corresponding no-net-translation (NNT, for stations) and no-net-rotation (NNR, for stations and sources) equations are provided in a matrix $N_D \in \mathbb{R}^{n \times n}$, while we assume that all other conditions are already contained in the matrices A and N as pseudo-observations. Then, the vector of best parameter estimates is finally given by

$$\boldsymbol{x} \;=\; \boldsymbol{x^0} + \boldsymbol{\Delta x} \;=\; \boldsymbol{x^0} + (N + N_D)^{-1}\, \boldsymbol{y}. \tag{8}$$

Its statistical properties will be discussed in Sect. 4.2. In the following, the above notations refer to an estimation process without any non-tidal loading applied.

3.1 Observation level

Let $\boldsymbol{\delta x}(t) \in \mathbb{R}^n$ be the vector of site displacements computed from non-tidal loading for each parameter x_j ($j = 1, \ldots, n$) at epoch t. As the coordinates of the observing stations are the only estimated parameters which are fixed to the Earth's crust, $\delta x_j = 0$ for all other parameters. When applying non-tidal loading at the observation level (OBS), this means changing the functional model,

$$f(i, \boldsymbol{x^0}) \;\mapsto\; \tilde{f}(i, \boldsymbol{x^0}, \boldsymbol{\delta x}(t_i)), \tag{9}$$

i.e. using the site displacements of each distinct observation epoch t_i, $i = 1, \ldots, m$. Since the temporal resolution of the displacements generally is not as fine as the observation epoch grid, an interpolation routine has to be defined as well. In the end, the Jacobi matrix and the OMC vector change:

$$\begin{aligned} &A \mapsto \tilde{A} \\ &l_i \mapsto \tilde{l}_i \;=\; b_i \;-\; \tilde{f}(i, \boldsymbol{x^0}, \boldsymbol{\delta x}(t_i)) \quad (i = 1, \ldots, m), \end{aligned} \tag{10}$$

which leads to a new observation equation with new residuals

$$\tilde{A}\, \boldsymbol{\Delta \tilde{x}} \;=\; \tilde{\boldsymbol{l}} + \tilde{\boldsymbol{v}}. \tag{11}$$

The partial derivatives in $\tilde{A}$ differ from those in A only to a very small extent (we plan to present the theoretical details in the follow-up paper). The best solution to Eq. (11) is again obtained by the corresponding normal equation

$$\tilde{N}\, \boldsymbol{\Delta \tilde{x}} \;=\; \tilde{\boldsymbol{y}}, \tag{12}$$

where

$$\tilde{N} = \tilde{A}^T P \tilde{A},$$
$$\tilde{\boldsymbol{y}} = \tilde{A}^T P \tilde{\boldsymbol{l}}. \tag{13}$$

As before, we need to add the datum conditions in N_D to invert the normal matrix. Then, we finally get the formula for parameter corrections with non-tidal loading applied at the observation level,

$$\boldsymbol{\Delta}\tilde{\boldsymbol{x}} = (\tilde{N} + N_D)^{-1}\, \tilde{\boldsymbol{y}}. \tag{14}$$

3.2 Normal equation level

Analysis solutions are often exchanged in the form of datum-free normal equations only. Usually, they do not contain non-tidal loading, and there is no possibility to recover the functional model and apply the corresponding displacements at the observation level, either. However, there is an alternative way to correct these equations for non-tidal loading. It is referred to as the application at normal equation level (NEQ) and described by Seitz et al. (2020), who use this approach to generate the DTRF2014.

To derive NEQ, we start with the OMC vector $\tilde{\boldsymbol{l}}$ for the application at observation level in Eq. (10),

$$\tilde{\boldsymbol{l}} = \boldsymbol{b} - \tilde{\boldsymbol{f}}, \tag{15}$$

where the components of $\tilde{\boldsymbol{f}}$ are computed with the distinct displacement vectors $\boldsymbol{\delta x}(t_i)$ for each observation epoch t_i ($i = 1, \ldots, m$). Then, we define a vector $\boldsymbol{\delta}\bar{\boldsymbol{x}} \in \mathbb{R}^n$ of mean displacements per parameter x_j ($j = 1, \ldots, n$), which could be the displacements interpolated at the mid-epoch of the session (as employed by Böhm et al. (2009)), or the averages of each parameter's displacements during the whole session (this work). First, this mean vector replaces the distinct displacement vectors,

$$\boldsymbol{\delta x}(t_i) \equiv \boldsymbol{\delta}\bar{\boldsymbol{x}} \quad \text{for } i = 1, \ldots, m. \tag{16}$$

Second, we use the vector to linearly approximate the functional model $\tilde{\boldsymbol{f}}$ of OBS,

$$\tilde{\boldsymbol{f}} \approx \boldsymbol{f} + A\, \boldsymbol{\delta}\bar{\boldsymbol{x}}, \tag{17}$$

such that the OMC vector $\bar{\boldsymbol{l}}$ for the application at normal equation level becomes

$$\bar{\boldsymbol{l}} := \boldsymbol{b} - (\boldsymbol{f} + A\, \boldsymbol{\delta}\bar{\boldsymbol{x}})\,. \tag{18}$$

This approach leads to a simple amendment of the right-hand side $\boldsymbol{y}$, ensuring that we can actually apply non-tidal loading although we are only provided with the normal equation. The modified right-hand side $\bar{\boldsymbol{y}}$ of NEQ per session is given by

$$\begin{aligned}\bar{\boldsymbol{y}} &:= A^T P\, \bar{\boldsymbol{l}} \\ &= A^T P\, (\boldsymbol{b} - (\boldsymbol{f} + A\, \boldsymbol{\delta}\bar{\boldsymbol{x}})) \\ &= A^T P\, (\boldsymbol{b} - \boldsymbol{f}) \;-\; A^T P\, A\, \boldsymbol{\delta}\bar{\boldsymbol{x}} \\ &= A^T P\, \boldsymbol{l} \;-\; N\, \boldsymbol{\delta}\bar{\boldsymbol{x}} \\ &= \boldsymbol{y} \;-\; N\, \boldsymbol{\delta}\bar{\boldsymbol{x}}.\end{aligned} \tag{19}$$

With the datum conditions N_D, the formula of the parameter corrections for the application of non-tidal loading at the normal equation level is finally given by

$$\boldsymbol{\Delta}\bar{\boldsymbol{x}} = (N + N_D)^{-1}\, \bar{\boldsymbol{y}}. \tag{20}$$

To summarize, we are modifying the theoretical observations for NEQ by three simplifications:

1. The removal of temporal variation in site displacements during the VLBI session (or other observation period) in Eq. (16).
2. The linear approximation of the change in the functional model after the application of site displacements in Eq. (17).
3. The assumption of invariance of the Jacobi matrix A and hence the normal matrix N to the application of site displacements in the functional model, i.e. $\tilde{A} \approx A$ and $\tilde{N} \approx N$.

We investigated the individual impact of these three items in the analysis of VLBI observations (and plan to also present these results in the follow-up paper). We came to the conclusion that the introduction of mean displacements is much more significant than the linearization of the theoretical signal delay and the changes in the Jacobi matrix. If the temporal variations of the site displacements are small during a session, we can hence expect the results for OBS and NEQ to be quite similar. Böhm et al. (2009, p. 1112) support the concept of a mean displacement: "the intra-day variation of atmospheric loading corrections is - at the present accuracy level - not critical for the analysis of VLBI observations". While this is encouraging, quite some progress in measuring and modelling has been made recently, and the current situation might be different, especially since we are also considering the other non-tidal loading effects.

3.3 Solution level

The parameter corrections $\boldsymbol{\Delta}\hat{\boldsymbol{x}}$ for the application at solution level (SOL) are obtained by

Table 2 Parametrization of the estimated variables in the analysis of VLBI sessions with DOGS-RI

Parameter	Representation	Resolution
Station coordinates	Offset	24 h
Source coordinates	Offset	24 h
Polar motion: x_{pole}, y_{pole}	Offset and drift	24 h
$\Delta UT1$	Offset and drift	24 h
Celestial pole offsets: ΔX_{CIP}, ΔY_{CIP}	Offset	24 h
Clock differences	Quadratic function	24 h
Additional clock corrections	Continuous piecewise linear functions	1 h
Zenith wet delay	Continuous piecewise linear functions	1 h
Tropospheric gradients (North and East)	Continuous piecewise linear functions	6 h

Table 3 Models and a priori data used for the analysis of VLBI sessions with DOGS-RI. This reference set-up (REF) does not yet include any non-tidal loading data

Component	Model
A priori station coordinates	ITRF2014, Altamimi et al. (2016)
A priori source coordinates	ICRF2, Fey et al. (2015)
A priori EOP	IERS 14 C04 series, Bizouard et al. (2017)
Zenith delay	Mapping functions 1 by TU Vienna (VMF1), Böhm et al. (2006), with actual meteorological data
Tropospheric gradients	Chen–Herring mapping function (CHM), Chen and Herring (1997), with a priori values by GSFC, MacMillan (1995)
Thermal antenna deformation	Nothnagel (2009)
Tidal atmospheric loading	Ray and Ponte (2003)
Tidal ocean loading	FES2004, Lyard et al. (2006)

$$\boldsymbol{\Delta x} = \boldsymbol{\Delta \hat{x}} + \boldsymbol{\delta \hat{x}} \tag{21}$$

$$\Leftrightarrow \quad \boldsymbol{\Delta \hat{x}} = \boldsymbol{\Delta x} - \boldsymbol{\delta \hat{x}}, \tag{22}$$

i.e. by simply subtracting the mean displacements

$$\boldsymbol{\delta x}(t_i) \equiv \boldsymbol{\delta \hat{x}} \quad \text{for } i = 1, \ldots, m, \tag{23}$$

from the original parameter corrections without non-tidal loading (compare Williams and Penna 2011, for example). It becomes clear that the TRF used to derive the site displacements is important at this level: the difference between CF- and CM-displacements is fully transferred to the new coordinate estimates, and hence the correct choice depends on the frame of the latter.

Since $\delta x_j = 0$ for parameters other than station coordinates, these are not modified at SOL. With respect to single VLBI sessions or other geodetic experiments, this leads to inconsistencies between the station coordinates and the other parameters like the EOP, as these have been estimated in connection with the original coordinate corrections in $\boldsymbol{\Delta x}$. The consistency can be restored if the modified coordinates are used for the estimation of new EOP in the context of a long-term TRF, for example.

SOL will not be treated in this work. Böhm et al. (2009), who focused on atmospheric loading, conclude that the a posteriori correction of station coordinates is not appropriate in real VLBI analysis. The authors attribute the degradation observed in their station height repeatabilities to network effects: they claim that un-modelled loading is to some extent distributed between the stations, especially when the corresponding networks only consist of few antennas. Adding site displacements to the final estimates results in a partly redundant consideration of non-tidal loading. (In our follow-up paper, we will analyse the difference between the application of displacements during and after the estimation process in VLBI analysis in more detail.)

4 Impact of non-tidal loading

We examine the effect of non-tidal loading on geodetic parameters derived from VLBI observations with our DGFI Orbit and Geodetic parameter estimation Software (DOGS, see Gerstl et al. 2000). The component DOGS-RI (Radio Interferometry) establishes the theoretical model and provides datum-free normal equations according to the Gauss–Markov model (compare Sect. 3). For each VLBI session, we estimate constant station and source coordinates, the full set of Earth orientation parameters (EOP), as well as parameters modelling the station clocks and the tropospheric delay. Details about the temporal resolutions and the functional representations are found in Table 2.

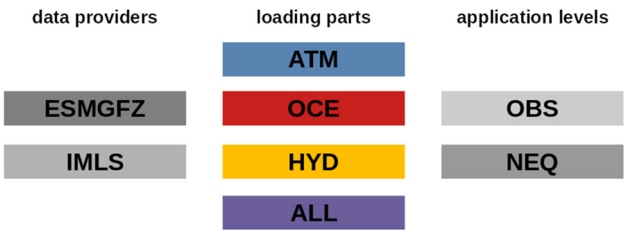

Fig. 4 In each scenario other than REF, one data provider, one non-tidal loading part, and one observation level are chosen

The geophysical models used in the estimation process are those of the IERS Conventions 2010 (Petit and Luzum 2010). Table 3 provides the corresponding overview for our reference set-up (REF), where all conventional station displacements are applied. Any displacements referring to non-tidal loading are only considered in subsequent set-ups. First, this happens at the observation level (OBS), i.e. distinct displacements are applied at their corresponding observation epoch within the theoretical delay function. For each non-tidal loading scenario, DOGS-RI generates a separate set of datum-free normal equations, which contain conditions for clock and tropospheric parameters as pseudo-observations. These equations are forwarded to the component DOGS-CS (Combination and Solution), where no-net-translation (NNT, for station coordinates) and no-net-rotation (NNR, for station and source coordinates) conditions are added in the form of separate normal matrices (compare Angermann et al. 2004). The parameter estimates for each scenario and VLBI session are finally obtained by inversion of their respective normal equation as shown in Eq. (14).

With the normal equation level (NEQ), only the datum-free normal equations of the reference set-up are forwarded to DOGS-CS. For each non-tidal loading scenario, the right-hand sides of the normal equations are modified with the vector of average site displacements per station coordinate for the corresponding session. Afterwards, the same NNT and NNR conditions as for OBS are added, and the parameter estimates for NEQ are again obtained by inversion.

In the following, we investigate the changes in the estimated parameters when moving from REF to one of the non-tidal loading scenarios: ATM—atmospheric only, OCE—oceanic only, HYD—hydrological only, ALL—atmospheric plus oceanic and hydrological. In each case, the application levels OBS and NEQ as well as the providers ESMGFZ and IMLS have been considered. On overview of the choices is presented in Fig. 4.

4.1 WRMS of station positions

We want to analyse whether the site displacements computed from non-tidal loading are appropriate for explaining parts of the sub-daily station motions, i.e. whether their application is able to reduce the variation in the time series of session-wise positions. The differences between OBS and NEQ will give an impression of the significance of the sub-daily displacement resolution.

In Fig. 5, we plot the changes in the weighted root mean square (WRMS) values of the local station coordinates (East, North, Up) for the distinct non-tidal loading scenarios with ESMGFZ data. The time series of coordinates ranges from 1984 to 2017, and we considered every session that was analysed at DGFI-TUM during that period. If the stations participated in at least 100 sessions, they are listed on the x-axis, and they are ordered descending by the number of such sessions. The leftmost station, WETTZELL, for example, made observations in 3,323 sessions, while the rightmost one, DSS65, only participated in 111 sessions.

As expected, the change in WRMS values is generally largest for the Up component (bottom panel in each subplot), irrespective of the application level. Furthermore, the majority of changes for the Up component is negative, which means that the WRMS is generally improved when applying non-tidal loading. The maximum improvement is -1.83 mm (-1.86 mm) for the VLBI station GILCREEK when the sum of all site displacements is applied at OBS (NEQ). Across the listed stations, the average improvement is about -0.39 mm for both levels in the ALL scenario, which is equivalent to a relative average improvement of -4.0%. For ATM, OCE, and HYD, the averages are about -0.23 mm (-2.4%), -0.04 mm (-0.4%), and -0.12 mm (-1.3%), respectively. For the horizontal components, the tendency is less obvious. The statistics (minimum, mean, median, maximum, portion of improved cases) of the relative changes in WRMS values for all local coordinates and non-tidal loading parts are listed in Table 5 of the Appendix. It also contains the scenario ALL including SLEL and reveals that the corresponding results are close to that of the original ALL scenario. Compared to the relative improvements which are obtained for GNSS (see Tregoning et al. 2009; Dach et al. 2010; van Dam et al. 2012, for example), our values are rather small. However, the behaviour is systematic, and the WRMS of station heights is larger for VLBI (1–2 cm) than for GNSS (< 1 cm).

If only a single non-tidal loading part is applied at OBS, for 25 out of the 41 listed stations the reduction in WRMS is largest for the atmospheric one (Up component). However, for 13 stations the greatest improvement is obtained with the exclusive application of hydrological loading. And even though the corresponding changes in WRMS are very small, there are three stations which benefit the most from non-tidal oceanic loading. Hence, all non-tidal loading parts are worth considering.

The largest reduction in WRMS per station is not necessarily given in the scenario which applies its dominant non-tidal loading part. The total site displacements of FORTLEZA,

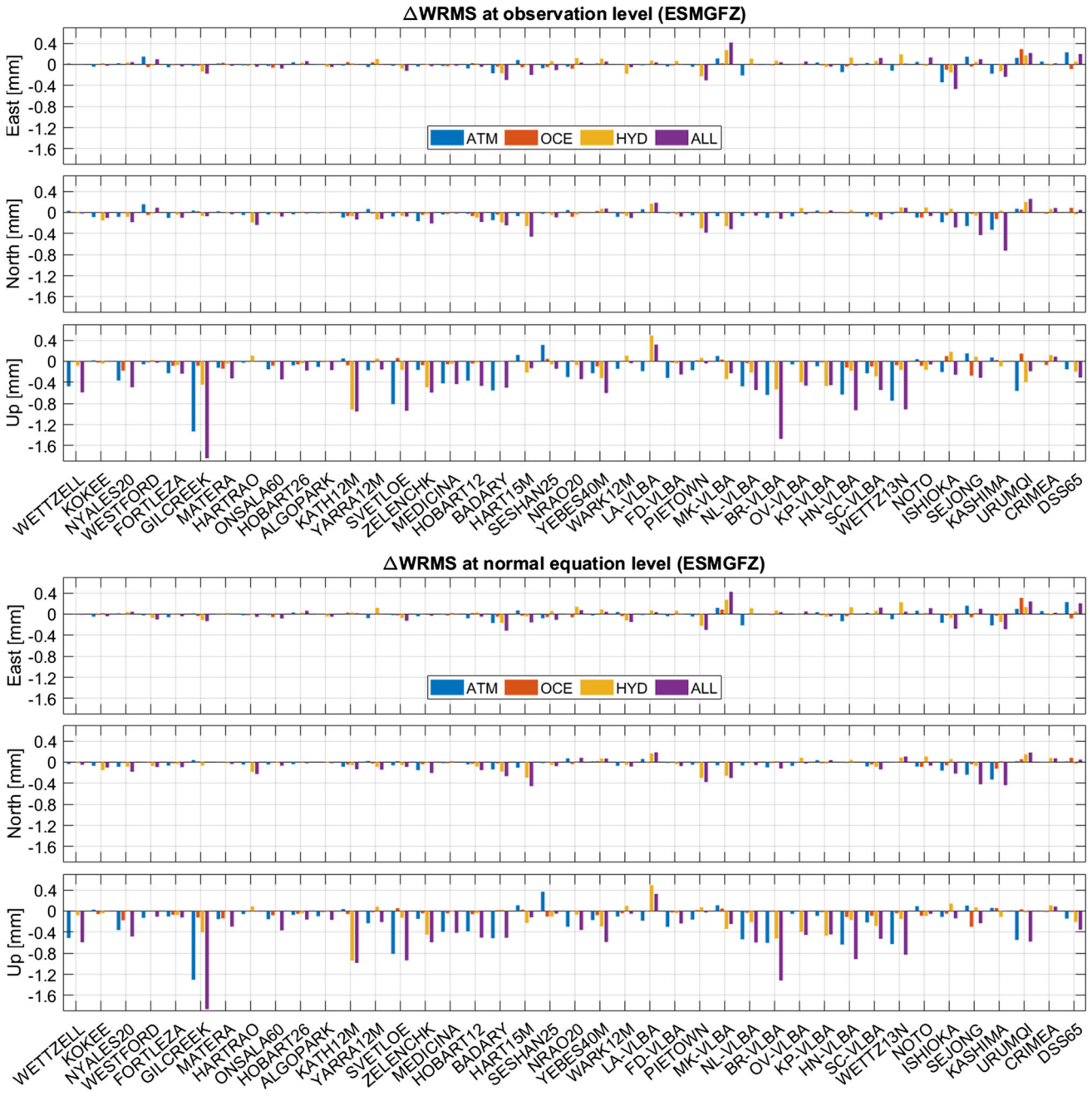

Fig. 5 Change in the WRMS of the local station coordinates when applying different non-tidal loading corrections at distinct levels (top subplot: OBS, bottom subplot: NEQ). The corresponding site displacements are provided by ESMGFZ

for example, are mainly composed of hydrological loading (due to its location near the equator; compare also Fig. 3), while the station's WRMS value hardly improves in the HYD scenarios (− 0.072 mm to − 0.089 mm). The reason for this behaviour is that the stations cannot be examined in isolation, but they have to be considered as being part of session-wise observation networks. Hydrological loading might be sufficient for FORTLEZA, but this does not hold for all of the other stations. As mentioned by Böhm et al. (2009), the missing displacements are transferred between the stations in the adjustment if non-deforming global datum conditions (i.e. NNR and NNT conditions) are used. This leads to adverse station motions and consequently the results for FORTLEZA deteriorate as well. This effect is present in all single non-tidal loading scenarios, and the overall impact depends on how much loading information is absent from the network. The best approach would be to apply all non-tidal loading parts together (under the assumption that all loading effects are modelled correctly).

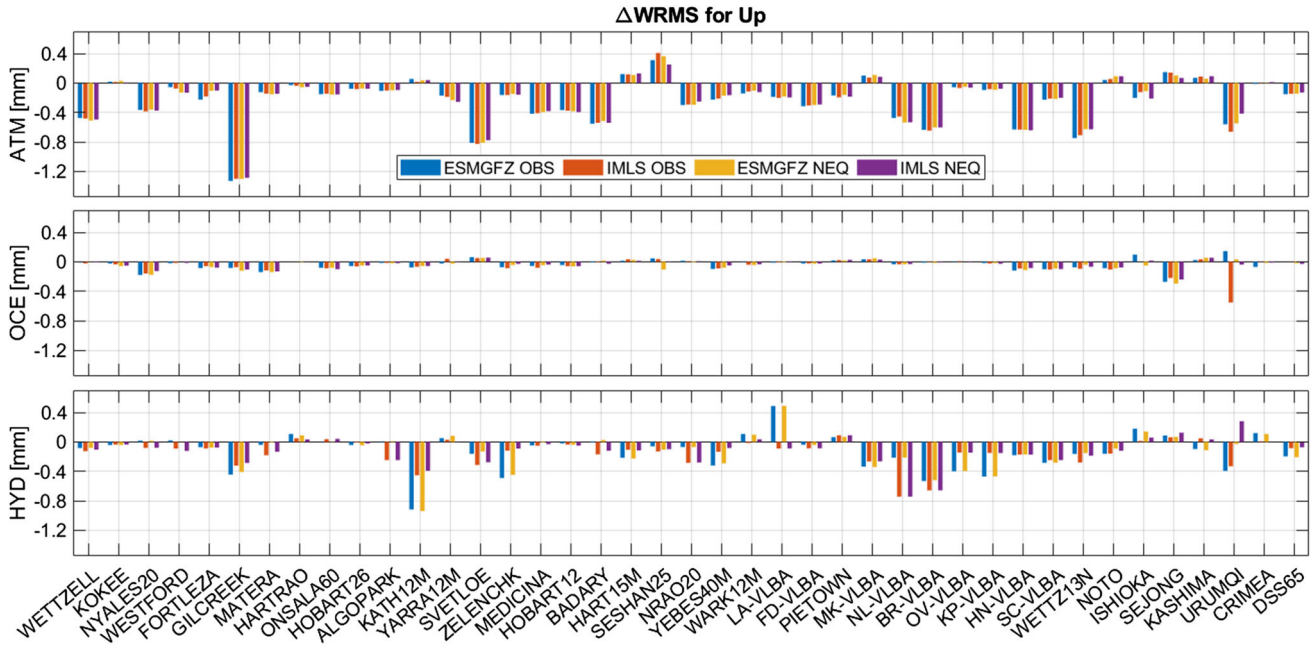

Fig. 6 Change in the WRMS of the vertical station coordinates when applying different non-tidal loading parts (top: ATM, middle: OCE, bottom: HYD) at distinct levels (OBS, NEQ) and with data from different providers (ESMGFZ, IMLS)

The corresponding plots for IMLS look very alike, with similar values for the average improvements of the WRMS (see Table 6 of the Appendix for the statistics). To highlight the similarities and differences, we present the IMLS results only for the vertical coordinates, and we plot the associated changes in the WRMS values next to those of ESMGFZ in Fig. 6. In Sect. 3.2, we mentioned that the main discrepancy between OBS and NEQ is the loss of temporal resolution. Hence, for HYD, where the time series of site displacements hardly contains any intra-session variation, the results for OBS and NEQ should be almost identical. Eriksson and MacMillan (2014) make a corresponding observation when applying session-wise average hydrology corrections in their study, and we can confirm this by looking at the bottom panel of Fig. 6. The reduction in WRMS values in the HYD scenario matches very well for both levels with the same data provider. On the other hand, the reductions are generally not of similar size for the same application level but different data providers. This again emphasizes the discrepancies between the two hydrology models LSDM and MERRA-2.

For ATM (top panel of Fig. 6), we observe the opposite behaviour. The site displacements generated from ECMWF and MERRA-2 are quite similar to each other, but characterized by a high sub-daily variability. Hence, the approximation by an average displacement per session is potentially worse than for HYD, and the reductions in WRMS values for OBS and NEQ need not match very well (compare stations WETTZ13N or YEBES40M, for example). On the other hand, the difference between the two levels is much smaller than the difference to REF for most stations. Consequently, like for HYD, the approximation of OBS by NEQ is generally appropriate as far as the reduction of station position variability is concerned. For single sessions with large intra-day variations in the site displacements, however, there can still be significant differences.

A summary of the relative changes in the WRMS of baseline lengths (*baseline length repeatability*, BLR) is also provided in Tables 5 and 6 of the Appendix. The picture is similar to that for station heights: for at least two-thirds of the baselines with more than 100 observations, the BLR is reduced after the application of any non-tidal loading. The largest improvements (about -3.0% on average) are again obtained for the ALL scenario, followed by ATM (about -1.6%) and HYD (about -1.0%). The statistics for OBS and NEQ are very close, and the differences between ESMGFZ and IMLS are largest for HYD, where there are less extreme changes for IMLS.

4.2 Standard deviations

The variance–covariance matrix of the estimated parameters is given by

$$C = \breve{\sigma}_0^2 \, (A^T P A + N_D)^{-1} \tag{24}$$

(see Koch 1999). When applying site displacements at the normal equation level, A, P, and N_D are not modified. When applying them at the observation level, P and N_D stay constant as well, and the changes in A are negligible (compare

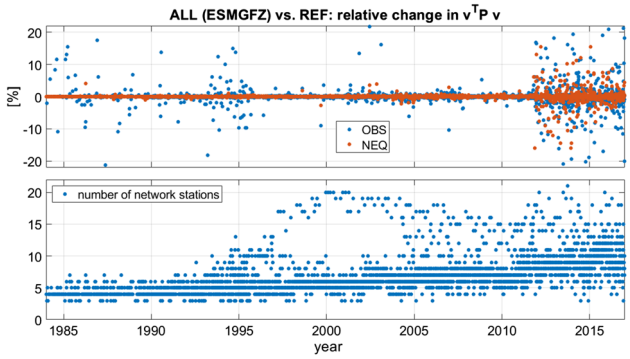

Fig. 7 Top panel: the relative change in the weighted sum of squared observation residuals ($\boldsymbol{v}^T P\, \boldsymbol{v}$) per session, when all non-tidal loading parts are applied simultaneously at the observation (blue dots) or at the normal equation level (red dots). Bottom panel: the number of stations in the corresponding networks

Sect. 3.2). Hence, the only variable is the common a posteriori variance factor

$$\breve{\sigma}_0^2 = \frac{\boldsymbol{v}^T P \boldsymbol{v}}{m + m_c - n}, \tag{25}$$

where m_c is the number of pseudo-observations (conditions).

Since the number of (pseudo-)observations and parameters is not altered between the scenarios, $\breve{\sigma}_0^2$ only depends on their weighted sums of squared observation residuals. As a consequence, the standard deviations vary proportionally to the square root of $\boldsymbol{v}^T P\, \boldsymbol{v}$. In the top panel of Fig. 7, we plot the relative changes of this weighted sum with respect to REF for each VLBI session in the ALL scenario. For most sessions, the changes are less than 1%. Furthermore, they are basically equally distributed around 0. Hence, the impact on the standard deviations is small and has no clear direction (i.e. improvement or deterioration). Regarding the application level, NEQ provides fewer extreme results, but in general the relative changes are similar to those of OBS.

A striking property, however, is the sharp and persistent increase in the relative change in $\boldsymbol{v}^T P\, \boldsymbol{v}$ at the end of 2011. The reason is not yet fully clarified, but we think this is related to the extension of the Australian–New Zealand network at this time, i.e. the introduction of the stations YARRA12M, KATH12M, and WARK12M. Almost simultaneously, the number of network stations—and hence baselines—per session increased (compare the bottom panel of Fig. 7). Furthermore, in the Continuous VLBI Campaign 2017 (CONT17[7]), where two networks processed daily 24-h sessions for 15 consecutive days, it is noticeable that almost all sessions of the XB network have a relative change of more than 1% (and up to 12%), while those of the XA network are close to zero. The XA network has only one station in the Southern Hemisphere, and most baselines are directed from East to West. In contrast to that, the XB network consists of five Southern Hemisphere stations and NYALES20 in the far North, so there are many more North–South baselines. Opposite seasonal effects of non-tidal loading on the two hemispheres might induce a larger impact for this direction.

Anyway, in terms of $\boldsymbol{v}^T P\, \boldsymbol{v}$, we observe a growing significance of non-tidal loading in the last decade. But the effect of the un-modelled site displacements appears to already be distributed among the station coordinates or the other estimated parameters, which is why the weighted sum of observation residuals is not necessarily improved. The plots for ATM, OCE, and HYD look very similar to Fig. 7.

4.3 Helmert transformation: scale

Vertical station positions experience the greatest impact by non-tidal loading. As VLBI stations are globally distributed, alterations in the stations' height will influence the scale of the used TRF. This is also supported by Böhm et al. (2009, p. 1112), who mention that "the network-scale parameter of a VLBI network [...] is significantly affected by un-modeled atmospheric loading corrections at the stations". We perform 7-parameter (three translation values, three rotation angles, and the scale parameter) Helmert transformations for all of our scenarios to investigate the impact on the scale. For each session, the transformation is computed with respect to the DTRF2014, which consists of linear representations of station motions via offsets and drifts (Seitz et al. 2020). Since there is a lot of noise in the resulting scale parameters for sessions before 2000, we restrict ourselves to the period from 2000 to 2017. Furthermore, we eliminate scales with an absolute value greater than 6 cm as outliers (less than 2% of the data). The remaining series is interpolated to a regular 1-day time grid, before we finally perform a frequency analysis.

The amplitude pattern for the scale time series in non-tidal loading scenarios with displacements by ESMGFZ applied at NEQ is provided in Fig. 8. For REF, where no non-tidal loading is considered, the most striking observation is the dominant annual signal with an amplitude of about 1.7 mm. As many authors report (Petrov and Boy 2004; van Dam et al. 2012; Eriksson and MacMillan 2014, for example), the 365-day period is also dominant for the site displacements themselves. Hence, we might expect that the application of the latter could dampen the annual variation in the station heights and, consequently, in the scale parameter. According to Fig. 8, this is partly true (compare the black box): the annual signal

- hardly changes, when only OCE is applied.
- slightly increases, when only ATM is applied.
- significantly decreases to about 0.9 mm, when only HYD or all non-tidal loading parts (ALL) are applied.

[7] https://ivscc.gsfc.nasa.gov/program/cont17/.

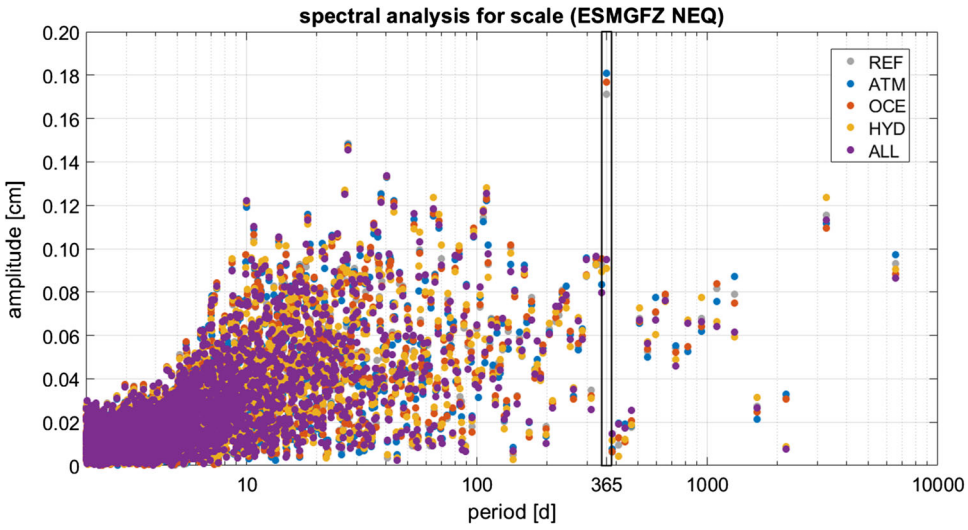

Fig. 8 Spectral analyses of the time series of scale parameters estimated in a 7-parameter Helmert transformation with respect to the DTRF2014. The site displacements for the distinct non-tidal loading scenarios generated by ESMGFZ have been applied at the normal equation level

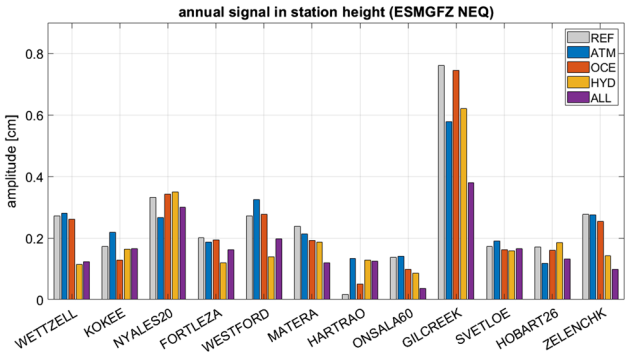

Fig. 9 The amplitude of the annual signal in the time series of station heights as obtained in various non-tidal loading scenarios with site displacements by ESMGFZ applied at the normal equation level

The same behaviour is observed for both the IMLS and OBS (not shown here), so the approximation at NEQ preserves these properties.

Since the impact of OCE is very small for most VLBI stations, its minor effect on the scale parameter is no surprise. But it is rather counter-intuitive that the annual amplitude gets larger in the ATM scenario, even though this was noticed by van Dam and Herring (1994) and Petrov and Boy (2004) for OBS already. An actual reduction of the annual signal in the scale was only observed by Seitz et al. (2020), who applied ATM and HYD together at the normal equation level. Here, we discover that HYD is the relevant part: it reduces the amplitude to almost the same extent as when all non-tidal loading parts are used jointly (ALL).

To investigate the origin of this behaviour, we take a look at the annual signals of the time series of station heights in Fig. 9, which have also been computed with ESMGFZ site displacements at NEQ. We only show stations that are part of the NNT / NNR conditions and hence relevant for the Helmert transformation. Furthermore, they must participate in at least 500 sessions during the period 2000–2017 to ensure a reliable spectral analysis. For about half of these stations, the amplitude of the annual signal in the ATM scenario is actually greater than the amplitude in the REF scenario. Likewise, the amplitudes for OCE are quite similar to those of REF for most stations. And finally, for 9 out of the 12 listed stations, the annual amplitude for HYD is (in parts significantly) smaller than that for REF. Since the respective figure looks very alike for OBS, this is in line with MacMillan and Boy (2004), who find a reduction in annual vertical amplitude for 70% of their VLBI stations after the application of HYD at the observation level. This property most probably causes the corresponding mitigation of the annual signal in the scale.

4.4 Earth orientation parameters

When applying all non-tidal loading parts, the absolute changes with respect to the reference scenario are generally below 100 μas for polar motion, below 3 μs for $\Delta UT1$, and below 10 μas for the celestial pole offsets. If the authors analysed the particular EOP, these are the same orders of magnitude as reported in Roggenbuck et al. (2015) and Männel et al. (2019). (We were able to produce plots very similar to their Figures 5 and 13, respectively, which contain the changes after introduction of non-tidal loading.) The mean formal errors of polar motion, $\Delta UT1$, and celestial pole offsets reported in the IERS Bulletins B[8] are about 30–60 μas, 10–20 μs, and 50-100 μas, respectively. Hence, the impact of non-tidal loading is often below the measurement precision, but it can be relevant for polar motion.

In Table 4, we present a summary of how the EOP are affected when non-tidal loading is applied. We computed

[8] https://www.iers.org/IERS/EN/Publications/Bulletins/bulletins.html.

Table 4 WRMS values of the differences between the EOP of each non-tidal loading scenario and those of the reference scenario without non-tidal loading. The units are $[\mu as]$ for polar motion and the celestial pole offsets, $[\mu as/d]$ for the polar motion rates, $[\mu s]$ for $\Delta UT1$, and $[\mu s/d]$ for $LOD = -\partial \Delta UT1/\partial t$

Scenario	x_{pole}	$\partial x_{pole}/\partial t$	y_{pole}	$\partial y_{pole}/\partial t$	$\Delta UT1$	$\partial \Delta UT1/\partial t$	ΔX_{CIP}	ΔY_{CIP}
ATM ESMGFZ OBS	13.818	6.793	16.653	7.485	0.840	0.386	2.052	1.875
ATM ESMGFZ NEQ	13.587	2.133	16.731	2.494	0.848	0.066	1.077	1.164
ATM IMLS OBS	13.959	6.523	16.569	7.111	0.823	0.375	2.051	1.844
ATM IMLS NEQ	13.738	2.084	16.607	2.434	0.830	0.065	1.025	1.163
OCE ESMGFZ OBS	8.224	5.289	8.628	5.568	0.414	0.290	1.610	1.462
OCE ESMGFZ NEQ	8.123	1.374	8.354	1.403	0.411	0.044	0.762	0.780
OCE IMLS OBS	7.645	4.660	7.786	4.858	0.368	0.250	1.401	1.271
OCE IMLS NEQ	7.559	1.308	7.490	1.333	0.370	0.042	0.730	0.747
HYD ESMGFZ OBS	18.502	2.722	19.697	2.937	1.042	0.090	1.205	1.299
HYD ESMGFZ NEQ	18.441	2.666	19.734	2.932	1.049	0.085	1.259	1.312
HYD IMLS OBS	14.063	2.629	16.219	2.803	0.736	0.080	1.194	1.180
HYD IMLS NEQ	13.963	2.419	16.242	2.697	0.744	0.071	1.167	1.169
ALL ESMGFZ OBS	24.054	7.917	27.614	8.778	1.265	0.431	2.653	2.449
ALL ESMGFZ NEQ	23.923	3.406	27.620	3.803	1.256	0.106	1.639	1.591
ALL ESMGFZ OBS (incl. SLEL)	25.515	7.925	28.177	8.841	1.283	0.432	2.656	2.468
ALL ESMGFZ NEQ (incl. SLEL)	25.429	3.623	28.290	4.009	1.286	0.108	1.766	1.633
ALL IMLS OBS	20.422	7.679	25.923	8.281	1.099	0.418	2.485	2.304
ALL IMLS NEQ	20.336	3.181	25.842	3.711	1.100	0.093	1.536	1.535

WRMS values for the differences between the parameters estimated in each loading scenario and those of REF, and the following properties are revealed:

- The largest impact for all EOP is given with the ALL scenario.
- For ATM and OCE, the WRMS values for ESMGFZ and IMLS are matching very well, while there is more deviation for HYD and (consequently) ALL.
- The application level is most relevant for all rates and the celestial pole offsets, while it has much less influence on polar motion and $\Delta UT1$.
- Of all parts, HYD has the largest effect on polar motion (offsets), but the smallest effect on the celestial pole offsets.

The first two observations are in line with our previous statements. The third observation can be explained with the high sensitivity of the EOP rates to sub-daily variations in the site displacements. As the latter are only preserved at OBS, the impact on the rates is much smaller at NEQ. When rates are estimated, the application at observation level should hence be preferred. Only for HYD, where the temporal variation is low at both levels, the WRMS values for OBS and NEQ are of similar (small) size. The same behaviour holds for ΔX_{CIP} and ΔY_{CIP}, because the celestial pole offsets are periodically highly correlated with the rates of polar motion. If the latter were not estimated at all, there would be no impact on nutation by non-tidal loading, either. In general, the EOP (i.e. Earth rotation) are more affected by the horizontal than by the vertical site displacements.

Table 4 also contains the ALL scenarios including the mass conserving component SLEL of ESMGFZ. As indicated in Sect. 2.2, the results are very close to those of the original ALL scenario, with a striking (small) impact on polar motion only.

4.5 Tropospheric and clock parameters

As shown in Table 2, the clock correction terms as well as the zenith wet delays (ZWD) are estimated once per hour during a 24-h session in DOGS-RI. These parameters are significantly correlated with the station heights (compare van Dam and Herring 1994; Nothnagel et al. 2002, for example), which are most affected by non-tidal loading. Hence, if the corresponding site displacements are applied, there is a potential impact on the clock corrections and the ZWD. And as the latter have a high temporal resolution, they might be more capable of dealing with sub-daily variations. (The same holds for the tropospheric gradients, but since their temporal resolution is lower, we will focus on the other parameter types here.)

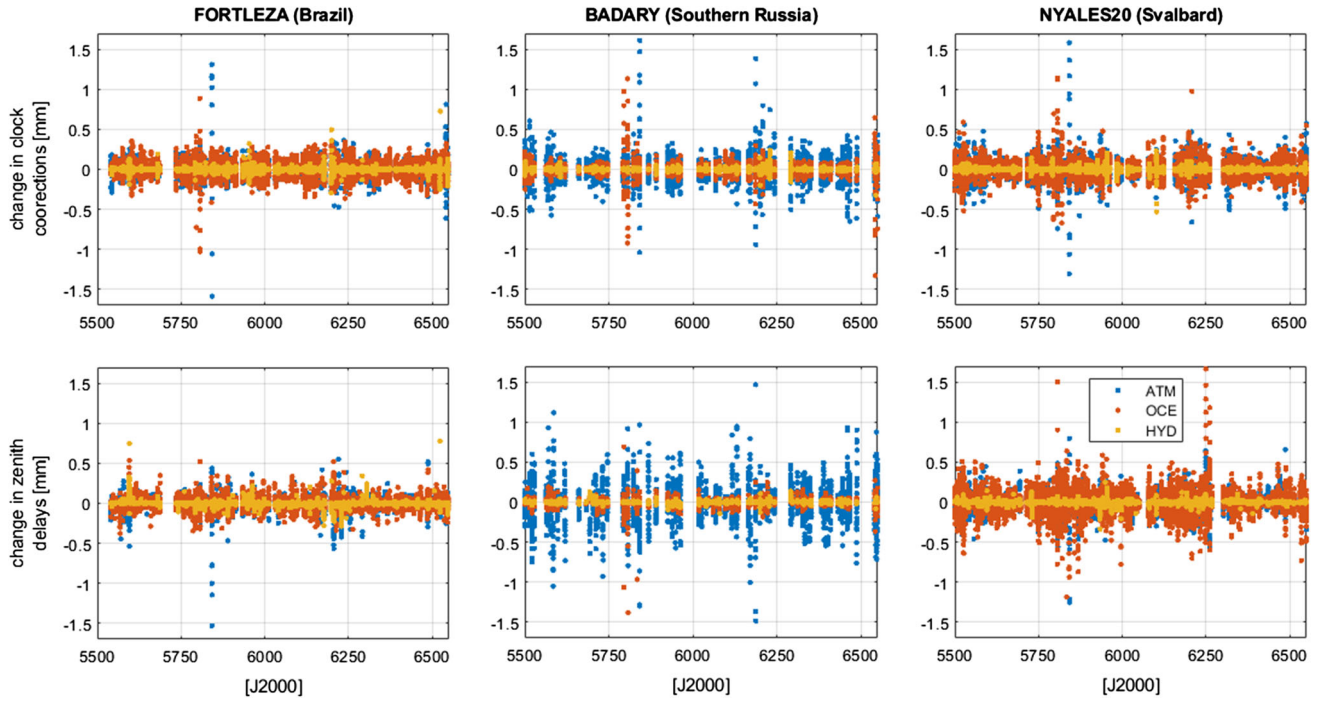

Fig. 10 Changes in clock correction (top panels) and zenith wet delay (bottom panels) parameters for the VLBI stations FORTLEZA (left), BADARY (middle), and NYALES20 (right), with respect to their values in REF when applying non-tidal atmospheric (blue dots), oceanic (red dots), or hydrological loading (yellow dots) at the observation level. The site displacements have been generated by ESMGFZ

Exemplary, in Fig. 10 the site displacements for ATM, OCE, and HYD (generated by ESMGFZ) have been applied at the observation level, and respective parameter changes are depicted for three VLBI stations. The changes are very small for both clock corrections and ZWD: they represent only a tiny fraction of the differences between two parameters estimated at distinct epochs during a session. This corresponds to the findings of Böhm et al. (2009, p. 1284), who say that "there is hardly any effect on the estimated ZWD because the estimated heights account for the atmospheric loading effect".

Even though the changes are small, we can derive certain properties from Fig. 10. Each dot refers to one estimated ZWD or clock correction term, and dots that appear to lie on a vertical line belong to the same session. The average spread of changes per session is about ± 0.3 mm for ATM and OCE, depending on the magnitude of the corresponding site displacements at a VLBI station. For HYD, however, the spread is significantly smaller (about ± 0.1 mm), even for VLBI stations with dominant hydrological loading (like FORTLEZA). The reason is the (missing) temporal variation of the associated site displacements during a session, as Fig. 11 indicates. There, we compare the changes in clock corrections and zenith wet delays for ATM at the two distinct application levels. At NEQ (as with HYD in general), only a constant displacement is applied, and this can be taken care of by the constant station coordinates. At OBS, on the other hand, the full temporal resolution of displacements is utilized, which cannot be accounted for by the constant corrections to the station coordinates alone. Hence, the remaining sub-daily variation is propagated into the supporting station parameters with finer resolution. Compared to their values in REF, the clock corrections and ZWD thus differ more for OBS (blue dots in Fig. 11) than for NEQ (red dots), and the degree of variation per session is directly proportional to the variation of the corresponding site displacements (grey dots).

As long as station coordinates (heights) are estimated, the overall effect of non-tidal loading on the supporting parameters is small. However, if one is mainly interested in estimating tropospheric delays with a high resolution, the impact becomes more significant and OBS should be used.

5 Conclusions

For VLBI, we have investigated the impact of the application of different non-tidal loading effects at the normal equation level (NEQ) in contrast to the observation level (OBS). The two main differences for NEQ are the linearization of the functional model with respect to the site displacements generated from non-tidal loading and the removal of temporal variation of these displacements during a session. The

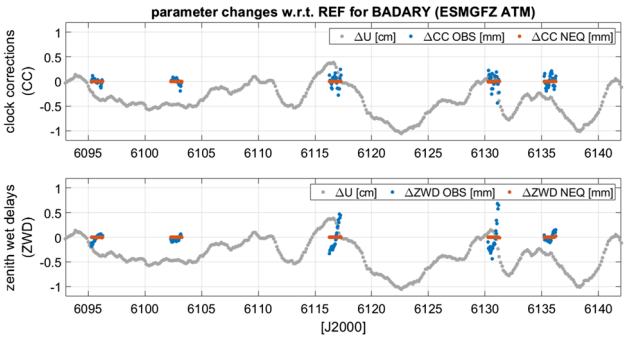

Fig. 11 Changes in clock correction (top panel) and zenith wet delay (bottom panel) parameters for the VLBI station BADARY, Russia, with respect to their values in REF when applying non-tidal atmospheric loading at the observation (blue dots) or the normal equation level (red dots). The corresponding vertical site displacements generated by ESMGFZ are also provided (grey dots) in their original resolution

linearization error is rather small for VLBI, so the main influence is given by the introduction of average displacement values.

Three different loading parts were applied both separately and jointly: non-tidal atmospheric (ATM), non-tidal oceanic (OCE), and hydrological loading (HYD). For HYD, the time series of site displacements is sufficiently smooth to be almost perfectly approximated by the session average, and hence the results for OBS and NEQ are nearly identical. But also for ATM, OCE, and the sum of all parts (ALL), we found that the approximation of OBS by NEQ is quite appropriate in most cases.

The overall impact of non-tidal loading is rather small at both application levels. The weighted sum of squared residuals and the formal errors of the estimates hardly change, since un-modelled displacements are already distributed between the parameters in the least-squares adjustment. Most of the displacements are shifted between the station coordinates themselves, but a minor part is also absorbed by the clock and tropospheric parameters. Due to their greater temporal resolution, and their significant correlation with the station heights, they are able to partly account for the sub-daily variation in the site displacements. Since there is no such variation at NEQ, some of the most striking differences between the application levels are observed for these parameters of station clocks and troposphere.

The same holds for EOP rates and celestial pole offsets: they are strongly affected by sub-daily variations, and hence we obtain greater differences between the results of OBS and NEQ than for the polar motion offsets. However, the impact of non-tidal loading is generally largest for the latter, with HYD representing the most dominant part.

Regarding the station positions, we found that the exclusive application of ATM or HYD is able to reduce the WRMS values with respect to long-term linear station motions by up to -12% for the vertical coordinate. Since the displacements for OCE are comparatively small, there is little reduction in the corresponding WRMS values, either (about -0.4% on average). The greatest improvement is obtained when all loading parts are applied jointly (up to -21.0% and about -4.0% on average), as there are different dominant parts at each station. These values are approximately equal for both application levels, and most importantly, we could show that the reduction in WRMS values is systematic across the VLBI stations.

We used site displacements from two providers: ESMGFZ and IMLS. Their data are quite similar, at least for ATM and OCE. The time series show significant differences only for HYD, and the reason are discrepancies in the underlying models for land water storage (LSDM and MERRA-2, respectively). However, both time series basically consist of a characteristic annual signal, and their application is capable of decreasing the corresponding signal for many stations' heights and the scale parameter of a 7-parameter Helmert transformation between the DTRF2014 and the networks of the various VLBI sessions. If ATM and OCE are applied separately, this reduction is not observed, but the behaviour of the annual signals is independent from the application level.

In total, the considered models for non-tidal loading make a valuable contribution. Furthermore, HYD was found to be as important as ATM. However, given the differences between LSDM and MERRA-2, the particular choice of the hydrological model is a crucial issue. From our results, it is hard to tell which model provides the better displacements. It is probably more relevant to long for consistency with the models for ATM and OCE and for global mass conservation (which is achieved with the component SLEL by ESMGFZ, for example).

We leave the effect on source coordinates for future research. It would also be interesting to investigate the impact on global station solutions (i.e. TRFs) or to examine the distinct application levels in connection with the other geodetic space techniques. The relevance of non-tidal loading in VLBI analysis might also further increase as soon as more error sources are removed, like the gravitational deformation of the VLBI antennas.

Acknowledgements Open Access funding provided by Projekt DEAL. We thank the IVS and its contributing institutions for generating and providing the VLBI observation data. Furthermore, we are grateful for the ESMGFZ and the IMLS supplying the non-tidal loading site displacements used in our study. Finally, we thank the two editors and three reviewers for their valuable feedback, which helped us to significantly improve the manuscript.

Author contributions MG and MB conceptualized the study; MG modified the analysis software DOGS-RI to incorporate the three different parts of non-tidal loading, performed the calculations of the distinct scenarios, and compiled the results; MB prepared the interface to create the VLBI solutions with DOGS-CS and process the Helmert transfor-

mations; MS improved the theoretical derivations; MG, MB, and MS discussed the results and set the focus of the investigations; FS supervised the work and discussed the results; MG wrote the manuscript with input by MB, MS, and FS.

Funding Open Access funding provided by Projekt DEAL.

Data availability The VLBI observation data can be found at ftp://cddis.nasa.gov/vlbi/ivsdata/vgosdb/. ESMGFZ and IMLS provide their site displacements computed from non-tidal loading at http://rz-vm115.gfz-potsdam.de:8080/repository and http://massloading.net, respectively. Other data sets generated and analysed during this study are available from the corresponding author on reasonable request.

Compliance with ethical standards

Conflict of interest The authors declare that they have no conflict of interest.

Appendix

See Tables 5 and 6.

Table 5 Statistics of the relative changes in WRMS (in [%]) for local station coordinates (East, North, Up) and baseline lengths (BLR) after application of individual and total site displacements provided by ESMGFZ. Negative values represent improvements, and "improv. portion" is the percentage of improved vs. total cases

Component	Statistic	ATM		OCE		HYD		ALL		ALL incl. SLEL	
		OBS	NEQ	OBS	NEQ	OBS	NEQ	OBS	NEQ	OBS	NEQ
East	Min	− 12.17	− 12.32	− 2.31	− 2.05	− 7.71	− 7.63	− 10.37	− 10.27	− 10.18	− 10.06
	Mean	− 0.61	− 0.63	− 0.33	− 0.29	0.63	0.71	− 0.28	− 0.27	− 0.24	− 0.19
	Median	− 0.28	− 0.32	− 0.20	− 0.27	0.16	0.39	− 0.43	− 0.17	− 0.44	− 0.11
	Max	4.24	4.25	3.24	3.44	6.77	6.77	10.30	10.54	11.20	11.47
	Improv. portion	61.0	63.4	63.4	73.2	46.3	36.6	58.5	58.5	56.1	56.1
North	Min	− 5.37	− 5.26	− 1.66	− 1.52	− 7.40	− 7.34	− 9.34	− 9.22	− 9.40	− 9.23
	Mean	− 0.93	− 0.95	− 0.38	− 0.28	− 0.49	− 0.45	− 1.69	− 1.66	− 1.66	− 1.62
	Median	− 0.95	− 0.72	− 0.32	− 0.27	− 0.58	− 0.44	− 1.42	− 1.36	− 1.38	− 1.39
	Max	3.53	3.40	0.93	0.90	9.63	9.63	10.64	10.74	11.28	11.39
	Improv. portion	70.7	73.2	75.6	73.2	68.3	65.9	75.6	73.2	75.6	75.6
Up	Min	− 9.23	− 9.11	− 1.97	− 1.95	− 9.25	− 9.20	− 20.97	− 18.78	− 21.01	− 18.75
	Mean	− 2.39	− 2.33	− 0.36	− 0.38	− 1.30	− 1.24	− 3.94	− 3.89	− 3.99	− 3.93
	Median	− 1.60	− 1.54	− 0.24	− 0.37	− 0.51	− 0.50	− 2.40	− 2.56	− 2.69	− 2.61
	Max	1.87	2.20	0.70	0.67	8.04	8.07	5.21	5.35	5.24	5.36
	Improv. portion	80.5	80.5	68.3	82.9	70.7	73.2	87.8	95.1	85.4	95.1
BLR	Min	− 11.38	− 11.60	− 3.92	− 3.60	− 24.16	− 24.11	− 30.85	− 31.03	− 30.85	− 30.98
	Mean	− 1.64	− 1.51	− 0.34	− 0.34	− 0.87	− 0.87	− 2.87	− 2.79	− 2.87	− 2.79
	Median	− 0.88	− 0.81	− 0.21	− 0.18	− 0.49	− 0.51	− 2.04	− 1.99	− 2.14	− 2.10
	Max	7.21	6.93	1.71	1.47	25.23	25.15	25.01	24.87	25.46	25.35
	Improv. portion	76.4	76.0	67.7	67.7	68.9	70.5	80.3	80.3	79.1	79.5

Table 6 Statistics of the relative changes in WRMS (in [%]) for local station coordinates (East, North, Up) and baseline lengths (BLR) after application of individual and total site displacements provided by IMLS. Negative values represent improvements, and "improv. portion" is the percentage of improved vs. total cases

Component	Statistic	ATM		OCE		HYD		ALL	
		OBS	NEQ	OBS	NEQ	OBS	NEQ	OBS	NEQ
East	Min	− 9.39	− 12.58	− 2.67	− 1.60	− 3.55	− 3.22	− 10.34	− 9.98
	Mean	− 0.55	− 0.63	− 0.44	− 0.27	− 0.21	0.06	− 1.27	− 1.12
	Median	− 0.25	− 0.27	− 0.16	− 0.18	− 0.44	0.17	− 0.98	− 0.99
	Max	4.27	4.27	3.44	3.21	2.74	3.20	3.94	3.81
	Improv. portion	63.4	63.4	73.2	70.7	63.4	46.3	70.7	68.3
North	Min	− 5.40	− 5.29	− 1.33	− 1.25	− 5.00	− 4.97	− 8.06	− 8.06
	Mean	− 0.93	− 0.92	− 0.28	− 0.25	− 0.71	− 0.60	− 2.00	− 1.92
	Median	− 0.92	− 0.72	− 0.27	− 0.25	− 0.69	− 0.44	− 1.56	− 1.38
	Max	3.11	3.06	0.97	0.90	4.70	4.74	2.48	2.27
	Improv. portion	73.2	75.6	70.7	73.2	70.7	68.3	82.9	85.4
Up	Min	− 9.23	− 9.21	− 1.76	− 1.38	− 12.42	− 12.40	− 20.85	− 20.48
	Mean	− 2.37	− 2.36	− 0.38	− 0.34	− 1.64	− 1.51	− 4.13	− 4.08
	Median	− 1.45	− 1.54	− 0.30	− 0.25	− 1.20	− 1.02	− 3.14	− 3.58
	Max	2.46	1.51	0.48	0.43	1.08	1.08	0.74	0.83
	Improv. portion	80.5	78.0	73.2	80.5	80.5	78.0	92.7	95.1
BLR	Min	− 11.56	− 11.88	− 4.05	− 3.21	− 9.11	− 9.33	− 22.42	− 22.63
	Mean	− 1.63	− 1.47	− 0.37	− 0.35	− 1.21	− 1.12	− 3.36	− 3.25
	Median	− 1.01	− 0.78	− 0.21	− 0.18	− 0.67	− 0.50	− 2.14	− 1.90
	Max	6.48	6.16	1.91	1.26	3.99	4.31	3.52	3.58
	Improv. portion	76.8	75.2	70.1	69.7	71.7	68.5	84.3	84.3

References

Altamimi Z, Rebischung P, Metivier L, Collilieux X (2016) ITRF2014: A new release of the international terrestrial reference frame modeling nonlinear station motions. J Geophys Res Solid Earth. https://doi.org/10.1002/2016JB013098

Angermann D, Drewes H, Krügel M, Meisel B, Gerstl M, Kelm R, Müller H, Seemüller W, Tesmer V (2004) ITRS combination center at DGFI: a terrestrial reference frame Realization 2003. Deutsche Geodätische Kommission, Reihe B, München

Bizouard C, Lambert S, Becker O, Richard JY (2017) Combined solution C04 for earth rotation parameters consistent with international terrestrial reference frame 2014. http://hpiers.obspm.fr/iers/eop/eopc04/C04.guide.pdf. Accessed 14 Jan 2020

Blewitt G (2003) Self-consistency in reference frames, geocenter definition, and surface loading of the solid Earth. J Geophys Res 108(B2):2103. https://doi.org/10.1029/2002JB002082

Böhm J, Schuh H (eds) (2013) Atmospheric effects in space geodesy. Springer, Berlin, p 138ff

Böhm J, Werl B, Schuh H (2006) Troposphere mapping functions for GPS and very long baseline interferometry from European Centre for Medium' Range Weather Forecasts operational analysis data. J Geophys Res. https://doi.org/10.1029/2005JB003629

Böhm J, Heinkelmann R, Mendes Cerveira PJ et al (2009) Atmospheric loading corrections at the observation level in VLBI analysis. J Geod 83:1107–1113

Chen G, Herring TA (1997) Effects of atmospheric azimuthal asymmetry on the analysis of space geodetic data. J Geophys Res 102(B9):20489–20502. https://doi.org/10.1029/97JB01739

Dach R, Böhm J, Lutz S, Steigenberger P, Beutler G (2010) Evaluation of the impact of atmospheric pressure loading modelling on GNSS data analysis. J Geod 85:75–91

Darwin GH (1882) On variations in the vertical due to elasticity of the earth's surface. Lond Edinb Dublin Philos Mag J Sci 14(90):409–427. https://doi.org/10.1080/14786448208628439

Dill R (2008) Hydrological model LSDM for operational Earth rotation and gravity field variations, Scientific Technical Report, 35p., STR08/09, GFZ Potsdam, Germany. https://doi.org/10.2312/GFZ.b103-08095.

Dill R, Dobslaw H (2013) Numerical simulations of global-scale high-resolution hydrological crustal deformations. J Geophys Res Solid Earth. https://doi.org/10.1002/jgrb.50353

Dill R, Klemann V, Dobslaw H (2018) Relocation of river storage from global hydrological models to georeferenced river channels for improved load-induced surface displacements. J Geophys Res 123(8):7151–7164. https://doi.org/10.1029/2018JB016141

Eriksson D, MacMillan DS (2014) Continental hydrology loading observed by VLBI measurements. J Geod 88:675–690

Farrell WE (1972) Deformation of the earth by surface loads. Rev Geophys Sp Phys 10(3):761–797

Fey AL, Gordon D, Jacobs CS, Ma C et al (2015) The second realization of the international celestial reference frame by very long baseline interferometry. Astron J 150(2):16

Gelaro R et al (2017) The Modern-era retrospective analysis for research and applications, version 2 (MERRA-2). J Clim 30(14):5419–5454

Gerstl M, Kelm R, Müller H, Ehrnsperger W (2000) DOGS-CS - Kombination und Lösung großer Gleichungssysteme. Internal Report, DGFI-TUM, München

Jungclaus J, Fischer N, Haak H, Lohmann K, Marotzke J, Matei D et al (2013) Characteristics of the ocean simulations in the Max Planck Institute Ocean Model (MPIOM) the ocean component of the MPI-earth system model. J Adv Model Earth Syst 5:422–446. https://doi.org/10.1002/jame.20023

Kock K-R (1999) Parameter estimation and hypothesis testing in linear models, 2nd edn. Springer, Berlin

Lyard F, Lefevre F, Letellier T, Francis O (2006) Modelling the global ocean tides: modern insights from FES2004. Ocean Dyn 56(5–6):394–415. https://doi.org/10.1007/s10236-006-0086-x

MacMillan DS (1995) Atmospheric gradients from very long baseline interferometry observations. Geophys Res Lett 22(9):1041–1044. https://doi.org/10.1029/95GL00887

MacMillan DS, Boy J-P (2004) Mass loading effects on crustal displacements measured by VLBI. In: IVS 2004 general meeting proceedings, pp 476–480

MacMillan DS, Gipson JM (1994) Atmospheric pressure loading parameters from very long baseline interferometry observations. J Geophys Res 99:18081–18087

Männel B, Dobslaw H, Dill R, Glaser S, Balidakis K, Thomas M, Schuh H (2019) Correcting surface loading at the observation level: impact on global GNSS and VLBI station networks. J Geod 93(10):2003–2017. https://doi.org/10.1007/s00190-019-01298-y

Nothnagel A (2009) Conventions on thermal expansion modelling of radio telescopes for geodetic and astrometric VLBI. J Geod 83(8):787–792. https://doi.org/10.1007/s00190-008-0284-z

Nothnagel A, Vennebusch M, Campbell J (2002) On correlations between parameters in geodetic VLBI data analysis. In: Vandenberg NR, Baver K (eds) IVS 2002 general meeting proceedings, pp 260–264

Petit G, Luzum B (eds) (2010) IERS Conventions, IERS Technical Note 36. Verlag des Bundesamts für Kartographie und Geodäsie, Frankfurt a. M

Petrov L (2015) The international mass loading service. arXiv:1503.00191 [physics.geo-ph]

Petrov L, Boy J-P (2004) Study of the atmospheric pressure loading signal in very long baseline interferometry observations. J Geophys Res 109:B03405. https://doi.org/10.1029/2003JB002500

Rabbel W, Zschau J (1985) Static deformations and gravity changes at Earth's surface due to atmospheric loading. J Geophys 56:81–89

Ray RD, Ponte RM (2003) Barometric tides from ECMWF operational analyses. Ann Geophys 21(8):1897–1910

Reichle R, Draper C, Liu Q, Girotto M, Mahanama S, Koster R, Lannoy GD (2017) Assessment of MERRA-2 land surface hydrology estimates. J Clim 30:2937–2960. https://doi.org/10.1175/JCLI-D-16-0720.1

Roggenbuck O, Thaller D, Engelhardt G, Franke S, Dach R, Steigenberger P (2015) Loading-Induced Deformation Due to Atmosphere, Ocean and Hydrology: Model Comparisons and the Impact on Global SLR, VLBI and GNSS Solutions. In: van Dam T (ed) REFAG 2014, International association of geodesy symposia, vol 146, Springer International Publishing Switzerland

Schuh H, Estermann G, Crétaux JF, Bergé-Nguyen M, van Dam T (2003) Investigation of hydrological and atmospheric loading by space geodetic techniques. In: Hwang C, Shum CK, Li J (eds) Satellite altimetry for geodesy, geophysics and oceanography, international association of geodesy symposia, vol 126. Springer, Berlin

Seitz M, Bloßfeld M, Angermann D, Schmid R, Gerstl M, Seitz F (2016) The new DGFI-TUM realization of the ITRS: DTRF2014 (data). Deutsches Geodätisches Forschungsinstitut, Munich https://doi.org/10.1594/PANGAEA.864046

Seitz M, Bloßfeld M, Angermann D, Gerstl M, Seitz F (2020) DTRF2014: The first secular ITRS realization considering non-tidal station loading, submitted to J. Geodesy

Sovers OJ, Fanselow JL, Jacobs CS (1998) Astrometry and geodesy with radio interferometry: experiments. Models Results Rev Mod Phys 70(4):1393–1454

Sun H-P, Ducarme B, Dehant V (1995) Effect of the atmospheric pressure on surface displacements. J Geod 70:131–139

Tregoning P, van Dam T (2005a) Effects of atmospheric pressure loading and seven-parameter transformations on estimates of geocenter motion and station heights from space geodetic observations. J Geophys Res 110:B03408. https://doi.org/10.1029/2004JB003334

Tregoning P, van Dam T (2005b) Atmospheric pressure loading corrections applied to GPS data at the observation level. Geophys Res Lett 32:L22310. https://doi.org/10.1029/2005GL024104

Tregoning P, Watson C, Ramillien G, McQueen H, Zhang J (2009) Detecting hydrologic deformation using GRACE and GPS. Geophys Res Lett. https://doi.org/10.1029/2009GL038718

van Dam TM, Herring TA (1994) Detection of atmospheric pressure loading using very long baseline interferometry measurements. J Geophys Res 99:4505–4518

van Dam TM, Wahr J (1987) Displacements of the Earth's surface due to atmospheric loading: effects on gravity and baseline measurements. J Geophys Res 92:1281–1286

van Dam T, Wahr J, Milly P, Shmakin A, Blewitt G, Lavallee D, Larson K et al (2001) Crustal displacements due to continental water loading. Geophys Res Lett 28:651–654. https://doi.org/10.1029/2000GL012120

van Dam T, Collilieux X, Wuite J et al (2012) Nontidal ocean loading: amplitudes and potential effects in GPS height time series. J Geod 86(11):1043–1057. https://doi.org/10.1007/s00190-012-0564-5

Williams SDP, Penna NT (2011) Non-tidal ocean loading effects on geodetic GPS heights. Geophys Res Lett 38:L09314. https://doi.org/10.1029/2011GL046940

P-4 Glomsda M., Seitz M., Bloßfeld M., and Seitz F. (submitted): **Effects of non-tidal loading applied in VLBI-only terrestrial reference frames**, submitted to *Journal of Geodesy*.

Abstract We investigate the impact of the correction for non-tidal loading (NTL) in the computation of terrestrial reference frames (TRF) from Very Long Baseline Interferometry (VLBI) observations. There are no conventional models for NTL in the geodetic community yet, but the Global Geophysical Fluid Center prepared a set of corresponding site displacements for the 2020 realization of the International Terrestrial Reference System. We make use of these data, which comprise the total NTL consisting of non-tidal atmospheric, oceanic, and hydrological loading. Since the displacement series contain trends, and since these affect the estimated station positions in a secular TRF, we remove the trends before the correction for NTL in most of our computations. The NTL is applied at two different levels of the parameter estimation process, the observation and the normal equation level. We find that the TRF statistics are hardly affected by the NTL, and the largest impact is given for the velocities of stations with short observation time spans. The application level is basically irrelevant for the estimated station positions, but it leads to differences in the rates of the jointly estimated Earth orientation parameters (EOP). Furthermore, due to the correlation between station coordinates and EOP of distinct session epochs in a TRF solution, the properties of the EOPs deviate from those in the single-session solutions. For both solution types, however, the correction for NTL reveals an annual signal in the newly estimated Earth rotation parameters. The latter are also influenced by the trends in the displacement series, if these are not removed.

Author contributions Matthias Glomsda and Manuela Seitz conceptualized the study. Matthias Glomsda prepared most of the non-tidal loading and all the VLBI data. He performed all calculations and analyses, compiled all but one figure and wrote the majority of the manuscript. Manuela Seitz provided the expertise and scripts for computing the TRFs. Mathis Bloßfeld prepared the final format of the non-tidal loading data. Both discussed the results and the validation strategy. Florian Seitz supervised the study and provides the basic resources. All authors read and improved the manuscript. The overall contribution of Matthias Glomsda is estimated to be 84%.

Noname manuscript No.
(will be inserted by the editor)

Effects of non-tidal loading applied in VLBI-only terrestrial reference frames

Matthias Glomsda* · **Manuela Seitz** · **Mathis Bloßfeld** · **Florian Seitz**

Received: date / Accepted: date

Abstract We investigate the impact of the reduction of non-tidal loading (NTL) in the computation of terrestrial reference frames (TRF) from Very Long Baseline Interferometry (VLBI) observations. There are no conventional models for NTL in the geodetic community yet, but the Global Geophysical Fluid Center prepared a set of corresponding site displacements for the 2020 realizations of the International Terrestrial Reference System. We make use of these data, which comprise the total NTL consisting of non-tidal atmospheric, oceanic, and hydrological loading. Since the displacement series contain trends, and since these affect the estimated station positions in a secular TRF, we remove the trends before reducing the NTL in most of our computations. The NTL is applied at two different levels of the parameter estimation process, the observation and the normal equation level. We find that the TRF statistics are hardly affected by the NTL, and the largest impact is given for the velocities of stations with short observation time spans. The application level is basically irrelevant for the estimated station positions, but it leads to differences in the rates of the jointly estimated Earth orientation parameters (EOP). Furthermore, due to the correlation between station coordinates and EOP of distinct session epochs in a TRF solution, the properties of the EOPs deviate from those in the single-session solutions. For both solution types, however, the reduction of the NTL reveals an annual signal in the newly estimated Earth rotation parameters. The latter are also influenced by the trends in the displacement series, if these are not removed.

*Matthias Glomsda
Deutsches Geodätisches Forschungsinstitut
der Technischen Universität München (DGFI-TUM),
Arcisstr. 21, 80333 München, Deutschland
E-mail: matthias.glomsda@tum.de

Keywords VLBI · non-tidal loading · normal equation level · ITRF · DTRF · GGFC

1 Introduction

The International Earth Rotation and Reference Systems Service (IERS) regularly publishes conventions for the geophysical models that should be applied in the analysis of the four geodetic space techniques: Very Long Baseline Interferometry (VLBI), Satellite Laser Ranging (SLR), the Global Navigation Satellite Systems (GNSS), and Doppler Orbitography and Radiopositioning Integrated by Satellite (DORIS). The latest version, the IERS Conventions 2010 (Petit and Luzum [2010]), contains models for the tidal deformation of the Earth's crust due to the gravitational forces of external bodies like the Sun and the Moon (Earth tides) or the rotation of the Earth (pole tides). The document further recognizes the existence of non-tidal deformations, which are generated from the redistribution of air and water masses on the Earth's surface. This non-tidal loading (NTL) is usually separated into atmospheric, oceanic, and hydrological components, and its relevance for the geodetic space techniques has been shown in many studies during the last decades (e.g., Rabbel and Zschau [1985], van Dam and Wahr [1987], MacMillan and Gipson [1994], van Dam et al. [2001], Tregoning and van Dam [2005a], Dach et al. [2010], Williams and Penna [2011], Eriksson and MacMillan [2014]). However, mainly because of the lack of generally accepted and/or accurate models for reducing the NTL, there still are none recommended in the current IERS Conventions. Only the International VLBI Service for Geodesy and Astrometry (IVS, Nothnagel et al. [2017]) requests its Analysis Centers (AC) to consider

non-tidal atmospheric loading (with arbitrary models) in the processing of VLBI observations.

A major application of the analysis results of the geodetic space techniques is the realization of the International Terrestrial Reference System (ITRS), which co-rotates with the Earth. Such realizations, called Terrestrial Reference Frames (TRF), contain the time-dependent coordinates of reference points (i.e., markers of the VLBI, SLR, GNSS, and DORIS observing stations) fixed to the Earth's crust. In secular TRFs, these coordinates change linearly with time, and hence the instantaneous, non-linear deformations of the Earth should ideally be reduced in the analysis. However, the contributions of the technique services IVS, International Laser Ranging Service (ILRS, Pavlis et al. [2021]), International GNSS Service (IGS, Johnston et al. [2017]), and International DORIS Service (IDS, Willis et al. [2010]) to the official realizations of the ITRS are not yet reduced by NTL, either. Besides the missing conventional models, this offers some flexibility for the handling of the residual signals w.r.t. the regularized station positions in the TRF combination.

To account for the non-tidal signals, the three IERS ITRS Combination Centers at the Institut national de l'information géographique et forestière (IGN, France), NASA's Jet Propulsion Laboratory (JPL, USA), and the Deutsches Geodätisches Forschungsinstitut der Technischen Universität München (DGFI-TUM, Germany) take distinct measures. In its two latest versions of the International Terrestrial Reference Frame (ITRF), the IGN estimated annual and semi-annual signals for the position time series of the four geodetic space techniques (both ITRF2014, Altamimi et al. [2016], and ITRF2020, Altamimi et al. [to be submitted]), as well as additional periodic signals for the first 8 draconitic harmonics of the Global Positioning System (GPS) for the position time series of the IGS (ITRF2020 only). After all, the ITRS realizations by IGN are based on a combination at the solution level. The ITRS realizations by DGFI-TUM, named DTRF, on the other hand, are combined at the normal equation level. DTRF2014 (Seitz et al. [2022]) and DTRF2020 (Seitz et al. [to be submitted]) are also reduced by NTL at the normal equation level, namely by the application of site displacements derived from geophysical models and provided by the Global Geophysical Fluid Center (GGFC). Finally, the ITRS realizations by JPL, named JTRF (e.g., JTRF2014, Abbondanza et al. [2017]), are no secular TRFs (like the ITRS realizations by IGN and DGFI-TUM) but epoch frames consisting of time series of reference points, which naturally contain any non-linear behaviour.

Collilieux et al. [2009] have analysed the application of site displacements due to NTL at the solution level for the ITRF combination. Their results were generally promising, but not significant enough to adapt this approach for the subsequent ITRF2014 or ITRF2020. The insufficient accuracy of the loading models was identified to be a major limitation. Seitz et al. [2022] describe the application at the normal equation level for the DTRF, and they also find that the reduction of NTL is basically beneficial, in particular for reducing annual signals in the datum parameters. The application at observation level, i.e., the reduction of NTL directly in the functional models of the geodetic space techniques, has mostly been discussed for daily or weekly single-technique solutions (e.g., Tregoning and van Dam [2005b], van Dam et al. [2012], Eriksson and MacMillan [2014]). Only few studies, e.g., Böhm et al. [2009] for VLBI, compute single-technique TRFs when reducing NTL. As long as the distinct technique services do not consider NTL consistently, and no institute processes all techniques jointly, the analysis of a combined TRF with NTL applied at the observation level is not possible.

Our study will not completely fill this gap, either. Nevertheless, we generate several VLBI-only TRFs, which reduce NTL at both the observation and the normal equation level. We make use of the same geophysical NTL models as will be applied in the DTRF2020 (compare Glomsda et al. [2022]), which represent recent updates and should be more accurate than the models used in the previous decades. We examine the discrepancies between the application levels and hence the suitability of a reduction of NTL at the normal equation level in a TRF. This might provide insights for the inter-technique combination as well. In previous studies (Glomsda et al. [2020], Glomsda et al. [2021]), we investigated the impact of NTL in VLBI single-session analysis, and we will check whether there are qualitative differences between the two types of solutions here. In particular, we will focus on the Earth orientation parameters (EOP) and verify the effect of trends in the NTL data.

In Section 2, we start with a description of the input data, i.e., the VLBI observations and the site displacements obtained from the NTL models. The theory of the computation of single-technique TRFs and the reduction of non-linear displacements is summarized in Section 3. The main results regarding the impact of the reduction of NTL on the estimated station coordinates and velocities and the EOP are presented in Section 4, before the final conclusions are drawn in Section 5.

2 Input data

2.1 VLBI single-session solutions

In this study, we basically use the same legacy VLBI observations that have been considered as input to the ITRS 2020 realization. These comprise all 24 hour VLBI sessions with at least three antennas involved between August 1979 and December 2020[1]. The official contribution by the IVS is a combination of the reprocessed data for these sessions provided by the distinct IVS ACs (Hellmers et al. [2022]). All ACs had to apply consistent geophysical models in their processing - in particular, the computed VLBI observations must not be reduced by any NTL. Since we are going to apply NTL at the observation level, however, we are not able to use the IVS contribution. Instead, we have to compute our own single-session solutions, generated with the DGFI-TUM Orbit and Geodetic parameter estimation Software (DOGS; Gerstl et al. [2000], Kwak et al. [2017]).

We did not exactly recycle our IVS input (DGFI-TUM is an operational AC of the IVS), but we included a few model updates for the new solutions, which are not expected to have an impact on our results. Most importantly, we chose the International Terrestrial Reference Frame 2020 (ITRF2020, Altamimi et al. [to be submitted]) for the a priori antenna positions. Furthermore, we applied the latest DGFI-TUM ocean tide model EOT20 (Hart-Davis et al. [2021]), and we increased the resolution of the estimated tropospheric gradients from 24 to 6 hours. Finally, the Galactic aberration of the radio source positions (see, e.g., MacMillan et al. [2019]) is no longer considered by a direct shift of the a priori positions of the International Celestial Reference Frame 3 (ICRF3, Charlot et al. [2020]), but by the delay correction in the theoretical VLBI model. The other geophysical and technique-specific models are in line with the IERS Conventions 2010 and the IVS requirements for the ITRS 2020 realization.

We could not include the full set of the aforementioned legacy sessions, because some of them either failed in the single-session reprocessing already, or their results were corrupting our subsequent TRF solutions. In the end, we used 5,878 (out of 6,519) sessions between 1980 and 2020.

2.2 Non-tidal loading data

Concerning the NTL data, we picked the contribution to the ITRS 2020 realization by the GGFC (Boy [2021]). The same data will be applied in the DTRF2020 and have been analysed extensively by Glomsda et al. [2022]. They consist of site displacements for the relevant geodetic observing stations, which have been derived from surface pressure anomalies by the common global convolution with weighting Green's functions (see, e.g., Farrell [1972], and Petrov and Boy [2004]). The driving geophysical and meteorological models for the pressure anomalies are ECMWF (European Center for Medium-range Weather Forecasts) ERA5 (Hersbach et al. [2020]) for the non-tidal atmospheric and hydrological loading, and the Toulouse Unstructured Grid Ocean model (TUGO-m, see Carrère and Lyard [2003], and Mémin et al. [2020]) for the non-tidal oceanic loading. The site displacements for these three NTL components are available separately, but Boy [2021] ensured the conservation of mass when they are combined.

All displacements are provided in the center of figure of the solid Earth (CF) frame, and in the center of mass of the total Earth system (CM) frame, which includes the atmosphere and the hydrosphere. The differences

$$\boldsymbol{\delta}^{CF}_{NTL}(\boldsymbol{S},t) - \boldsymbol{\delta}^{CM}_{NTL}(\boldsymbol{S},t) = \boldsymbol{g}_{NTL}(t) \tag{1}$$

between the CF and CM displacements $\boldsymbol{\delta}_{NTL}$ at a site $\boldsymbol{S}$ and an epoch t yield the geocenter motion contributions $\boldsymbol{g}_{NTL}(t)$ generated by NTL, which are equal for all sites. Geocenter motion is the time series of the distance between the origins of the CF and CM frames (see, e.g., Dong et al. [2003]), and it plays a crucial role in the realization of the ITRS (see Altamimi et al. [2016], or Seitz et al. [2022]). For the DTRF2020, we will apply the site displacements of the CM frame (see Glomsda et al. [2022]), as the center of mass is the origin of the ITRS (realized by SLR). For VLBI, the choice of the frame is basically irrelevant (see, e.g., Eriksson and MacMillan [2014], and Glomsda et al. [2021]), because this technique depends on the baselines between each two radio antennas. When computing the difference between two antennas' positions $\boldsymbol{S}_1$ and $\boldsymbol{S}_2$, which have both been shifted by displacements $\boldsymbol{\delta}_{NTL}$, the site-independent translation $\boldsymbol{g}_{NTL}$ cancels, such that

$$\begin{aligned}&\boldsymbol{\delta}^{CF}_{NTL}(\boldsymbol{S}_2,t) - \boldsymbol{\delta}^{CF}_{NTL}(\boldsymbol{S}_1,t)\\ &= \boldsymbol{\delta}^{CM}_{NTL}(\boldsymbol{S}_2,t) - \boldsymbol{\delta}^{CM}_{NTL}(\boldsymbol{S}_1,t).\end{aligned} \tag{2}$$

To recycle the NTL data for the DTRF2020, we applied the CM displacements in this study, too. The CF displacements, however, can be computed with Eq. (1) and the geocenter contribution time series, which is also provided by Boy [2021].

The time series of the site displacements and the corresponding geocenter motion contribution contain linear trends (compare Glomsda et al. [2022]), in particular for the hydrological component. Such trends distort the estimated station positions and velocities of

[1] https://ivscc.gsfc.nasa.gov/IVS_AC/IVS-AC_ITRF2020.htm

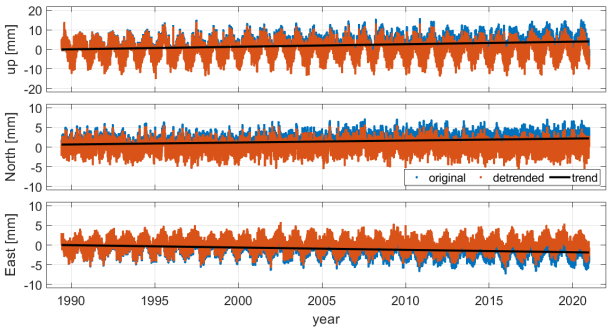

Fig. 1 Time series of the combined site displacements generated from non-tidal atmospheric, oceanic, and hydrological loading for the VLBI antenna NOTO in Italy. The original values (blue) have been reduced by the linear trend (black) to obtain the detrended series (red). Top: up component, middle: North component, bottom: East component.

secular reference frames, i.e., a part of the linear station motions will be captured by the NTL. To avoid this for both the DTRF2020 and the VLBI-only TRFs generated in this study, the trends are removed from the displacement time series before they are applied (see Fig. 1). However, we will also investigate the case which includes these trends.

Finally, since the input data for the ITRS 2020 realization have not been reduced by NTL at the observation level, only the normal equations of the distinct geodetic space techniques can be reduced during the computation of the DTRF2020. At the normal equation level, however, the temporal resolution of the site displacements gets reduced. Originally, the data by Boy [2021] has a resolution of 1 hour, but only one displacement value can be applied per site and normal equation. Hence, average values have to be computed for the reduction in the DTRF2020. For VLBI and GNSS, this would be the average displacement (per antenna) for each 24 hour observing session. For SLR and DORIS, on the other hand, these would even be 7-day (15-day in the early years of SLR) averages.

3 VLBI-only terrestrial reference frame

3.1 General computation

At first, observation and normal equations are set up for the single VLBI sessions with DOGS-RI (Radio Interferometry). The estimated variables comprise constant antenna coordinates, constant radio source coordinates, linear Earth rotation parameters (ERP), constant celestial pole offsets, as well as piece-wise linear clock and tropospheric parameters. The estimation process itself is based on the Gauss-Markov model (see, e.g., Koch [1999]), which we will recap briefly.

The linearized observation equations of each session s are given by

$$\boldsymbol{A}^s \boldsymbol{\Delta x}^s = \boldsymbol{l}^s, \tag{3}$$

with the matrix of partial derivatives $A^s_{ij} = \partial f^s(t_i)/\partial x^s_j$ of the theoretical VLBI delay model f w.r.t. the parameters x^s_j $(j = 1, \ldots, n^s)$, the vector $\boldsymbol{\Delta x}^s$ of corrections to the a priori parameter vector $\boldsymbol{x}^{s,0}$, and the observed minus computed (OMC) vector

$$\boldsymbol{l}^s = \boldsymbol{b}^s - \boldsymbol{f}(\boldsymbol{x}^{s,0}). \tag{4}$$

The optimum solution in terms of the minimum sum of squared residuals

$$\boldsymbol{v}^s = \boldsymbol{A}^s \boldsymbol{\Delta x}^s - \boldsymbol{l}^s \tag{5}$$

is given by the solution of the normal equation

$$\boldsymbol{\Delta x}^s = (\boldsymbol{N}^s + \boldsymbol{N}^s_D)^{-1} \boldsymbol{y}^s, \tag{6}$$

where $\boldsymbol{N}^s = (\boldsymbol{A}^s)^T \boldsymbol{P}^s \boldsymbol{A}^s$ is called the normal equation matrix with right-hand-side $\boldsymbol{y}^s = (\boldsymbol{A}^s)^T \boldsymbol{P}^s \boldsymbol{l}^s$. $\boldsymbol{N}^s_D$ is a matrix of datum constraints (usually no-net-translation, NNT, for antenna coordinates, and no-net-rotation, NNR, for the antenna and radio source coordinates), which is necessary to regularize the normal equation matrix. $\boldsymbol{P}^s$ is a (usually diagonal) weight matrix filled with the reciprocals of the squared formal errors of the real observations b^s_i $(i = 1, \ldots, m^s)$. Finally, the a posteriori variance factor of the single-session solutions is

$$(\hat{\sigma}^s_0)^2 = \frac{(\boldsymbol{v}^s)^T \boldsymbol{P}^s \boldsymbol{v}^s}{m^s - n^s} \quad (m^s \gg n^s). \tag{7}$$

When computing the single-session and TRF solutions with DOGS-CS (Combination & Solution) for this study, we reduce the clock and tropospheric parameters, and fix the radio source coordinates to their a priori values. For our secular TRFs, we additionally transform the constant antenna coordinates $p(t_s)$ at the session epochs t_s into linear ones, parameterized by an offset $o(t_0)$ at a suitable reference epoch t_0 and a constant velocity d (compare Angermann et al. [2004], Seitz et al. [2022]):

$$p(t_s) = o(t_0) + (t_s - t_0)\, d. \tag{8}$$

As a consequence, the left-hand-side of the observation equation (3) is modified,

$$\boldsymbol{A}^s \boldsymbol{\Delta p}^s \leftarrow [\boldsymbol{A}^s \;\; \boldsymbol{A}^s \boldsymbol{B}^s] \begin{bmatrix} \boldsymbol{\Delta o}^s \\ \boldsymbol{\Delta d}^s \end{bmatrix}, \tag{9}$$

with matrix

$$\boldsymbol{B}^s = \begin{pmatrix} (t_s - t_0) \ldots & 0 \\ \vdots & \ddots \quad \vdots \\ 0 & \ldots (t_s - t_0) \end{pmatrix} \tag{10}$$

(see Bloßfeld [2015]; for ease of notation, we restrict the formulas to the antenna coordinates in $\boldsymbol{p}$). Likewise, the normal equation system is transformed,

$$\boldsymbol{N}^s \leftarrow \begin{bmatrix} \boldsymbol{N}^s & \boldsymbol{N}^s\boldsymbol{B}^s \\ \boldsymbol{B}^s\boldsymbol{N}^s & \boldsymbol{B}^s\boldsymbol{N}^s\boldsymbol{B}^s \end{bmatrix}, \; \boldsymbol{y}^s \leftarrow \begin{bmatrix} \boldsymbol{y}^s \\ \boldsymbol{B}^s\boldsymbol{y}^s \end{bmatrix}, \tag{11}$$

and the new a priori values fulfill $\boldsymbol{o}^{s,0} + \boldsymbol{B}^s\boldsymbol{d}^{s,0} = \boldsymbol{p}^{s,0}$.

The secular TRF can now be obtained from the combination of the single-session normal equation systems. The q transformed, datum-free, and session-wise components are stacked like this:

$$\boldsymbol{M} = \sum_{s=1}^{q} \boldsymbol{N}^s, \quad \boldsymbol{z} = \sum_{s=1}^{q} \boldsymbol{y}^s, \tag{12}$$

where the normal matrices $\boldsymbol{N}^s$ and right-hand-sides $\boldsymbol{y}^s$ have been extended by rows and columns of zeros to match a dimension of the total number of estimated parameters. With an a priori variance factor σ_0^2, the weight matrix of the combination is given by

$$\boldsymbol{P} = \sigma_0^2 \begin{pmatrix} \boldsymbol{P}^1 \ldots & 0 \\ \vdots & \ddots \quad \vdots \\ 0 & \ldots \boldsymbol{P}^q \end{pmatrix}. \tag{13}$$

The datum constraints in a matrix $\boldsymbol{M}_D$ are only applied to the stacked normal equation system, and they now consist of NNT and NNR conditions for the antenna positions and velocities. Finally, the TRF solution is obtained by solving

$$\boldsymbol{\Delta x} = (\boldsymbol{M} + \boldsymbol{M}_D)^{-1}\, \boldsymbol{z} \tag{14}$$

for the transformed and stacked parameter vector $\boldsymbol{x}$, and the a posteriori variance factor is computed as

$$\hat{\sigma}_0^2 = \frac{\boldsymbol{v}^T \boldsymbol{P}\, \boldsymbol{v}}{\left(\sum\limits_{s=1}^{q} m^s\right) - n^{TRF}}. \tag{15}$$

3.2 Application of site displacements

As mentioned in Section 2.2, the reduction of NTL is performed by the application of site displacements to the observing stations during the analysis. Different application levels are available:

1. the *observation level*, where the site displacements are directly considered in the linearized observation equations (see, e.g., van Dam and Wahr [1987], or Petrov and Boy [2004]). This is the most rigorous approach.

2. the *normal equation level*, where the normal equation system is modified (see, e.g., Seitz et al. [2022], or Glomsda et al. [2020]). This is only an approximate approach.

3. the *solution level*, where the site displacements are simply removed from the final coordinate estimates (see, e.g., Böhm et al. [2009], or Williams and Penna [2011]). This approach does not allow for a consistent estimation of regularized positions and other parameters (e.g., EOP).

We present some theoretical implications of the application of NTL in a secular (VLBI-only) TRF. Glomsda et al. [2021] have done this for VLBI single-session analysis.

3.2.1 Observation level

If site displacements (e.g., generated from NTL) are applied at the observation level of the Gauss-Markov model, the theoretical delay function f changes to $\tilde{f}$. Following Glomsda et al. [2021], we end up with new normal equation systems for each session s,

$$\boldsymbol{\Delta}\tilde{\boldsymbol{x}}^s = \left(\tilde{\boldsymbol{N}}^s + \boldsymbol{N}_D^s\right)^{-1} \tilde{\boldsymbol{y}}^s, \tag{16}$$

and consequently a new stacked normal equation system for the TRF:

$$\tilde{\boldsymbol{M}} = \sum_{s=1}^{q} \tilde{\boldsymbol{N}}^s, \quad \tilde{\boldsymbol{z}} = \sum_{s=1}^{q} \tilde{\boldsymbol{y}}^s. \tag{17}$$

Glomsda et al. [2021] claimed that $\tilde{\boldsymbol{A}}^s \approx \boldsymbol{A}^s$, and hence $\tilde{\boldsymbol{N}}^s \approx \boldsymbol{N}^s$ for most s. However, the contingently small discrepancies per session might accumulate to a significant deviation of the new matrix $\tilde{\boldsymbol{M}}$ from $\boldsymbol{M}$. In addition, the new offset and velocity parameters $\tilde{\boldsymbol{o}}^s$ and $\tilde{\boldsymbol{d}}^s$ depend on $\tilde{\boldsymbol{A}}^s$, respectively.

3.2.2 Normal equation level

Applying average site displacements in a vector $\bar{\boldsymbol{\delta}}^s_{NTL}$ at the normal equation level means approximating the new theoretical (delay) function by

$$\tilde{\boldsymbol{f}}^s \approx \bar{\boldsymbol{f}}^s := \boldsymbol{f}^s + \boldsymbol{A}^s\, \bar{\boldsymbol{\delta}}^s_{NTL} \tag{18}$$

(see Seitz et al. [2022]). As a consequence, the right-hand-side of the normal equation system converts to

$$\begin{aligned}\bar{\boldsymbol{y}}^s &:= (\boldsymbol{A}^s)^T \boldsymbol{P}^s\, \bar{\boldsymbol{l}}^s \\ &:= (\boldsymbol{A}^s)^T \boldsymbol{P}^s \left(\boldsymbol{b}^s - \bar{\boldsymbol{f}}^s\right) \\ &= (\boldsymbol{A}^s)^T \boldsymbol{P}^s \left(\boldsymbol{l}^s - \boldsymbol{A}^s\, \bar{\boldsymbol{\delta}}^s_{NTL}\right) \\ &= \boldsymbol{y}^s - \boldsymbol{N}^s\, \bar{\boldsymbol{\delta}}^s_{NTL},\end{aligned} \tag{19}$$

while the normal equation matrices $\boldsymbol{N}^s$ remain unchanged. The new stacked system becomes

$$\bar{\boldsymbol{M}} = \boldsymbol{M} = \sum_{s=1}^{q} \boldsymbol{N}^s, \quad \bar{\boldsymbol{z}} = \sum_{s=1}^{q} \bar{\boldsymbol{y}}^s. \tag{20}$$

3.2.3 Comparison of application levels

Comparing Eqs. (17) and (20), we identify several potential sources for deviations between the TRFs with NTL applied at the observation and the normal equation level, respectively:

- the loss of temporal resolution by the average displacement vector $\bar{\boldsymbol{\delta}}^s_{NTL}$ in Eq. (18).
- the differences in the single-session normal equation matrices, $\tilde{\boldsymbol{N}}^s$ vs. $\boldsymbol{N}^s$.
- the differences in the single-session observation matrices, $\tilde{\boldsymbol{A}}^s$ vs. $\boldsymbol{A}^s$, which affect the estimated station motions in Eq. (9).

The impact of the application level on the estimated antenna positions might mostly be low in VLBI single-session analysis (compare Glomsda et al. [2020], and Glomsda et al. [2021]), especially if the temporal variation of the displacements is small during a session (which holds for the hydrological loading). However, if thousands of sessions are stacked, the various small and sometimes large deviations could produce more significant differences for a TRF solution.

On the other hand, a linear station motion is estimated in a TRF. Seasonal and other variations in single-session positions are hence averaged out, at least if the coordinate time series are long enough (e.g., more than 2.5 years according to Blewitt and Lavallée [2002]). As a consequence, the differences between the application levels might be averaged out as well. Significant deviations might rather be observable for the jointly estimated EOP, which are not bound to a linear motion across all sessions.

3.2.4 Single-sessions vs. TRF

An eminent difference between single-session and TRF solutions is given by the datum constraints. There is a separate matrix $\boldsymbol{N}^s_D$ for each session, and Böhm et al. [2009] and Glomsda et al. [2021] claim that the choice of datum stations determines how the (NTL) site displacements are transformed into changes in the estimated antenna coordinates. Hence, there is a network effect in the position time series created from single-session solutions. In a TRF computation, on the other hand, the datum constraints are only applied after the stacking of the datum-free normal equation systems. These constraints are defined for a fixed set of stable stations and across all sessions. As a consequence, there is no comparable network effect related to the NTL, at least no time-dependent one.

Table 1 The distinct setups for VLBI-only TRFs computed in this study.

scenario	description
REF	reference solution without any NTL
ATM	non-tidal atmospheric loading without trends at observation level
SUM	total NTL without trends at observation level
NEQ	total NTL without trends at normal equation level
SU2	total NTL including trends at observation level

4 Impact of non-tidal loading on TRF

4.1 NTL scenarios

In Tab. 1, we summarize the distinct VLBI-only TRF scenarios that we investigate in this study. REF is the reference scenario, where no NTL is applied at all. The formulas and notations of Section 3.1 belong to this case. In the scenario ATM, we apply only non-tidal atmospheric loading (i.e., the ECMWF ERA5 data with the inverted barometer hypothesis for the atmospheric pressure above the oceans, compare Boy [2021], and Glomsda et al. [2022]) at the observation level. This is the setup for the regular, non-ITRS IVS contributions. All three (atmospheric, oceanic, hydrological) components of NTL are applied at the observation level in scenario SUM. As with scenario ATM, the linear trends have been removed from the displacements (compare Section 2.2). In scenario NEQ, we apply the combined and detrended NTL data at the normal equation level, as is done for the DTRF2020. Finally, in scenario SU2, we return to the observation level, but this time we apply the sum of all NTL components inclusive of linear trends, i.e., the original displacement series as provided by Boy [2021].

4.2 Specific TRF computation

We basically generate all VLBI-only TRFs according to the approach described in Section 3.1. Some more details, however, need to be mentioned.

A few antennas do not show a linear motion across the whole observation period, because their positions have been abruptly shifted by Earthquakes. After these events, the antenna coordinates follow non-linear motions due to post-seismic deformation (PSD; compare Altamimi et al. [2016]) of the Earth's crust. Such deviations from the constant velocity d need to be accounted for, and we apply the same approach as will be used for the DTRF2020. Namely, we model the PSD by exponential or logarithmic functions, or by combinations of the latter, for each corresponding antenna coordinate separately. The resulting site displacements are valid for certain periods after each Earthquake, and all normal equations of VLBI sessions that take place during these periods and contain an antenna affected by an Earthquake are corrected for these displacements before being stacked.

The introduction of antenna velocities according to Eqs. (8) and (11) is only performed after the single-session normal equations have been corrected for PSD. As a priori values $\boldsymbol{o}^0$ and $\boldsymbol{d}^0$ for the new antenna offsets at the reference epoch and the velocities, we use the values of the previous DTRF2014 (Seitz et al. [2022]) and zero, respectively. The reference epoch t_0 is set to 2010.0, like for the DTRF2020. For each observation period before and after a position series discontinuity, new offsets and velocities need to be set up. As a consequence, a single antenna can have several so-called *solutions*, which are valid at distinct intervals. Next to the ones created by Earthquakes, there are also other antenna-specific discontinuities (compare Seitz et al. [2022]). For example, we introduced a break at 2017-10-18 for the 20m antenna at Ny Alesund, Svalbard, due to post-glacial uplift (Kierulf et al. [2022]), and another one at 2011-11-10 for the 40m antenna at Yebes, Spain, due to the introduction of the gravitational deformation model (Nothnagel et al. [2014]).

We are not estimating parameters for all antennas in our set of single sessions. In particular, we reduce all solutions that participate in less than 20 sessions to obtain sufficiently stable data. In the end, we estimate offsets and velocities for 119 solutions of 84 stations.

As already mentioned in Section 3.1, the remaining free parameters are the linear antenna positions and the EOP. The datum constraints $\boldsymbol{M}_D$ consist of NNT and NNR conditions w.r.t. the antenna offsets and drifts of 33 steady stations. The EOP have been loosely constrained with standard deviations of 10 mas, 50 mas, and 5 ms for the nutation (DX_{CIP}, DY_{CIP}), polar motion (dx_{pol}, dy_{pol}, as well as their rates), and Earth rotation ($\Delta UT1, LOD$) parameters, respectively. These values ensure numerical stability but keep the diversity of the estimated formal errors between the EOP.

Table 2 Statistics of the distinct VLBI-only TRF scenarios.

scenario	$\boldsymbol{v}^T\boldsymbol{P}\,\boldsymbol{v}$	$\hat{\sigma}_0$
REF	21,141,960	1.18057
ATM	21,117,324	1.17989
SUM	21,097,685	1.17934
NEQ	21,100,572	1.17942
SU2	21,098,917	1.17937

4.3 Solution statistics and formal errors

In Tab. 2, we summarize the statistics for our distinct TRF solutions. They do not change significantly after the reduction of any NTL, so the least-squares optimization for a secular TRF appears to be rather insensitive to this effect. At least, we observe an improvement in the weighted square sum of residuals $\boldsymbol{v}^T\boldsymbol{P}\,\boldsymbol{v}$ in each case. The best, i.e., smallest value is obtained when all three NTL components are considered (SUM), and the values are quite close for the two application levels (SUM and NEQ).

The ratios between the a posteriori variance factors $\hat{\sigma}_0^2$ of the NTL scenarios and the reference scenario will determine the size of the change in the formal errors of the estimated parameters. Namely, the parameter covariance matrix is given by

$$\boldsymbol{C}_{\hat{x}\hat{x}} = \hat{\sigma}_0^2 \begin{cases} (\boldsymbol{M}+\boldsymbol{M}_D)^{-1} & \text{for REF, NEQ;} \\ (\tilde{\boldsymbol{M}}+\boldsymbol{M}_D)^{-1} & \text{for ATM, SUM, SU2.} \end{cases} \tag{21}$$

From these equations, we see that the formal errors are additionally affected by the new entries in the combined normal matrix $\tilde{\boldsymbol{M}}$ when the NTL has been applied at the observation level.

In Fig. 2, we show the changes in formal errors for the estimated x-coordinate velocities after the application of NTL. The absolute changes are very small (with a magnitude of a few micrometers, compare the top panel), and the relative changes are basically located on the lines representing $(\hat{\sigma}_0^X)^2/(\hat{\sigma}_0^{REF})^2$ (bottom panel). However, there is some additional variation for the scenarios where the covariance matrix of the TRF contains $\tilde{\boldsymbol{M}}$, i.e., all except for NEQ. The formal errors are ordered by the length of the observation periods for their corresponding antennas. The absolute changes in

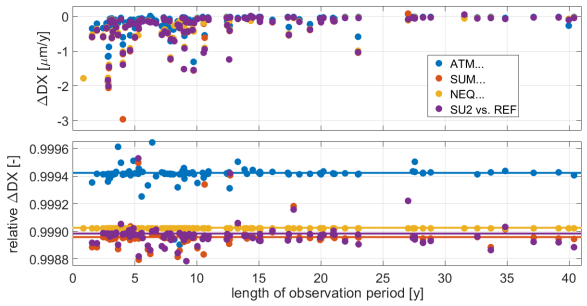

Fig. 2 Original (top) and relative (bottom) changes in the formal errors of the estimated x-coordinate velocities for our NTL scenarios (blue: ATM, red: SUM, yellow: NEQ, purple: SU2) w.r.t. the reference scenario REF. The corresponding antennas (x-axes) are ordered by the length of their observation periods. The straight lines indicate the ratios between the a posteriori variance factors of the NTL scenarios and the scenario REF.

formal errors are largest for antennas with short observation periods, mainly because the relative changes are more or less constant, and the errors are largest for these antennas in the reference scenario in the first place. The same behaviour is also observed for the formal errors of the other estimated parameters.

4.4 Estimated antenna motions

The estimated positions and horizontal velocities of the reference scenario and the scenario with all NTL components applied at the observation level are shown in Figure 3. The differences in velocities are rather small and hardly visible, also for the vertical velocities (not shown here). Hence, they are plotted again in local (North, East, up) coordinates in Fig. 4, in which the antennas are still ordered by the length of their observation periods. When reducing NTL, the position offsets can change by a few millimeters, but mostly for antennas with short observation periods. The largest vertical velocity change is about 6 mm/y for the antenna RAEGYEB, Spain, which has the shortest observation period of less than 1 year. According to Blewitt and Lavallée [2002], at least 2.5 years of observations are necessary to estimate a reliable velocity. But, if we reduce residual signals like NTL, we expect the velocity estimates to be improved for the short periods. As Fig. 4 suggests, the impact of NTL is basically negligible for observation periods longer than 15 years, since the non-linear signals are almost completely averaged out. Soja et al. [2016] emphasize that the period length itself is not the main criterion, but an antenna also needs to participate in a sufficiently large number of sessions. If there are only few sessions available for particular antennas, this is also reflected in large formal errors of the estimated position parameters. The impact of the reduction of NTL is seldom exceeding these formal errors, anyways (compare Figure 4 again).

Another conclusion from Fig. 4 is the minor relevance of the application level of the NTL for the linear station motions. The differences in estimates for scenarios SUM and NEQ w.r.t. the reference scenario are very similar, so the potential sources for deviations listed in Section 3.2 do not take much effect. Regarding the pure TRF, reducing NTL at the normal equation level hence is a suitable approximation for the reduction at the observation level.

An important open question is whether the new antenna motions are beneficial. When comparing our VLBI-only TRFs to the VLBI single-technique solution of the ITRF2020 (Altamimi et al. [to be submitted]), we found a very good agreement for stations with an observation period longer than 15 years (independent of the scenario). However, for many of the stations with a less long or dense observation history, the discrepancies in estimated velocities already were much larger than the impact of any NTL in our study. The ITRF2020 is combined at the solution level, and semi-annual and annual signals are fitted to the position time series, so the approaches are quite different in the first place. For this reason, maybe, we could not show that our velocities approach those of the ITRF2020 when we apply NTL, either.

Another validation procedure would be to check for an improvement of local ties of co-located stations, as done by Collilieux et al. [2009] and Seitz et al. [2022]. However, since we are only using the VLBI-technique, we do not have that possibility here (this analysis could be caught up with the DTRF2020). Instead, we use an indirect approach: we artificially introduce discontinuities and divide the observation periods of various stations into a long part, solution A01, and a short part, A02. Thereby, the short parts have lengths of 0.5 to 3 years with a step size of 0.5 years, and for each case we compare the station velocities estimated for A01 and A02 with and without reducing NTL. Ideally, the velocity of A02 would agree more with that of A01 (which is supposed to be the true velocity) when NTL is considered.

The estimated velocities in x, y, and z directions for the distinct solutions of the antennas WETTZELL, Germany, and SESHAN25, China, are shown in Figure 5 . The black lines refer to the respective solutions A01 with the long observation periods, and we observe that the velocities basically agree independent of the application of NTL. The difference between WETTZELL and SESHAN25 is the number of participations in the sessions, with the former having much more ap-

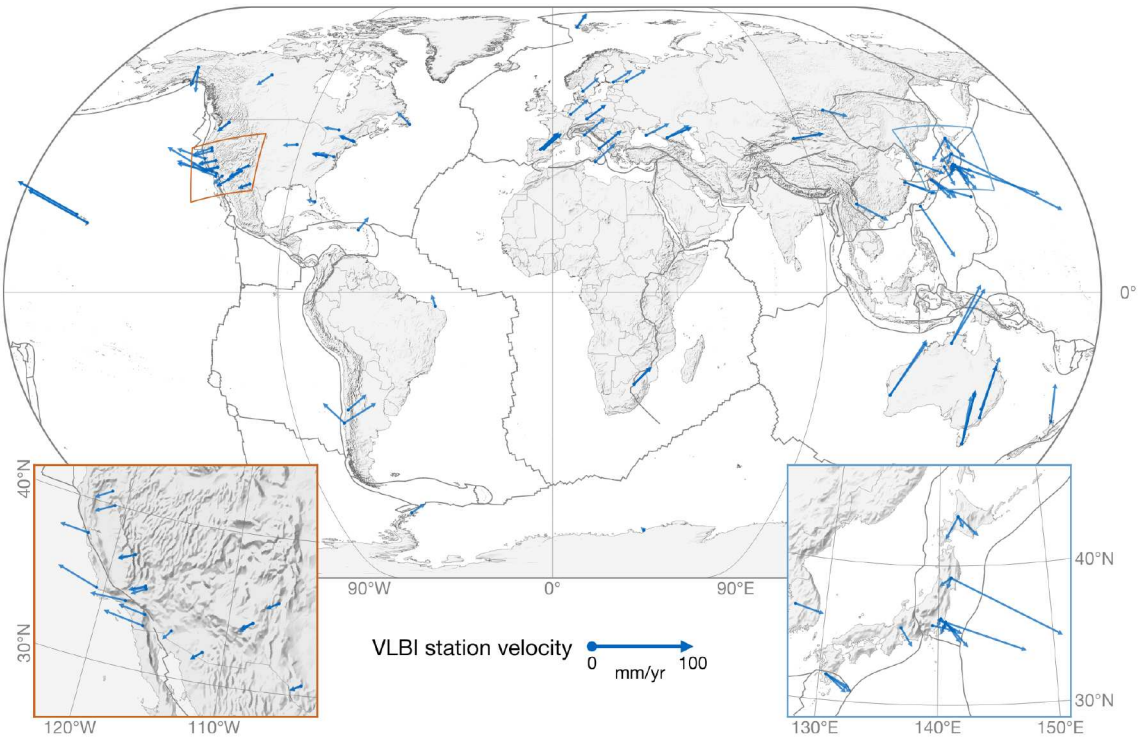

Fig. 3 Estimated antenna positions and horizontal velocities for the scenario with the total NTL applied at the observation level (SUM). In Japan, the distinct antenna velocities due to earthquakes are highly visible.

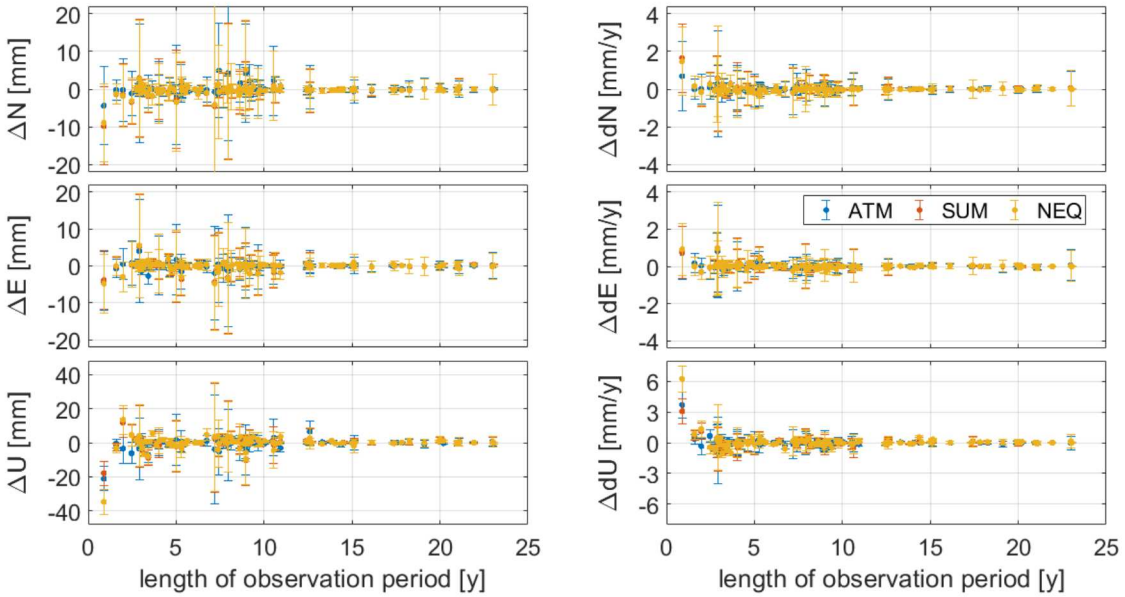

Fig. 4 Changes in estimated local coordinate offsets (left column) and velocities (right column) between the reference scenario REF and the NTL scenarios (blue: ATM, red: SUM, yellow: NEQ). The corresponding antennas (x-axes) are ordered by the length of their observation periods. Top: North, middle: East, bottom: up.

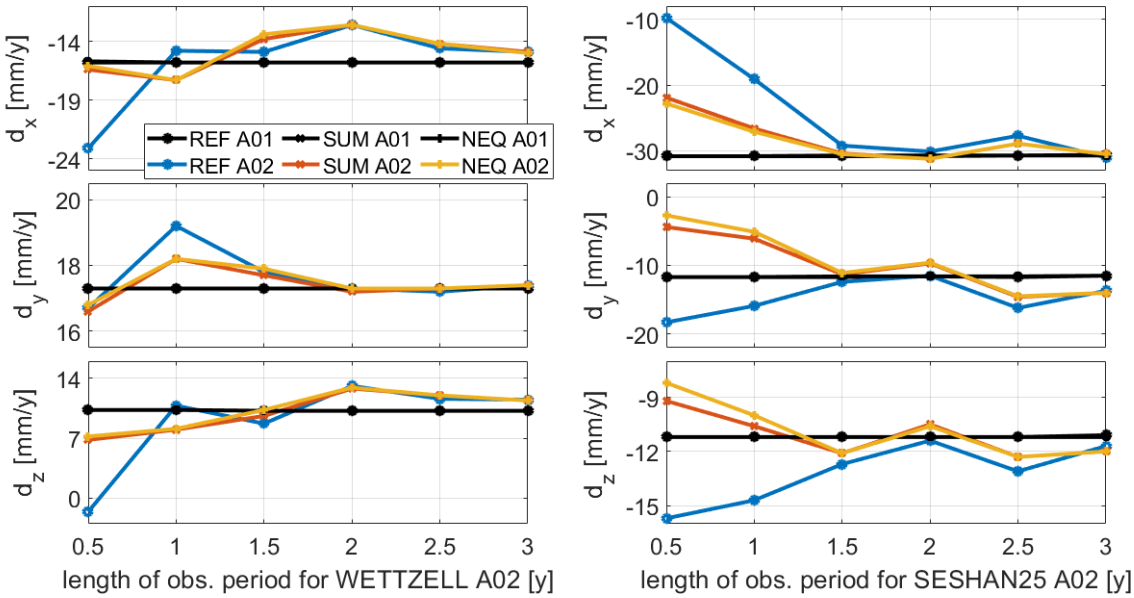

Fig. 5 Estimated velocities for solutions A01 (black) and A02 (colored) for different lengths of the observation periods for solutions A02 (x-axis). The scenarios REF (blue), SUM (red), and NEQ (red) are considered for two sample antennas. Left: WETTZELL, right: SESHAN25. Top: x, middle: y, bottom: z.

pearances than the latter. Hence, the displacement series due to NTL are also reflected more densely for WETTZELL. Both properties will probably promote the stability of the estimated velocities, and this might be confirmed by the agreement for the solutions A02 of WETTZELL for observation periods greater or equal to 2 years, which is not as close for SESHAN25. The impact of NTL is particularly strong for observation periods shorter than 2 years in both examples, and although it is not always the case, the velocities estimated for A02 with the reduction of NTL are often closer to the velocities of A01. But this is only an indication: the ability to improve the velocity estimates for antennas with short observation periods (and hence to include them in a TRF computation) by considering NTL depends on the particular antennas and their session appearances. Furthermore, the relation between the amplitudes of the displacements and the antenna position residuals is important, as well as contingent phase shifts.

4.5 Helmert-transformations

We perform 14-parameter Helmert-transformations at epoch 2010.0 between the TRF from scenario REF and each TRF from the NTL scenarios. That is, we estimate three translations, three rotations, and a scale parameter, as well as their rates. All estimated parameters, their formal errors (standard deviations from the unweighted least-squares adjustment) and the root mean square (RMS) values of the position and velocity residuals can be found in Table 3. Although the parameter values are mostly statistically significant, they are all below 1 mm, just like the RMS values. Hence, there is no major change in the datum or deformation of the networks induced by the reduction of NTL. Since the corresponding parameters for the scenarios SUM and NEQ are very close, we have further evidence for the good agreement of the application levels. The site displacements generated from the NTL models are largest in the vertical direction, so the scale difference is the most interesting transformation parameter here, also because the scale is the datum parameter which can be realised by VLBI. As expected, its values are greater when reducing all NTL components instead of the non-tidal atmospheric loading only. The relevance of trends in the site displacements is highlighted by the differences between the parameters for scenario SU2 as opposed to those for scenarios SUM and NEQ, which reach values of about 0.8 mm for the scale and 1.1 mm for T_y. We will investigate these trends in more detail in the next section.

4.6 Trends in displacement series

To not distort the estimated linear positions in a secular reference frame, it is recommended to remove the long-term trends from any site displacements, including those generated from NTL (Collilieux et al. [2009],

Table 3 Helmert-parameters and their formal errors (in parenthesis) for the transformation at epoch 2010.0 between the reference and each NTL scenario. The rotations R and the scale S are given in mm at the Earth's surface.

parameter	ATM	SUM	NEQ	SU2
T_x [mm]	0.152 (0.023)	-0.281 (0.036)	-0.281 (0.035)	-0.140 (0.064)
$\dot{T}_x$ [mm/y]	0.005 (0.003)	-0.000 (0.004)	0.002 (0.004)	0.031 (0.007)
T_y [mm]	-0.044 (0.024)	-0.200 (0.037)	-0.272 (0.037)	0.848 (0.070)
$\dot{T}_y$ [mm/y]	0.013 (0.003)	-0.004 (0.004)	-0.004 (0.004)	-0.000 (0.007)
T_z [mm]	0.313 (0.022)	0.219 (0.035)	0.222 (0.034)	-0.146 (0.064)
$\dot{T}_z$ [mm/y]	0.007 (0.003)	0.016 (0.004)	0.020 (0.004)	0.012 (0.007)
R_x [mm]	0.079 (0.030)	0.093 (0.047)	0.178 (0.046)	-0.414 (0.088)
$\dot{R}_x$ [mm/y]	-0.010 (0.003)	-0.005 (0.005)	-0.005 (0.005)	0.007 (0.010)
R_y [mm]	0.039 (0.029)	-0.131 (0.046)	-0.141 (0.046)	-0.131 (0.082)
$\dot{R}_y$ [mm/y]	0.008 (0.003)	0.021 (0.005)	0.017 (0.005)	0.044 (0.009)
R_z [mm]	0.033 (0.020)	0.096 (0.031)	0.138 (0.030)	0.199 (0.059)
$\dot{R}_z$ [mm/y]	-0.002 (0.002)	-0.000 (0.003)	0.005 (0.003)	0.002 (0.006)
S [mm]	-0.177 (0.019)	-0.296 (0.031)	-0.288 (0.030)	0.510 (0.056)
$\dot{S}$ [mm/y]	0.006 (0.002)	-0.013 (0.003)	-0.015 (0.003)	0.024 (0.006)
RMS pos. [mm]	0.203	0.315	0.254	0.560
RMS vel. [mm/y]	0.021	0.042	0.041	0.050

Glomsda et al. [2022]). Similarly, Soja et al. [2016] detrend the NTL data before deriving the process noise model for antenna coordinates in their Kalman filter approach for TRF computation. We want to investigate how these trends actually affect the estimated linear motions.

When we subtract the estimated coordinate $\hat{p}_{SU2}(t)$ of some antenna in the scenario SU2 (including trends) from the coordinate $\hat{p}_{SUM}(t)$ in the scenario SUM (excluding trends), then this difference should theoretically be close to the trend in the applied site displacement at the same epoch t (compare Glomsda et al. [2021], Glomsda et al. [2022]):

$$\begin{aligned} & \hat{p}_{SUM}(t) - \hat{p}_{SU2}(t) \;\approx\; \delta^{trend}_{NTL}(t) \\ \Leftrightarrow \quad & \left(\hat{o}_{SUM}(t_0) + (t-t_0)\,\hat{d}_{SUM}\right) \\ & - \left(\hat{o}_{SU2}(t_0) + (t-t_0)\,\hat{d}_{SU2}\right) \\ & \approx\; \delta^{o}_{NTL}(t_0) + (t-t_0)\,\delta^{d}_{NTL}. \end{aligned} \tag{22}$$

The displacements now need to refer to the CF frame, since the estimated antenna coordinates refer to this frame, too. Namely, after the application of datum conditions, our TRF solutions are aligned to DTRF2014 and thus represent a CF frame (compare, e.g., Dong et al. [2003]).

In Fig. 6, we plot the coordinate position and velocity differences against the trend values and drifts of the CF site displacements for the total NTL. Each cross and circle belongs to one antenna solution from our TRFs, and each colour refers to a distinct epoch t. The crosses (circles) represent solutions with an observation period of less (more) than 15 years, and we can see that the approximation in Eq. (22) holds quite well for the majority of solutions, in particular for those with a long observation period.

Next to the antenna motions, the trends in the site displacements also affect the ERP offsets, as is shown in Figure 7. Unlike the differences in the estimated ERP between the other scenarios, the ones for scenarios SUM and SU2 do not vary around 0 but reveal a trend as well. In Section 4.7, we will show that the ERP offsets and the antenna positions and velocities are correlated in a TRF. The trends in Fig. 7 probably reflect the residuals of the approximation in Eq. (22), while the corresponding differences in the ERP rates and celestial pole offsets do not display any systematic behaviour.

To summarize, we have verified that the handling of trends in site displacements (generated from, e.g., NTL) is crucial in the computation of secular reference frames.

4.7 Earth orientation parameters

To analyse the impact of the reduction of NTL on the EOP, we also use our estimated secular TRFs as a priori reference frames to compute single-session solutions. That is, we take the datum-free normal equations for scenarios REF, ATM, SUM, and NEQ, and transform the a priori antenna positions to the values picked from the respective TRFs (compare Bloßfeld [2015]). Dur-

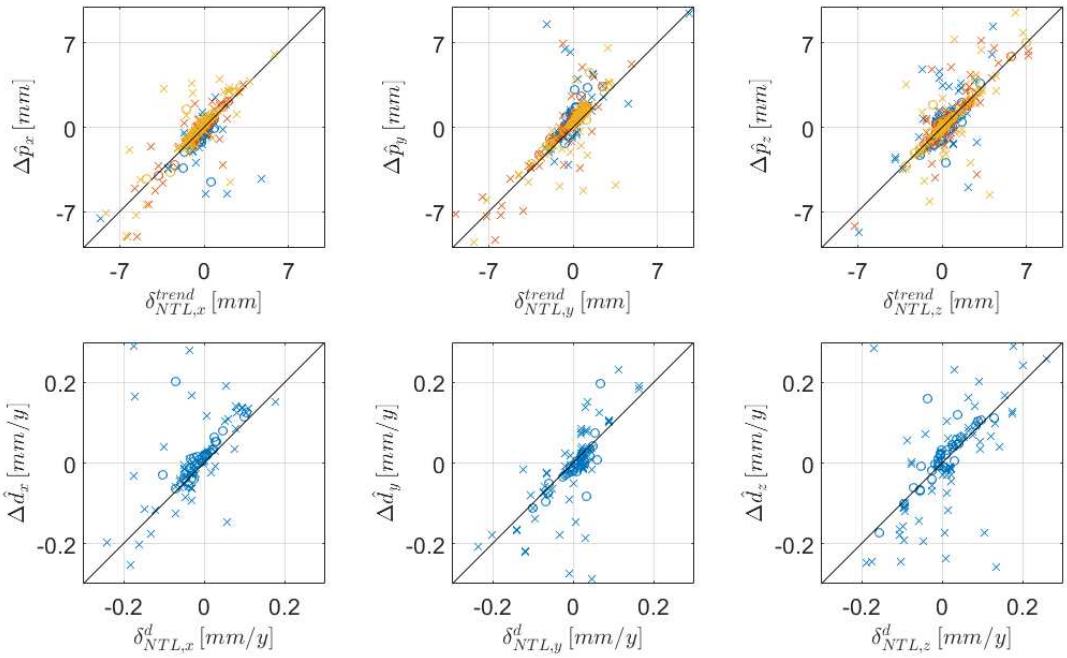

Fig. 6 Differences in estimated coordinate offsets (top row) and velocities (bottom row) between the scenarios SUM and SU2 (y-axes), plotted against the offsets (top row) and drifts (bottom row) of the trend in the corresponding CF site displacements generated from the combined NTL (x-axes). Crosses (circles) refer to antenna solutions with an observation period of less (more) than 15 years. The blue, red, and yellow markers in the top row represent offsets at epochs $t \in \{1990.0, 2010.0, 2020.0\}$, respectively, while the velocities and drifts in the bottom row are equal for all epochs. The black diagonals indicate the lines of identity, and the 1st, 2nd, and 3rd columns refer to the x, y, and z coordinates, respectively.

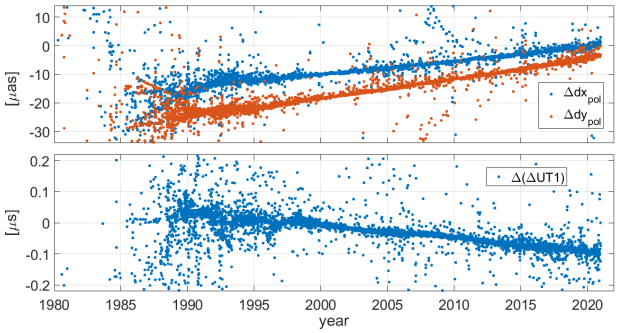

Fig. 7 Top panel: the differences between the polar motion offsets (blue: dx_{pol}, red: dy_{pol}) estimated in the TRFs for scenarios SUM and SU2. Bottom panel: the corresponding differences for $\Delta UT1$.

ing the solution of the session-wise equation systems, the NNT and NNR conditions hence align the estimated antenna positions to our new TRFs instead of the ITRF2020. As we have seen in Section 4.4, the effect of NTL on the estimated antenna motions in the TRF is rather small, and there are hardly any discrepancies between the application levels. Maybe this situation changes for the EOP, which are estimated per session epoch and not overarchingly.

If we pick a scenario from Tab. 1 and compare the EOP from the single-session and the TRF solutions, the differences are significantly larger than the differences between two scenarios for the same solution type. As an example, we show the differences for dy_{pol} in Figure 8. The spread for scenario REF between the single-session and the TRF values for dy_{pol} is about 0.2 mas. The spread between the single-session values for scenarios REF and SUM, on the other hand, is only half as large. And the spread between the TRF values for scenarios REF and SUM is still smaller. Hence, the nature of the EOP estimated in a TRF deviates from that of EOP estimated in single-session solutions.

Since their positions are moving only linearly with time, the station networks are more stable in a TRF. With a fixed celestial reference frame as in our solutions, we might expect the same for the EOP, at least for the ERP (dx_{pol}, dy_{pol}, $\Delta UT1$), which are responsible for the terrestrial part of Earth rotation. When determining the correlation matrix from the covariance matrix of the estimated parameters in Eq. (21), we indeed observe that the correlations between the antenna positions and the ERP offsets (as opposed to their rates in a discontinuous piece-wise linear representation) are the largest among the EOP (see Fig. 9). We conclude

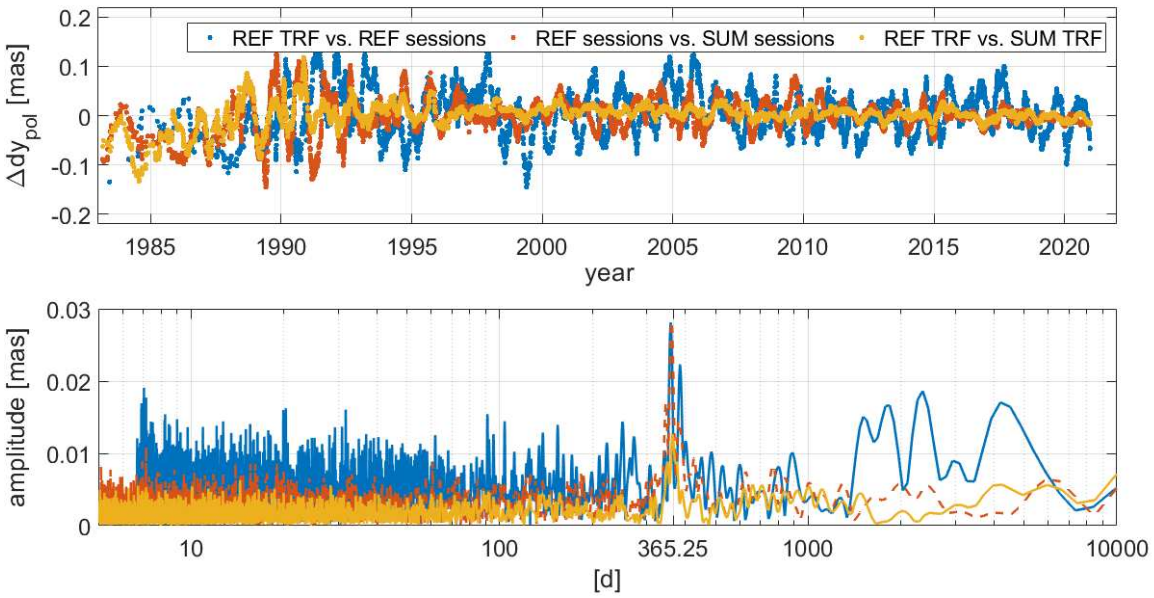

Fig. 8 Top panel: moving 30-day means of the differences between the estimated polar motion offsets dy_{pol} in various solutions. Bottom panel: Lomb-Scargle periodogram of the corresponding original difference series. There is an annual signal for all difference series.

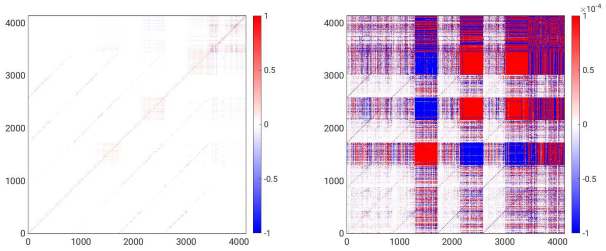

Fig. 9 Left panel: correlation matrix of the estimated antenna positions and EOP for a version of the reference scenario REF where all EOP are reduced except for the years 2000-2002. Right panel: the same matrix, but with a different scale for the color map, so that the non-zero correlations are highlighted. The order of the estimated parameters is: DX_{CIP} (1-430), DY_{CIP} (431-860), LOD (861-1290), $\Delta UT1$ (1291-1720), dx_{pol} rates (1721-2150), dx_{pol} (2151-2580), dy_{pol} rates (2581-3010), dy_{pol} (3011-3440), antenna positions and velocities (3441-4154).

that the ERP offsets will probably show less variability in TRF solutions than in single-session solutions.

The correlation values of the estimated parameters are mostly small, especially for the ERP rates and the celestial pole offsets. The latter are mainly correlated with their counterparts at the same epoch, which is indicated by the diagonals in Figure 9. The ERP offsets and the antenna parameters, however, are also correlated with the EOP at other epochs, including the rates and the celestial pole offsets. Hence, the EOP in a TRF are not as independent as the ones from the single-session solutions. In Tab. 4, we show the WRMS values of the differences between the EOP estimated in the TRF and the respective single-session solutions. The values are given for the reference scenario and the two scenarios with the total NTL applied. The results for both application levels are again very close, and we observe that the discrepancies between the EOP of the two solution types are systematically decreased by about 3-4% when NTL is reduced.

Table 4 WRMS values of the differences between the EOP estimated in the TRF and the respective single-session solutions.

EOP	REF	SUM	NEQ
dx_{pol} [μas]	100.20	96.52	96.82
$\dot{dx}_{pol}$ [μas/d]	71.54	69.72	69.66
dy_{pol} [μas]	113.59	109.04	109.28
$\dot{dy}_{pol}$ [μas/d]	75.24	72.59	72.89
$\Delta UT1$ [μs]	5.11	4.95	4.96
LOD [μs/d]	3.11	2.99	2.99
DX_{CIP} [μas]	18.25	17.72	17.53
DY_{CIP} [μas]	18.17	17.75	17.70

The application of NTL has yet another effect on the ERP offsets. Figure 8 reveals an annual signal for the differences between dy_{pol} estimated with and without considering NTL, both in the TRF and the single-

Table 5 Annual amplitudes of the differences in the estimated ERP w.r.t. the reference scenario without the reduction of NTL.

ERP	ATM	SUM	NEQ
dx_{pol} [μas]	6.06	8.12	8.33
dy_{pol} [μas]	2.87	6.87	7.34
$\Delta UT1$ [μs]	0.18	0.28	0.31

session solutions. This annual signal w.r.t. scenario REF appears for the scenarios ATM, SUM, and NEQ, and the corresponding amplitudes for the TRF solutions are listed in Table 5. Generally, the annual signal in the differences is larger when the total NTL is applied than when only the non-tidal atmospheric loading is applied, and the application level is little relevant. The size of the signal is about half of the WRMS values of the differences, compare Figure 10.

When comparing our EOP with external data, i.e., the 14 C04 (Bizouard et al. [2019]) and IAU2000 finals series of the IERS, we find that the differences (again expressed as WRMS values) for the ERP offsets are smaller for the TRF solutions (see Tab. 6). For the celestial pole offsets (DX_{CIP} and DY_{CIP}) and the length-of-day (LOD, the negative rate of $\Delta UT1$), this is also mostly the case, but the percentage changes are less significant (at least compared to the polar motion offsets). This might confirm that the ERP offsets actually are more stable in a TRF solution, since the external series have been derived from the combination of various single-technique series and thus should be quite robust, too.

The deviations between scenario REF and the NTL scenarios are all significantly smaller than the deviations to the reference series (i.e., the current precision level), which was also reported by, e.g., Petrov and Boy [2004], or Collilieux et al. [2009]. In Fig. 10, we show the corresponding WRMS values for both single-session and TRF solutions. First, we observe that the ERP offsets do not behave like their rates and the celestial pole offsets. The ERP are parameterized as discontinuous piece-wise linear functions per session. If constant site displacements are applied in a single session, as with scenario NEQ, then mainly an ERP's offset will be shifted, while only a minor impact on its rate is expected. If, on the other hand, the site displacements have a large intra-session variation, then also an ERP's rate will probably change more strongly, while its offset might only reflect the average level of the displacements. This is potentially the case in scenario SUM. As a consequence, we expect a significant deviation between the results for the two application levels for the ERP rates rather than the ERP offsets. This is exactly

Table 6 EOP differences w.r.t. external series for the reference scenario REF ("rel. diff." means "relative difference").

EOP	solution	WRMS 14 C04	WRMS finals
dx_{pol} [μas]	TRF	96.2	103.6
	session-wise	118.7	126.4
	rel. diff.	23.5%	22.0%
dy_{pol} [μas]	TRF	98.4	107.8
	session-wise	123.5	130.0
	rel. diff.	25.4%	20.5%
$\Delta UT1$ [μs]	TRF	13.7	13.4
	session-wise	14.0	13.9
	rel. diff.	2.6%	3.6%
LOD [μs/d]	TRF	14.2	14.2
	session-wise	14.2	14.4
	rel. diff.	0.3	1.9%
DX_{CIP} [μas]	TRF	42.3	47.2
	session-wise	41.9	47.3
	rel. diff.	-1.0%	0.2%
DY_{CIP} [μas]	TRF	42.0	46.9
	session-wise	42.0	47.0
	rel. diff.	0.0%	0.3%

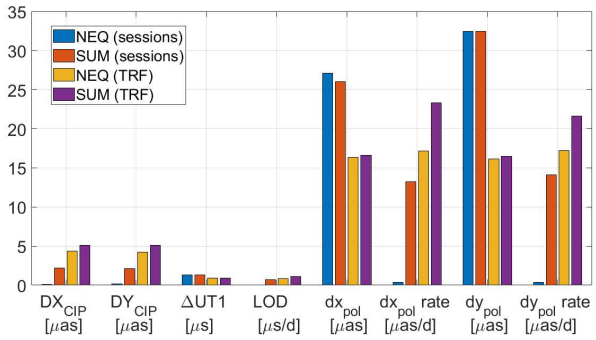

Fig. 10 WRMS values of the differences between the estimated EOP (x-axis) in scenarios SUM or NEQ and those in REF. In each case, the differences refer to either the single-session analysis (red, blue) or the TRF (purple, yellow).

what we see in Figure 10, and what Glomsda et al. [2020] have found in the VLBI single-session analysis before.

We also observe different properties for the TRF and the single-session solutions again. Earlier, we claimed that the EOP between the distinct session epochs are correlated in a TRF solution, and that their time series will be less noisy than for the single-session solutions. The first assumption is reflected by the fact that the impact of NTL at the normal equation level on the ERP rates is significantly larger in the TRF solution. The second assumption might be supported by the fact that the influence of NTL on the ERP offsets is smaller in the TRF solution for both application levels.

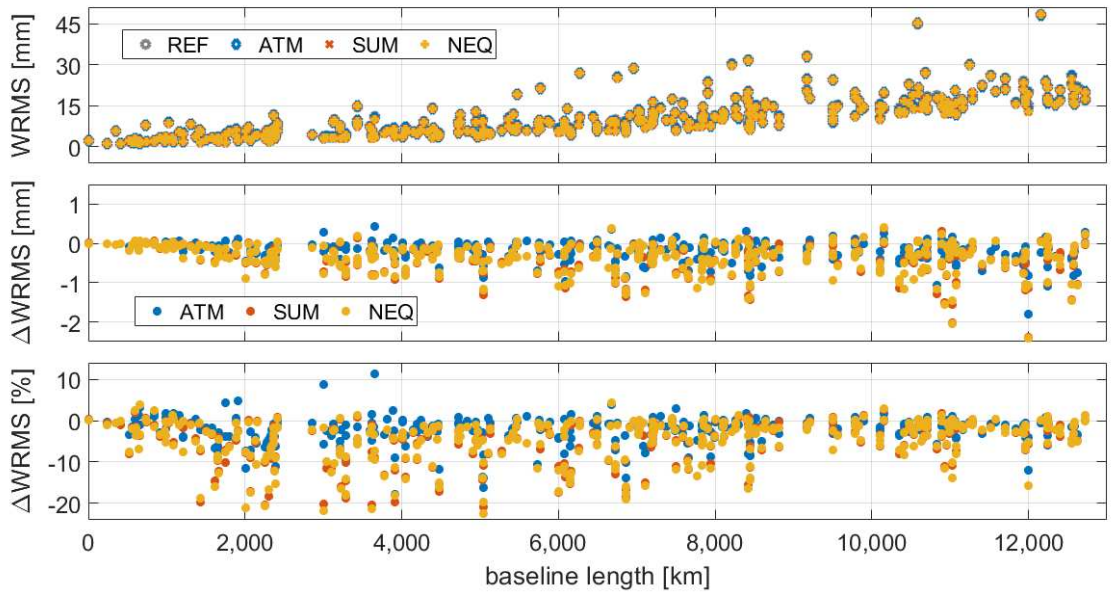

Fig. 11 Baseline length repeatabilities (top) for single-session solutions with corresponding TRFs as a priori reference frames, as well as the absolute (middle) and relative changes (bottom) in the former w.r.t. the scenario without any reduction of NTL.

Together, we note that the impact of NTL is more distributed between ERP offsets and rates in TRF than in single-session solutions for both levels. Finally, we find that the celestial pole offsets behave like the ERP rates. Their connection with the terrestrial site displacements is rather weak, and their correlation structure resembles that of the rates, too (compare Fig. 9 again).

In absolute numbers, the impact of NTL on the ERP offsets did not increase compared to previous VLBI studies. Petrov and Boy [2004] report RMS values of 100 prad for polar motion ($\approx$ 0.02 mas) and $\Delta UT1$ ($\approx$ 0.001 ms) when applying the horizontal component of atmospheric loading. When reducing all components of NTL, Roggenbuck et al. [2015] and Männel et al. [2019] obtain changes in polar motion and $\Delta UT1$ usually below 0.1 mas and 0.003 ms, respectively, which will provide (W)RMS values close to those of ours and Petrov and Boy [2004]. Only Collilieux et al. [2009] find larger WRMS values of $0.062-0.068$ mas for polar motion, while the value of 0.002 ms for $\Delta UT1$ is again similar to that of the other studies. However, the latter authors apply a combination at solution level.

Since the effect of NTL is concealed by the differences to the reference EOP series, we cannot tell whether the annual signals of Fig. 8 and Table 5 imply a decrease of residual annual signals in the ERP estimates. However, we have good reason to assume this, because the reduction of the total NTL also lessens the annual signals in antenna heights and the scale parameter in similarity transformations of VLBI single-session solutions (e.g., Glomsda et al. [2020]).

4.8 Baseline length repeatabilities

We finally use the single-session solutions for a plausibility check of both the TRFs and the NTL data. In the top panel of Fig. 11, we plot the baseline length repeatabilities (BLR) of the scenarios REF, ATM, SUM, and NEQ, where the BLR equals the WRMS values of the session-wise baseline lengths w.r.t. their long-term linear approximation. In the middle and bottom panels, we show the absolute and relative changes in the BLRs when reducing NTL in the distinct scenarios, respectively. We observe that the BLRs systematically improve by up to 20% when the total NTL is applied at either the observation or the normal equation level in both the TRF and the single-session solutions. For the non-tidal atmospheric loading, the improvement is smaller and some BLRs even degrade slightly. This is a strong confirmation for the benefit of the reduction of NTL. However, the improvement is mainly achieved by modifying the actual observation or normal equations in the single-session solutions: only using an a priori TRF reduced by NTL does not systematically decrease the BLRs. By the way, one should not isolate the computation of a TRF from its application as a priori reference frame in single-session solutions, but consistently reduce NTL in both cases.

5 Conclusion

We have generated various VLBI-only terrestrial reference frames with and without the reduction of NTL. The latter have been applied in the form of antenna site displacements at the observation (i.e., within the theoretical delay model) or the normal equation level of the geodetic parameter estimation process. Trends in the displacement time series have mostly been removed to not distort the estimated antenna velocities, but their relevance has been investigated as well.

Although both the VLBI analysis and the geophysical models for NTL have improved during the last years, the impact of NTL is still quite small. In particular for TRFs, where long-term linear positions are estimated, the non-linear effects of NTL are averaged out for antennas with a sufficiently long and dense observation history. The overall statistics and the formal errors of the estimation process hardly change. Nevertheless, for stations with only short observation histories or sparse data, the reduction of NTL will be relevant and beneficial. The application of NTL at the normal equation level is a suitable approximation for the application at the observation level, since the results for the linear station motions agree very well for both approaches.

The effect of NTL is more striking for the epoch-wise estimated Earth orientation parameters. While the absolute changes are small as well, we observe quite different behaviours for the Earth rotation parameter offsets compared to those of their rates and the celestial pole offsets. The former have a larger correlation with the estimated antenna positions in the TRF than the latter, while all EOP are mathematically uncorellated between the single-session solutions. As a consequence, the variability and the dependence on NTL of the EOP is also different between TRF and single-session solutions. The ERP rates are more affected by the sub-diurnal variation of the site displacements, thus the choice of the application level is especially relevant for them (in contrast to the ERP offsets). Finally, there is an annual signal in the differences between the ERP offsets estimated with and without the reduction of (the total) NTL.

Trends in the time series of site displacements affect both estimated antenna positions and ERP offsets. That is, the estimated positions change by about the size of the trends in the displacements, and the remainder is transferred to the ERP. Hence, it is crucial to identify and handle trends in the NTL data.

After all, it appears that the precision of VLBI results (both TRF and single-session solutions) is still suffering from the sparse observation network and the sub-network variations between the distinct sessions. Furthermore, unmodelled errors such as radio source structure (e.g., Anderson and Xu [2018]) might impair a larger impact of the reduction of NTL. Maybe the increased precision of the next generation system, the VLBI Global Observing System (VGOS, e.g., Niell et al. [2018]), will also increase the significance of the reduction of NTL. Nevertheless, as confirmed by the improvement of the baseline length repeatabilities, the benefits are already systematic for the legacy system (e.g., Glomsda et al. [2020]), so the total NTL should generally be reduced in routine VLBI analyses.

Acknowledgements We thank the IVS and its member institutions for generating and sharing the VLBI observation data. We also thank the GGFC for providing the NTL data for the ITRS 2020 realization. Without both of them, this study would not have been possible. Last but not least, we thank Daniel Scherer for creating Figure 3.

Data Availability Statement

The VLBI observation data can be found at *ftp://cddis.nasa.gov/vlbi/ivsdata/vgosdb/*, and the contribution of the GGFC to the ITRS 2020 realization at *http://loading.u-strasbg.fr/ITRF2020/*. Other data sets generated and analysed during this study are available from the corresponding author on reasonable request.

Author Contribution Statement

MG and MS conceptualized the study. MG prepared most of the non-tidal loading and all the VLBI data. He performed the calculations and analyses, compiled all but one figure and wrote the majority of the manuscript. MS provided the expertise and scripts for computing the TRFs. MB prepared the final format of the non-tidal loading data. MG, MS, and MB discussed the results and the validation strategy. FS supervised the study and provides the basic resources. All authors read and improved the manuscript.

Conflict of interest

The authors declare that they have no conflict of interest.

References

Abbondanza C., Chin T.M., Gross R.S., Heflin M.B., Parker J.W., Soja B.S., van Dam T., and Wu X. (2017), JTRF2014, the JPL Kalman filter and

smoother realization of the International Terrestrial Reference System, J. Geophys. Res. Solid Earth, Vol. 122 (10). pp. 8474–8510. doi:10.1002/2017JB014360

Altamimi Z., Rebischung P., Metivier L., and Collilieux X., ITRF2014: A new release of the International Terrestrial Reference Frame modeling nonlinear station motions, J. Geophys. Res. Solid Earth, Vol. 121 (2016). doi:10.1002/2016JB013098

Altamimi Z., et al., ITRF2020: A new release of the International Terrestrial Reference Frame, to be submitted.

Anderson J.M., and Xu, M.H., Source structure and measurement noise are as important as all other residual sources in geodetic VLBI combined, Journal of Geophysical Research: Solid Earth, Vol. 123, pp. 10,162–10,190 (2018). https://doi.org/10.1029/2018JB015550

Angermann D., Drewes H., Krügel M., Meisel B., Gerstl M., Kelm R., Müller H., Seemüller W., and Tesmer V., ITRS combination center at DGFI: a Terrestrial Reference Frame Realization 2003, Deutsche Geodätische Kommission, Reihe B, München (2004).

Bizouard C., Lambert S., Gattano C., Becker O., and Richard J.Y., The IERS EOP 14C04 solution for Earth orientation parameters consistent with ITRF 2014, J. Geod., Vol. 93, pp. 621-633 (2019).

Blewitt G., and Lavallée D., Effects of annual signals on geodetic velocity, J. Geophys. Res., 107(B7), 2145 (2002). doi:10.1029/2001JB000570

Bloßfeld M., The key role of Satellite Laser Ranging towards the integrated estimation of geometry, rotation and gravitational field of the Earth, PhD thesis, Technische Universität München, Reihe C der Deutschen Geodätischen Kommission (2015). ISBN: 978-3-7696-5157-7

Böhm J., Heinkelmann R., Mendes Cerveira P.J., et al., Atmospheric loading corrections at the observation level in VLBI analysis, J. Geod., Vol. 83, pp. 1107-1113 (2009).

Boy J.-P., GGFC contribution to the ITRS 2020 realization, http://loading.u-strasbg.fr/ITRF2020/ggfc.pdf (2021). Accessed 16 December 2021.

Carrère L., and Lyard F., Modeling the barotropic response of the global ocean to atmospheric wind and pressure forcing - comparisons with observations, Geophys. Res. Lett., 30, 1275 (2003). doi: 10.1029/2002GL016473

Charlot P., Jacobs C.S., Gordon D., et al., The third realization of the International Celestial Reference Frame by very long baseline interferometry, Astronomy & Astrophysics, 644 (2020). doi:10.1051/0004-6361/202038368

Collilieux X., Altamimi Z., Coulot D., van Dam T., and Ray J., Impact of loading effects on determination of the International Terrestrial Reference Frame, Adv. Sp. Res., Vol. 45, pp. 144-154 (2009).

Dach R., Böhm J., Lutz S., Steigenberger P. and Beutler G., Evaluation of the impact of atmospheric pressure loading modelling on GNSS data analysis, J. Geod., Vol. 85, pp. 75-91 (2010).

Dong D., Yunck T., and Heflin M. (2003), Origin of the International Terrestrial Reference Frame, J. Geophys. Res., Vol. 108 (B4), 2200. doi:10.1029/2002JB002035

Eriksson D., and MacMillan D.S., Continental hydrology loading observed by VLBI measurements, J. Geod., Vol. 88, pp. 675-690 (2014).

Farrell W. E., Deformation of the Earth by Surface Loads, Reviews of Geophysics and Space Physics, Vol. 10, No. 3, pp. 761-797 (1972).

Gerstl M., Kelm R., Müller H., and Ehrnsperger W., DOGS-CS - Kombination und Lösung großer Gleichungssysteme, Internal Report, DGFI-TUM, München (2000).

Glomsda M., Bloßfeld M., Seitz M., and Seitz F., Benefits of non-tidal loading applied at distinct levels in VLBI analysis, J. Geod., Vol. 94 (90) (2020). doi:10.1007/s00190-020-01418-z

Glomsda M., Bloßfeld M., Seitz M., and Seitz F., Correcting for site displacements at different levels of the Gauss-Markov model - a case study for geodetic VLBI, Adv. Sp. Res., Vol. 68 (4), pp. 1645-1662 (2021). doi:10.1016/j.asr.2021.04.006

Glomsda M., Bloßfeld M., Seitz M., Angermann D., and Seitz F., Comparison of non-tidal loading data for application in a secular terrestrial reference frame, Earth, Planets and Space, 74:87 (2022). doi:10.1186/s40623-022-01634-1

Hart-Davis M., Piccioni G., Dettmering D., Schwatke C., Passaro M., and Seitz F., EOT20 - A global Empirical Ocean Tide model from multi-mission satellite altimetry, SEANOE (2021). doi:10.17882/79489

Hellmers H., Modiri S., Bachmann S., Thaller D., Bloßfeld M., Seitz M., and Gipson J., Combined IVS contribution to the ITRF2020, IAG Symp. Series (2022).

Hersbach H., Bell B., et al. , The ERA5 global reanalysis, Q. J. R. Meteorol Soc., Vol. 146, pp. 1999-2049 (2020). doi:10.1002/qj.3803

Johnston G., Riddell A., and Hausler G. (2017), The International GNSS Service, in Teunissen, Peter J.G. and Montenbruck O. (Eds.), Springer Handbook of Global Navigation Satellite Systems, 1st ed., pp. 967-982. doi:10.1007/978-3-319-42928-1

Kierulf H.P., Kohler J., Boy J.-P., et. al., Time-varying uplift in Svalbard — an effect of glacial changes, Geophysical Journal International, Vol. 231(3), pp. 1518–1534 (2022) doi:10.1093/gji/ggac264

Koch K.-R., Parameter Estimation and Hypothesis Testing in Linear Models, 2. edition, Springer-Verlag Berlin Heidelberg, original German edition published by Dümmlers, Bonn (1999).

Kwak Y., Gerstl M., Bloßfeld M., Angermann D., Schmid R., and Seitz M., DOGS-RI: new VLBI analysis software at DGFI-TUM, Proceedings of the 23rd EVGA Meeting (2017).

MacMillan D.S., and Gipson J.M., Atmospheric pressure loading parameters from very long baseline interferometry observations, J. Geophys. Res., Vol. 99, pp. 18081–18087 (1994).

MacMillan D.S., Fey A., Gipson J., et al., Galactocentric acceleration in VLBI analysis: Findings of IVS WG8, Astronomy and Astrophysics, 630, 2019. doi:10.1051/0004-6361/201935379

Männel B., Dobslaw H., Dill R., Glaser S., Balidakis K., Thomas M., and Schuh H., Correcting surface loading at the observation level: impact on global GNSS and VLBI station networks, J. Geod., Vol. 93(10), pp. 2003-2017 (2019). doi:10.1007/s00190-019-01298-y

Mémin A., Boy J.-P., and Santamaria-Gómez A. , Correcting GPS measurements for non-tidal loading, GPS Solut. 24:45 (2020). doi:10.1007/s10291-020-0959-3

Niell A., Barrett J., Burns A., et al., Demonstration of a Broadband Very Long Baseline Interferometer System: A New Instrument for High-Precision Space Geodesy, Radio Science, Vol. 53, pp. 1269-1291 (2018).

Nothnagel A., Springer A., Heinz E., Artz T., and de Vicente P., Graviational Deformation Effects. The YEBES40M Case, IVS 2014 General Meeting Proceedings (2014).

Nothnagel A., Artz T., Behrend D., and Malkin Z., International VLBI Service for Geodesy and Astrometry – Delivering high-quality products and embarking on observations of the next generation, J. Geod., Vol. 91 (7), pp. 711–721 (2017). doi:10.1007/s00190-016-0950-5

Pavlis E., Luceri V., Basoni A., Sarrocco D., Kuzmicz-Cieslak M., Evans K., and Bianco G. (2021), ITRF2020: The International Laser Ranging Service (ILRS) Contribution, presented at AGU Fall Meeting, December 13-17, 2021. doi:10.1002/essoar.10509208.1

Petit G., and Luzum B. (eds.), IERS Conventions (V. 1.3.0), IERS Technical Note 36, Verlag des Bundesamts für Kartographie und Geodäsie, Frankfurt am Main (2010).

Petrov L., and Boy J.-P., Study of the atmospheric pressure loading signal in very long baseline interferometry observations, J. Geophys. Res., 109, B03405 (2004). doi:10.1029/2003JB002500.

Rabbel W., and Zschau J., Static deformations and gravity changes at Earth's surface due to atmospheric loading, J. Geophys., vol. 56, pp. 81-89 (1985).

Roggenbuck, O., Thaller D., Engelhardt G., Franke S., Dach R. and Steigenberger P., Loading-Induced Deformation Due to Atmosphere, Ocean and Hydrology: Model Comparisons and the Impact on Global SLR, VLBI and GNSS Solutions, T. van Dam (eds), REFAG 2014, International Association of Geodesy Symposia, Vol. 146, Springer International Publishing Switzerland (2015).

Seitz M., Bloßfeld M., Angermann D., and Seitz F., DTRF2014: DGFI-TUM's ITRS realization 2014, Advances in Space Research, Vol. 69(6), pp. 2391-2420 (2022). doi:10.1016/j.asr.2021.12.037

Seitz M., Bloßfeld M., Angermann D., and Seitz F., DTRF2020: DGFI-TUM's ITRS realization 2020, to be submitted.

Soja B., Nilsson T., Balidakis K., et al., Determination of a terrestrial reference frame via Kalman filtering of very long baseline interferometry data, J Geod, Vol. 90, pp. 1311–1327 (2016). doi:10.1007/s00190-016-0924-7

Tregoning P., and van Dam T., Effects of atmospheric pressure loading and seven-parameter transformations on estimates of geocenter motion and station heights from space geodetic observations, J. Geophys. Res., Vol. 110, B03408 (2005). doi:10.1029/2004JB003334

Tregoning P., and van Dam T., Atmospheric pressure loading corrections applied to GPS data at the observation level, Geophysical Research Letters, Vol. 32, L22310 (2005). doi:10.1029/2005GL024104

van Dam T.M., Wahr J., Displacements of the Earth's surface due to atmospheric loading: effects on gravity and baseline measurements, J. Geophys. Res., Vol. 92, pp. 1281–1286 (1987).

van Dam T., Wahr J., Milly P., Shmakin A., Blewitt G., Lavallee D., Larson K. et al., Crustal displacements due to continental water loading, Geophys. Res. Lett. 28, pp. 651-654, (2001). doi:10.1029/2000GL012120

van Dam T., Collilieux X., Wuite J. et al., Nontidal ocean loading: amplitudes and potential effects in GPS height time series, J. Geod., Vol. 86, 11, pp. 1043–1057 (2012). doi:10.1007/s00190-012-0564-5

Williams S.D.P., and Penna N.T., Non-tidal ocean loading effects on geodetic GPS heights, Geophys. Res. Lett., Vol. 38, L09314 (2011).

doi:10.1029/2011GL046940
Willis P., Fagard H., Ferrage P., Lemoine F. G., Noll C. E., Noomen R., Otten M., Ries J. C., Rothacher M., Soudarin L., Tavernier G., and Valette J.-J. (2010), The International DORIS Service (IDS): toward maturity, Adv. Space Res., Vol. 45 (12), pp. 1408-1420. doi:10.1016/j.asr.2009.11.018

Danksagung

Zuallererst möchte ich mich bei meinem Doktorvater Prof. Dr.-Ing. habil. Florian Seitz für die großartige Möglichkeit bedanken, als Quereinsteiger am Deutschen Geodätischen Forschungsinstitut der Technischen Universität München (DGFI-TUM) zu promovieren. Da ich ursprünglich ein Studium der Wirtschaftsmathematik abgeschlossen hatte, musste ich mich erst in der Geodäsie zurechtfinden, und ich danke Prof. Seitz herzlich für seine Geduld und seine exzellente Betreuung und Unterstützung während der gesamten Promotionszeit. Das betrifft sowohl die wissenschaftlichen als auch die organisatorischen Herausforderungen, die sich uns in den letzten Jahren gestellt haben.

Ebenso danke ich meinen weiteren Prüfern, Prof. Dr. techn. Johannes Böhm und Prof. Dr. techn. Benedikt Soja, für die fachlich hervorragende Begutachtung meiner Dissertation. Beide sind bedeutende Persönlichkeiten in der VLBI-Gemeinschaft und überaus sympathische Kollegen. Es ist mir eine Ehre, dass sie zu meinen Gutachtern zählen.

Ein riesengroßes Dankeschön hat sich auch mein Mentor Dr.-Ing. Mathis Bloßfeld verdient. Ohne seine großartige und engagierte Unterstützung hätte ich diese wissenschaftliche Leistung nicht vollbringen können. Darüber hinaus hat er auch bei den nicht-fachlichen Fragen immer ein offenes Ohr und einen hilfreichen Rat gehabt, so dass ich mich jederzeit auf ihn verlassen konnte.

Außerdem möchte ich mich herzlich bei Dr.-Ing. Manuela Seitz bedanken, die mit mir die VLBI-Aufgaben des Instituts wahrnimmt und ebenfalls einen sehr großen wissenschaftlichen Beitrag zu meinen Veröffentlichungen geleistet hat. Ich konnte viel von ihr lernen, und vor allem in den letzten Jahren und Monaten hat sie mir sehr geholfen, die Konzentration auf die Promotion hochzuhalten.

Ein weiterer Kollege, der meine Entwicklung stets gefördert hat, ist der Leiter unserer Referenzsystem-Forschungsgruppe, Dr.-Ing. Detlef Angermann. Ich danke auch ihm aufrichtig für die ausgezeichnete fachliche und persönliche Führung und Unterstützung.

Des Weiteren bedanke ich mich sehr bei Dr. rer. nat. Michael Gerstl. Er ist der Programmierer von DOGS-RI, und ohne seine Vorarbeit wäre meine Forschung nicht möglich gewesen. Die meisten meiner Ergebnisse basieren auf dieser Software, und während unserer gemeinsamen Zeit am DGFI-TUM hat er mich hervorragend eingearbeitet. Letzteres gilt ebenso für Younghee Kwak, PhD, meine Vorgängerin im IVS

Analysis Center des DGFI-TUM. Auch ihr danke ich sehr für die gemeinsame Zeit und die vielen lehrreichen Einblicke in die VLBI.

Ich danke auch allen anderen ehemaligen und derzeitigen Kollegen am DGFI-TUM, insbesondere den legendären *DGFI-Kids*, für die angenehme und kurzweilige Atmosphäre am Institut, die sich nicht nur auf die Arbeitszeit beschränkt. Ganz speziell bedanke ich mich bei meinen (ehemaligen) Mit-Doktoranden Dr.-Ing. Alexander Kehm, Dr.-Ing. Felix Müller und Christian Schwatke, die mir während meiner gesamten Zeit in München auch privat zur Seite gestanden haben.

Ohne die externen Kollegen der Geodäsie und insbesondere der VLBI, die die Beobachtungen ermöglichen, durchführen, verarbeiten und zur Verfügung stellen, wäre meine Forschung und Dissertation natürlich ebenfalls undenkbar. Daher bedanke ich mich ausdrücklich auch bei diesen Personen, bei denen ich das Glück hatte, viele auf diversen Konferenzen persönlich kennenzulernen.

Und schließlich bedanke ich mich von Herzen bei ganz lieben Menschen, die nicht in der Geodäsie arbeiten aber trotzdem einen riesigen Anteil am Erfolg meiner Promotion haben. Das sind zum einen meine Eltern, Karola und Hans-Wilhelm, die mir überhaupt erst mein Studium ermöglicht haben, und die bis heute eine große Unterstützung in allen Belangen geblieben sind. Zum anderen ist das meine Verlobte Andrea, die mich durch alle Höhen und Tiefen der Doktorandenzeit be- und geleitet hat, und ohne deren Geduld, Mitgefühl, Antrieb, Hilfe und Zuspruch ich es niemals geschafft hätte...

Du bist mein Ein und Alles.